SELECTED TOPICS IN NANOSCIENCE AND NANOTECHNOLOGY

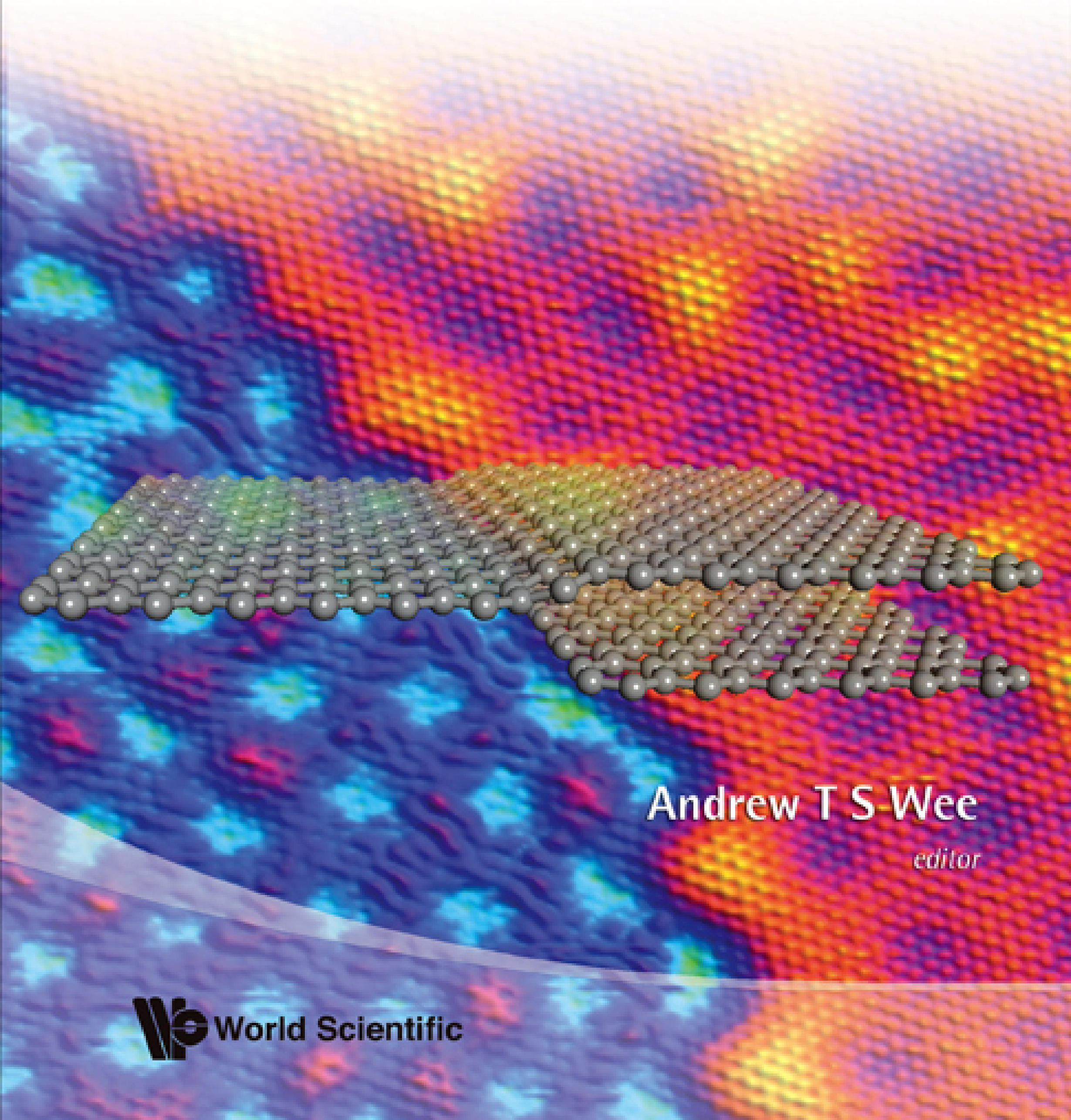

Andrew T S Wee

editor

World Scientific

SELECTED TOPICS IN NANOSCIENCE AND NANOTECHNOLOGY

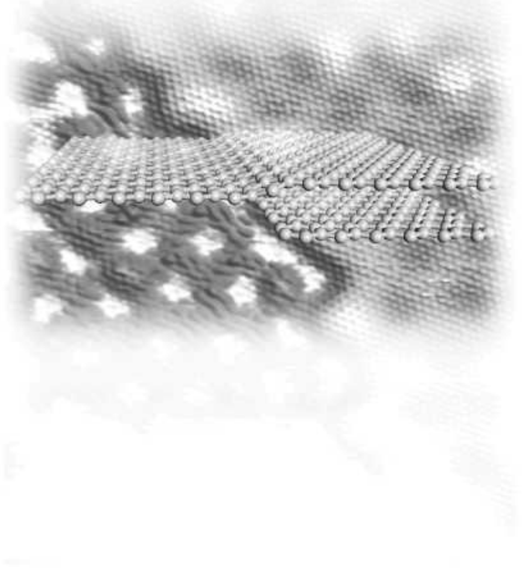

This page intentionally left blank

SELECTED TOPICS IN NANOSCIENCE AND NANOTECHNOLOGY

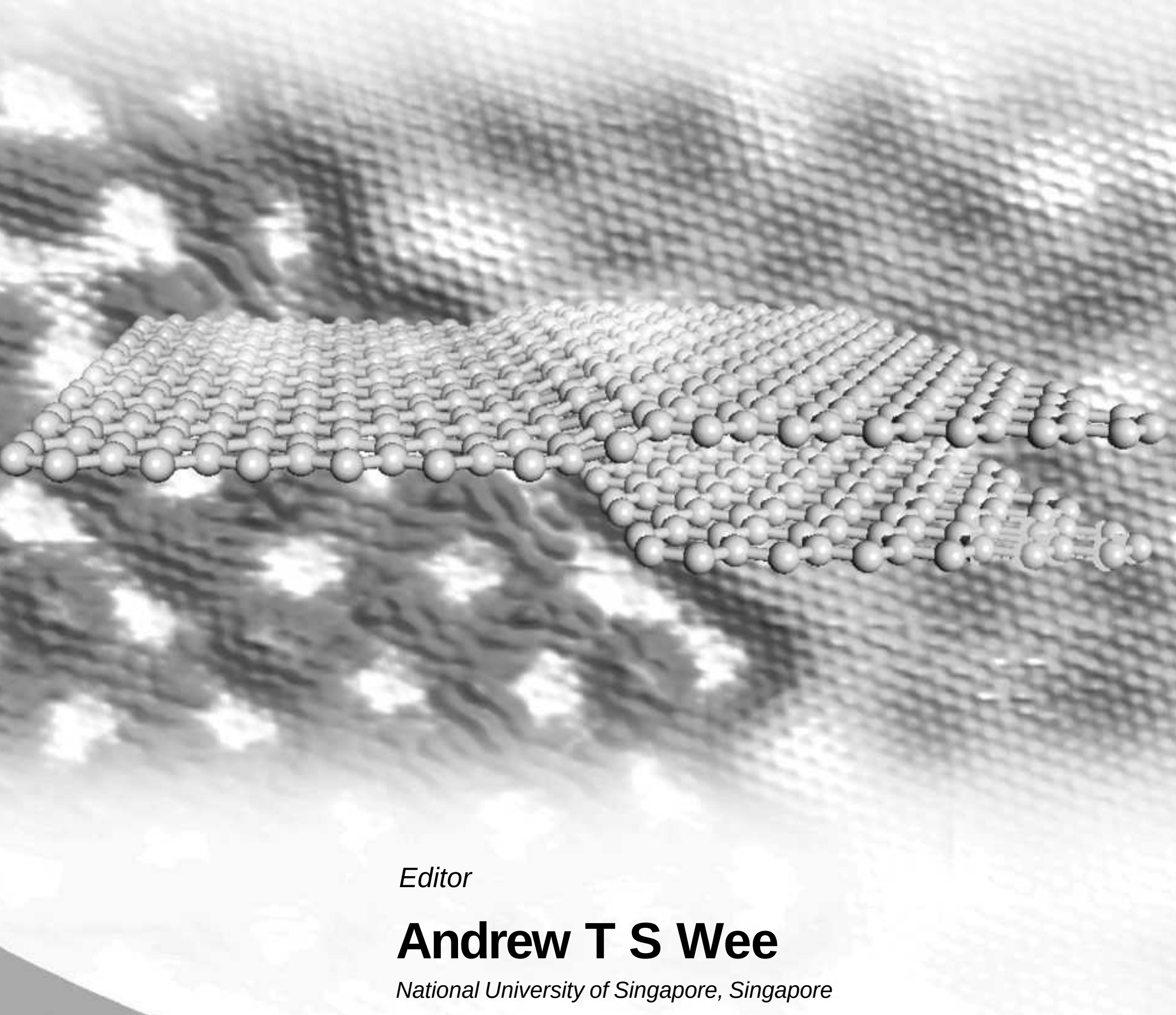

Editor

Andrew T S Wee

National University of Singapore, Singapore

World Scientific

NEW JERSEY • LONDON • SINGAPORE • BEIJING • SHANGHAI • HONG KONG • TAIPEI • CHENNAI

Published by

World Scientific Publishing Co. Pte. Ltd.
5 Toh Tuck Link, Singapore 596224
USA office: 27 Warren Street, Suite 401-402, Hackensack, NJ 07601
UK office: 57 Shelton Street, Covent Garden, London WC2H 9HE

British Library Cataloguing-in-Publication Data
A catalogue record for this book is available from the British Library.

Cover: STM image of Epitaxial Graphene adapted from paper:
Huang H, Chen W, Chen S, Wee ATS
Bottom-up Growth of Epitaxial Graphene on 6H-SiC(0001)
ACS NANO, 2008, **2**(12), pp 2513–2518

SELECTED TOPICS IN NANOSCIENCE AND NANOTECHNOLOGY

ISBN-13 978-981-283-955-8
ISBN-10 981-283-955-0

Typeset by Stallion Press
Email: enquiries@stallionpress.com

Printed in Singapore.

Preface

Nanotechnology is the study of the control of matter on an atomic and molecular scale. Nanotechnology has promised to be one of the important growth areas in the twenty first century: it has the potential to create many new materials and devices with wide-ranging applications in medicine, electronics, energy production and so on. Since the invention of the scanning tunnelling microscope and the discovery of fullerenes in the 1980s, researchers worldwide have devoted much resources and effort to harness the potential of technology at the nanoscale.

This book is a collection of twelve review articles written by experts in their respective fields, and is classified under the sub-headings:

- Scanning Probe Techniques
- Nanofabrication
- Functional Nanomaterials
- Molecular Engineering
- Bionanotechnology and Nanomedicine

Although the coverage is not exhaustive, these reviews are representative of the current research areas in nanoscience and nanotechnology. This book is suitable as a resource volume for a senior undergraduate or introductory graduate course in nanoscience and nanotechnology, as well as for general scientific readership. The articles were originally written for the review journal *COSMOS* (Volume 3 Issue 1 and Volume 4 Issue 2).

We believe you will find this book useful and informative.

Andrew T S Wee (Editor)
National University of Singapore
2009

CONTENTS

Part 1

SCANNING PROBE TECHNIQUES

SCANNING PROBE MICROSCOPY BASED NANOSCALE PATTERNING AND FABRICATION

XIAN NING XIE*, HONG JING CHUNG
and ANDREW THYE SHEN WEE
NUS Nanoscience and Nanotechnology Initiative and
Department of Physics
National University of Singapore
2 Science Drive 3, 117542, Singapore
**nnixxn@nus.edu.sg*

Nanotechnology is vital to the fabrication of integrated circuits, memory devices, display units, biochips and biosensors. Scanning probe microscope (SPM) has emerged to be a unique tool for materials structuring and patterning with atomic and molecular resolution. SPM includes scanning tunneling microscopy (STM) and atomic force microscopy (AFM). In this chapter, we selectively discuss the atomic and molecular manipulation capabilities of STM nanolithography. As for AFM nanolithography, we focus on those nanopatterning techniques involving water and/or air when operated in ambient. The typical methods, mechanisms and applications of selected SPM nanolithographic techniques in nanoscale structuring and fabrication are reviewed.

Keywords: Nanolithography; nanofabrication; scanning probe microscopy; AFM nanolithography.

1. Introduction

Nanotechnology is vital to the fabrication of integrated circuits, memory devices, display units, biochips and biosensors. One of the key processes in nanofabrication is the creation and construction of functional units in the size regime of less than 100 nm. A number of commercial techniques have been developed for nanofabrication, and some typical examples include photolithography, electron beam lithography and focused ion beam lithography. Although these techniques are widely implemented in the manufacturing industry, their high capital and operating cost and multiple-step processes largely restrict their applicability in many important areas. A few new methods appear to be flexible alternatives for nanoscale patterning and fabrication. Some demonstrated novel techniques are molding, embossing, printing, self-assembly and scanning probe microscopy (SPM) nanolithography. These methods have the potential to be low-cost techniques for nanoscale pattern formation and replication.

Among the new techniques, SPM has emerged to be a unique tool for materials structuring and patterning with atomic and molecular resolution.[1] SPM includes scanning tunneling microscopy (STM)[2] and atomic force microscopy (AFM)[3] which were invented in the 1980's for surface characterization. The SPM-based nanolithography has extreme site-specificity and locality, and can be operated in a variety of media such as vacuum, air and fluids. Large families of materials ranging from inorganic, organic, polymer and biological species can be patterned by SPM nanolithography. Table 1 compares the operational characteristics and applications of SPM nanolithography with other lithographic techniques.[4–7] In SPM nanolithography, the pattern formation is based on interactions in the nanometer-sized tip–sample junction. Such interactions may be of a physical nature involving mechanical/electrical forces, and/or of chemical nature involving the break and formation of chemical bonds. The limitations of SPM nanolithography are related to its serial patterning processes, its poor reproducibility and difficulty in the mass production of patterns.

Most STM-based nanofabrication experiments are operated in ultrahigh vacuum (UHV, $< 10^{-9}$ torr) conditions, and the pattern formation is often related to carrier (electron or hole) injections and field applications.[8] The majority of reported AFM nanolithographic experiments are conducted in ambient conditions.[1] The presence of air and the formation of condensed water meniscus in the tip–surface nanojunction allow more mechanisms and routes to nanostructure formation. This is due to the rich physical processes and chemical reactions mediated by air and water during the nanolithographic operations. For example, the water meniscus can facilitate ink transport from the tip to the substrate in dip-pen nanolithography (DPN).[9] The ionic dissociation of water supplies OH^- oxidants in AFM nanooxidation,[10] and the water–bridge-assisted ionic conduction facilitates the local heating and melting of polymer films.[11] Table 2 compares the operational and mechanistic features and applications of STM and AFM nanolithography.[1,8]

In general, STM nanolithography is mostly performed in UHV for high resolution manipulation of single atoms and molecules, although it can also be operated in air and liquids. AFM nanolithography, in addition to its applications in single atom manipulation, is well suited for operations in air or liquids to fabricate relatively larger nanostructures. To avoid overlap in the description of their applications, the atomic and molecular manipulation capabilities of STM nanolithography will be selectively discussed. As for AFM nanolithography, the focus is on those nanopatterning techniques involving water and/or air when operated in ambient. In the following sections, we summarize the typical methods, mechanisms and applications of some SPM nanolithographic techniques in nanoscale structuring and fabrication.

2. STM Nanolithographic Techniques

In STM nanolithography, there are basically three methods of pattern fabrication: (i) direct tip–surface interaction, (ii) field effect and (iii) electron effect.[8]

Table 1. Comparison of SPM nanolithography with other lithographic techniques.

Lithographic techniques	Patterning methods	Operation conditions	Resolution	Advantages	Limitations
SPM	Based on tip–sample interaction	Ambient vacuum or liquid phase	Single atom, A few Å	— Easy to operate — Low cost — Applicable to wide range of materials — High sensitivity and site-specific	— Serial patterning — Controllability and accessibility for large scale production
Photolithography	Selectively exposing parts of substrate to light (often Ultraviolet)	Vacuum	Usually sub 100 nm[4]	— Parallel patterning — Good controllability	— High operation cost — Multiple process steps — Poor accessibility
Electron-beam lithography	Interaction between e-beam and substrate	Vacuum	$\leq 50\,\text{nm}$[5]	— Well developed for research — Good controllability	— High operation cost — Multiple process steps — Poor accessibility
Focus ion beam (FIB) lithography	Interaction between ion-beam and substrate	Vacuum	$\sim 50\,\text{nm}$[6]	— High sensitivity — Good controllability — Well developed for research	— High operation cost — Multiple process steps — Poor accessibility
Nanoimprint lithography (NIL)	Mechanical deformation of imprint resist	Vacuum or ambient	$\sim 100\,\text{nm}$[7]	— Low cost — High throughput — Parallel writing	— Precision issue — Multiple steps for large scale production

Table 2. Operational and mechanistic features and applications of STM and AFM nanolithography.[1,8]

	STM nanolithography	AFM nanolithography
Tip control	Feedback based on tunneling current	Feedback based on force
Operation medium	Commonly operated in UHV conditions Operations in air and liquids are possible	Commonly operated in vacuum, air and liquids
Nanolithography mechanism	Physical processes and chemical reactions in the tip–sample nanojunction.	Force-assisted and bias-assisted physical processes and chemical reactions in the tip–sample nanojunction
Pattern resolution and mass production	Single atom resolution readily achievable Mass production not demonstrated	Single atom resolution achievable Mass production demonstrated by millipede technique
Availability of tips	Commercially available Home-making of tips is easy Tip radius: atomically sharp, a few Å	Commercially available Home-making of tips is difficult Tip radius: typically 20–50 nm
Substrates used	Conducting and semiconducting materials such as metals and semiconductors	Insulating, semiconducting and conducting materials such as inorganic, organic, polymeric and biological materials

The tip–surface distance is determined by the tunneling current in an exponential relation. So by varying the tunneling current in different regimes, one may push or pull atoms and molecules through direct tip–surface interactions. The field effect is important in STM nanolithography because the typical field applied to the tip–surface nanojunction is in the order of 10^{9-10} V/m. Such an extremely high field may induce processes such as field evaporation of materials and the repositioning of dipolar molecules on a surface. In addition, the tunneling current can provide Joule heating of materials, and this may lead to the excitation of adsorbate vibrational states. These operational modes can facilitate the removal, addition, diffusion, desoprtion and chemical reaction of atoms and molecules in the tip–surface nanojunction.

2.1. *Pattern formation by direct tip–surface interactions*

Lateral and vertical manipulations are commonly used for atomic and molecular manipulation by direct tip–surface interactions. In STM lateral manipulation, three modes are demonstrated to displace the adsorbates laterally on the substrate. The pull mode makes use of the weak attractive tip–surface interaction, such that an adatom jumps to a neighboring surface site following the tip's trajectory. In the push mode, the repulsive tip–surface interaction is so strong that the surface atom jumps to a neighboring site to escape from the tip. The slide mode involves the direct interaction of adsorbates with the tip in which the adsorbates' lateral movement follows exactly the trajectory of the tip. The three modes can be distinguished by recording the tunneling current as a function of lateral position of the tip in the constant-height scanning mode.[8] The selection of the modes for manipulation depends on the tunneling parameters and the chemical nature between the tip and substrate surface.

There are two approaches in vertical manipulation. The first is fully based on a voltage pulse to transfer an adsorbate from the surface to the tip, or vice versa, depending on the polarity of the voltage pulse. In this case, the tip is first positioned above the adsorbate at certain tip–adsorbate distance. The application of voltage pulse enables the attachment of the adsorbate to the tip. When the adsorbate has been carried by the tip to the desired site, it is released from the tip by the application of an opposite pulse. In the second approach, the adsorbate is first attached to the tip apex *via* tip–adsorbate chemical binding. The tip is then repositioned to the desired surface site, and the adsorbate is delivered to the site by applying a voltage pulse to the tip.

Bartels *et al.* performed detailed tip height measurements during STM manipulations of single atoms, molecules, and dimers on a Cu(2 1 1) surface.[12] They identified both attractive manipulation of Cu, Pb atoms and Pb dimers and repulsive manipulation of CO molecules. Using the pull mode, discontinuous hopping of Cu and Pb atoms from one adsorption site to the next can be induced. Pb dimers were pulled by STM with repeated single, double, and triple hops. They also found that Pb atoms can be slid continuously by the tip. In the push mode, they observed that the CO adsorbate is repelled by the approaching tip and perform single adsorption hops away from the tip. Moreover, the authors demonstrated that controlled initiation of hops over multiple adsorption site distances is possible and that the different hopping width can be used in turn to probe effects of adjacent surface defects on the local hopping barrier.

Recently, Hla *et al.* described a complete picture of how single Ag atoms move on the various potential energy landscapes of a Ag(1 1 1) surface during a quantum corral construction using STM manipulation at 6 K.[13] The threshold tunneling resistance and tip-height to move the Ag atom across the surface were experimentally measured to be ∼ 210 kΩ and ∼1.3 Å, respectively. Through the STM atomic manipulation signals, they derived detailed surface-orientation-dependent atom movement behaviors that contain atomic-level tribological information of the surface. Figure 1 illustrates the processes of constructing the quantum corral consisting of 36 Ag atoms on the Ag(1 1 1) surface using STM manipulation. Initially, each Ag atom was positioned at the center of the corral (see Figs. 1(a) and 1(c)) and then relocated to a final position. The manipulation path of the first atom was chosen along a surface atomic close-packed (CP) row (see Fig. 1(c)), i.e., along

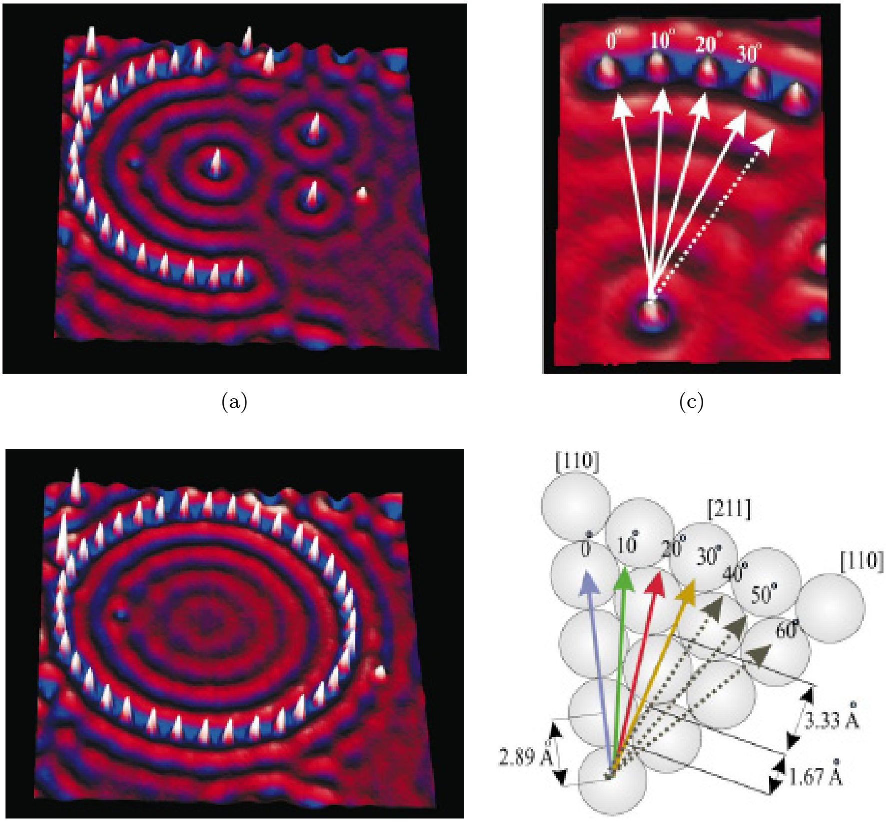

(a) (c)

(b) (d)

Fig. 1. Quantum corral construction. 3D STM images show (a) during construction and (b) after completion of the corral. 36 Ag atoms (white protrusions) are used (diameter = 31.2 nm). A STM image (c) and a sphere model (d) demonstrate the tip–paths and the surface geometry encountered during manipulations. Reprinted with permission from Ref. 13, © 2003, The American Physical Society.

[1 1 0]. The subsequent atoms were moved along a direction 10° rotated from the previous paths (see Figs. 1(c) and 1(d)). Thus a total of 36 atoms were required for 360° to complete a circle. In the manipulation, the Ag atoms were moved in the pull mode along CP rows by attractive tip-atom interactions. The CP rows are the most favored atom-traveling paths due to their lower diffusion barrier. The hop length was determined to be 2.89 Å, and complex manipulation signals were observed when the paths deviated from the CP rows.

In another work, Bartels *et al.* demonstrated a reliable procedure for controlled vertical transfer of single CO molecules between a Cu(1 1 1) surface and STM tip and vice versa. Figure 2 shows the idealized sketch of the picking up and putting down procedures of CO molecules on Cu(1 1 1).[14] The CO molecule is adsorbed in on-top sites and stands upright on the Cu surface with the C bonding to the

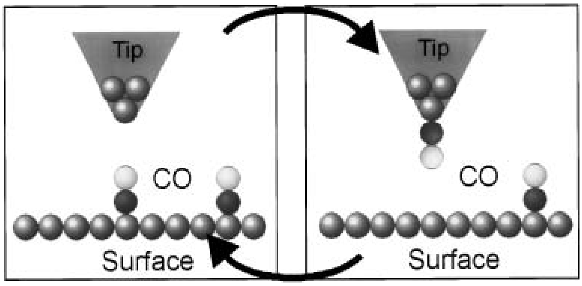

Fig. 2. Sketch of the picking up and putting down procedures of CO molecules on Cu(1 1 1). Notice that the CO stands upright on the surface and has to switch its orientation when being transferred to the tip. Reprinted with permission from Ref. 14, © 1997, American Institute of Physics.

metal atoms. As the CO molecules have similar adsorption geometries on isolated Cu atoms adsorbed on Cu substrates, the CO molecules have to flip around when being transferred vertically. This extended number of degrees of freedom associated with a diatomic molecule makes the manipulation more complicated than in the case of single atoms. At first, a tip voltage bias of +3 V was used to transfer the CO molecule from the surface to the tip. When the tip was repositioned at the target sites, the CO molecule was released to the surface by positioning the tip at −2.5 V bias and then ramping the voltage from −4.5 to −0.5 V. Such a procedure could be repeated several times without breaking the tip or changing the substrate, thus enabling the transfer of more than one molecule to different destinations. The authors observed that during vertical transfer, the CO molecules do not dissociate; and the picking up and putting down of the molecules do not disturb neighboring CO molecules or change the initial tip structure. In addition to CO transfer, the authors also showed that with a tip having a single CO molecule at its apex, chemical contrast can be achieved allowing discrimination between adsorbed CO molecules and oxygen atoms, which look very similar to the bare metallic tip.

2.2. *Pattern formation by field effect*

The effect whereby an electric field drives the diffusion of atoms on a surface was first observed in field ion microscopy. This effect was applied in STM nanolithography by Whitman *et al.* to manipulate adsorbed atoms and create new structures on room-temperature surfaces.[15] Diffusion of single atoms over a surface is usually seen as a random walk process through small potential barriers. At the typical STM tip voltage of a few mV, the driving force is so small that the random distribution of adatoms is not modified. However, when a high tip voltage of a few V is used, the localized high field would significantly modify the surface potential energy distribution, thus leading to the directed-diffusion of adatoms on the surface.

Whitman *et al.* demonstrated that by applying an appropriate voltage pulse between the sample and tip, adsorbed atoms can be induced to diffuse into the region beneath the tip.[15] The field-induced diffusion occurs preferentially towards the tip during the voltage pulse because of the local potential energy gradient arising from the interaction of the adsorbate dipole moment with the electric field gradient at the surface. Using different surface conditions and pulse parameters, the authors created Cs structures from one nanometer to a few tens of nanometers on GaAs(1 1 0) and InSb(1 1 0) surfaces. The patterns fabricated by field-induced diffusion include novel structures that do not form naturally following room-temperature adsorption. The authors also pointed out that the field-induced diffusion may be a generic technique suitable for moving atoms and molecules on both semiconductor and metal surfaces.

In the above work, Cs atoms are field-induced to move due to their high static dipole moment. Méndez *et al.* later showed that the field effect is more general and can be used even in systems that have a small dipole moment, such as the surface Au adatoms of Au(1 1 1).[16] By applying a voltage and maintaining a constant tunneling current, the authors were able to produce protrusions under the tip of several atom-heights and small clusters occupying large areas. They studied the influence of the time duration of the pulse and the voltage amplitude. Surface modifications were produced at a low field strength of 0.2 V/Å. It was suggested that clusters are produced by an increase of the density of free adatoms in the high electric field region. Figure 3(a) shows a STM image ($63 \times 63\,\mathrm{nm}^2$) recorded for the Au(1 1 1) surface before surface modification. After applying a 2.5 V pulse of 30 s duration, bright clusters were fabricated on the surface by field-induced diffusion (see Fig. 3(b)).

2.3. *Pattern formation by electron effect*

Shen *et al.* used the STM tip as an atomic-sized electron source to desorb hydrogen atoms from a Si(1 0 0) surface.[17] By controlling the dose of incident electrons, a

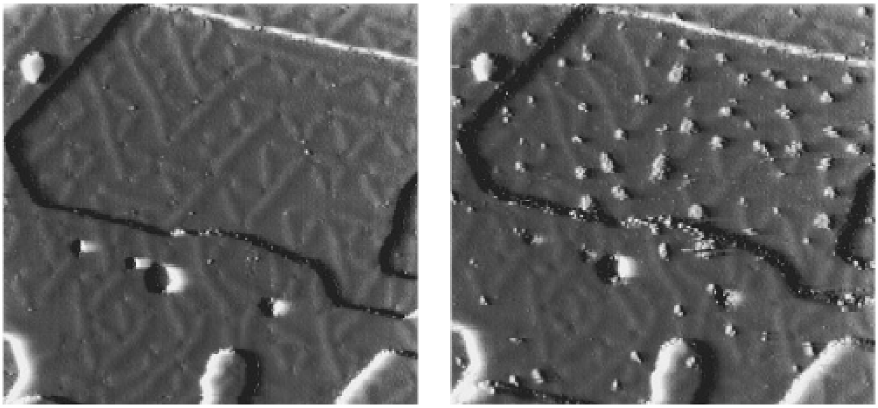

(a) (b)

Fig. 3. Modifications produced by a 2.5 V pulse of 30 s duration. (a) STM image ($63 \times 63\,\mathrm{nm}^2$) of the region before the pulse. (b) Image taken immediately after the pulse. Reprinted with permission from Ref. 16, © 1996, American Vacuum Society.

countable number of desoption sites were created and the field and cross section of these sites were thereby obtained. The authors observed two distinct mechanisms: (i) direct electron excitation of the Si–H bond by field-emission electrons and (ii) an atomic resolution mechanism that involves multiple-vibrational excitation by tunneling electrons at low applied tip voltage. In the second case, H desorption arises from the accumulation of a large number ($\sim$10) of inelastic electron interactions. This vibrational heating effect by electrons is potentially useful for controlling surface reactions involving adsorbed individual atoms and molecules.

Soukiassian *et al.* investigated in detail the influence of various parameters (i.e., tunneling current, mode of excitation, tip structure and doping of substrate) on the extraction yield.[18] They used both p- and n-type silicon substrates, chose to keep the surface voltage constant and explored the detailed current dependence of the extraction yield. They obtained experimental results which cannot be explained by the vibrational heating model involving a large number of inelastic electron collisions. Their observations suggest a model involving coherent multiple excitation of electrons. In this model, the tunneling electrons are resonantly scattered by the adsorbates producing single electron multiple vibrational adsorbate excitations. The large number of excited vibrational quanta is associated with dramatic changes of the Si–H bonds and of the scattered electron wave functions.

Recently, Nouchi *et al.* reported that carrier injection into C_{60} close-packed layers leads to a ring-shaped distribution of C_{60} polymers.[19] In their experiments, a closed-packed structure of C_{60} was first formed on a Si(1 1 1)-7 × 7 surface. To induce polymerization of C_{60} molecules, the authors performed carrier injection by application of a certain bias voltage for durations of 30 s. It was observed that continued carrier injections enlarge the ring, and both electrons and holes can induce polymerization and depolymerization of C_{60}. Figure 4 shows the evolution of a C_{60} polymer ring by sequential injection of carriers from an STM tip. The outer diameter of the ring shown in Fig. 4(a) is 23 nm. After further hole injections (see Figs. 4(b) and 4(c)) and electron injection (see Fig. 4(d)), the ring diameter is finally enlarged to 38 nm (see Fig. 4(d)). The authors proposed that injected carriers interact with inter- and/or intra-molecular phonons through electron–phonon coupling, and dissipate their energy gradually as they spread from the injection point. Carriers with energies above a certain threshold can induce the polymerization and depolymerization of C_{60}. Therefore, carrier injection at higher bias voltage results in C_{60} rings with larger diameters.

3. AFM Nanolithographic Techniques

Numerous AFM lithographic techniques have been developed in the last two decades. Generally, these techniques can be classified into two groups based on their operational principles: force-assisted and bias-assisted AFM nanolithography (see Table 3).[1] In force-assisted AFM nanolithography, a large force is applied to the tip for pattern fabrication, and the tip–surface interaction is mainly mechanical. Typical methods in this category include mechanical indentation and plowing,

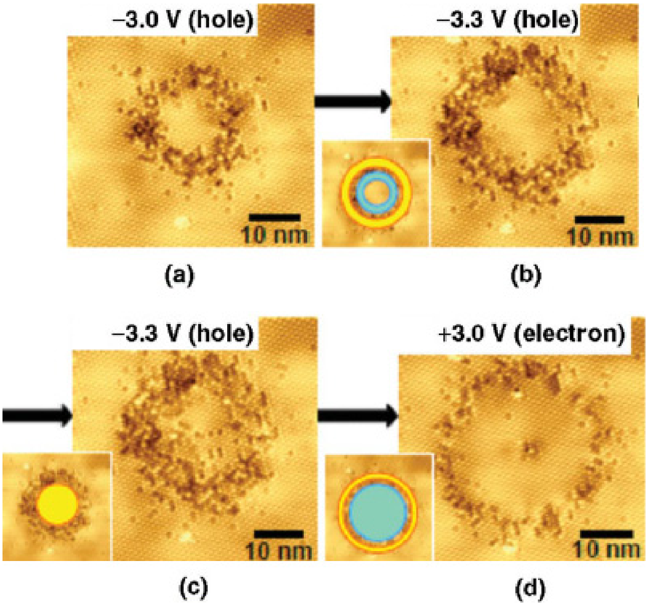

Fig. 4. Evolution of a ring of C_{60} polymers by sequential carrier injection. STM images acquired sequentially after carrier injections into the same point with different bias values. The injection point is at the center of the rings. Attached insets display areas in which polymerization (yellow) and depolymerization (blue) events occurred by the carrier injection. (a) Ring formed by hole injection at −3 V sample bias. (b) Ring enlarged by hole injection at −3.3 V bias. (c) Sequential hole injection at the same bias induces polymerization around the center of the ring. (d) Ring enlarged by electron injection at +3 V sample bias. Reprinted with permission from Ref. 19, © 2006, The American Physical Society.

Table 3. Comparison of force-assisted and bias-assisted AFM nanolithographic techniques.[1]

	Force-assisted AFM nanolithography	Bias-assisted AFM nanolithography
Operational principle	Large force applied to tip	Bias applied to tip
Tip–surface interaction	Mainly mechanical	Tip acts as nanoscale electrode and induce physical and/or chemical processes
Pattern formation modes	Patterns are formed by mechanically scratching, pulling or pushing the surface atoms and molecules with the probe	Under high field, electrostatic, electrochemical, field emission, dielectric breakdown and explosive gas discharge processes can be initiated to facilitate pattern formation
Typical examples	Indentation, plowing, manipulation, thermomechanical writing and dip-pen nanolithography (DPN)	Nanooxidation, field evaporation, electrochemical deposition and reactions, electrical cutting and nicking, electrostatic deformation, nanoexplosion and charge deposition

thermomechanical writing, nanomanipulation and dip-pen nanolithography (DPN). As for bias-assisted AFM nanolithography, the AFM tip is biased to create a localized electric field in the regime of 10^8–10^{10} V/m, and the tip acts as a nanoscale electrode for current injection or collection. Depending on the magnitude of tip bias and substrate materials, the application of tip voltage can lead to nanooxidation, electrochemical deposition, electrostatic attraction, nanoscale explosion and shock wave propagation.[1] In the following sections, we discuss some selected techniques in force- and bias-assisted AFM nanolithography.

3.1. *Dip-pen nanolithography (DPN)*

DPN was developed by Mirkin *et al.* to deliver collections of molecules in a positive printing mode.[9] It is an AFM-based direct-write lithographic technique in which the AFM probe is used as a pen to directly deliver materials (inks) to a nanoscopic region on a target substrate. In most cases, the transport of ink molecules from the tip to the substrate is mediated by a water meniscus which is formed through capillary condensation (see Fig. 5). Depending on the selection of ink molecules, DPN is capable of creating structures made of various materials such as metal, inorganic compounds, organic molecules and biological species (see Table 4).[20] The fabrication of a wide range of functional structures by DPN has been demonstrated, and some typical structures include high resolution organic features, metallic and magnetic patterns, polymer brush arrays and biological devices. A comprehensive and dedicated description on the evolution of DPN can be found in a recent review article by Mirkin *et al.*[21] While significant progress has been achieved in DPN-based nanofabrication, there is an on-going debate on the detailed mechanism for ink transport and diffusion. Theoretical and experimental results showed that the transport and deposition of ink depends on several factors such as the formation of water meniscus, the properties of the tip and the substrate, the ink deposition time and temperature.[1]

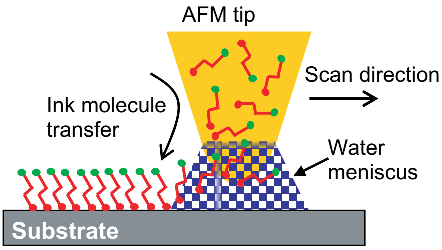

Fig. 5. Schematic showing the transport of ink from the AFM tip to the substrate through the water meniscus. Adapted from Ref. 1.

Table 4. Types of inks used in DPN and their applications (adapted from Ref. 20).

Types of ink	Applications
Organics	— Study of diffusion dynamics of ODT on Au — Effects of temperature and humidity on patterning of ODT and MHA molecules — Redox-active ferrocenyl alkylthiol inks on Au — Rhodamine 6G(R6G) dye deposition — Patterning of poly-EDOT nanowires — Patterning of conducting polymer
Biological materials	— Collagen nanoarrays — Direct-write of proteins on SiO_2 — Patterning of oligonucleotides on Au and SiO_2 — DNA coupled to MHA pattern
Inorganics	— Au nanoclusters and nanoparticles — Magnetic nanopatterns — Deposition of Pt nanofeatures by E-DPN — Hard magnetic barium hexaferrite pattern — Composite nanostructures consisting of Al_2O_3, SiO_2 and SnO_2

3.2. *Thermomechanical writing and millipede technique*

In thermomechanical writing, a resistively heated AFM probe writes a data bit by scanning over a polymer surface. The combined heat and mechanical force of the tip causes the polymer to soften and flow, thus facilitating the writing of data bits in a storage medium. This technique was pioneered by the IBM Zurich research group, and systematic descriptions on its working principles and applications can be found in their publications.[22,23] In this technique, an electrical current is passed through the cantilever, and a large force is loaded on the hot tip to indent the polymer medium. Thermomechanical writing is a reversible nanofabrication technique in which data bits can be written, erased and rewritten. Data erasing is simply achieved by thermal reflow of the storage field as a whole. No alteration of the polymer film takes place after repeated writing and erasing. With this approach, storage fields of a few hundred microns can be erased en bloc. Subsequently, a data-storage concept called the "millipede" that combines ultrahigh density, terabit capacity, small form factor and high data rate was developed. A 32×32 array chip can generate 1024 storage fields on an area of less than 3 mm × 3 mm. The corresponding data capacity of the 1024 storage fields is 0.9 Gb assuming an areal density of 500 Gb/in^2. In general, the storage capacity of the system scales with the areal density, the cantilever pitch and the number of cantilevers in the array.

3.3. *AFM nanooxidation*

AFM nanooxidation is one of the earliest and most extensively studied techniques in bias-assisted AFM nanolithography.[1,10] In this method, the water meniscus formed in the tip–sample nanojunction is dissociated by the applied tip bias voltage, and the O^- and OH^- oxidative ions react with the substrate to form localized oxide nanostructures. Because the molecular volume of the oxides is usually larger than that of the substrate materials, raised nanopatterns are formed after the oxidation reaction. AFM nanooxidation has been used to fabricate nanoscale devices such as metal–oxide–semiconductor (MOS) transistors through the precise control of local oxide growth by the AFM probe. In addition, the anodic oxide features can act as reactive sites for the further assembly of molecules and nanoparticles through chemical linkages and affinities. Alternatively, the anodic oxides can also be etched to produce negative structures on the substrates for pattern transfer. Table 5 summarizes the applications of AFM nanooxidation of metals, semiconductors and molecularly passivated substrates.[1,24–33] The semiconductor substrates used in AFM nanooxidation include Si, SiC and Ga[Al]As.[24–27] The nanooxidation of a wide range of metal substrates, such as Ti, Al, Cr and Nb, has also been reported.[28–30] Various approaches to use self-assembled monolayers (SAM) or Langmuir–Blodgett (LB) films as a resist for local oxidation were proposed.[31–33]

It is suggested that the nanooxidation mechanism and kinetics are closely related to electrical field, surface stress, water meniscus formation, and OH^- diffusion. Specifically, various models such as the Cabrera–Mott model,[34] power-law model,[35] log kinetic model,[36] and space-charge model[37] have been proposed to account for

Table 5. Applications of AFM nanooxidation on different substrates.[1,24–33]

Type of substrate	Nanostructures fabricated
Semiconductors	— Fabrication of nanometer-scale side-gated silicon field-effect transistors — High speed and large area writing, e.g. fabrication of 0.1 mm metal oxide semiconductor field effect transistors on amorphous silicon (α:Si) films — Fabrication of high quality antidot lattices, e.g. 20×20 antidot array with a lattice period of 300 nm — Electrical conduction on hydrogenated diamond
Metals	— Fabrication of metal–oxide devices on thin Ti films ~ 7 nm) — Probe-grown nickel oxide as a catalytic template for selective growth of CNTs — Oxidation of molybdenum (Mo) film to form MoO_3 patterns
Molecularly functionalized/passivated surfaces	— Oxidation of Si covered by organosilane TMS monolayer. — Poly(benzylether) dendrimers terminated with both benzyl and tert-butyldiphenylsilyl ether groups as resists for AFM oxidation lithography — Oxidation of surfaces passivated by mixed SAM layer comprising 1,12-diaminododecane dihydrochloride (DAD · 2HCl) and *n*-tridecylamineahydrochloride (TDA · HCl)

the oxidation behavior. There is an on-going debate on the limiting-factors of oxide growth due to the complexity of such nanoscale oxidation processes. Several studies focused on oxidation in non-contact AFM mode, and in particular the formation of a water bridge between the tip and surface.[38,39]

Recently, Xie *et al.* reported a new OH^- spreading mechanism in AFM nanooxidation which is based on the generation and propagation of transient shock wave events.[40] As shown in Fig. 6(a), nanoexplosion is initiated due to bias application to the tip–surface nanojunction. The stochastic nanoexplosion generates single or double shock wave events which significantly facilitate the spreading of OH^- ions a few micrometers out of the explosion zone. The OH^- ions then react with the Si substrate to form distinct single-disk, double-disk and central-dot/outer-disk oxide patterns. The authors performed numerical hydrodynamic calculations to simulate the microscopic shock wave propagation (see Fig. 6(b)). Their results confirm that transient shock events can be initiated by the nanoexplosion, and the shock front

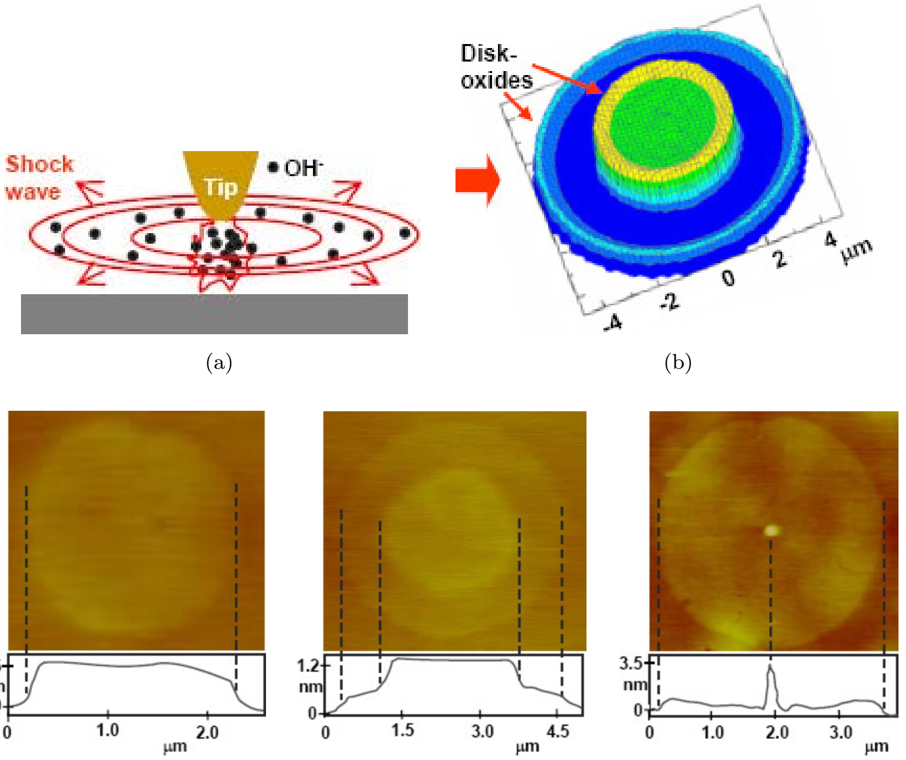

(a) (b)

(c) (d) (e)

Fig. 6. (a) Proposed model of OH^- spreading by shock wave propagation. (b) Simulated double-disk oxide formation due to two shock wave events. AFM images of (c) single-disk, (d) double-disk, and (e) central-dot/outer-disk oxide structures fabricated by shock wave-assisted OH^- spreading. Adapted from Ref. 40.

can travel a few micrometers to spread the OH^- oxidants. Figures 6(c)–6(e) display the experimental observations of the single-disk, double-disk and central-dot/outer-disk oxide patterns created by the initiation of shock events. The authors also investigated the fundamental differences between the conventional ionic diffusion model and their shock wave propagation model. Their results showed that shock propagation may be a general phenomenon in AFM nanolithography involving bias application, and the transient event could critically affect the modes of pattern formation.

3.4. *Electrostatic deformation and electrohydrodynamic nanofluidic motion*

The ability to directly pattern and write polymers at the nanometer scale is crucial to applications in data storage and molecular electronics. Lyuksyutov *et al.* introduced AFM electrostatic nanolithography (AFMEN) to generate nanoscale polymeric features by Joule heating and mass transport on initially featureless polymer films.[41] In this technique, current flow generated by tip biasing produces effective Joule heating which locally softens the polymer film. The extremely non-uniform electric field gradient polarizes the viscoelastic polymer and attracts it towards the tip apex, leading to the formation of protruding structures on the film. The attractive force arises from the imbalance between the Laplace, viscous and electrostatic pressures. When the electrostatic pressure overcomes the combination of Laplace and viscous pressures, electrostatic deformation of the polymer melt takes place. The optimal polymer film for patterning relies on the materials selection and processing that provides gradual dielectric breakdown under the electric field.

Further to electrostatic nanolithography, Chung and Xie *et al.* demonstrated the creation of Taylor cones on PMMA using higher tip voltages of 30–60 V.[11,42] Under such conditions, the strong electric field initiates electrohydrodynamic (EHD) instability and nanofluidic motion of the polymer melt. In the probe-induced local EHD, unstable surface waves are generated by electrostatic pressure, and the vertical transport of the fluid is decoupled from the lateral propagation of surface waves, thus enabling the formation of localized conical structures at selected sites. Fig. 7(a) displays a Taylor cone consisting of a central cone and a surrounding circular groove. When an AFM tip with a larger radius was used, the formation of triple cones was observed (see Fig. 7(b)). The formation of multiple cones uncovers the correlation between the number of unstable waves and the tip end diameter: a larger tip electrode can enable more periods of unstable maximum in the perturbed polymer fluid. Therefore, three periods of waves were initiated when a blunt tip was used as electrode as shown in Fig. 7(b). Xie *et al.* investigated the conduction mechanism by monitoring the current–voltage (I–V) and current–time (I–t) curves *in situ* during Taylor cone formation under different humidity conditions.[11] It was revealed that the charge transport is dominated by water bridge-assisted ionic conduction.

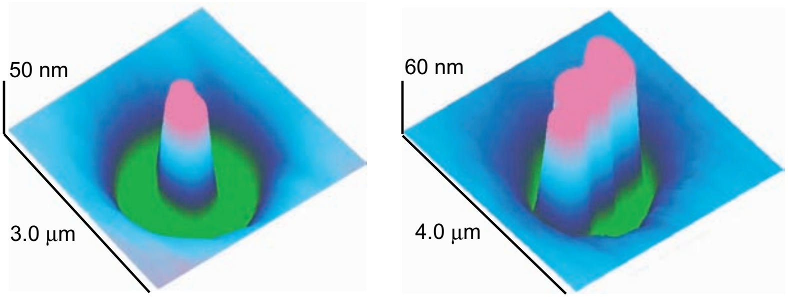

(a) (b)

Fig. 7. (a) AFM image of a single Taylor cone generated on PMMA. (b) AFM image of a triple-cone generated using larger tips. Adapted from Ref. 42.

The ionic conductivity was observed to be very sensitive to humidity conditions which directly affect the formation of the water bridge between the tip and substrate. High humidity conditions enhance water condensation and subsequent water dissociation, leading to higher H^+ and OH^- concentrations, which would promote the overall conductivity. High humidity conditions also help improve carrier mobility in polymer melts, as the polymer viscosity would be lower if it was heated by an initial high ionic current.

3.5. *Polymer patterning by nanoexplosion*

Xie and co-workers demonstrated the application of nanoexplosion for the creation of localized conductive structures on an insulating poly(N-vinylcarbazole) (PVK) matrix.[43] In this case, the native PVK reacts with the discharged oxygen-containing particles generated in the nanoexplosion to form cross-linked carbazole groups. The cross-linking and oxygenation leads to the formation of extended π-conjugation in the patterned PVK, which narrows the HOMO–LUMO energy gap of the PVK molecular orbitals. Therefore, the PVK pattern exhibits higher electric conductivity due to the lowering of energy barrier for electron injection. Figure 8(a) shows a PVK pattern composed of a central and outer parts fabricated by the nanoexplosion technique. The height of the central structure is about 15 nm, while the radius of the outer ring is $\sim 2.1\,\mu$m. Fig. 8(b) shows the current map collected for such a PVK pattern using conductive AFM. Higher current was detected for the central structure and outer ring, indicating the electric conductive nature of the PVK pattern as opposed to the insulating native PVK matrix.

To elucidate the physico-chemical characteristics of the patterned structure, the PVK samples were exposed to large-scale discharges generated by a Van de Graaff generator. The discharge conditions were comparable to those in the nanoexplosion, except that the reacted area of PVK was large enough for Fourier Transform Infrared (FTIR) and photoelectron spectroscopy (PES) characterizations. Xie *et al.* also investigated the impact of cross-linking and oxygenation on the electric functionality of PVK patterns by calculating the HOMO–LUMO gap of

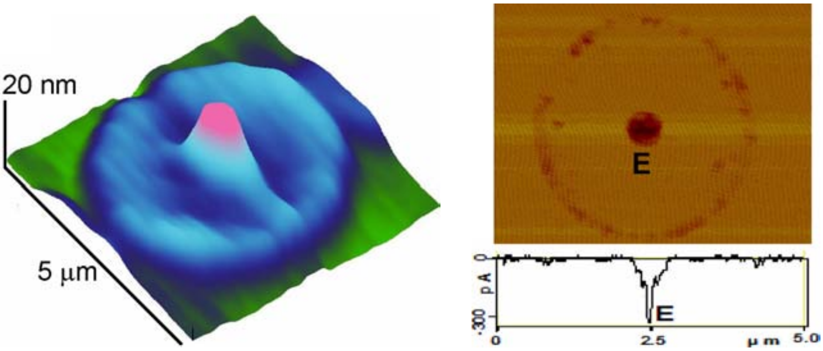

(a) (b)

Fig. 8. (a) AFM image of a PVK pattern. (b) current map of the PVK pattern showing its higher electric conductivity. Adapted from Ref. 43.

various configurations. They found that the cross-linking of carbazole groups by oxygen can lower the HOMO–LUMO gap of PVK patterns. As the number of cross-linked carbazole groups increases, a higher degree of cross-linkage and oxygenation occurs, leading to a narrower energy gap. Current-voltage curves measured by conductive AFM revealed that the electric conduction in PVK patterns is governed by Fowler–Nordheim electron injection. The narrowing of HOMO–LUMO gap helps reduce the energy barrier for current injection from the tip, therefore significantly facilitating electrical conduction in the patterned PVK structures.

3.6. *Charge deposition and manipulation*

AFM nanolithography has also been employed to deposit charges onto the substrates to form charge patterns, and assemble nanostructures on the basis of the charge patterns.[1,44–50] Crook *et al.* introduced an erasable electrostatic lithography technique for charge deposition and manipulation.[44] In this technique, patterns of charge are deposited on a device surface with a negatively biased scanning probe in a low-temperature and high-vacuum environment. The charge patterns locally deplete electrons from a subsurface two-dimensional electron system (2DES) to define working quantum components and can be erased with opposite bias or globally by illuminating the device with red light. The defined charge spot area is an order of magnitude larger than the tip–surface contact area. Smaller charge spots, and therefore higher resolution, would be attained using a less negative probe bias with a shallower 2DES. This technique may be particularly useful in the construction of a solid-state scaleable quantum computer, where the required level of uniformity between quantum components is hard to achieve using other schemes.

In the work of Pioda *et al.*, a metallic AFM tip was coupled capacitively to electrons confined in a lithographically defined gate-tunable quantum dot.[45] Single electrons were made to hop on or off the dot by moving the tip or by changing the tip bias voltage due to the Coulomb-blockade effect. Spatial images of conductance resonances were recorded to obtain quantitative spatial maps of the interaction potential between the tip and individual electrons. Their scanning-gate measurements on a quantum dot demonstrated that single electrons can be manipulated one by one with a scanning probe. Barrett *et al.* investigated charge storage in a nitride-oxide-silicon (NOS) medium using a biased AFM probe.[46] The stored charge can act as a digital memory. Bit sizes as small as 75 nm have been stored, and they are stable over a period of seven days. The stored charge can also be removed by applying a reverse bias to the region, and the bit can be subsequently rewritten. By simultaneously measuring capacitance and topography images, the authors confirmed that the stored information is not a result of any topographic change to the surface. Instead, the observed writing and erasing effect is due to electronic changes inside the insulator and semiconductor.

4. Concluding Remarks

In this article, the development of SPM nanolithographic techniques for nanoscale patterning and fabrication has been reviewed. The technical characteristics and applications of SPM nanolithography were discussed in comparison with conventional lithographic techniques. The features of STM- and AFM-based nanofabrication methods were compared in terms of their resolution and operational conditions. In STM nanolithography, we highlighted the three general approaches to atomic and molecular structure formation: (i) direct tip–surface interaction, (ii) field effect and (iii) electron effect. As for AFM nanolithography, we selectively reviewed a few techniques such as dip-pen nanolithography, thermomechanical writing and millipede technique, nanooxidation, electrostatic deformation and EHD motion, nanoexplosion and charge deposition. Although this chapter emphasized the diverse techniques in SPM nanolithography, it should be noted that the fundamental understanding of the many pattern formation mechanisms remains incomplete. This is mainly due to the difficulty in directly monitoring and characterizing the pattern formation processes in the nanoscopic tip–surface junctions. Another challenge in SPM nanolithography is its reproducibility and pattern mass production. Further work is needed to fully understand the fabrication mechanism, to control and optimize nanofabrication processes.

Acknowledgment

This work is supported by NUS Nanoscience and Nanotechnology Initiative (NUSNNI), National University of Singapore.

References

1. Xie XN, Chung HJ, Sow CH and Wee ATS, Nanoscale materials patterning and engineering by atomic force microscopy nanolithography, *Mater Sci Eng R* **54**:1–48, 2006.
2. Binnig G, Rohrer H, Gerber H and Weibel E, Surface studies by scanning tunneling microscopy, *Phys Rev Lett* **49**:57–61, 1982.

3. Binnig G, Quate CF and Gerber C, Atomic force microscope, *Phys Rev Lett* **56**:930–933, 1986.
4. Hashioka S and Matsumura H, 10-nm-size fabrication of semiconductor substrates and metal thin lines by conventional photolithography, *Jpn J Appl Phys* **39**:7063–7066, 2000.
5. Subramanian KRV, Saifullah MSM, Tapley E, Kang DJ, Welland ME and Butler M, Direct writing of ZrO_2 on a sub-10 nm scale using an electron beam, *Nanotechnology* **15**:158–162, 2004.
6. Enkrich C, Pérez–Willard F, Gerthsen D, Zhou J, Koschny T, Soukoulis CM, Wegener M and Linden S, Focused-ion-beam nanofabrication of near-infrared magnetic metamaterials, *Adv Mater* **17**:2547–2549, 2005.
7. Chou SY, Krauss PR and Renstrom PJ, Imprint lithography with 25-nanometer resolution, *Science* **272**:85–87, 1996.
8. Otero R, Rosei F and Besenbacher F, Scanningtunneling microscopy manipulation of complex organic molecules on solid surfaces, *Annu Rev Phys Chem* **57**:497–525, 2006.
9. Piner RD, Zhu J, Xu F, Hong S and Mirkin CA, Dip-pen nanolithography, *Science* **283**:661–663, 1999.
10. Snow ES and Campbell PM, Fabrication of si nanostructures with an atomic-force microscope, *Appl Phys Lett* **64**:1932–1934, 1994.
11. Xie XN, Chung HJ, Sow CH, Bettiol AA and Wee ATS, Water-bridge-assisted ionic conduction in probe-induced conical polymer pattern formation, *Adv Mater* **17**:1386–1390, 2005.
12. Bartels L, Meyer G and Reider KH, Basic steps of lateral manipulation of single atoms and diatomic clusters with a scanning tunneling microscope tip, *Phys Rev Lett* **79**:697–700, 1997.
13. Hla SW, Braun KF and Reider KH, Single-atom manipulation mechanisms during a quantum corral construction, *Phys Rev B* **67**:201402–201405, 2003.
14. Bartels L, Meyer G and Reider KH, Controlled vertical manipulation of single CO molecules with the scanning tunneling microscope: A route to chemical contrast, *Appl Phys Lett* **71**:213–215, 1997.
15. Whitman LJ, Stroscio JA, Dragoset RA and Celotta RJ, Manipulation of adsorbed atoms and creation of new structures on room-temperature surfaces with a scanning tunneling microscope, *Science* **251**:1206–1210, 1991.
16. Mendez J, Gomex–Herrero J, Pascual JI, Saenz JJ, Soler JM and Baro AM, Diffusion of atoms on Au(111) by the electric field gradient in scanning tunneling microscopy, *J Vac Sci Technol B* **14**:1145–1148, 1996.
17. Shen TC, Wang C, Abeln GC, Tucker JR, Lyding JW, Avouris Ph and Walkup RE, Atomic-scale desorption through electronic and vibrational-excitation mechanisms, *Science* **268**:1590–1592, 1995.
18. Soukiassian L, Mayne AJ, Carbone M and Dujardin G, Atomic-scale desorption of H atoms from the Si(100)-2x1 : H surface: Inelastic electron interactions, *Phys Rev B* **68**:035303–035307, 2003.
19. Nouchi R, Masunari K, Ohta T, Kubozono Y and Iwasa Y, Ring of C-60 polymers formed by electron or hole injection from a scanning tunneling microscope tip, *Phys Rev Lett* **97**:196101–196104, 2006.
20. Ginger DS, Zhang H and Mirkin CA, The evolution of dip-pen nanolithography, *Angew Chem Int Ed.* **43**:30–45, 2004.
21. Salaita K, Wang YH and Mirkin CA, Applications of dip-pen nanolithography, *Nat Nanotechnol* **2**:145–155, 2007.

22. Vettiger P, Cross G, Despont M, Drechsler U, Dürig U, Gotsmann B, Häberle W, Lantz MA, Rothuizen HE, Stutz R and Binnig GK, The "millipede"–Nanotechnology entering data storage, *IEEE T Nanotechnol* **1**:39–55, 2002.
23. Dürig U, Cross G, Despont M, Drechsler U, Häberle, Lutwyche MI, Rothuizen H, Stutz R, Widmer T, Vettiger P, Binnig GK, King WP and Goodson KE, Millipede — An AFM data storage system at the frontier of nanotribology, *Tribol Lett* **9**:25–32, 2000.
24. Day HC and Allee DR, Selective area oxidation of silicon with a scanning force microscope, *Appl Phys Lett* **62**:2691–2693, 1993.
25. Xie XN, Chung HJ, Xu H, Xu X, Sow CH and Wee ATS, Probe-induced native oxide decomposition and localized oxidation on 6H–SiC (0001) surface: An atomic force microscopy investigation, *J Am Chem Soc* **126**:7665–7675 (2004).
26. Chien FSS, Chang JW, Lin SW, Chou YC, Chen TT, Gwo S, Chao TS and Hsieh WF, Nanometer-scale conversion of Si_3N_4 to SiOx, *Appl Phys Lett* **76**:360–362, 2000.
27. Ishii M and Matsumoto K, Control of current in 2deg channel by oxide wire formed using AFM, *Jpn J Appl Phys* **34**:1329–1331, 1995.
28. Snow ES and Campbell PM, AFM fabrication of sub-10-nanometer metal-oxide devices with in-situ control of electrical-properties, *Science* **270**:1639–1641, 1995.
29. Snow ES, Park D and Campbell PM, Single-atom point contact devices fabricated with an atomic force microscope, *Appl Phys Lett* **69**:269–271, 1996.
30. Wang D, Tsau L, Wang KL and Chow P, Nanofabrication of thin chromium film deposited on Si(100) surfaces by tip induced anodization in atomic-force microscopy, *Appl Phys Lett* **67**:1295–1297, 1995.
31. Sugimura H and Nakagiri N, Nanoscopic surface architecture based on scanning probe electrochemistry and molecular self-assembly, *J Am Chem Soc* **119**:9226–9229, 1997.
32. Lee H, Bae E and Lee W, Fabrication of nanometer scale patterns with organized molecular films, *Thin Solid Films* **393**:237–242, 2001.
33. Onclin S, Ravoo BJ and Reinhoudt DN, Engineering silicon oxide surfaces using self-assembled monolayers, *Angew Chem Int Ed* **44**:6282–6304, 2005.
34. Gordon AE, Fayfield RT, Litfin DD and Higman TK, Mechanisms of surface anodization produced by scanning probe microscopes, *J Vac Sci Technol B* **13**:2805–2808, 1995.
35. Teuschler T, Mahr K, Miyazaki S, Hundhausen M and Ley M, Nanometer-scale field-induced oxidation of Si(111)h by a conducting-probe scanning force microscope — Doping dependence and kinetics, *Appl Phys Lett* **67**:3144–3146, 1995.
36. Stiévenard D, Fontaine PA and Dubois E, Nanooxidation using a scanning probe microscope: An analytical model based on field induced oxidation, *Appl Phys Lett* **70**:3272–3274, 1997.
37. Dagata JA, Perez-Murano F, Martin C, Kuramochi H and Yokoyama H, Current, charge and capacitance during scanning probe oxidation of silicon. I. Maximum charge density and lateral diffusion, *J Appl Phys* **96**:2386–2392, 2004.
38. García R, Calleja M and Rohrer H, Patterning of silicon surfaces with noncontact atomic force microscopy: Field-induced formation of nanometer-size water bridges, *J Appl Phys* **86**:1898–1903, 1999.
39. Dagata JA, Perez-Murano F, Martin C, Kuramochi H and Yokoyama H, Current, charge, and capacitance during scanning probe oxidation of silicon. II. Electrostatic and meniscus forces acting on cantilever bending, *J Appl Phys* **96**:2393–2399, 2004.
40. Xie XN, Chung HJ, Liu Z, Yang SW, Sow CH and Wee ATS, A new scenario in probe local oxidation: transient pressure-wave-assisted ionic spreading and oxide pattern formation, *Adv Mater* **19**:2618–2623, 2007.

41. Lyuksyutov SF, Vaia RF, Paramonov PB, Juhl S, Waterhouse L, Ralich RM, Sigalov G and Sancaktar E, Electrostatic nanolithography in polymers using atomic force microscopy, *Nat Mater* **2**:468–472, 2003.
42. Chung HJ, Xie XN, Sow CH, Bettiol AA and Wee ATS, Polymeric conical structure formation by probe-induced electrohydrodynamical nanofluidic motion, *Appl Phys Lett* **88**:023116–023118, 2006.
43. Xie XN, Deng M, Xu H, Yang SW, Qi DC, Gao XY, Chung HJ, Sow CH, Tan BC and Wee ATS, Creating polymer structures of tunable electric functionality by nanoscale discharge-assisted cross-linking and oxygenation, *J Am Chem Soc* **128**:2738–2744, 2006.
44. Crook R, Graham AC, Smith CG, Farrer I, Beere HE and Ritchie DA, Erasable electrostatic lithography for quantum components, *Nature* **424**:751–754, 2003.
45. Pioda A, Kičin S, Ihn T, Sigrist M, Fuhrer A, Ensslin K, Weichselbaum A, Ulloa SE, Reinwald M and Wegscheider W, Spatially resolved manipulation of single electrons in quantum dots using a scanned probe, *Phys. Rev. Lett.* **93**:216801–216804, 2004.
46. Barrett RC and Quate CF, Charge storage in a nitride-oxide-silicon medium by scanning capacitance microscopy, *J Appl Phys* **70**:2725–2733, 1991.
47. Schaadt DM, Yu ET, Sankar S and Berkowitz AE, Charge storage in Co nanoclusters embedded in SiO_2 by scanning force microscopy, *Appl Phys Lett* **74**:472–474, 1999.
48. Mesquida P, Knapp HF and Stemmer A, Charge writing on the nanometre scale in a fluorocarbon film, *Surf Interface Anal* **33**:159–162, 2002.
49. Mesquida P and Stemmer A, Attaching silica nanoparticles from suspension onto surface charge patterns generated by a conductive atomic force microscope tip, *Adv Mater* **13**:1395–1398, 2001.
50. Kado H and Tohda T, Nanometer-scale recording on chalcogenide films with an atomic-force microscope, *Appl Phys Lett* **66**:2961–2962, 1995.

NANOSCALE CHARACTERIZATION BY SCANNING TUNNELING MICROSCOPY

HAI XU*, XIAN NING XIE, M. A. K. ZILANI, WEI CHEN
and ANDREW THYE SHEN WEE

Department of Physics and NUS Nanoscience
and Nanotechnology Initiative (NUSNNI)
National University of Singapore
2 Science Drive 3, 117542, Singapore

**hxu@zyvexasia.com*

Nanoscale characterization is a key field in nanoscience and technology as it provides fundamental understanding of the properties and functionalities of materials down to the atomic and molecular scale. In this article, we review the development and application of scanning tunneling microscope (STM) techniques in nanoscale characterization. We will discuss the working principle, experimental setup, operational modes, and tip preparation methods of scanning tunneling microscope. Selected examples are provided to illustrate the application of STM in the nanocharacterization of semiconductors. In addition, new developments in STM techniques including spin-polarized STM (SP-STM) and multi-probe STM (MP-STM) are discussed in comparison with conventional non-magnetic and single tip STM methods.

Keywords: Scanning probe microscopy; scanning tunneling microscopy; LEED-energy electron diffraction; photoemission spectroscopy; surface relaxation and reconstruction; semiconductor surface structure; spin-polarization; self-assembly; adatoms; molecular beam epitaxy; ferromagnetic surface; electrical transport.

1. Introduction

Nanoscale characterization is a key field in nanoscience and technology as it provides fundamental understanding of the properties and functionalities of materials down to the atomic and molecular scale. The direct study of atoms and nanostructures became possible with the invention of scanning probe microscopy (SPM). The SPM family consists of scanning tunneling microscopy (STM)[1] and scanning force microscopy (SFM) or atomic force microscopy.[2] SPM provides new opportunities for investigating locally the geometric and electronic properties of nanostructures on surfaces, and the recent advances in scanning tunneling microscopy and spectroscopy of nanostructures have been reviewed by Schneider *et al.*[3] STM, coupled with theoretical studies, has contributed significantly to the understanding of atomic structures and their electronic properties. In particular, the realization of spin-polarized scanning tunneling microscopy (SP-STM)[4,5] offers a rather straightforward approach to imaging the magnetization with ultimate resolution down to the atomic scale. In addition, the multi-probe STM technique[6] has also been recently developed, and is a combination of scanning electron microscope (SEM) and STM with double-, triple-, or quadruple-probes. This multi-technique tool can be implemented to both characterize and fabricate nanoscale devices. The full STM capability is used not only for obtaining atomic resolution morphologies, but also for enabling fine tip positioning with ultimate accuracy to make nanoscale electrical contacts for electrical conductivity measurements of various nanostructures. For example, for electrical characterization of nanodevices, the quadruple-probe STM allows measurement and application of both voltage and current. Moreover, the combination with high resolution SEM enables tip navigation on complex structures for fast location and even chemical analysis by combination with scanning Auger microscopy (SAM).

Another probe-related characterization technique is scanning force microscopy (SFM)[2] which was developed slightly later than STM. The concept of force microscopy is a general one and is not limited to atomic forces. Over the last two decades, techniques such as magnetic force microscopy (MFM),[7] electrostatic force microscopy (EFM),[8] scanning capacitance microscopy (SCM),[9] and scanning near-field optical microscopy (SNOM)[10,11] have been demonstrated to detect a variety of forces, including magnetic, electrostatic and van der Waals forces. While both STM and SFM have been widely used as surface characterization methods, this chapter specifically describes the development and applications of STM in nanoscale characterization.

2. Scanning Tunneling Microscopy (STM)

2.1. *STM and scanning tunneling spectroscopy*

The scanning tunneling microscope (STM), invented by Nobel laureates Binnig and Rohrer,[1] makes use of the quantum mechanical tunneling current between a small metal tip and a conductive or semiconductive surface to electrically and topographically characterize a given sample surface. Figure 1 shows a schematic drawing of a typical STM setup. In STM, a bias voltage is applied between a sharp metal tip and a conducting sample. After bringing the tip and sample surface to a separation of below 1 nanometer (10 Angstrom), a tunneling current can be observed to flow due to the quantum tunneling effect. The tunneling current is very sensitive to small changes in separation between tip and sample surface. The voltage-dependent magnitude of such a tunneling current, $I(V)$, can be approximated as

$$I(V) \approx e^{-z\kappa} \int_0^{ev} \rho_s(E_F - eV + E)dE \tag{1}$$

where V is the bias applied to the sample surface relative to the tip, z the distance between tip and surface, ρ_s the surface local density of states (LDOS), and κ a

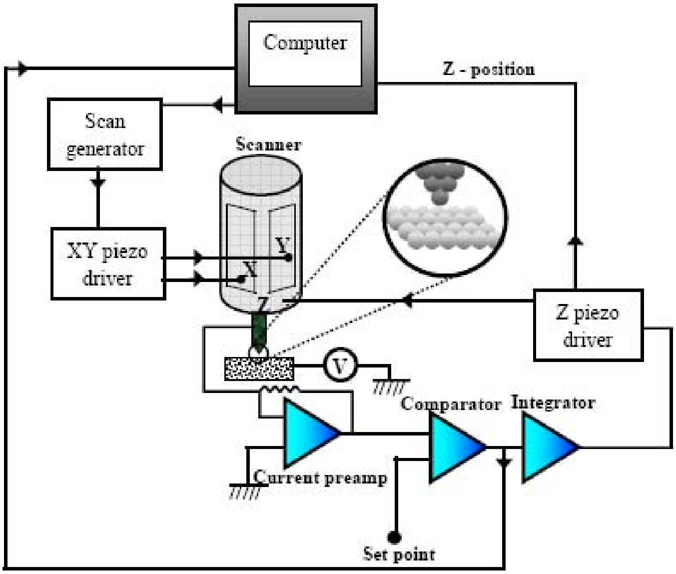

Fig. 1. STM system setup and working principle.

positive decay constant. The strong exponential dependence of I on the tip-sample spacing z allows the STM to trace the surface topography with atomic-scale sub-angstrom-level lateral and vertical resolution, as well as to control the separation between tip and sample exactly. In general, STM is used in three primary modes of operation: (i) constant-current mode; (ii) scanning tunneling spectroscopy (STS) mode; and (iii) current image tunneling spectroscopy mode. In constant-current mode, one defines a set-point tunneling current, which is then maintained by varying the STM tip height via a digitally controlled feedback loop while the tip is laterally raster-scanned across the surface. When this constant-current approach is applied to an electrically uniform sample, the height of the tip tracks the surface topography, providing a spatial mapping of the sample's physical features. Images obtained from this tip height information are referred to as "STM topography". In STS mode, spatially selective tunneling current-voltage (I–V) characteristics are recorded by pausing the STM tip at predetermined positions within the imaging window, holding the tip height constant by switching off the feedback loop, and sweeping the applied sample bias over a specified range. STS measures the differential conductivity dI/dV of the tunneling gap between a metallic tip and the sample, which can be calculated from the recorded tunneling I–V data. Parameters set are the applied voltage V and the position of the tip with respect to the samples. At low voltage ($V < 200\,\text{mV}$) and a spatially homogeneous electron decay into vacuum, $dI/dV(s, V)$ is directly proportional to the local density of states (LDOS). In some cases, varying the tip height during I–V acquisition is necessary to obtain an accurate measure of the surface electronic character. When such a variable-spacing spectroscopic approach is taken, a normalized dI/dV, $(dI/dV/(I/V))$, can be calculated and used as an estimate of the surface LDOS. The current image tunneling spectroscopy (CITS)[12] mode is a hybrid of the above two approaches in which a full I–V spectrum is acquired at each pixel in the imaging mesh. The result is a dense array of sub-nanometer spatially resolved electronic data, which can then be correlated with the associated topograph.

Figure 2 shows a typical tunneling spectrum of Si(1 1 1)-(2 × 1) surface reported by Stroscio *et al.*[13] who obtained tunneling spectra at various fixed tip sample separations from 7.8 to 19.5 Å. The bottom portion of Fig. 2 displays a plot of the tip sample separation versus voltage at constant tunneling current. The average work function and initial tip-sample separation can be determined from this s–V data.

Zilani *et al.*[14] studied the electronic structure of cobalt-induced magic clusters grown on a Si(1 1 1)-7 × 7 surface using STM and STS. Figure 3 exhibits a series of empty- and filled-state STM images and the corresponding line profiles of the same Si(1 1 1)-7×7 unit cell containing a magic Co cluster taken at various bias voltages. It can be seen that even at low bias voltages of ±0.4 V, the adatoms in the unfaulted half unit cell (UFHUC) (i.e., with no cluster) are very clear due to appreciable tunneling current, indicating that the Si(1 1 1) adatoms are characterized by metallic surface states.

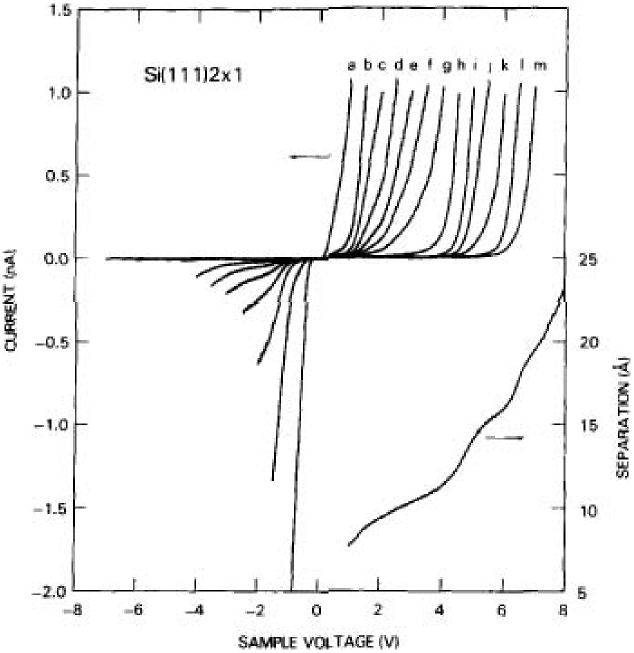

Fig. 2. Tunneling current vs. voltage (I–V) for a tungsten probe tip and Si(1 1 1)-(2 × 1) sample, at tip-sample separations of 7.8, 8.7, 9.3, 9.9, 10.3, 10.8, 11.3, 12.3, 14.1, 15.1, 16.0, 17.7, and 19.5 Å for the curves labeled a–m, respectively. Reprinted with permission from Ref. 13, © 1986, The American Physical Society.

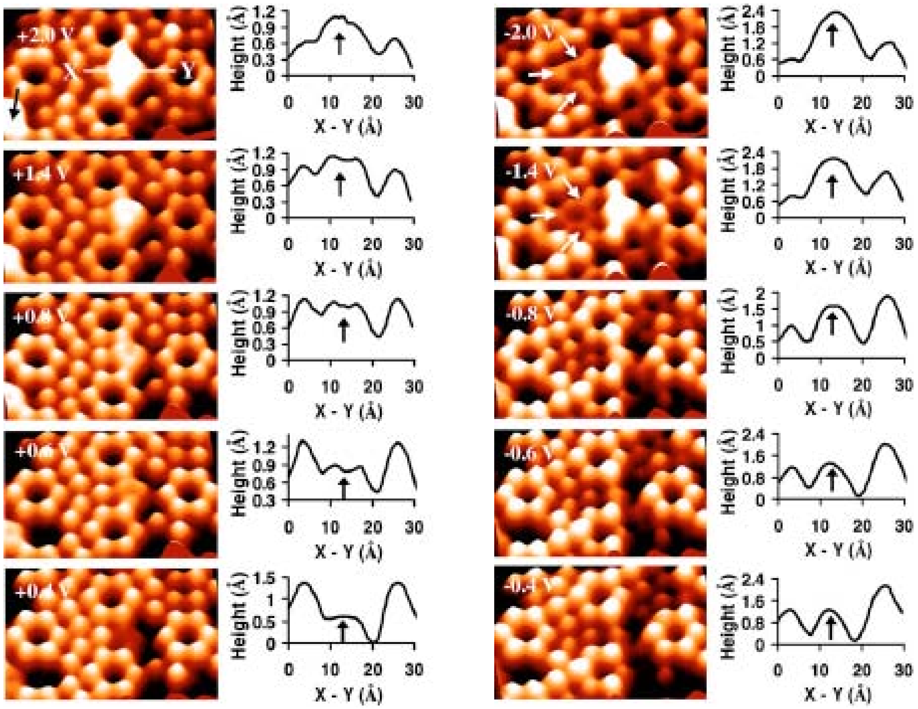

(a)

(b)

Fig. 3. Empty (a) and filled (b) state STM images of a Si(1 1 1)-7 × 7 unit cell comprising a Co induced magic cluster obtained at bias voltages ±0.4, ±0.6, ±0.8, ±1.4, and ±2.0 V, respectively. Adapted from Ref. 14.

2.2. *STM tip preparation*

2.2.1. *Conventional STM tip*

The formation of a useful tip is the key to a productive tunneling microscope. The operating characteristics of the entire microscope are dependent upon the single atom at the very end of the probe tip. In general, a relatively hard material is used in tip fabrication because contact between tip and sample surface can occur during scanning. Tungsten (W) tips are widely used in STM studies, particularly under UHV (ultrahigh vacuum) conditions. However, the electrochemical etching of W tips involves the formation of an unwanted oxide layer, hence other noble metals including platinum and gold are also viable candidate materials for tip-making due to their inert properties. The problem with these materials is that they are relatively soft and can easily be damaged during accidental contacts with the sample surfaces. Therefore, Pt-Ir alloys which are oxide-free and of increased hardness, have been most commonly used as tip materials. In addition, carbon nanotube (CNT) tips and diamond coated tips have also been employed in STM studies due to their high aspect ratio and hardness respectively.[15–17]

Table 1. Tip polishing procedures for various tip materials.

Tip material	Polishing solution	Procedure
GaAs	$4H_2SO_4 + H_2O_2 + H_2O$	Dip into hot solution
Iridium	20% KCN (aq. sol.)	2–15 VAC; start at higher voltage
	$HCI + HNO_3 + H_3PO_4$	5–15 VAC
	Molten NaC1	2–3 VAC
	Molten $NaNO_2$	0.5–1 VAC
	Molten $3NaNO_3 + 7KOH$	2–3 VAC
Molybdenum	KOH (conc. aq. sol.)	5–10 VAC or DC
	$8NH_4OH$ (aq. sol.) + (conc.) 2KOH	3–6 VAC
	20% KCN (aq. sol.)	1–5 VAC; start at higher voltage
Platinum/alloys	20% KCN (aq. sol.)	3–15 VAC; start at higher voltage
	Molten $4NaNO_3 + NaC1$	I–5 VDC
	Molten NaC1	6 VDC
Tantalum	Molten $NaNO_2$ or KOH	8 VAC
	2HF (48% sol.) + $0.5CH_3COOH$ + conc. $H_3PO_4 + H_2SO_4$ (36N)	5–15 VDC
Tungsten/alloys	Same as molybdenum	AC or DC depending on tip shape

Tips for STM scanning are usually fabricated by etching a wire in an appropriate electrochemical solution. The different etchants suitable for etching different tip materials are summarized in Table 1.[18,19] In the preparation of STM tips using the drop-off technique,[20,21] a tungsten wire is positioned vertically through a noble metal (Au/Pt) ring supporting the electrolytic lamellar suspension. Application of a positive voltage to the tungsten wire (relative to the grounded gold ring counterelectrode) results in the etching of the wire portion within the lamella. Generally, the bottom, or "drop-off," portion of the tungsten wire is saved and used for scanning in our UHV systems. Tips are often characterized after fabrication by transmission electron microscope (TEM) imaging. Figure 4 displays a typical TEM image

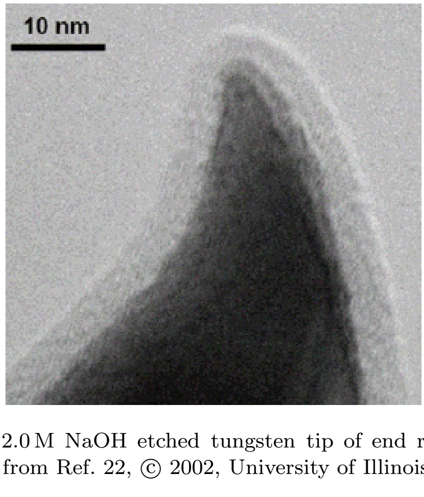

Fig. 4. TEM image of a 2.0 M NaOH etched tungsten tip of end radius of curvature < 2 nm. Reprinted with permission from Ref. 22, © 2002, University of Illinois at Urbana-Champaign.

recorded for an etched tungsten tip. The end radii of curvature of tips created in this manner are often in the order of tens of nanometers, as estimated by TEM measurements, though they may occasionally reach the single nanometer regime.[22] As-etched tips frequently possess a significant oxide coating, additional processing is sometimes required to remove this insulating layer and improve the tip shape. Various techniques, such as post-fabrication HF and KOH dips and electroless gold deposition, have been attempted, but no consistent significant improvements in tip characteristics have been achieved. A more reproducible tip-sharpening method based on field-directed sputter sharpening has been recently reported.[22]

2.2.2. *Atomically precise tip development*

Single-atom tips (SATS) are metal tips ending with only one atom, which are ideal probes for STM as they can achieve the highest spatial resolution and allow for manipulation of single atoms. There is an urgent need to develop reproducible STM tips for atomic resolution patterning with STM. SATS is one of the excellent candidates with an invariant geometry and a single atom tunneling point. Recently, Kuo *et al.*[23,24] developed a simple and reliable method for preparing single-atom tips. They applied electrochemical techniques to deposit a noble metal film on a W(1 1 1) tip. With the protection of the metal film, the tip can be stored and transferred in ambient conditions. After a gentle annealing of the plated tip in vacuum, a thermally and chemically stable nano-pyramid with single atom sharpness can be generated at the tip apex. The authors subsequently electrochemically deposited approximately 1 monolayer of a noble metal such as Pt, Pd, Rh, or Ir on the W(1 1 1) tip. Their procedures for the preparation of SATS are depicted in the left column of Fig. 5.

The experimental evidence for the formation of SATS is shown in the right column of Fig. 5. The authors[23,24] used field ion microscopy (FIM) to monitor the evolution of the tip shape during the preparation process. Image (a) corresponds to the shape after degassing the Pd-plated tip in UHV at 700 K for 5 min. The scattered image spots indicate that Pd atoms are deposited randomly on the tip surface. After annealing at 1000 K for 20 min, an ordered atomic structure starts to appear as shown in image (b). When the tip is annealed for an additional 5 min, a perfect bcc (body centered cubic) atomic structure is clearly identified (see image (c)). The tip is further annealed to 1000 K for 5 min, and the single-atom tip is observed (see image (d)).

2.3. *STM nanocharacterization of semiconductors*

2.3.1. *Silicon (Si)*

The real-space atomic resolution imaging capability of STM has exerted a significant impact in the field of surface science. In recent decades, with the development of the nanoelectronics industry and the STM technique, interest in studying semiconductor surfaces has been largely driven by the importance of understanding the structural

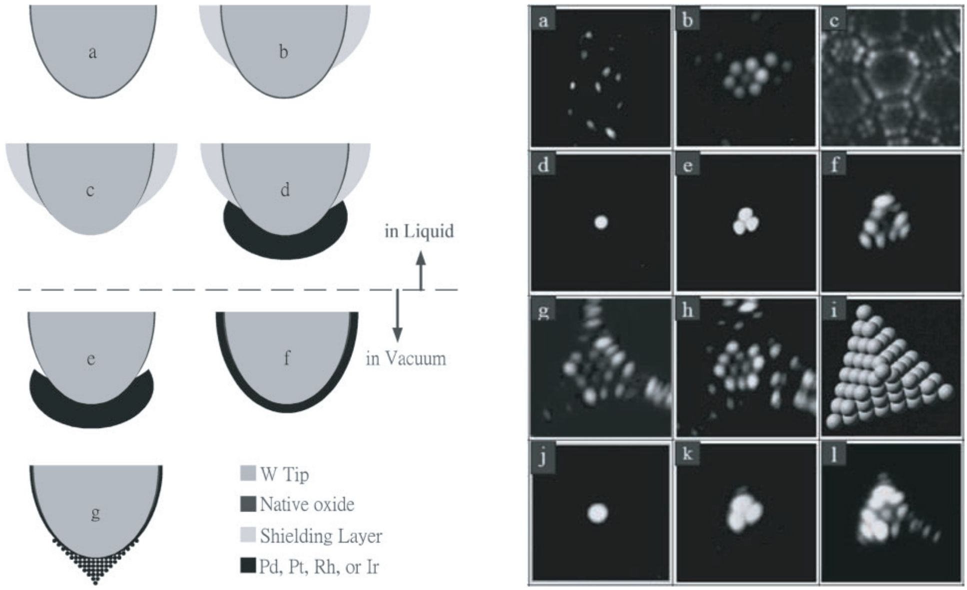

Fig. 5. Left column: schematic diagram for the preparation of SATS. (a) Etch a single crystal W wire to a tip shape. (b) Cover the tip with nail polish except for the apex. (c) Reduce native oxide by cathodic polarization. (d) Electroplate a noble-metal film on the tip. (e) Remove the nail polish and transfer the tip into vacuum. (f) Anneal the tip to diffuse noble metal atoms to other parts of the tip. (g) When the tip is covered by only one physical layer of a noble metal, a pyramidal single-atom tip builds up spontaneously. Right column: FIM images showing structure of Pd-plated W(1 1 1) tip: (a) As-deposited tip. (b) Tip after annealing at 1000 K for 20 min. (c) Tip after annealing at 1000 K for 25 min. (d) Tip after annealing at 1000 K for 30 min. The top layer ends with only 1 atom. (e) The second layer consists of 3 atoms. (f) The third layer consists of 10 atoms. (g) The fourth layer consists of 15 atoms. (h) The pyramidal structure is destroyed by continuous field evaporation. (i) 3D hardball model of nano pyramid. (i) Regenerated single atom tip after annealing at 1000 K for 5 min. (k) The second layer consists of 3 atoms. (l) The third layer consists of 9 atoms. Reprinted with permission from Ref. 23, © 2006, Institute of Pure and Applied Physics.

and electronic properties of surfaces for a variety of technologies, particularly in the area of semiconductor devices and the processing steps used to fabricate them. The most fundamental properties that characterize a clean surface are the positions of its atoms and the changes in the electronic properties of the bonds associated with these atoms that result from their reduced coordination at a surface.

The Si(1 0 0) surface is a widely studied surface due to its importance both in the semiconductor industry and scientific community. Cutting a silicon crystal to expose a (1 0 0) surface leaves each surface atom with two dangling bonds per surface atom, with the appearance of 'rabbit ears'. Si(1 0 0) exhibits a variety of surface reconstructions based on the surface annealing processes. Among them, the (2×1) and $(2 \times n)$ reconstructions are two stable structures commonly observed on clean Si(1 0 0) surfaces.[25–27] For the formation of a surface structure, surface dimerization, surface defects and impurities, and surface preparation procedures play a vital role. The Si(1 0 0) dimer row structure has been very extensively studied, and here we show an example of the $(2\times n)$ reconstruction. The $(2\times n)$ $(6 < n < 11)$ surface is formed by missing dimer channels along the Si dimerization direction.[28] It is widely accepted that trace amounts of metal impurity, particularly Ni, on the surface is responsible for this reconstruction.[29,30] By using STM and LEED (low energy electron diffraction) techniques, Xu *et al.*[31] observed a metastable higher-order Si(1 0 0)-c(8×8) superstructure on Si(1 0 0). The formation of the c(8×8) reconstruction was found to be very sensitive to the surface annealing history, and was observed when the Si(1 0 0) sample was quickly cooled from 1200°C to 700°C and kept at this temperature for 5 minutes, and then slowly cooled down to room temperature (RT) at a cooling rate of 1.2°C/sec. It can be seen in Fig. 6 that the c(8×8) reconstruction exhibits long range order over a wide surface area. Figure 6(a) shows a high resolution STM image of the c(8×8) superlattice structure, and a unit cell is marked by the white box. Each rectangular-cell consists of three pairs of protrusions. The electronic height of the middle-pair, which appears as a pair of bright dots in the STM image and indicated by the white arrow in Fig. 6(a), is higher than the two end-pairs labeled by the black arrows. The end-pair of protrusions in the longer side of the rectangular-cell is separated from the nearest end-pair of the next rectangular-cell by rectangular gaps of 15.6 ± 0.2 Å. The gap corresponds to the length of one rectangular cell, and its replication leads to the formation of a rectangular checkerboard repeat pattern. Based on the STM results, Xu *et al.*[31] suggested a new dimer model for the Si(1 0 0)-c(8×8) superstructure (see Fig. 6(c)).

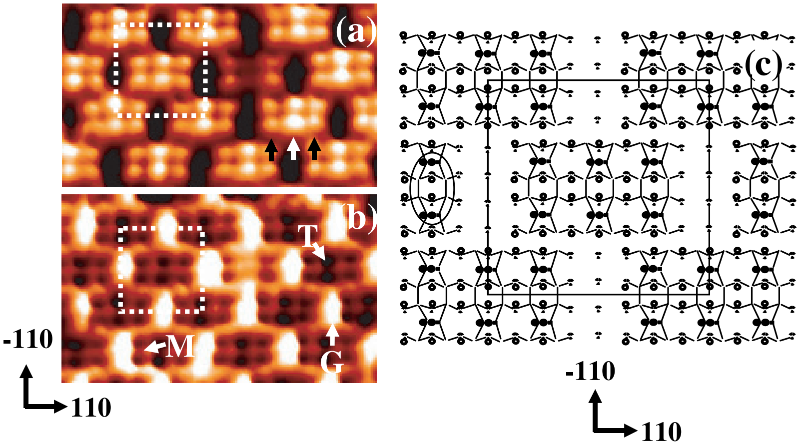

Fig. 6. (a) Empty-state STM image (scan size = 108 Å × 62 Å, V = 2.0 V) of a small portion of the Si(1 0 0)-c(8×8) reconstructed surface. Here the [1 1 0] direction is along the longer direction of the rectangular-cells. A single Si(1 0 0)-c(8×8) unit cell identified by a dotted square. (b) The same surface in inverted representation. The deepest portion of surface topography appears here as brightest (highest). Three layers ground, middle and top are marked by G, M and T respectively. (c) Proposed model to explain the Si(1 0 0)-c(8×8) reconstruction. The first, second and third layer atoms are denoted by solid, hollow and dotted circles respectively. For simplicity dimerization of third layer Si-atoms (within the rectangular holes) have not shown here.

2.3.2. *Gallium arsenide (GaAs)*

GaAs is a technologically important substrate for optoelectronic and photonic devices. It displays a variety of surface reconstructions[32–34] depending on the method of sample preparation. For example, the surface prepared by molecular beam epitaxial growth gives the As-rich (2×4) reconstruction, while the GaAs(0 0 1)-(1×6) phase is a surface reconstruction commonly observed after the GaAs substrate is cleaned by a combination of sputtering and annealing.[35–37] Jona first observed the GaAs(0 0 1)-(1×6) surface structure using the LEED technique.[37] Apart from the (1×6) phase, other transitional phases such as (2×6), (3×6), (6×6), and (4×6) surface reconstructions have also been reported.[38–41] Unlike surfaces prepared by MBE growth, the formation of these phases with 6× periodicity is very sensitive to the conditions used such as the sputtering rates and annealing temperatures. In general, it is difficult to identify the $(n \times 6)$ phase and resolve its atomic structure by LEED alone. Xu *et al.*[42,43] used STM to systemically study the detailed atomic configurations of GaAs(0 0 1)-6×6 and Ga-rich GaAs(0 0 1)-c(8×2) surface reconstructions, as well as phase transition between two structures. They found a new GaAs(0 0 1)-6×6 phase consisting of one alternating single As-dimer row on the top layer and two Ga-dimer rows between the As chains. These As-dimer chains show an average 2× local periodicity along the As dimerization direction. The Ga-dimer rows, on the other hand, possess a 3× periodicity, which well explains why (6×6)-like patterns have been observed in LEED/RHEED (reflection high energy electron diffraction) experiments.

Figure 7 shows STM images of a n-type GaAs(0 0 1) surface annealed at about 570°C after Ar ion-bombardment.[43] Figure 7(a) displays a filled state image (scan size $= 50 \times 50\,\mathrm{nm}^2$; sample bias $= -1.8\,\mathrm{V}$) in which the cross-sectional profile indicates a well ordered 6× periodicity (24 Å) along the [1 1 0] direction. The profile does not show a regular zigzagged As-dimer structure as reported in Ref. 44. Figure 7(b) displays the corresponding empty state image (sample bias $= +1.8\,\mathrm{V}$) of the same region. The As-dimer rows observed in the empty state image look broader than those in the filled state image. This arises from additional electronic contributions from the second-layer Ga atoms. Between the As-dimer chains, a series of the periodic oblong shaped dots are observed along the [−1 1 0] direction. The dots are not well defined in the filled state image shown in Fig. 7(a). These dots are thought to arise from Ga-dimers that are more prominent in the empty-state images. Strong tunneling into the empty state Ga-dimer rows increases the contrast of Ga-dimers, as can be seen in the missing As-dimer regions in Fig. 7(b). The line profile along the [−1 1 0] direction displayed in Fig. 7(b) indicates that these Ga-dimers are separated by 12.3 Å, which is about three times the bulk lattice period, i.e. 3× periodicity. Figures 7(c) and 7(d) show high-resolution dual bias STM images (with scan sizes of 100×100 Å, and 90×90 Å, respectively) taken sequentially on the GaAs(0 0 1) surface. The alternating single As-dimer chain and double Ga-dimer chains in the trough between the As chains are highlighted in Figs. 7(c) and 7(d) respectively. The

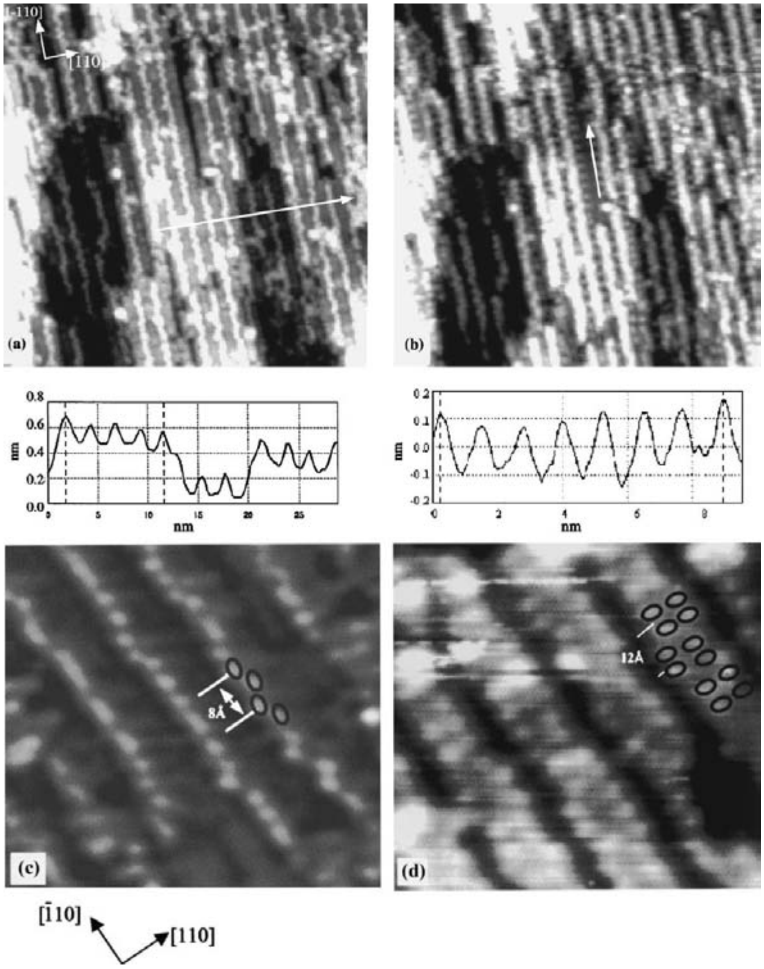

Fig. 7. (a) Filled and (b) empty state images captured on the same area of a GaAs(0 0 1) surface. (c) Filled and (d) empty state high resolution STM images showing the (6 × 6) structure at the atomic scale. Adapted from Ref. 43.

bright As-dimer rows at the top layer separated by 8 Å (2× periodicity) along the [−1 1 0] direction is clearly observed in Fig. 7(c). It is obvious that the periodicity is localized with the rows appearing straight in some sections and zigzagged in others. The 3× periodicity in the [−1 1 0] direction is clearly seen in Fig. 7(d). The STM results show that (6 × 6) structure represents a transitional phase and the proposed models are idealized in that they only represent local periodicity observed in the images. In fact, no perfect (6 × 6) image has been observed over a reasonable length scale, and this explains why no sharp (6 × 6) LEED or RHEED patterns have been reported.

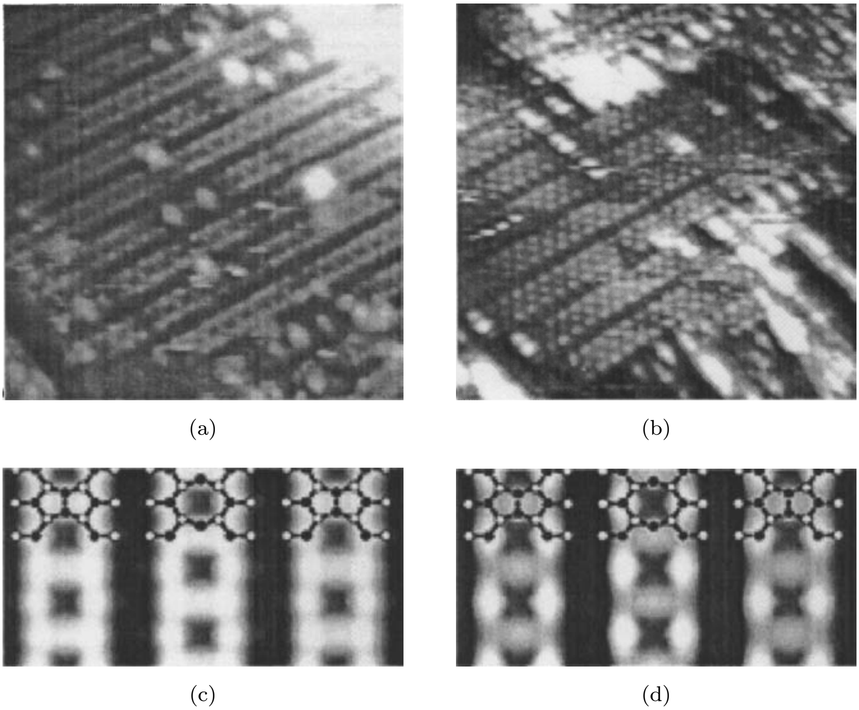

Fig. 8. Atomically resolved STM images of GaAs(0 0 1)-c(8 × 2) surface obtained at Vs = +1.9 V (a) and Vs = +1.6 V (b). The scan size is 150 × 150 Å. Simulated STM images at +1.8 V (c) and +1.5 V (d) bias voltages, which are given with respect to the valence-band maximum. Adapted from Ref. 42.

The c(8 × 2) phase is known to be the most prominent high-temperature phase and often coexists with one of several proposed As-rich ($n \times 6$) phases in the temperature range 500–650°C.[45] On GaAs(0 0 1), the c(8 × 2) domains are usually surrounded by ($n \times 6$) domains which are one atomic layer higher. Figures 8(a) and 8(b) displays the high-resolution empty-state STM images obtained at +1.9 V and +1.6 V sample bias, respectively.[42] Triple-protrusion rows can be clearly seen in both images, where the bright rows are separated by dark trenches and the distance between the centers of two adjacent trenches. Figures 8(c) and 8(d) shows the simulated STM images at +1.8 and +1.5 V sample bias respectively, and the theoretical STM images in good agreement with the experimentally observed images shown in Figs. 8(a) and (b).

2.3.3. *Silicon carbide (SiC)*

Silicon carbide (SiC) is a wide-band-gap compound semiconductor which is a promising candidate for high power, high frequency and high temperature applications. The hexagonal polytype of SiC, e.g., 4H-SiC and 6H-SiC, is of particular interest due to its high thermal conductivity, high breakdown field, and large electronic band gap of 3.0 eV.[46] It is known that SiC crystals take a variety of surface reconstructions depending on the annealing temperatures. For the C-terminated SiC(0 0 0 1) surface, Johansson *et al.*[47] reported that heating the as-introduced sample at 1050°C in ultra-high vacuum (UHV) led to the formation of a 3×3 structure. Such a 3×3 surface reconstruction was also observed by annealing a SiC-$\sqrt{3} \times \sqrt{3}$ silicate surface at 1050°C for 15 min in UHV. In particular, an interesting nanotemplate due to the formation of a $6\sqrt{3} \times 6\sqrt{3}$ R30° reconstruction on 6H–SiC(0 0 0 1) surface has been observed. The reconstructed $6\sqrt{3} \times 6\sqrt{3}$ R30° phase resembles a honeycomb structure composed of unit cells with diameter of about 2 nm.[48–50] It was demonstrated that the honeycomb structure can be used as a nanotemplate for the growth of size-controlled metal clusters.[48,49] The $6\sqrt{3} \times 6\sqrt{3}$ R30° reconstruction on 6H–SiC(0 0 0 1) or on the closely-related 3C–SiC(1 1 1) surface displays a $6\sqrt{3} \times 6\sqrt{3}$ R30° LEED diffraction pattern, whereas it manifests as an incommensurate 6×6 honeycomb superstructure in STM studies.[51–54] Recently, Chen *et al.* investigated the detailed atomic structure of the complicated $6\sqrt{3} \times 6\sqrt{3}$ R30° phase by combining STM, LEED, photoemission spectroscopy (PES) and density-functional theory (DFT) methods.[55] They revealed that the formation of the $6\sqrt{3} \times 6\sqrt{3}$ R30° reconstruction (the so-called carbon nanomesh) is a result of the self-organization of carbon atoms during the evaporation of silicon atoms from the SiC(0 0 0 1) surface and subsurface at ~1100°C. Figure 9 shows a series of filled state STM images recorded for the $6\sqrt{3} \times 6\sqrt{3}$ R30° phase with different tip biases from 1.5 V to 2.5 V and a fixed tunneling current of 0.2 nA. It can be seen that the nanomesh template comprises incommensurate honeycombs. Most honeycombs exhibit diameters of 20.0 ± 2.0 Å, which is very close to the $6{\times}6$ periodicity (~19 Å) of pristine SiC(0 0 0 1). The apparent height of the honeycombs is 1.5 ± 0.1 Å as determined from the line profiles of the STM images. Figure 9(e) shows an empty state STM image (scan size: $50 \times 50\,\text{nm}^2$) of the carbon nanomesh surface ($V_T = -2.0\,\text{V}$), which again clearly displays the honeycomb structures. A comparison of STM images recorded for the same region with reverse bias polarity is made in Figs. 9(f) and (g). The result indicates that the carbon nanomesh is a real physical structure, and not of electronic origin as opposed to the electronic Moire' patterns on lead (Pb) quantum islands.[56]

Figure 10 shows the LEED patterns (left panel) and corresponding STM filled state images (right panel) of SiC(0 0 0 1) after annealing at different temperatures.[55] After annealing at 1050°C for 5 min (see Fig. 10(a)), the STM image clearly shows the coexistence of two structures: the upper region corresponds to the disordered $6\sqrt{3} \times 6\sqrt{3}$ R30° reconstruction and the lower region corresponds to the carbon nanomesh structures. Such a surface is referred to as a "$6\sqrt{3} \times 6\sqrt{3}$ R30° + carbon nanomesh mixed surface". The corresponding LEED pattern of this surface displayed in the left panel of Fig. 10(a) was previously referred to as the $6\sqrt{3} \times 6\sqrt{3}$ R30° LEED pattern.[46,50,57] The white circles in the LEED pattern shown in Fig. 10(a) highlight the $6\sqrt{3} \times 6\sqrt{3}$ R30° LEED diffraction spots. This

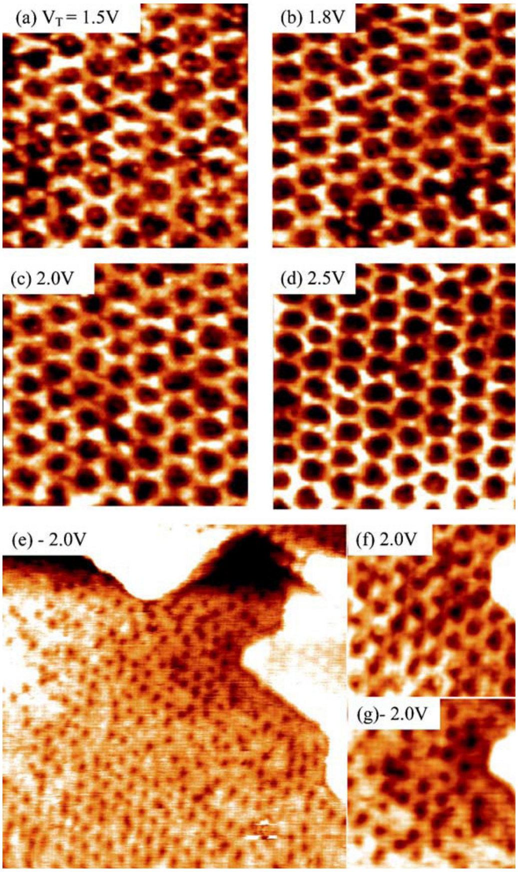

Fig. 9. Filled state STM images (scan size: 20 × 20 nm^2) obtained for the carbon nanomesh at different tip bias of (a) 2.5 V, (b) 2.0 V, (c) 1.8 V, (d) 1.5 V. (e) Empty state STM image (50 × 50 nm^2) obtained at tip bias of −2.0 V. STM images (17 × 17 nm^2) with reverse tip bias polarity at the same region: (f) 2.0 V and (g) −2.0 V. Adapted from Ref. 55.

surface was further annealed at 1100°C for 5 min. At this stage, the $6\sqrt{3} \times 6\sqrt{3}$ R30° reconstructions vanished from the STM image (see Fig. 10(b)), and the surface was fully covered by the incommensurate honeycomb-like nanomesh structure with approximately 6 × 6 periodicity. The LEED pattern displayed in Fig. 10(b) clearly shows the disappearance of the $6\sqrt{3} \times 6\sqrt{3}$ R30° diffraction spots, indicating that this surface is now the pure carbon nanomesh.

Figure 11 shows the evolution of C 1s core-level spectra recorded by Chen *et al.* during annealing of the SiC(0 0 0 1) surface.[55] First, the 3 × 3 surface was prepared by annealing the SiC substrate at 850°C under silicon flux for 2 min. The 3 × 3 reconstruction was confirmed by LEED and STM. The surface was then annealed at 950°C for 5 min in the absence of Si flux and a sharp $\sqrt{3} \times \sqrt{3}$ LEED diffraction pattern was formed. The C 1s core-level spectrum (see Fig. 11(a)) is dominated by

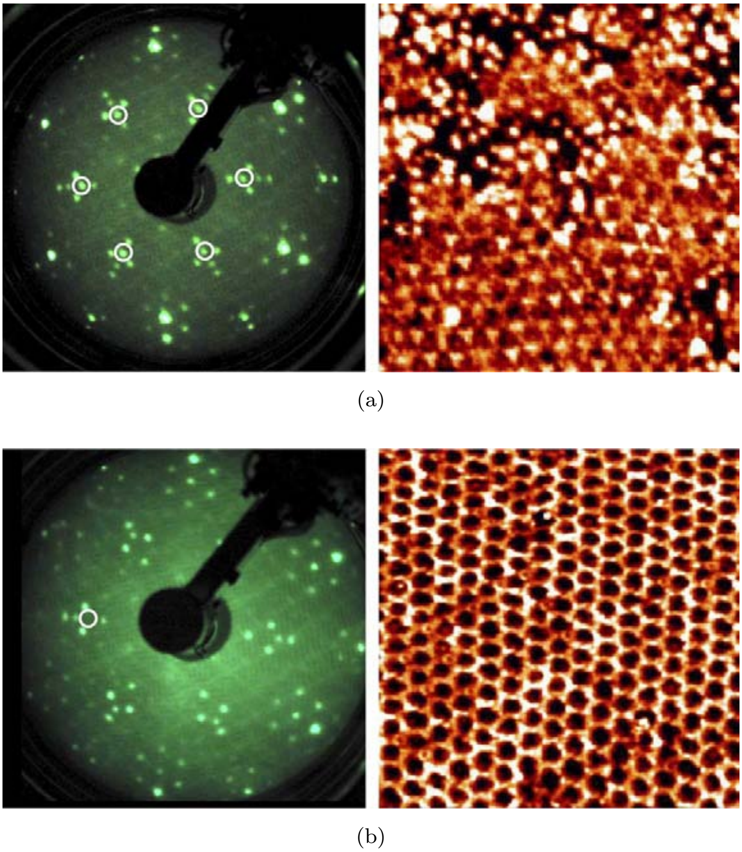

Fig. 10. LEED patterns (left) and corresponding filled state STM images of 30 × 30 nm^2 scan size (right) of (a) $\sqrt{3} \times \sqrt{3}$ R30° + carbon nanomesh mixed surface and (b) well-developed carbon nanomesh surface on 6H–SiC(0 0 0 1). The white circles highlight the $\sqrt{3} \times \sqrt{3}$ R30° LEED spots. Adapted from Ref. 55.

the bulk SiC peak at a binding energy of 282.9 eV. The $\sqrt{3} \times \sqrt{3}$ R30°C surface was free of oxygen and other contamination, as determined by wide scan PES spectrum using a photon energy of 700 eV. Further annealing at 1050°C for 5 min led to the formation of the "$6\sqrt{3} \times 6\sqrt{3}$ R30°C + carbon nanomesh mixed surface". A new component peak at 285.1 eV appears in the C 1s spectrum as shown in Fig. 11(b). The "pure carbon nanomesh surface" was formed after annealing the SiC substrate at 1100°C for 5 min. At this stage, the 285.1 eV peak dominates the C 1s spectrum (see Fig. 11(c)) accompanied by a shoulder at 238.8 eV; the bulk-related SiC component at 282.9 eV almost vanishes. After further annealing at 1200°C for 5 min, the C 1s spectrum (see Fig. 11(d)) broadens to the lower binding energy side, and a new component peak at 284.4 eV is just resolvable. A freshly cleaved highly ordered pyrolytic graphite (HOPG) sample was used as the reference sample, with a C 1s binding energy of 284.5 eV. This new component peak at 284.4 eV is attributed to

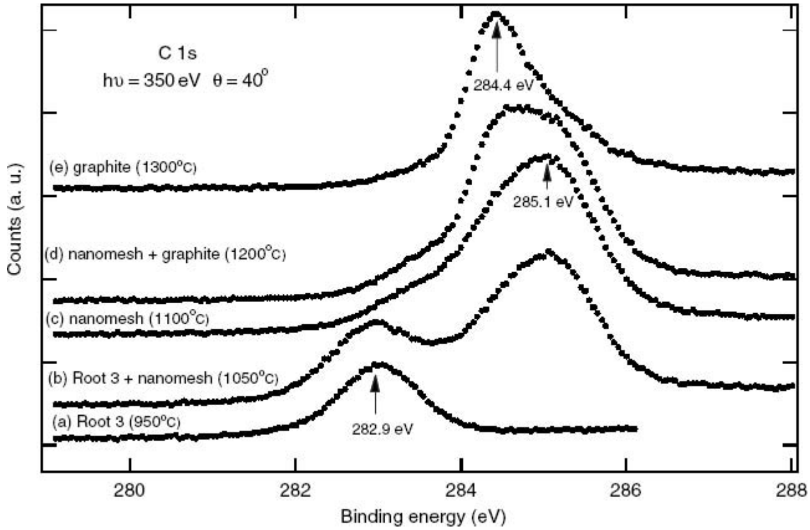

Fig. 11. C 1s core-level spectra recorded from the $\sqrt{3} \times \sqrt{3}$ R30°C surface and after different heat treatments, measured at a photon energy of 350 eV and an emission angle of 40°. (a) $\sqrt{3} \times \sqrt{3}$ R30°C surface, (b)$\sqrt{3} \times \sqrt{3}$ R30°C + carbon nanomesh mixed surface, (c) pure carbon nanomesh surface, (d) carbon nanomesh + graphite mixed surface and (e) graphite surface. Adapted from Ref. 55.

the crystalline graphite layers formed at 1200°C. Annealing at 1300°C for 5 min gives a C 1s spectrum dominated by the signal from the graphite or 'graphene' layer, which is currently of much research interest (see Fig. 11(e)). Hence, graphitization of the SiC surface only occurs at temperatures higher than that required for the formation of the "pure carbon nanomesh surface".

In order to understand the atomic structure of the carbon nanomesh surface, Chen *et al.* carried out first-principles total energy calculations using the Vienna ab initio simulation package (VASP).[55] They proposed a 6×6 supercell model that best fits both their STM and PES results. Figures 12(c) and (d) shows the top and side views respectively of the 6×6 supercell model. In the 6×6 model, there are two kinds of surface-related carbon atoms that make up the carbon nanomesh structures. The first type is carbon atom (A) that bonds to one underlying Si atom. The binding energy of these C atoms is expected to be higher than that of the bulk SiC-related C atoms (282.9 eV, bonded to four Si atoms), but lower than that of the C atoms from graphite (284.4 eV). The second type is carbon atom (B) that lies above the SiC surface without formation of Si–C bonds. These B atoms form the 6 C-rings or graphene-like structures with delocalized p-electrons to minimize the total energy. In the model, the B atoms are located above Si atoms that possess one unsaturated bond or dangling bond as highlighted by the white spheres in Fig. 12(c). To lower the total energy of the system, the B atoms may partially share their delocalized p-electrons with the unsaturated bond on the Si atoms, hence causing the B atoms

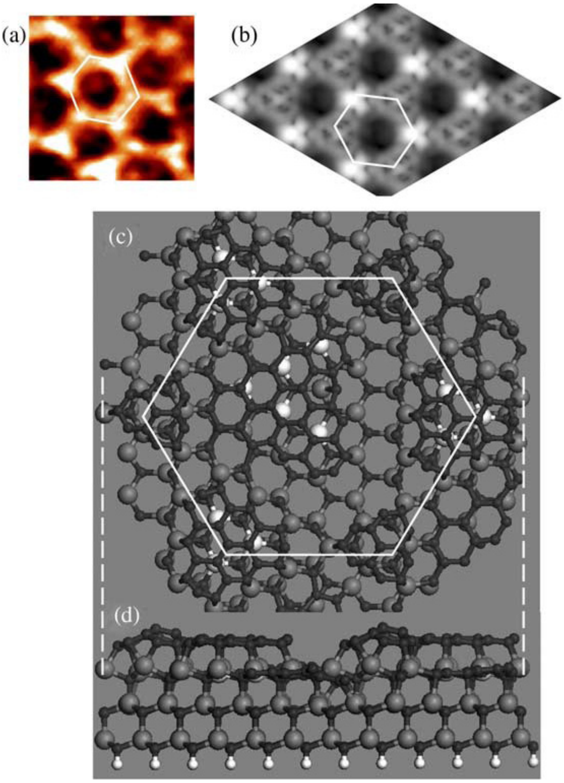

Fig. 12. (a) Experimental filled state STM image of the carbon nanomesh surface. (b) Calculated fill state STM image. (c) top and (d) side views of the 6×6 model, the small dark spheres represent C atoms, big grey spheres for Si atoms, big white spheres for the Si atoms with dangling bonds, and small white spheres for H atoms. The white hexagon highlights the honeycomb unit cell in the experimental and calculated STM images, and in the 6×6 supercell model. Adapted from Ref. 55.

to be slightly positively charged compared to graphite. Calculation of STM images was performed by Chen *et al.* on the basis of the proposed model. The calculated STM image (see Fig. 12(b)) is in qualitative agreement with the experimentally observed image shown in Fig. 12(a).

3. Spin-Polarized Scanning Tunneling Microscopy (SP-STM)

As one of important SPM techniques, spin-polarized scanning tunneling microscopy (SP-STM)[4,5] not only images the electron density near the sample surface as in conventional STM, but also maps the spin polarization signal on the sample surface. Thus, local magnetic information of the surface can be simultaneously captured while acquiring its topography. In conventional STM, the spin of the electron is neglected in the scanning process. For most materials, this simplification is well justified as the electron density does not depend on the spin of the electron. But for ferromagnetic or antiferromagnetic samples, the density of states is spin-split into majority and minority states. A net spin polarization is present in individual atoms. In SP-STM, the tip is made of magnetic material which has spin-polarized electrons. Therefore, the spin polarization signal of the sample surface may be obtained via the spin–dependent tunneling process between tip and sample.

3.1. *Basics of SP-STM*

The principle of SP-STM is based on the relative magnetization orientation of both electrodes (tip and sample) as schematically represented in a simplified Stoner model as shown in Fig. 13.[58] Due to the spin–sensitive exchange interaction, the density of states splits up into minority and majority densities. The imbalance causes spin polarization. For paramagnetic samples where the distributions of spin-up and spin-down electrons are identical, no spin polarization is present. However, STM generally only measures the tunneling current instead of the spin polarization. Julliere[59] discovered the so-called tunneling magneto resistance (TMR) effect. He found that the tunneling conductance G depends on the relative orientation of the magnetization. For parallel orientation, the majority/minority electrons of the first electrode tunnel into the majority/minority states in the second electrode respectively, hence G is higher than for anti-parallel orientation. The conductance G for parallel and anti-parallel oriented magnetizations is given by

$$G_{\uparrow\uparrow} \propto N^i_{\uparrow} N^f_{\uparrow} + N^i_{\downarrow} N^f_{\downarrow} \tag{2}$$

$$G_{\uparrow\downarrow} \propto N^i_{\uparrow} N^f_{\downarrow} + N^i_{\downarrow} N^f_{\uparrow} \tag{3}$$

G is proportional to the density N of initial (i) and final (f) states at the Fermi edge. It can be seen from Eqs. (2) and (3) that the two conductivities, $G_{\uparrow\uparrow}$ and $G_{\uparrow\downarrow}$, are

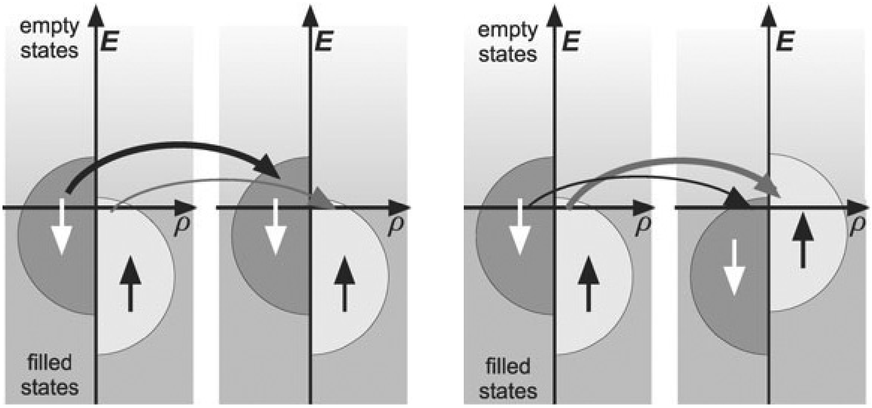

(a) (b)

Fig. 13. Principle of spin-polarized tunneling between magnetic electrodes that exhibit (a) parallel and (b) antiparallel magnetization, respectively. The conductivities for tunneling from the left to the right electrode are indicated by arrows. Reprinted with permission from Ref. 58, © 2003, Institute of Physics.

in general not identical. This leads to a variation of the tunneling current with the magnetic configuration of the electrodes, which can be easily distinguished by STM.

3.2. *Surface topography and local magnetism*

Figure 14 shows an example of surface topography and magnetism study by SP-STM on single crystal Cr(0 0 1).[58] Figure 14(a) displays the topography image which shows a regular step-structure with terrace widths of 100–200 nm. The line-section at the bottom of Fig. 14(a) reveals that all step edges in the field of view are of single atomic height, i.e. 1.4 Å. According to the theoretically predicted model of Blugel *et al.*[60] ('topological antiferromagnetism') this topography should lead to a surface magnetization that periodically alternates between adjacent terraces. Indeed, this has been observed experimentally (see Fig. 14(b)). The line-section of the dI/dU signal drawn along the same path as in Fig. 14(a) indicates two discrete levels with sharp transitions at the step edges.

Another typical example is on single crystal Fe_3O_4 surface. Fe_3O_4 is a natural magnetite that exhibits a cubic inverse spinal structure containing pure Fe^{3+} (0 0 1) planes as well as two types of Fe–O (0 0 1) planes, namely C_a and C_b planes.[58] The structure model for both types of Fe–O planes is shown in Fig. 15(a). It is characterized by Fe rows which change their orientation by 90° from one atomic plane to the next with a separation between these rows of 6 Å. In particular, these Fe–O planes

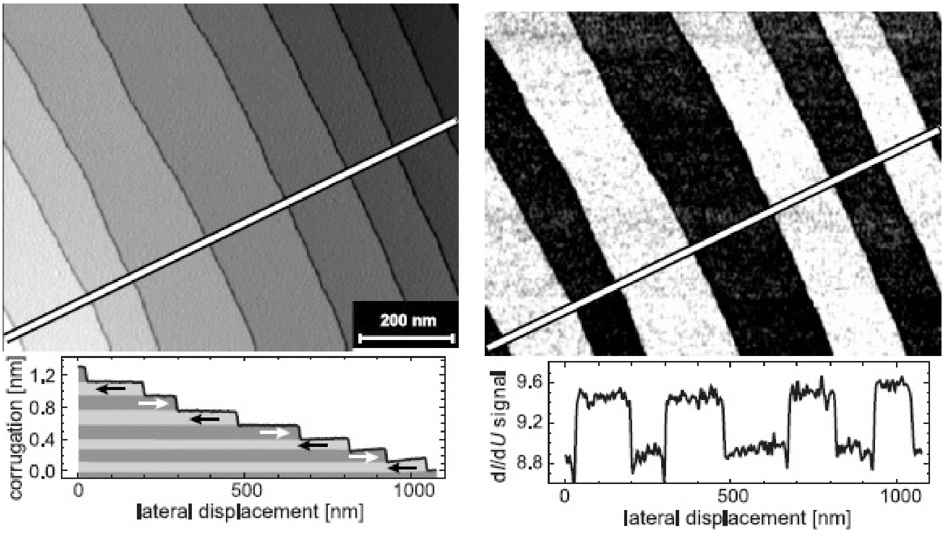

(a) (b)

Fig. 14. (a) Constant-current mode STM image of the Cr(0 0 1) surface. Nine terraces separated by monatomic steps are visible. (b) Simultaneously acquired spin-resolved dI/dU map at U = −290 mV sample bias. The signal changes at every step between low and high due to antiparallel magnetization of adjacent terraces. Reprinted with permission from Ref. 58, © 2003, Institute of Physics.

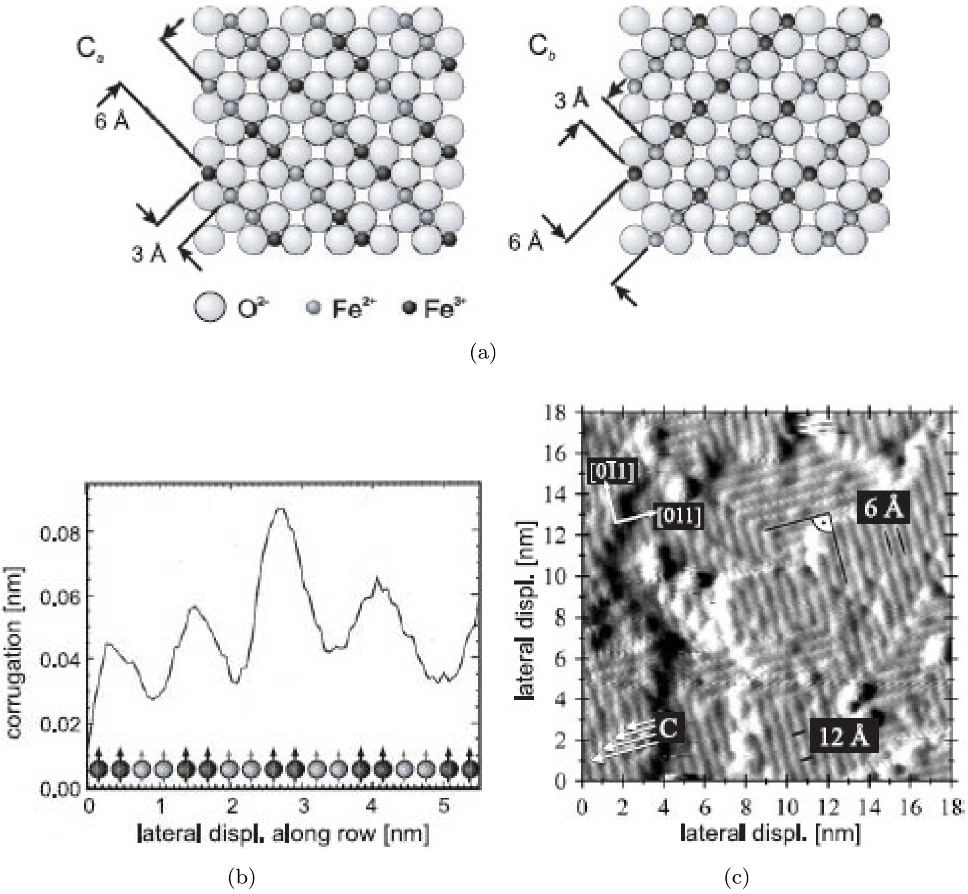

(a)

(b)

(c)

Fig. 15. (a) Structure model of Ca and Cb Fe–O(0 0 1) planes of magnetite (Fe_3O_4). Fe-rows with alternating Fe^{2+} and Fe^{3+} can be found. A periodic corrugation was found which was interpreted in terms of atomic scale spin-polarized tunneling into Fe ions of different spin configurations. (c) Constant-current STM image. Reprinted with permission from Ref. 58, © 2003, Institute of Physics.

contain different ionic species of Fe, i.e. Fe^{2+} and Fe^{3+}, which are due to different spin configurations — $3d5\uparrow 3d\downarrow$ for Fe^{2+} and $3d5\uparrow$ for Fe^{3+}. Wiesendanger and co–workers[61,62] investigated Fe_3O_4 single crystal (0 0 1) surface using SP-STM. Atomic resolution images obtained on FeO planes exhibited a qualitative dependence on whether magnetic or non-magnetic tips were used. The authors reported that line-sections measured along the Fe row with a non-magnetic W tip appear featureless, i.e. the surface corrugation is lower than the noise level of 0.1 Å. In contrast, the line-section (see Fig. 15(b)) obtained with a bulk Fe tip along the Fe rows exhibits an oscillation with an amplitude of 0.2–0.4 Å. The most frequently observed periodicity was 12 Å, which is inconsistent with the structural periodicity of 3 Å but fits the repeat period of Fe^{2+} and Fe^{3+} ions of magnetite below the Verwey transition temperature. These observations were interpreted in terms of atomic-scale spin-polarized tunneling from a ferromagnetic tip into a ferrimagnetic sample allowing one to distinguish atomic sites of different magnetic moments. Recently, Koltun *et al.*[4] confirmed the results of Wiesendanger *et al.*[61,62] by investigating the surface of an artificially manufactured Fe_3O_4 single crystal: their constant-current image displayed in Fig. 15(c) shows a modulation of the corrugation along the Fe rows too, with the same periodicity of 12 Å.

Recently, Yang *et al.*[5] observed an atomic magnetic structure on Mn_3N_2 (0 1 0) using SP-STM. Mn_3N_2 (0 1 0) is a magnetic transition metal nitride surface. The authors prepared the Mn_3N_2 (0 1 0) surface using a solid source effusion cell for Mn and a RF (radio frequency) plasma source for N. All STM imaging was performed at 300 K in constant current mode. For normal STM measurements, Yang *et al.*[5] used W tips cleaned in UHV by electron bombardment. For SP-STM measurements, they coated the cleaned W tips *in situ* at 300 K with either 5–10 ML of Mn or 5–10 ML of Fe. Figure 16(a) displays a STM image of Mn_3N_2 (0 1 0) acquired using a very sharp W tip. Individual Mn atoms are clearly resolved in the high-resolution image shown in Fig. 16(b). The image provides a perfect match with the Mn atom sublattice shown in Fig. 16(c) in which the higher and lower maxima correspond to the Mn(1) and Mn(2) atoms, respectively. The measured height difference between Mn(1) and Mn(2) atoms is 0.07 A, which is attributable to surface relaxation. Almost no bias dependence of the atomic resolution image was observed, indicating that this surface has metallic character in agreement with the calculated results. The surface unit cell, containing six Mn atoms and four N atoms (3:2 ratio), can be denoted as $C(1 \times 1)$ whereas the surface magnetic unit cell is just 1×1 (since $\mu_{\mathrm{Mn}(1)} \neq \mu_{\mathrm{Mn}(2)}$).

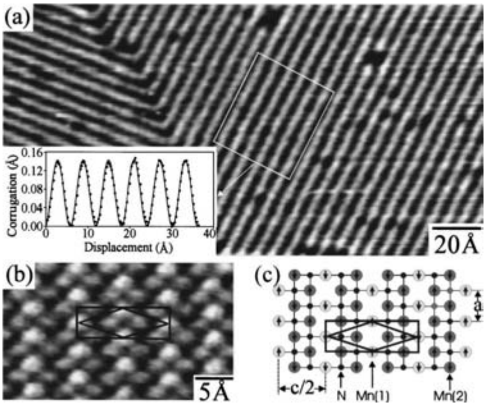

Fig. 16. (a) STM image of Mn_3N_2 (0 1 0) surface acquired at Vs = −0.4 V and Is = −0.4 nA. The inset shows the average line profile (data points) over the indicated region. The solid line is a sinusoid fitted to the data. (b) Atomic resolution STM image acquired at Vs = −0.3 V and It = 0.3 nA. (c) Bulk terminated surface model. The $c(1 \times 1)$ geometrical unit cell and 1×1 magnetic unit cell are indicated by the black rhombus and black rectangle, respectively. Reprinted with permission from Ref. 5, © 2002, The American Physical Society.

3.3. *Multi-probe scanning tunneling microscopy (MP-STM)*

3.3.1. *Four probe STM*

The great interest in nanoscale science and technology is focused on manipulating nanoscale material and measuring the electrical transport, optical and mechanical properties. The multi-tip tunneling microscopy technology has been shown to be a versatile tool for electrical transport measurements at the nanometer scale. For general purpose resistance and I–V curve measurements, 2-point electrical measurements are normally used. To determine the resistance, Ohm's law $R = V/I$ is used; a known current flows through the unknown resistance,, and the voltage that develops across the resistance is measured; the resistance is determined by dividing the measured voltage by the source current. A problem that occurs using the 2-point setup is that the voltage is measured not only across the resistance in question, but also includes the resistance of the leads and contacts as well (see Fig. 17(a)). When using an ohmmeter to measure resistances above a few ohms, this added resistance is usually not a problem. However, when measuring low resistances or when the contact resistance is high, obtaining accurate results with a two-point measurement may be a problem. The multi-probe STM provides a solution to this problem, since it can be operated in double-, triple-, or quadruple-probe modes, and is operated in combination with scanning electron microscope (SEM). The MP-STM technique has been applied to investigate nanodevices and implement nanofabrication.[6] For example, for electrical characterization of nanodevices, the STM-based 4-point measurement allows determination of both voltage and current (see Fig. 17(b)). Since a second set of probes is used for sensing and since negligible current flows in these probes, only the voltage drop across the device under test is measured. As a result, resistance measurement or I–V curve generation is more accurate. The improved accuracy (current-measuring capability $< 1\,\mathrm{pA}$) is very important for the characterization of the electrical properties of nanostructures and devices. Another important

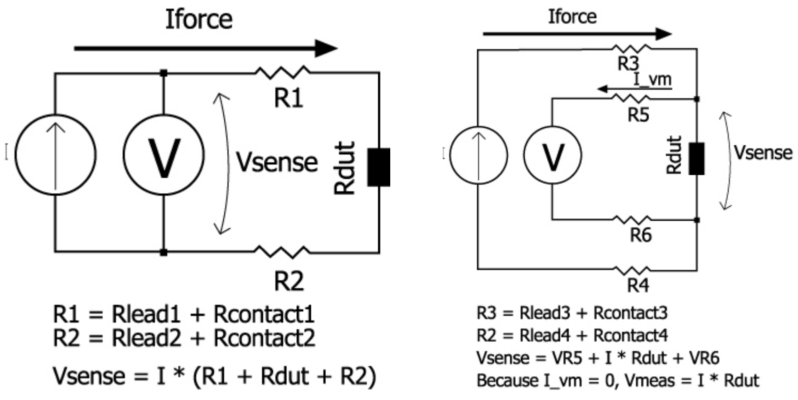

(a) (b)

Fig. 17. Electrical circuits for (a) 2-point and (b) 4-point measurements.

advantage of MP-STM is that each tip can be operated independently with fine positioning down to atomic scale. With the application of voltage on tips, measurements can be performed *in situ* on nanodevices such as single electron tunneling transistors. Moreover, the combination with high resolution SEM not only enables tip navigation on complex structures for fast and precise location of the desired testing points, but also adds functions such as chemical analysis and focused electron-beam (FEB) irradiation.

3.3.2. *Electrical transport measurement*

Lin *et al.*[63] manipulated and measured the electrical transport and optical properties of a perylene nanostick using their four-probe STM system in UHV conditions. To manipulate a nanostick, they first made some differently-shaped hooks (type A and C hooks) at the top of STM tips using special tip crashing skills. They then used type A hook to stop the nanostick moving and used type C hook to contact the nanostick firmly. The *I*–*V* characteristic measured by their MP-STM method is shown in Fig. 18. It can be seen that the leakage current is about 30 fA when the voltage is 1 V. The very low leak current and noise arises from the good shielding of the system and the cable. Their vacuum chamber made of stainless steel 15 provided shielding of the nanostructure and probes from electrostatic or magnetic interference. The Triax cable and connector used in their experiments provided very high leak resistance and very low cable–capacitance.

To measure the local electrical conductivity of well defined crystal surfaces *in situ* in ultrahigh vacuum, Hasegawa *et al.*[64] developed microscopic four-point probes with a probe spacing of several micrometers. They installed their four probes in a scanning electron-microscope/electron-diffraction chamber. The probe was precisely positioned at targeted areas of the sample surface using piezo actuators. This apparatus enabled conductivity measurements with extremely high surface sensitivity. By directly measuring the surface-state conductivity of superstructures, they were

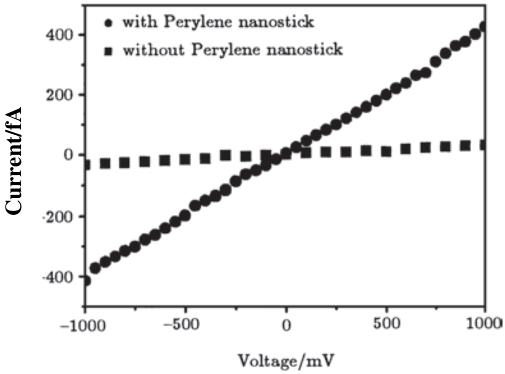

Fig. 18. *I*–*V* curve (●) of the perylene nanostick measured by two probes. *I*-*V* curve (■) of the leak current. Reprinted with permission from Ref. 63, © 2003, Chinese Physical Society.

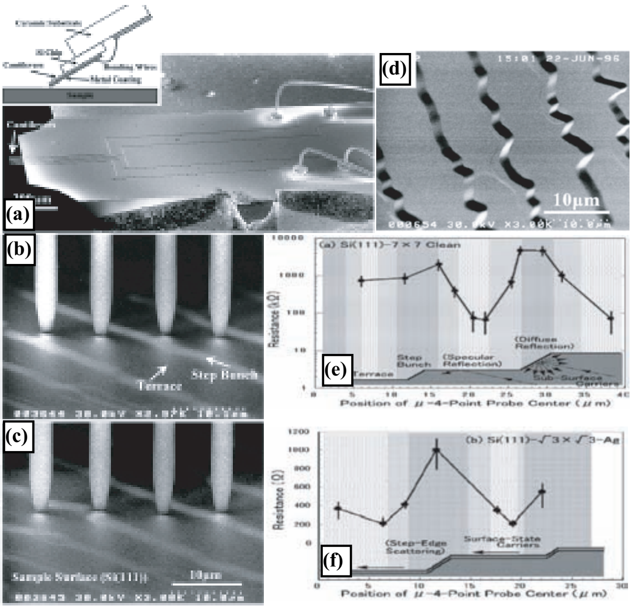

Fig. 19. Resistance measurements across a step bunch on the clean Si(1 1 1)-7 × 7 and Si(1 1 1)-$\sqrt{3} \times \sqrt{3}$-Ag surface with a monolithic μ-4PP (a) SEM image of the μ-4PP chip. (b), (c) SEM images of the μ-4PP contacting the sample surface in UHV. The resistance is measured across a step bunch in (b) while the resistance on a terrace is measured in (c). (d) SEM image of the step-bunched surface. (e), (f) Line profile of resistance measured by making the μ-4PP move along line across step bunches on the Si(1 1 1)-7 × 7 and Si(1 1 1)-$\sqrt{3} \times \sqrt{3}$-Ag surface respectively. Reprinted with permission from Ref. 64, © 2002, Institute of Physics.

able to clarify the influence of atomic steps in surface conductivity. Figure 19(a) shows a scanning electron micrograph (SEM) of a chip using the micro-four-point probe, which was produced by silicon micro-fabrication technology. Figures 19(b) and 19(c) shows SEM images of their sample (i.e., a Si(1 1 1)-7 × 7 clean surface) and the micro-four-point probe with 8 μm spacing contacting the sample surface. The probe is shifted laterally by about 5 μm in Fig. 19(c) from the position shown in Fig. 19(b). In this way, the local conductance of the targeted areas can be measured by fine positioning the probe with the aid of *in situ* SEM. Hasegawa *et al.*[64] found that the resistance increases by two orders of magnitude at step-bunch regions on the 7 × 7 surface (see Fig. 19(e)), whereas it increases by only a factor of four on the $\sqrt{3} \times \sqrt{3}$-Ag surface (see Fig. 19(f)).

4. Concluding Remarks

In this chapter, we have reviewed the development and application STM techniques in nanoscale characterization. The STM working principle, experimental setup, operation modes, and tip preparation are described. Selected results pertaining to the STM nanocharacterization of semiconductors Si, GaAs, and SiC were presented as illustrator examples. The capability of STM in real space visualization and its application in conjunction with other methods in resolving atomic arrangements and structures are demonstrated. New developments in STM techniques including SP-STM and MP-STM are discussed in comparison with conventional non-magnetic and single tip STM methods. SP-STM is able to detect the local magnetization of the surface below the apex of the STM tip by making it sensitive to the spin of the tunneling electron. It can image the magnetic domain structure of the sample with ultimate resolution down to the atomic scale. MP-STM offers a versatile tool for electrical transport measurements at the nanometer scale. The STM probes act as current sources, voltage pick up probes, and field-gate electrodes. It is useful not only for fundamental nanoscience research, but also for testing the electrical characteristics of nanodevices. At present, the most difficulty of SPM nanofabrication is on its reproducibility and pattern mass production in atomic precise scale. Further work is needed to control and minimize SPM's environmental drafts, e.g., scanner thermal and piezo non-linear draft etc., as well as develop an invariant STM tip, to qualify for durable and reproducible nanofabrication processes in atomic precise scale.

References

1. Binnig G, Rohrer H, Gerber C and Weibel E, Tunneling through a controllable vacuum gap, *Appl Phys Lett* **40**:178–180, 1982.
2. Binnig G, Quate CF and Gerber C, Atomic force microscope, *Phys Rev Lett* **56**:930–933, 1986.
3. Schneider WD, Scanning tunneling microscopy and spectroscopy of nanostructures, *Surf Sci* **514**:74–83, 2002.
4. Koltun R, Herrmann M, Guntherodt G and Brabers VAM, Enhanced atomic-scale contrast on Fe_3O_4 (1 0 0) observed with an Fe STM tip, *Appl Phys A: Mater Sci & Processing* **73**:49–53, 2001.
5. Yang HQ, Smith AR, Prikhodko M and Lambrecht WRL, Atomic-scale spin-polarized scanning tunneling microscopy applied to Mn_3N_2(0 1 0), *Phys Rev Lett* **89**:226101–226103, 2002.
6. Ehrichs EE, Smith WF and Delozanne AL, Four-probe resistance measurements of nickel wires written with a scanning tunneling microscope/scanning electron microscope system, *Ultramicroscopy* **42**:1438–1442, 1992.
7. Martin Y and Wickramasinghe HK, Magnetic imaging by "force microscopy" with 1000 Å resolution, *Appl Phys Lett* **50**:1455–1457, 1987.
8. Jo YJW, Yang Y and Park S, Biofilm formation and local electrostatic force characteristics of Escherichia coli O157:H7 observed by electrostatic force microscopy, *Appl Phys Lett* **90**:143901–143903, 2007.
9. Wong KM, Chim WK, Ang KW and Yeo YC, Spatial distribution of interface trap density in strained channel transistors using the spread of the differential capacitance characteristics in scanning capacitance microscopy measurements, *Appl Phys Lett* **90**:153507–153509, 2007.
10. Jia B, Gan X and Gu M, Direct observation of a pure focused evanescent field of a high numerical aperture objective lens by scanning near-field optical microscopy, *Appl Phys Lett* **86**:131110–131112, 2005.

11. Bouhelier A, Beversluis M, Hartschuh A and Novotny L, Near-field second-harmonic generation induced by local field enhancement, *Phys Rev Lett* **90**:013903–013906, 2003.
12. Hamers RJ, Tromp RM and Demuth JE, Surface electronic structure of Si(1 1 1)-(7×7) resolved in real space, *Phys Rev Lett* **56**:1972–1975, 1986.
13. Stroscio JA, Feenstra RM and Fein AP, Electronic structure of the Si(1 1 1) 2 × 1 surface by scanning-tunneling microscopy, *Phys Rev Lett* **57**:2579–2582, 1986.
14. Zilani MAK, Xu H, Liu T, Sun YY, Feng YP, Wang XS and Wee ATS, Electronic structure of Co-induced magic clusters grown on Si(1 1 1)-(7 × 7): Scanning tunneling microscopy and spectroscopy and real-space multiple-scattering calculations, *Phys Rev B* **73**:195415–195419, 2006.
15. Akita S, Nishijima H, Nakayama Y, Tokumasu F and Takeyasu K, Carbon nanotube tips for a scanning probe microscope: Their fabrication and properties, *J Phys D: Appl Phys* **32**:1044–1048, 1999.
16. Dai HJ, Hafner JH, Rinzler AG, Colbert DT and Smalley RE, Nanotubes as nanoprobes in scanning probe microscopy, *Nature* **384**:147–150, 1996.
17. Akita S and Nakayama Y, Extraction of inner shell from multiwall carbon nanotubes for scanning probe microscope tip, *Jpn J Appl Phys Part 1* **42**:3933–3936, 2003.
18. Kubby JA and Boland JJ, Scanning tunneling microscopy of semiconductor surfaces, *Surf Sci Rep* **26**:61–204, 1996.
19. Muller EW and Tsong TT, *Field Ion Microcopy Principles and Applications*, Elsevier, New York, 1969.
20. Kerfriden S, Nahle AH, Campbell SA, Walsh FC and Smith JR, The electrochemical etching of tungsten STM tips, *Electrochim Acta* **43**:1939–1944, 1998.
21. Song JP, Pryds NH, Glejbol K, Morch KA, Tholen AR and Christensen LN, A development in the preparation of sharp scanning tunneling microscopy tips, *Rev Sci Instrum* **64**:900–903, 1993
22. Ruppalt LB, Integration of single-walled carbon nanotubes with gallium arsenide(110) and indium arsenide(110) surfaces: A scanning tunneling microscopy study, p26, Ph.D. dissertation, 2007, University of Illinois at Urbana-Champaign, 2007 Urbana, Illinois.
23. Kuo HS, Hwang IS, Fu TY, Lin YC, Chang CC and Tsong T, Noble metal/W(1 1 1) single-atom tips and their field electron and ion emission characteristics, *Jpn J Appl Phys Part 1* **45**:8972–8983, 2006.
24. Itagaki T, Rokuta E, Kuo HS, Nomura K, Ishikawa T, Cho BL, Hwang LS, Tsong TT and Oshima C, Stabilities in field electron emissions from noble-metal covered W nano-tips: Apex structure dependence, *Surf Interface Anal* **39**:299–303, 2007.
25. Chadi DJ, Stabilities of single-layer and bilayer steps on Si(001) surfaces, *Phys Rev Lett* **59**:1691–1694, 1987.
26. Chabal YJ and Raghavachari K, Surface infrared study of Si(1 0 0)-(2 × 1)H, *Phys Rev Lett* **53**:282–285, 1984.
27. Swartzentruber BS, Mo YW, Kariotis R, Lagally MG and Webb MB, Direct determination of step and kink energies on vicinal Si(0 0 1), *Phys Rev Lett* **65**:1913–1916, 1990.
28. Niehus H, Kohler UK, Copelm M and Demuth JE, A real space investigation of the dimer defect structure of silicon(0 0 1)-(2×8), *J Microscopy-Oxford* **152**:735–742, 1988.
29. Kato K, Ide T, Miura S, Tamura A and Ichinokawa T, *Surf Sci* **194**:L87, 1988.
30. Ichinokawa T, Ampoh H, Miura S and Tamura A, Formation of surface superstructures by heat treatments on Ni-contaminated surface of Si(1 1 0), *Phys Rev B* **31**:5183–5186, 1985.

31. Zilani MAK, Xu H, Sun YY, Wang XS, Feng YP and Wee ATS, Scanning tunneling microscopy study of metastable Si(1 0 0)-c(8×8) surface structure, unpublished work.
32. Kaxiras E, Baryam Y, Joannopoulos JD and Pandey KC, Variable stoichiometry surface reconstructions: New models for GaAs(1 1 1) (2×2) and ($\sqrt{19} \times \sqrt{19}$), *Phys Rev Lett* **57**:106–109, 1986.
33. Stroscio JA, Feenstra RM and Fein AP, Local state density and long-range screening of adsorbed oxygen atoms on the GaAs(110) surface, *Phys Rev Lett* **58**:1668–1771, 1987.
34. Qian GX, Martin RM and Chadi DJ, Stoichiometry and surface reconstruction: An Ab initio study of GaAs(1 0 0) surfaces, *Phys Rev Lett* **60**:1962–1965, 1988.
35. Behrend J, Wassermeier M, Daweritz L and Ploog KH, Domain formation on the reconstructed GaAs(001) surface, *Surf Sci* **342**:63–68, 1995.
36. Pashley MD and Haberern KW, Compensating surface defects induced by Si doping of GaAs, *Phys Rev Lett* **67**:2697–2700, 1991.
37. Jona F, Observations of "Clean" Surfaces of Si, Ge, and GaAs by low-energy electron diffraction, *IBM Res Develop* **9**:375–387, 1965.
38. Xue QK, Hashizume T, Zhou JM, Sakata T, Ohno T and Sakurai T, Structures of the Ga-Rich 4×2 and 4×6 reconstructions of the GaAs(0 0 1) surface, *Phys Rev Lett* **74**:3177–3180, 1995.
39. L. Li, Han B, Gan S, Qi H and Hicks RF, Observation of the atomic surface structure of GaAs(001) films grown by metalorganic vapor-phase epitaxy, *Surf Sci* **398**:386–394, 1998.
40. Kuball M, Wang DT, Esser N, Cardona M, Zegenhagen J and Fimland BO, Hydrogen adsorption on the GaAs(001)-(2×4) surface: A scanning-tunneling-microscopy study, *Phys Rev B* **52**:16337–16340, 1995.
41. Biegelsen DK, Bringans RD, Northrup JE and Swartz LE, Reconstructions of GaAs(1 1 1) surfaces observed by scanning tunneling microscopy, *Phys Rev Lett* **65**:452–455, 1990.
42. Xu H, Sun YY, Li YG, Feng YP, Wee ATS and Huan ACH, STM observation of Ga-dimers on a GaAs(001)-c(8×2)-Ga surface, *Phys Rev B* **70**:R081313–R081317, 2004.
43. Xu H, Li YG, Wee ATS, Huan CHA and Tok ES, On STM imaging of GaAs(0 0 1)-($n \times 6$) surface reconstructions: Does the (6×6) structure exist?, *Surf Sci* **513**:249–255, 2002.
44. Biegelsen DK, Bringans RD, Northrup JE and Swartzle LE, Surface reconstructions of GaAs(1 0 0) observed by scanning tunneling microscopy, *Phys Rev B* **41**:5701–5706, 1990.
45. Ohtake A, Tsukamoto S, Pristovsek M, Koguchi N and Ozeki M, Structure analysis of the Ga-stabilized GaAs(001)-c(8×2) surface at high temperatures, *Phys Rev B* **65**:233311–233314, 2002.
46. Xie XN, Wang HQ, Wee ATS and Loh KP, The evolution of 3×3, 6×6, $\sqrt{3} \times \sqrt{3}$ R30° and $6\sqrt{3} \times 6\sqrt{3}$ R30° superstructures on 6H–SiC (0001) surfaces studied by reflection high energy electron diffraction, *Surf Sci* **478**:57–71, 2001.
47. Johansson LI, Glans PA and Hellgren N, A core level and valence band photoemission study of 6H-SiC(000-1), *Surf Sci* **405**:288–297, 1998.
48. Chen W, Loh KP and Wee ATS, Growth of monodispersed cobalt nanoparticles on 6H–SiC(0001) honeycomb template, *Appl Phys Lett* **84**:281–283, 2004.
49. Chen W, Loh KP, Xu H and Wee ATS, Nanoparticle dispersion on reconstructed carbon nanomeshes, *Langmuir* **20**:10779–10784, 2004.

50. Northrup JE and Neugebauer J, Theory of the adatom-induced reconstruction of the SiC(0001)$\sqrt{3} \times \sqrt{3}$ surface, *Phys Rev B* **52**:R17001–R17004, 1995.
51. Johansson LI, Owman F and Martensson P, High-resolution core-level study of 6H-SiC(0001), *Phys Rev B* **53**:13793–13802, 1996.
52. Johansson LI, Owman F, Martensson P, Persson C and Lindefelt U, Electronic structure of 6H-SiC(0001), *Phys Rev B* **53**:13803–13807, 1996.
53. Forbeaux I, Themlin JM and Debever JM, Heteroepitaxial graphite on 6HInterface formation through conduction-band electronic structure $-$SiC(0001), *Phys Rev B* **58**:16396–16406, 1998.
54. Hollering M, Bernhardt J, Schardt J, Ziegler A, Graupner R, Mattern B, Stampfl APJ, Starke U, Heinz K and Ley L, Electronic and atomic structure of the 6H-SiC(000-1) surface studied by ARPES, LEED, and XPS, *Phys Rev B* **58**:4992–5000, 1998.
55. Chen W, Xu H, Liu L, Gao XY, Qi DC, Peng GW, Tan SC, Feng YP, Loh KP and Wee ATS, Atomic structure of the 6H–SiC(0001) nanomesh, *Surf Sci* **596**:176–186, 2005.
56. Lin HY, Chiu YP, Huang LW, Chen YW, Fu TY, Chang CS and Tsong TT, Self-organized growth of nanopucks on Pb quantum islands, *Phys Rev Lett* **94**:136101–136104, 2005.
57. Chang CS, Tsong IST, Wang YC and Davis RF, Scanning tunneling microscopy and spectroscopy of cubic β-SiC(1 1 1) surfaces, *Surf Sci* **256**:354–360, 1991.
58. Bode M, Spin-polarized scanning tunnelling microscopy, *Rep Prog Phys* **66**:523–582, 2003.
59. Julliere M, Tunneling between ferromagnetic films, *Phys Lett A* **54**:225–226, 1975.
60. Blugel S, Pescia D and Dederichs PH, Ferromagnetism versus antiferromagnetism of the Cr(001) surface, *Phys Rev B* **39**:1392–1394, 1989.
61. Wiesendanger R, Shvets IV, Burgler D, Tarrach G, Guntherodt HJ, Coey JMD and Graser S, Topographic and magnetic-sensitive scanning tunneling microscope study of magnetite, *Science* **255**:583–586, 1992.
62. Coey JMD, Shvets IV, Wiesendanger R and Guntherodt HJ, Charge freezing and surface anisotropy on magnetite (1 0 0), *J Appl Phys* **73**:6742–6744, 1993.
63. Lin X, He XB, Lu JL, Gao L, Huan Q, Shi DX and Gao HJ, Four probe scanning tunnelling microscope with atomic resolution for electro-optical property measurements of nanosystems, *Chinese Physics* **14**:1536–1543, 2005.
64. Hasegawa S, Shiraki I, Tanikawa T, Petersen CL, Hansen TM, Boggild P and Grey F, Direct measurement of surface-state conductance by microscopic four-point probe method, *J Phys Condens Mat* **14**:8379–8392, 2002.

Part 2

NANOFABRICATION

EUV LITHOGRAPHY FOR SEMICONDUCTOR MANUFACTURING AND NANOFABRICATION

HIROO KINOSHITA
University of Hyogo
Laboratory of Advanced Science and Technology for Industry
1-1-2 Kouto Kamigori Ako-Gun
Hyogo Pref., Japan 678-1205

kinosita@lasti.u-hyogo.ac.jp

EUV lithography is the exposure technology in which even 15 nm node which is the limit of Si device can be achieved. Unlike the conventional optical lithography, this technology serves as a reflection type optical system, and a multilayer coated mirror is used. Development of manufacturing equipment is accelerated to aim at the utilization starting from 2011. The critical issues of development are the EUV light source which has the power over 115 W and resist with high sensitivity and low line edge roughness (LER).

Keywords: Nanofabrication; EUV lithography; semiconductor; mirror system.

1. Introduction

According to the latest semiconductor road-map, extreme ultraviolet lithography (EUVL) will be introduced for the fabrication of large-scale integrated circuits (LSIs) at the 32-nm node in 2011. Research institutions, equipment makers, and infrastructure makers throughout the world are now accelerating development with the goal of fabricating devices by EUVL. Although the optical system is reflective, employing mirrors covered with a multilayer film, rather than refractive, as in a conventional system, this technology can be considered an extension of conventional ultraviolet lithography. That is, advances in lithography for device fabrication have so far come about by improving the numerical aperture (NA) of the optical system and shortening the exposure wavelength. Recently, the required minimum feature size has reached one-half the wavelength or less, and the influence of diffraction has become appreciable. Even so, a conventional refractive system can still be used due to the development of resolution enhancement technologies, such as a phase-shift mask and a ring illumination system, which result from the engineering of optical components. Furthermore, a new technique called ArF immersion technology is making rapid progress.

Ultraviolet lithography employs reduction exposure and a bulk mask, and covers several generations. Any technology worthy of being called a "lithography standard" for device fabrication must satisfy these three conditions. EUVL does satisfy them, and can be considered an extension of ultraviolet lithography. Moreover, a fine pattern less than 30 nm can be replicated without the resolution enhancement or optical proximity correction (OPC) techniques developed for KrF excimer lithography.

In contrast to conventional ultraviolet lithography, which employs refractive optics, EUVL employs a reflective optical system consisting of multilayer-coated mirrors.[1–4] Each aspect of this technology (coating, polishing, metrology, vacuum mechanism, etc.) requires an extremely high precision of less than 1 nm, although nanotechnology seems to have grabbed the world's attention lately. On the road to the establishment of a workable technology, solutions to critical problems in each field must be found, and their impact will spread widely into other fields. For example, consider the light source, which is based for instance, on laser-produced plasma. If a high-intensity light source is realizable, it will lead to improvements in the performance of X-ray microscopes and analytical tools. Progress in optical polishing and figuring will have an impact on the quality of many products. Research on multilayer films promotes the study of the process by which a single atomic layer is formed and also research on the surface and interface of materials. Furthermore, the advances in metrology required to make EUVL a practical production tool will revolutionize evaluation methods based on the conventional point diffraction interferometer.

Thus, although difficult problems must be solved in each technology related to EUVL, this research is part of the process by which we are progressing into the nano-scale regime; and this same process will eventually carry us into the pico-scale regime. In this sense, the development of EUVL will have a large ripple effect on all fields. This article discusses the principle of EUVL, the current status of the individual technologies, and future prospects.

2. Principle of Extreme Ultraviolet Lithography

Figure 1 illustrates the principle of extreme ultraviolet lithography. The system consists of a source, illumination optics, a mask, an objective lens and a wafer. The mask, the objective optics and parts of the illumination optics are coated with a reflective multilayer film. Since the aberration-free area in a reflective system is limited, the exposure area is expanded by synchronously moving the mask and wafer in the optical system.

The diffraction-limited resolution is determined by Fraunhofer diffraction when aberration in the optical system is completely eliminated:

$$\mathrm{d} = \mathrm{K}_1\lambda/(\mathrm{NA}). \tag{1}$$

And the depth of focus, $\mathrm{D_f}$, is given by the Rayleigh equation:

$$\mathrm{D_f} = \lambda/(\mathrm{NA}^2), \tag{2}$$

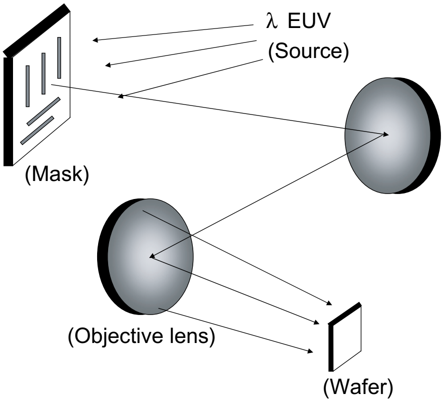

Fig. 1. Principle of extreme ultraviolet lithography.

Table 1. Estimated resolution and depth of focus.

NA	0.25	0.3	0.4
d (nm)	27	22.5	17
D_f (nm)	216	150	84

where λ is the wavelength of the X-ray source and NA is the numerical aperture of the objective lens. Table 1 gives estimates of the resolution and depth of focus, assuming a K_1 factor of 0.5 and a wavelength of 13.5 nm.

If a K_1 factor of 0.4 is allowable, optics with an NA of 0.25 can be used for the 22-nm node without any narrowing of the depth of focus. Furthermore, assuming a K_1 factor of 0.3, it can extend to the 15-nm node. This is one of the biggest advantages of EUVL.

At the start of system design, the choice of X-ray wavelength is the most important consideration because many other things (optical characteristics, multilayer reflectivity, resist materials, etc.) depend on it. Figure 2 shows the numerical aperture and X-ray wavelength for the target resolution and depth of focus both in the early stages (1980's) and now. In the early stages, the target resolution was less than $0.2\,\mu$m, but it has now become less than 45 nm. In this figure, a larger numerical aperture provides a better resolution and a smaller depth of focus. However, it is extremely difficult to design optics with a high numerical aperture, such as 0.4. Another way to improve the resolution is to shorten the wavelength, but this reduces the reflectivity of the multilayer and narrows the bandwidth.

Generally, the peak reflectivity is obtained at the wavelength of minimum absorption of the low-index material, such as carbon, boron, beryllium or silicon for the wavelength range of 4.0–40 nm. It occurs at a wavelength of 4.47 nm for carbon, 6.7 nm for boron, 11.4 nm for beryllium and 12.4 nm for silicon. The peak

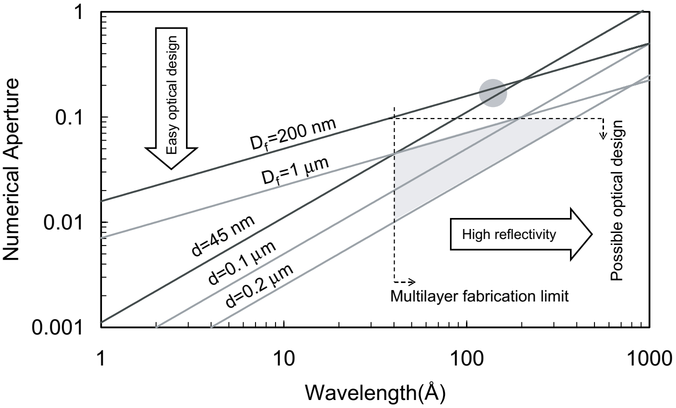

Fig. 2. Numerical aperture and X-ray wavelength for the target resolution and depth of focus.

reflectivity and the bandwidth are easily calculated from Fresnel's equations. For instance, assuming that the wavelength is beyond the absorption edge of each material and also assuming normal incidence, the calculated peak reflectivity is 17% for Cr/C, 33% for Ru/B_4C, 73% for Mo/Be and 72% for Mo/Si. The experimental reflectivity must be over 65%, from the standpoint of a practical throughput. The values for Mo/Si and Mo/Be satisfy the requirement. Furthermore, since demagnifying optics usually consist of two or more mirrors, a bandwidth of 0.3–0.4 nm is required to adjust the multilayer mirrors to the wavelength of the peak reflectivity. The bandwidths of multilayer mirrors made of Mo/Si (for $\lambda = 13$ nm) and Mo/Be (for $\lambda = 11.4$ nm) satisfy the requirements.

The sensitivity and exposure depth of the resist depend on its X-ray absorption coefficient. Since the characteristics of organic resists depend primarily on the X-ray absorption of carbon, the exposure depth is easily calculated. At a wavelength of 4.47 nm or a little longer, the X-ray absorption of an organic resist is small, which allows a thick resist (thickness $> 0.5\,\mu$m) to be used. For wavelengths longer than 4.47 nm, the X-ray absorption becomes appreciable; and only a thin top layer at the surface is exposed.

Figure 3 shows the relationship between the exposure depth of polymethylmethacrylate (PMMA) resist and the incident dose of synchrotron radiation (SR). Two pairs of Schwarzschild-type multilayer mirrors were used to monochromatize the SR source, which was adapted for wavelengths of 5 nm and 11.8 nm. For a wavelength of 11.8 nm, the exposure depth reaches a limit at $0.08\,\mu$m; while for 5 nm, it is more than $0.3\,\mu$m. So, the use of wavelengths greater than about 10 nm requires the development of either a bilayer resist process or a new resist that permits exposure depths of at least $0.3\,\mu$m.

As mentioned above, considering all the factors (required numerical aperture, multilayer reflectivity, resist characteristics, etc.), only one wavelength region from 11.4 to 13.0 nm appears to be suitable. The final selection of the wavelength will

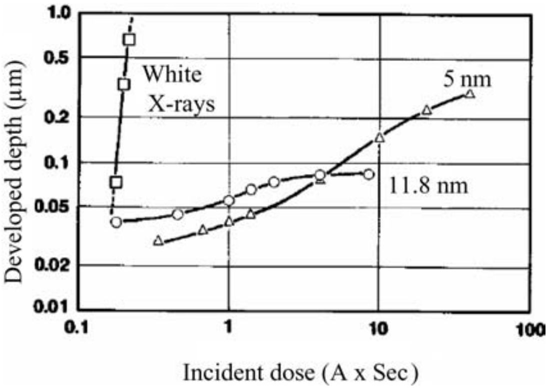

Fig. 3. Relationship between the exposure depth of PMMA resist and the incident dose of synchrotron radiation (SR).

be decided on the basis of further studies on optical design for a high numerical aperture, the resist process and the ability to deposit highly reflective multilayers.

Until the target feature size reached 45 nm, a single-layer resist was adequate, since penetration depth did not need to be considered. The exposure wavelength was set to around 13.5 nm. Table 2 shows the critical issues for EUVL components.

3. Critical Issues of EUV Lithography

3.1. *Optics design and fabrication*

To design EUVL optics with a large exposure field, the following factors need to be considered: (i) the construction of optics with the fewest mirrors; (ii) telecentricity on a wafer for easier alignment and a large depth of focus; (iii) a demagnification

Table 2. Critical issues in individual EUVL technologies.

Component	Issue	Goal
Optics	Design	6 mirrors
	Aspherical-mirror fabrication	0.3 nm
	Alignment accuracy of optics	0.5 nm
Source	High power	115–180 W
	Low debris	>5 st
	Large collection angle	$>10^{11}$
	Long life	
Mask	High reflectivity	>67%
	Low defect density	0.001/cm^2
Resist	High sensitivity	2–5 mJ/cm^2
	Low LER	1.5 nm @ 32 nm
Exposure system	Contamination & temperature control	
	Mask & wafer handling	
	Scan stage	

of 1/4 to 1/5 to make mask fabrication easier; (iv) an modulation transfer function (MTF) of over 70% (the MTF needs to be high enough to provide the required resolution) and (v) a minimum blur of an exposure pattern of less than 0.01% in the scanning mode.

Figure 4 illustrates a two-aspherical-mirror system for the replication of 0.06 μm patterns in a large exposure area demonstrated by NTT.[3,5] The incident angle to the optics is nearly normal ($\sim 2°$). The focused beam strikes the wafer perpendicularly; that is, the optics is telecentric with respect to the plane of a wafer. The demagnification is 1/5. The numerical aperture is 0.1 and the exposure area has a ring field image 20 mm × 0.4 mm in size, in which the aberration is less than 0.01 μm. The square-wave modulation transfer function for these optics is 75% at 5000 cycles/mm, which yields a resolution of less than 0.1 μm for incoherent 13-nm wavelength radiation. This design satisfies requirements (i) to (iv) above.

This optics design employs two mirrors with the same radius of curvature to compensate for the curvature of the image plane. However, the difference in distortion in the ring field is not negligible. In this case, assuming a distortion of 0.25%, the blur of a pattern is 0.2 μm in a ring field with a size of 20 mm × 0.4 mm on a wafer. A two-mirror system is not good enough to eliminate various types of aberration, especially the distortion in a wide field. However, this design can be considered the illustration of "the principle of an EUVL optical system."

Figure 5 shows the characteristics of replicated patterns simulated using SPLAT program, assuming a wavelength of 13.5 nm. Increasing the NA makes finer hole and elbow patterns. In resolving a 30-nm hole and elbow pattern, the NA of over around 0.3 is required. On the other hand, influence of the value of figure accuracy (σ) does not make a significant change.

Figure 6 shows the six-aspherical-mirror optics devised by Williamson in 1998.[6] This system provides even more degrees of freedom to correct residual aberration, enabling a 4× reduction with an NA in excess of 0.25 and a ring field over 2.0 mm

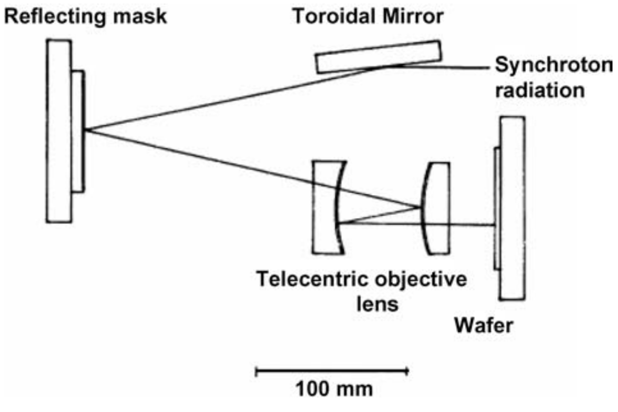

Fig. 4. A two-aspherical-mirror system.

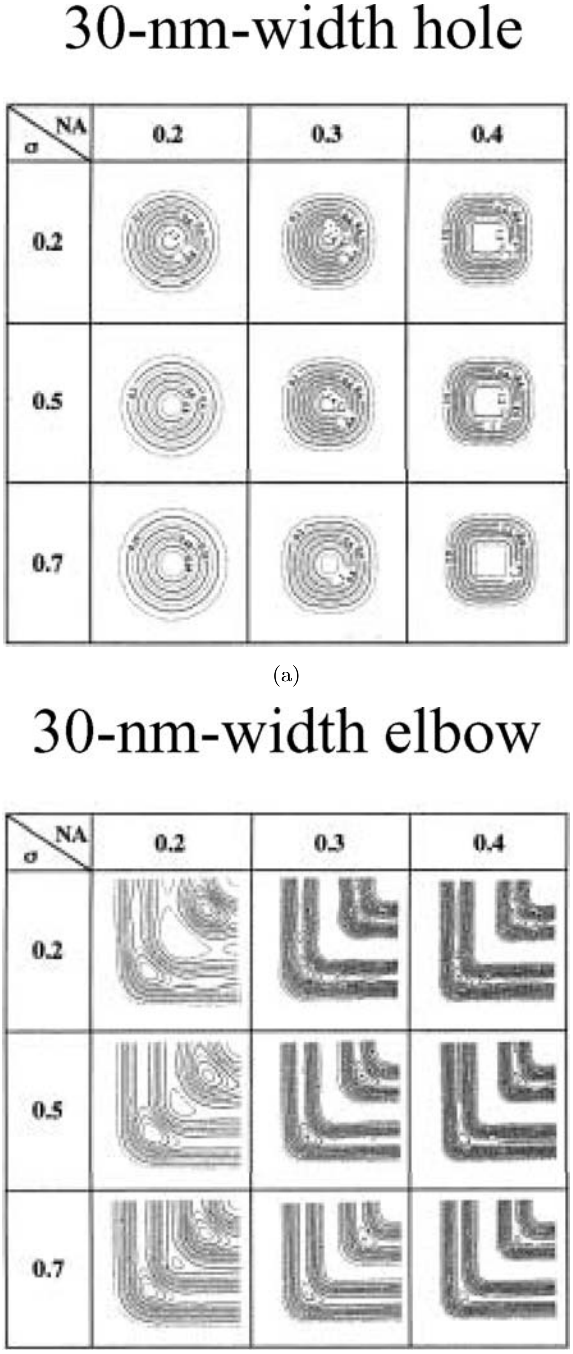

(a)

(b)

Fig. 5. Characteristics of replicated patterns simulated using SPLAT.

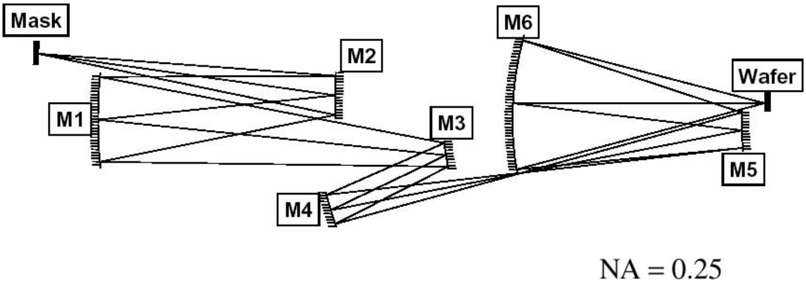

Fig. 6. A six-aspherical-mirror optics devised by Williamson in 1998.

wide on a wafer. For a 2.0-mm-wide ring field, the residual distortion can be reduced to less than 0.25 nm. This camera enables 20-nm patterns to be replicated.[7] ASML, Nikon, and Canon have developed a practical EUVL system employing this type of optics.

Aspherical mirrors are key optical elements of the imaging optics and require high-precision fabrication. In general, the figure accuracy of one mirror can be obtained from Rayleigh's equation (3) and Marechal's equation (4):

$$\sigma = \lambda/4\mathrm{n} \quad \text{(P-V)}, \tag{3}$$

$$\mathrm{G} = \lambda/28\sqrt{\mathrm{n}} \quad \text{(RMS)}, \tag{4}$$

where n is the number of mirrors. For example, the figure error for each mirror of imaging optics with six aspherical mirrors (Fig. 7) must be less than 0.56 nm P-V and 0.2 nm RMS.

Improvement in the precision of mirror fabrication is due to progress in the technology for measuring figure error. Utilizing computer-controlled polishing and

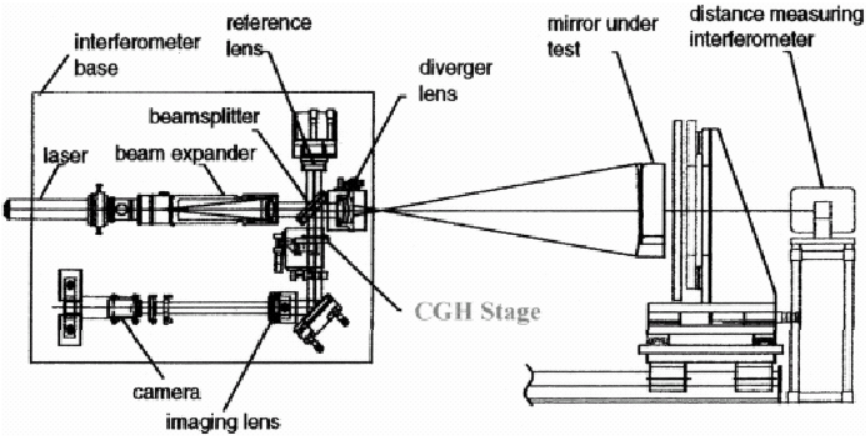

Fig. 7. Fabrication process for aspherical mirrors.

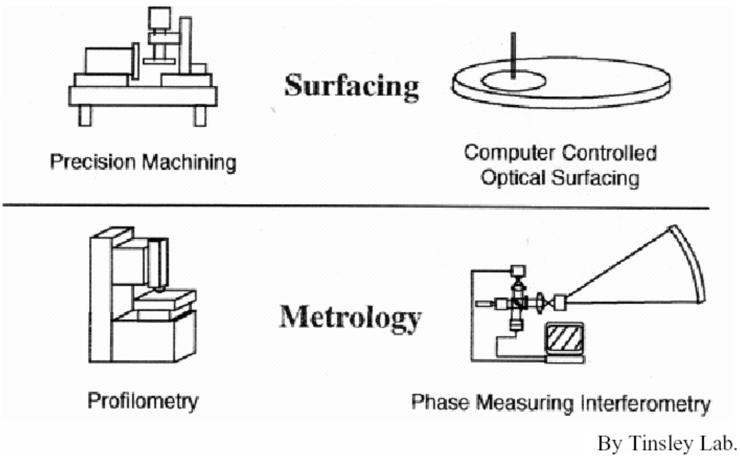

Fig. 8. Aspherical mirror measurement using CGH.

a laser interferometer, to which phase analyzing equipment was added, Tinsley achieved a figure error of 0.3 nm (RMS).

Figure 8 illustrates the fabrication process for aspherical mirrors.[8] First, precision machining with a diamond grinding wheel produces the initial spherical surface to an accuracy of 1–2 μm, as measured with a contact-type profilometer. Second, an aspherical surface meeting the required specifications is fabricated by CCOS (Computer Controlled Optical Surfacing), which employs iterative polishing with substrate polishing tools and a phase-measuring interferometer to measure the shape. The final shape is acquired by repeated polishing and measurement. In 1993, the two aspherical mirrors for the system in Fig. 4 were delivered; but the accuracy was only 1.5 nm for the concave mirror and 1.8 nm for the convex one.[9]

A new metrological method was needed to fabricate a mirror with an accuracy of better than 1 nm. Figure 8 shows a Twyman-Green interferometer based on a computer generated hologram (CGH), which applies a Fourier transform to the aspherical surface. Computer generated hologram calculates interference fringes for actual and ideal wave fronts, and it enables the precision to reach the required value. That is, this technique of processing the Fourier transform rather than the actual wave front provides an accuracy of 0.5 nm. Further advances in the technology have reduced the roughness in the mid-frequency range, allowing an accuracy of 0.3 nm to be achieved in 2000.

An interferometer is used to measure the surface figure, and the measurement accuracy depends on the accuracy of the optics of the instrument itself. The need to overcome this limitation engendered the concept of a new type of interferometer for which the accuracy of the instrument optics is not a factor determining measurement accuracy.

Gary E. Sommargren of LLNL considered the spherical wave emitted from a glass fiber and came up with the idea of determining shape from the interference fringes formed by the wave front reflected from the measurement optics and an ideal spherical wave, taking the uniformity of the diameter of the fiber core into account (Fig. 9).[10,11] Up to that time, a processed pinhole had been used, which produced a spherical wave that was far from ideal. The new system was a technological breakthrough that eliminated spatial restrictions on measurements and provided an accuracy in the sub-nanometer region. This method can measure the figure error

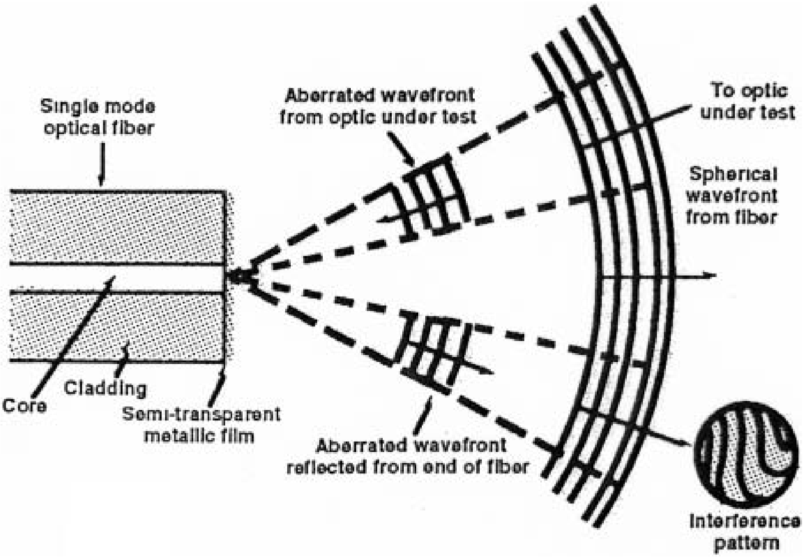

(a)

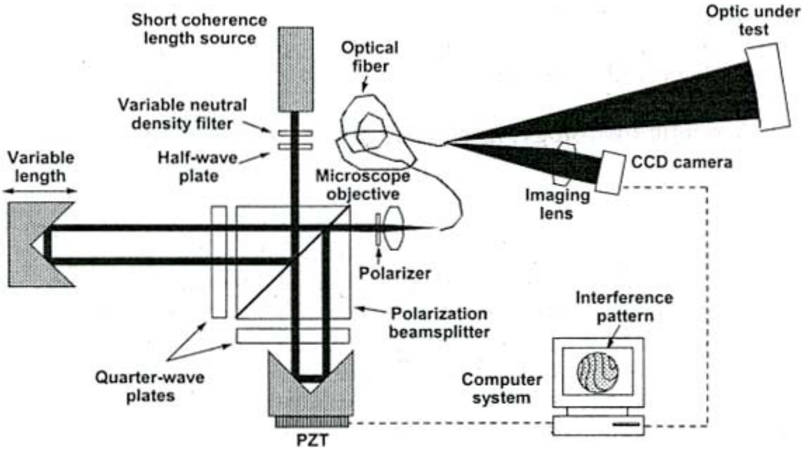

(b)

Fig. 9. PDI system devised by Gary E. Sommargren of LLNL: (a) principle of point diffraction interferometer, (b) configuration of spherical mirror test stand.

of single-element optics and the wave-front error of optics with a couple of elements. Above mentioned technologies of aspherical mirror fabrication and measurement are introduced to the practical fabrication system.

3.2. *Source*

Early research on EUVL employed synchrotron radiation (SR),[12] but it soon became apparent that SR could not provide the required throughput. Thereafter, hopes have been centered on laser-produced plasma (LPP) because it has a smaller footprint than SR, and an exposure system with LPP is compatible with conventional equipment on a semiconductor production line.

To build a practical system with 6 aspherical mirrors and a reflective mask, stepper companies (ASML, Nikon, Canon, etc.) carried out simulations to determine the requirements of the source. They found that a source power of 115 W at the intermediate focus point is needed to obtain a throughput of 100 8-inch wafers/hour, assuming a resist sensitivity of $5\,\mathrm{mJ/cm^2}$.

Currently, two types of EUV sources, LPP (Fig. 10) and discharge-produced plasma (DPP:Fig. 11), are being investigated. In general, LPP has the advantages of collection over a large solid angle, little debris and a high repetition rate. On the other hand, DPP has the advantages of high power and high efficiency, although ablation of the electrode and the amount of debris are serious problems. Discharge-produced plasma directly changes electrical energy into EUV light, while LPP first changes electrical energy into laser energy, which is then converted into EUV light.

Cymer Co. has been developing an LPP source for a practical system.[13] They are carrying out fundamental studies on the emission spectrum and conversion efficiency of a Sn droplet target and the condensing efficiency of a normal-incidence mirror using a XeF (Deep UV) driving laser with an output of 800 W and a repetition frequency of 4 kHz. The typical conversion efficiency (CE) of this system is 0.5% into 2% BW and 2π sr. However, the efficient conversion of laser energy into EUV energy is critical to obtaining the required power. Several combinations of laser wavelength and source element CE have been examined. Plans call for the use of a Li

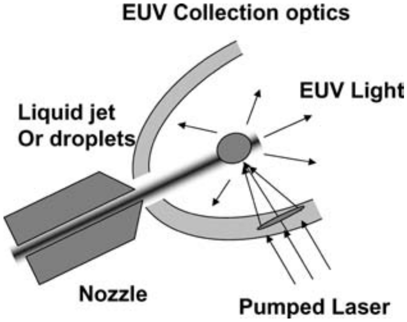

Fig. 10. Gas-jet typed laser produced source.

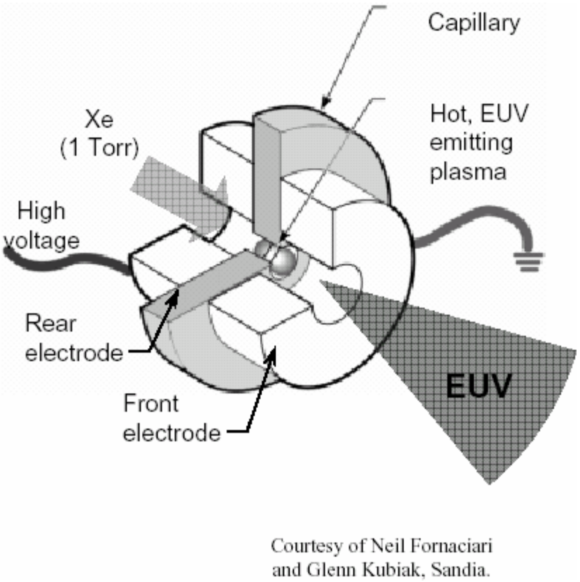

Courtesy of Neil Fornaciari and Glenn Kubiak, Sandia.

Fig. 11. Discharge-produced plasma (DPP).

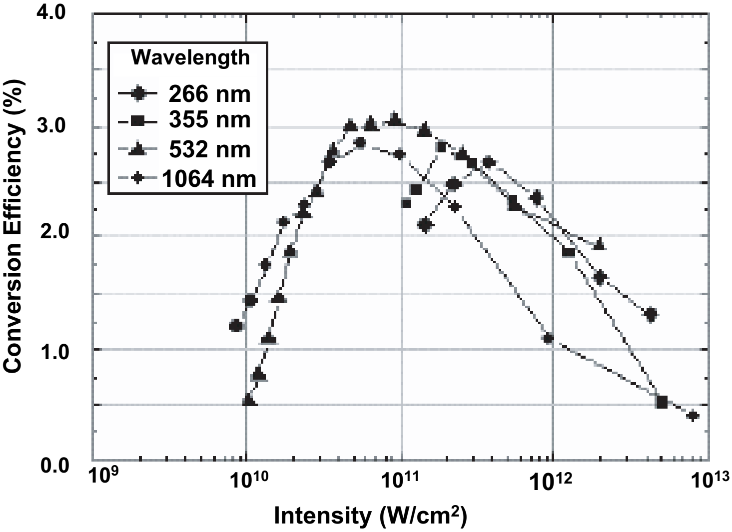

Fig. 12. Measured lithium CE as a function of intensity.

rather than a Sn target and a CO_2 laser in a system for high-volume manufacturing (HVM).

Figure 12 shows the measured lithium CE as a function of intensity for five different driving laser wavelengths. Even under non-optimized conditions, the lithium CE

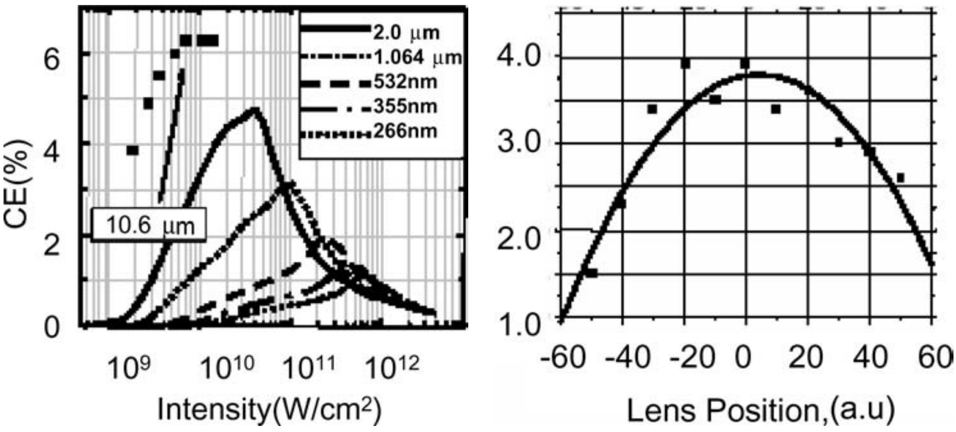

(a) (b)

Fig. 13. (a) The estimated Sn CE as a function of intensity for different driving laser wavelengths; and (b) the CE of a CO_2 laser as a function of lens position.

is quite high, approaching 3%. Beside it is relatively insensitive to laser wavelength in the wavelength range from 266 nm to 1064 nm.

Figure 13(a) shows the estimated Sn CE as a function of intensity for different driving laser wavelengths, and Fig. 13(b) the CE of a CO_2 laser as a function of lens position. A longer laser wavelength yields a higher CE, and a CE of 4% can be obtained for a CO_2 laser at a wavelength of 10.6 μm. A CE as high as 5% has been reported for a wavelength of 1064 nm. Based on these experimental results, a Sn LPP source appears to be a viable option for an HVM source.

A DPP source for EUVL is potentially much simpler and less expensive than an LPP source. It employs high-voltage, high-current discharge pulses to form a 15 eV to 50 eV plasma in a gaseous medium, such as Xe, Sn or Li vapor. Angle-integrated EUV outputs of 7 mJ/eV pulses and repetition rates of up to 1000 Hz have recently been achieved for a Xe capillary discharge source, suggesting that it may be possible to scale the average power of this source to meet commercial requirements.

Xtreme Co. developed the first commercial Xenon GDPP source in 2003. It is based on the Z-pinch, which generates a power of 35 W within a solid angle of 2π sr. This source has been integrated into micro-exposure tools from Exitech Co., UK. The first tool has produced more than 100 million pulses without visible degradation of the source collection optics. Xtreme Co. has a GDPP source under development with a power of 115 W at the intermediate focus point for an HVM system.[14] It utilizes a Sn source and a rotating disk electrode.

The Philips Co. Nova Sn GDPP source uses an electrical input power of over 10 kW and continuously delivers a power of 200 W in the EUV band over a solid angle of 2π sr.[15] 500 million shots have been generated, and the electrode lifetime is estimated to be at least 2 billion shots. The debris mitigation system is based on a two-step method that employs a foil-trap-based stage and a chemical cleaning stage. The total collector lifetime should be over 10 billion shots.

Although both systems have great potential, the best type of system will become clear after a suitable resist has been developed. Moreover, the lifetimes of the condensing efficiency and the condensing mirror are important factors determining conversion efficiency. Further studies will be carried out in the future.

3.3. *Reflection mask*

The EUV mask is one of the key technologies for establishing EUV lithography, with the production of defect-free substrates and phase defect measurements being critical issues. An EUV mask (Fig. 14) consists of a low thermal expansion (LTE) glass substrate, a multilayer, a capping layer, a buffer layer, and an absorber pattern.[16–18] Table 3 shows the specifications of EUVL mask.

A multilayer consisting of Si and Mo has been found to be the most suitable for obtaining a high reflectivity at EUV wavelengths of 13–14 nm. One with 40 bilayers has a peak reflectivity of 69%, which meets the minimum reflectivity requirement of 67%. The reflectivity spectrum (Fig. 15) of typical multilayer blanks was measured with the reflectometer at the NewSUBARU SR facility. The deviation from the theoretical value of around 73% is thought to be due to the formation of interdiffusion layers between the Si and the Mo layers. Improvement of the deposition process should yield a reflectivity of 67% or more.

TaN and Cr films have been reported to be the best candidates for the EUV absorber material.[19–22] SiO_2, SiON, C and Ru films are commonly used as repair buffers for a TaN or Cr absorber.[23–25] A buffer layer is required to protect the

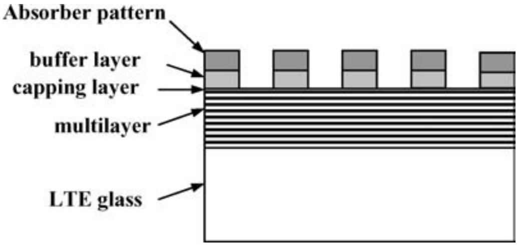

Fig. 14. Configuration of EUVL mask.

Table 3. Specifications of EUVL mask.

Item	Specification
Substrate size & properties	6025, LTE
Surface roughness of substrate	<0.15 nm (RMS)
Flatness of substrate	<50 nm (P-V)
Defect density of substrate	Zero (for defect size>50 nm)
Defect density of blank	<0.003/cm^2 (for 30-nm defects)
Reflectivity of blank	<67% ($13.4\,\text{nm} \le \lambda \le 13.5\,\text{nm}$)

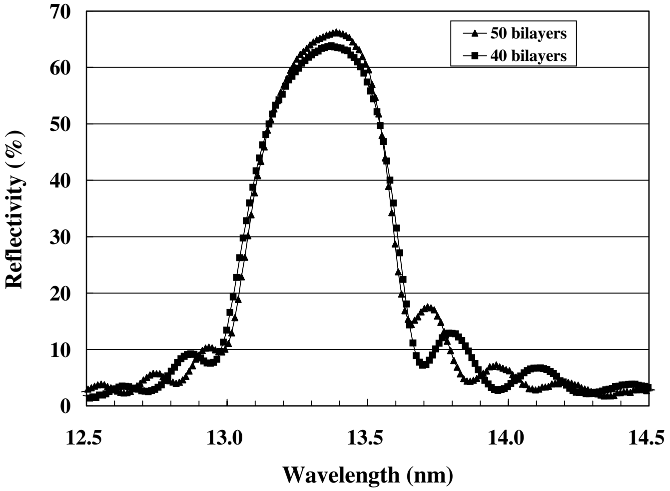

Fig. 15. Reflectivity spectrum of typical multilayer blanks measured with the reflectometer at the NewSUBARU SR facility.

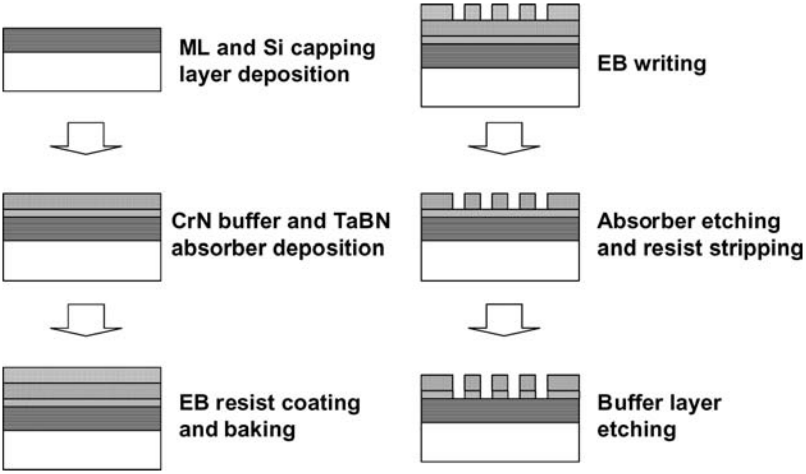

Fig. 16. Typical mask fabrication process.

multilayer from damage during the repair of absorber defects with a focused ion beam (FIB). It needs to be patterned along with the EUV absorber layer as a stack to prevent any degradation in the EUV reflectivity of the multilayer.[26–29]

In a typical mask fabrication process (Fig. 16), a Mo/Si multilayer (ML) composed of 40 bilayers and an 11-nm-thick Si capping layer are deposited on a ULE® glass substrate.[21,24,25,30] The RMS surface roughness of an as-deposited multilayer is 0.16 nm in a $5\,\mu\text{m}^2$ area on a polished ULE substrate, as measured with an atomic force microscope (AFM). A CrN buffer layer and a TaBN absorber are then deposited on the Si capping layer by direct current (DC) magnetron sputtering. After the lithography process, the TaBN absorber is etched in an inductively coupled plasma (ICP) etching system using Cl_2 gas; the etching selectivity of TaBN with respect to the CrN buffer layer is around 20:1. Finally, the TaBN absorber pattern acts as a hard mask for the removal of the CrN buffer layer. The CrN buffer layer is etched with Cl_2/O_2 plasma; it has a high etching selectivity of 20:1 with respect to the Si capping layer. The surface roughness shows no change after this processing due to the high etching selectivity between CrN and Si. The Si layer was slightly thicker after the etching process, as measured with low-angle X-ray diffracto meter (XRD). This is thought to be due to the oxidization of the Si layer by oxygen plasma. EUV masks can be produced without a significant drop in EUV reflectivity by optimizing the mask process and by using newly developed mask blanks.

4. Exposure Tools and Experiments

In Japan, the (NTT), Nikon, SORTEC and Hitachi groups are carrying out exposure experiments using Schwarzschild optics. Patterns with sizes of 0.05–0.1 μm have been replicated (Fig. 17).[31,32] In USA, the AT&T, (SNL) and LLNL-groups have replicated patterns with a size of 0.05 μm (Fig. 18).[33–39] Since spherical mirrors, which can easily be fabricated to a high accuracy, are employed for the optics, the resolution obtained (0.05 μm) is close to the diffraction limit. But a practical field size on a wafer is required. Thus, optics with a high resolution and a large field are being investigated.

The NTT group is investigating large-field exposure in an area 20 mm × 0.4 mm in size using a two-aspherical-mirror system. Patterns with a size of 0.15 μm have been replicated at a wavelength of 13 nm. In addition, a large field 10 mm × 12.5 mm in size has been achieved using illumination optics and synchronized mask and wafer stages (Fig. 19).[40]

The SNL, LLNL, (LBL), and AT&T groups have developed exposure tools (Fig. 20) for laboratory use.[41] They employ a laser-produced plasma X-ray source

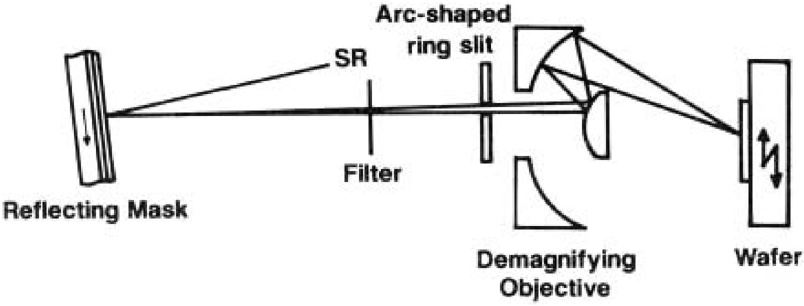

Fig. 17. Exposure system developed by NTT in 1989.

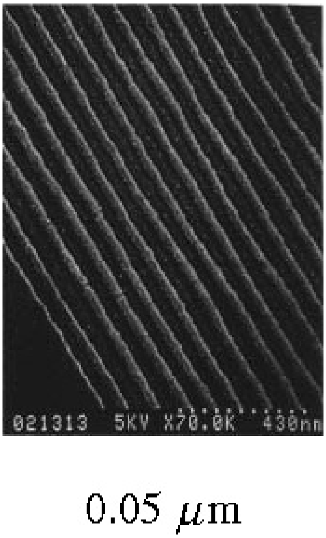

Fig. 18. The replicated patterns with a size of 0.05 μm replicated by AT&T.

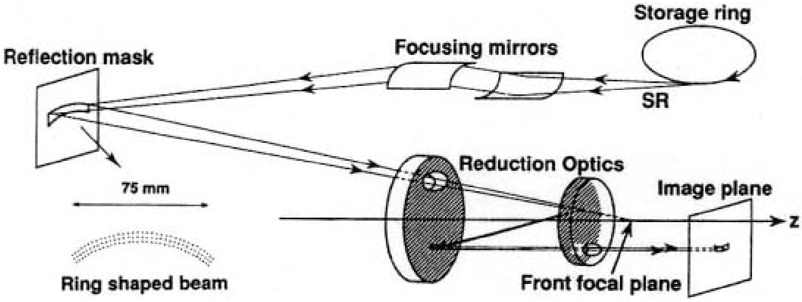

Fig. 19. A two aspherical mirror system developed by NTT in 1991.

with a Cu wire target. The amount of debris is reduced to a practical level by using a rapidly rotating slit and a helium atmosphere. The optics, mask and wafer stage are installed in the exposure chamber. The Schwarzschild optics consist of two aspherical mirrors with a wave-front aberration of less than 1 nm. They have the potential to replicate patterns with a size of 0.1 μm in an exposure area $0.4\,\text{mm}^2$. The wafer stage consists of a fine-positioning stage (stroke length: $300\,\mu$m) and a coarse-positioning stage (stroke area: $100\,\text{mm} \times 74\,\text{mm}$). The fine-positioning stage has 16 magnetic suspensions and 6 shafts for repositioning. The alignment between mask and wafer is carried out by matching Moiré interference fringes from Moiré patterns on the mask and wafer through observation of an image from a CCD camera on a display. The measured resolution is 10–15 nm (3σ) for the X- and Y-directions. A wafer held by an electrostatic chuck and wafer distortion is measurable to an

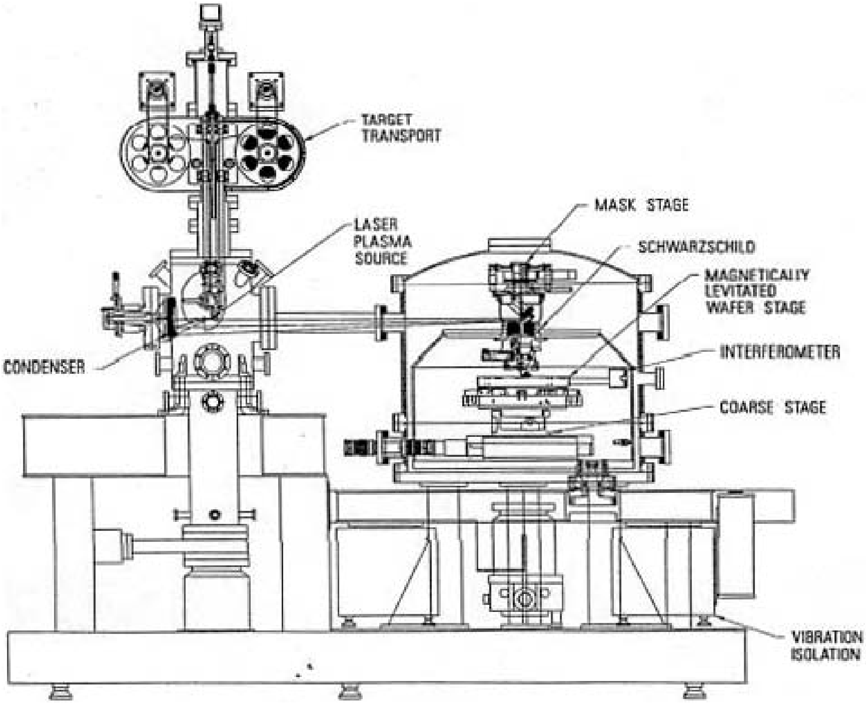

Fig. 20. Exposure system developed by SNL, LLNL, LBL and AT&T groups in 1995.

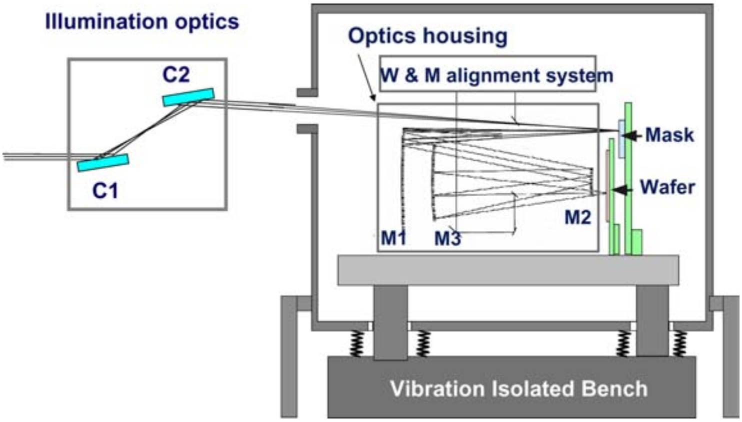

Fig. 21. Configuration of a three-aspherical-mirror system developed by HIT, Nikon and Hitachi.

accuracy of $\pm 0.15\,\mu$m by detecting the focus position on a wafer. The mask stage, the wafer stage, and the imaging optics are mounted on a vibration isolation table. The whole system is mounted in a vacuum chamber. Utilizing this exposure tool, 0.1-μm NMOS transistors have been fabricated with an i-line hybrid exposure tool.[42]

Figure 21 shows the configuration of a three-aspherical-mirror system.[43–45] It consists of illumination optics, mask and wafer scanning stages, mask and wafer alignment optics, a reduction camera, and a load-lock chamber for loading wafers. The reduction camera consists of three aspherical mirrors. The magnification of the optics is 1/5. There is a distortion-free area less than 0.01 μm wide in a 1.0-mm-wide ring image field with a chord length of 30 mm on a wafer. So, by moving the mask stage in synchronization with the wafer stage, an exposure area of 30 mm × 38 mm can be achieved. The mask stage has five degrees of freedom. The Y-axis is used for scanning the mask, and the Z-axis is for focus and magnification alignment. The wafer stage consists of coarse- and fine-positioning stages. The coarse-positioning stage is driven by a pulse motor and a mechanical bearing guide. The Z-axis of the wafer coarse-positioning stage has a measurement system with a resolution of 0.1 μm. The fine-positioning stage for mask and wafer alignment and focus alignment employs a piezoelectric transducer, which provides a resolution of 1 nm in the X- and Y-directions and 10 nm in the Z-direction. The photograph in Fig. 22 shows an overview of the system. The system is in a thermal clean chamber, in which the temperature is controlled to ±0.1°C. The dimensions of the chamber are approximately 1 m × 1.2 m × 1 m. In 2000, this system was used to clearly observe 60-nm-wide L&S patterns and 40-nm-wide isolated lines in an exposure area 10 mm × 10 mm in size.

Figure 23 shows the ETS-1 developed by EUV-LLC.[46] It is a step-and-scan system with an operating wavelength of 13.4 nm. The projection optics box (POB)

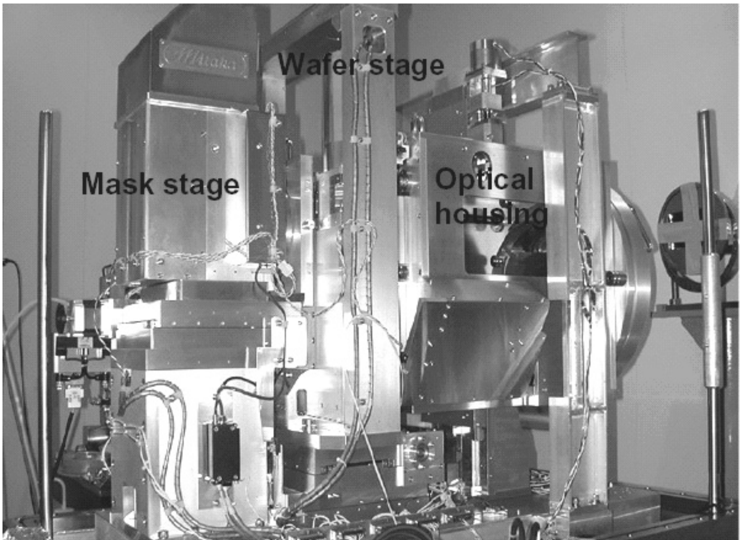

Fig. 22. Photograph of overview of the system of a 3-aspherical-mirror system.

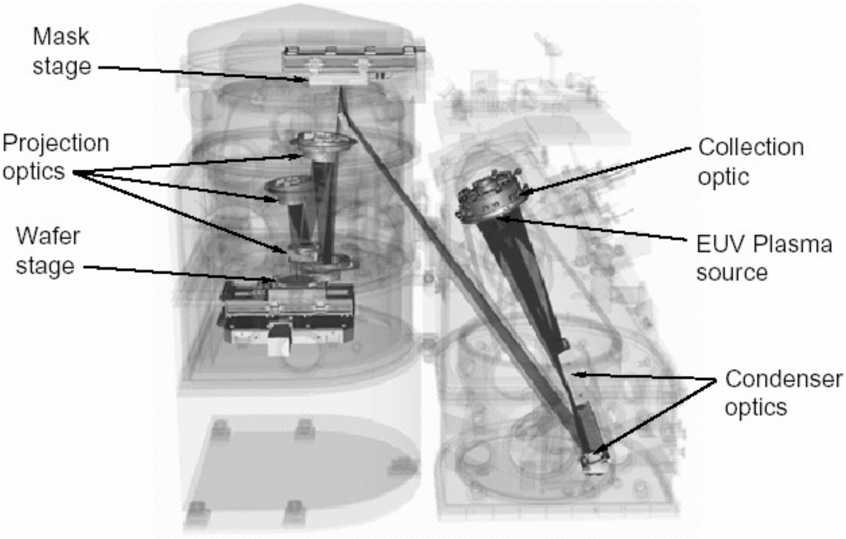

Fig. 23. ETS-1 developed by EUV-LLC.

is a multilayer-coated, four-mirror, ring-field system with a NA of 0.1 and an image reduction of 4:1. The field is a 30° sector of a ring field with a radius of 211 mm (chord length of 96 mm × width of 6 mm at the reticle). The reticle is a reflective multilayer-coated ULE substrate with a patterned absorber. The EUV radiation comes from laser-produced plasma generated by focusing a pulsed Nd:YAG beam onto a Xe cluster target. The source has a diameter of approximately 300 μm. It employs a 40-W laser, which delivers an EUV power of 0.11 mW/cm^2 on a wafer.

An experimental projection optics box was assembled and characterized by both visible-light and EUV interferometry. The wave-front error was measured by both techniques at 45 field points throughout the ring field. The mean RMS wave-front error across the field is 1.20 nm (λ/l 1) in a 36-term Zernike polynomial decomposition, and varies between 0.90 nm and 1.4 nm. On average, the difference between the EUV and visible-light measurements was 0.25 nm RMS.

Scanned images are formed by scanning the reticle at a constant velocity through the illuminated field of the projection optics. The wafer is synchronously scanned at a quarter of the mask velocity so that the scanned image appears stationary on the wafer. Any deviation from true synchronization, either in speed or direction, will blur the printed image. A feedback control system synchronizes the stages and dynamically references their positions to the POB structure. Several full-field scanned images, each measuring 24 mm × 32.5 mm, have been printed. The reticle scan speed was approximately 40 μm/s (limited by the EUV intensity). At velocities of zero and 40 μm/s the RMS jitter of the reticle stage is below 5 nm, and the jitter of the wafer stage is below 10 nm. The stages have also been tested at speeds of 20 mm/s, and were found to have the same jitter performance.

Static resist images of dense 1:1 elbow patterns, ranging in size from 100 to 300 nm, show as-expected image quality across the entire ring field of the projection optics. The 100-nm patterns, including both dense and isolated features, are well resolved throughout the entire field, and 80-nm patterns are well resolved at the center of the field, where aberrations are lowest. Full-field (24 mm × 32.5 mm) scanned images have been acquired. The scanned images of dense 100-nm elbow patterns are almost indistinguishable from the static images, proving that neither stage motion nor the POB static distortion field impacts image quality. Figure 24 shows isolated 3:1 elbow patterns with sizes of 45 nm and 39 nm. Although the system has an NA of 0.1, it has been proven that the NA can be increased to 0.25, which would enable patterns with a size of 32 nm or less to be replicated.

The Micro Exposure Tool (MET) (NA = 0.3) was built to clarify the minimum feature size of replicable patterns and to promote the development infrastructure in EUV-LLC (Fig. 25).[47] This technology was subsequently transferred to ASML and a European company. Four systems are now available.[48–50] This system has a 2-aspherical-mirror system with a numerical aperture of 0.3, and a demagnification of 1/5. The exposure area is 100 μm × 200 μm. This system was used to replicate the 25-nm L&S pattern. Regarding the performance of the optical system, the diffraction limit is 20 nm. Moreover, Exitech developed a commercial system with a DPP source in 2004. The two systems have been delivered and are being used for process studies.

On the other hand, an EUVL α-demo tool developed[51,52] by ASML was used to replicate the pattern in Fig. 26. It has been used to replicate a 40-nm L&S pattern. One feature of the system is that it employs newly developed wafer handling technology. This system will be tested at ISEMATECH this year (2006). Table 4 below shows the specifications.

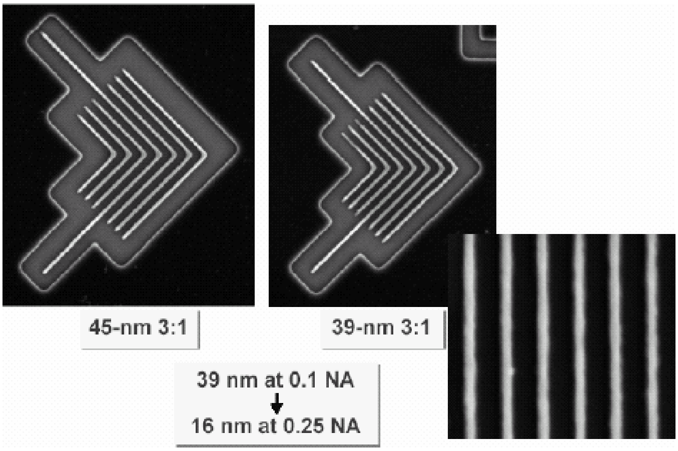

Fig. 24. Exposure pattern using ETS-1.

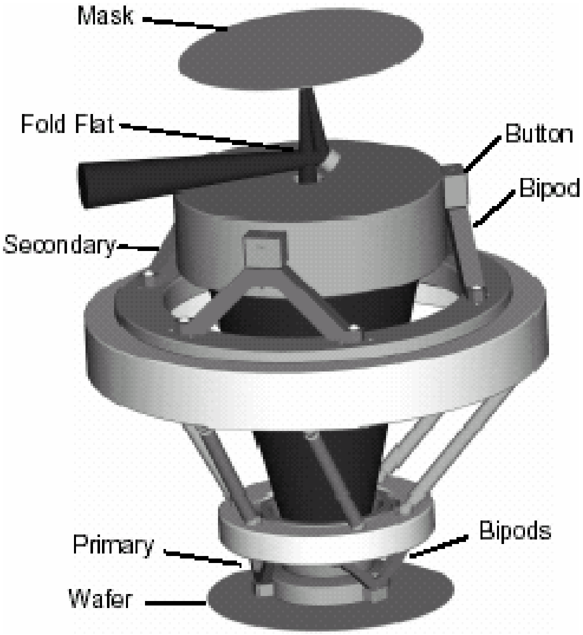

Fig. 25. Micro Exposure Tool (MET) By SAMATECH.

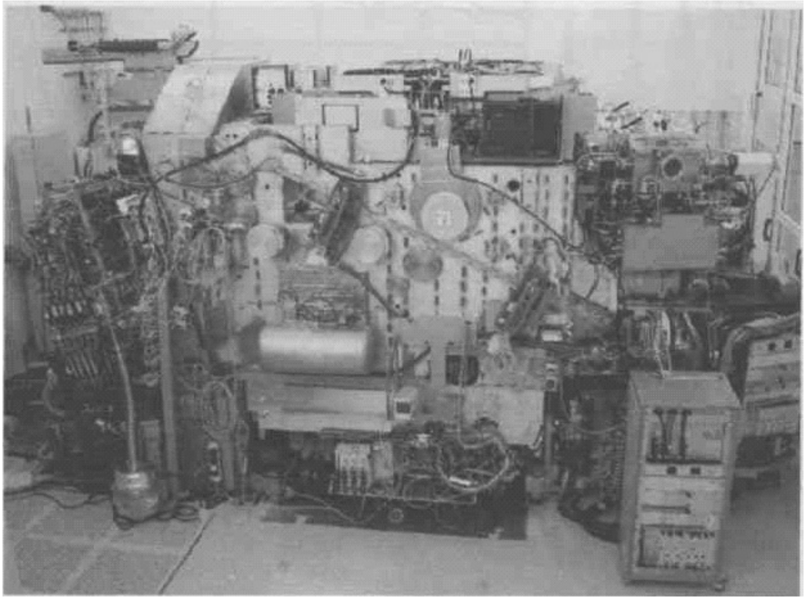

Fig. 26. EUVL α-demo tool developed by ASML.

Table 4. Specification of EUVL α-demo tool.

Item	Specification
λ	13.5 nm
NA range	0.15–0.25
Field size	26 mm × 33 mm
Wafer size	300 mm
Magnification	4
Flare	16%
Dense L/S	40 nm
Isolated lines	30 nm
Iso/dense contact	55 nm
Overlay	12 nm
Throughput	~10 wph

5. Conclusions

To achieve that goal, the trial production of 32-nm LSIs using a beta version of the apparatus must be accomplished by 2009. Experimental equipment with an NA of 0.3 and an exposure area with a diameter of less than 1 mm is already on the market; and exposure tests in cooperation with ISEMATEC, etc. have already begun. This apparatus provides a resolution of 30 nm or less on a resist, and less than 20 nm is possible, considering the performance of the optics. The critical issue right now is the development of a light source that can provide a throughput of 100 8-inch-wafers/hour. Since the specifications of the optical system have already been decided on the development side, the problem is how to boost the intensity of the light source to 115 W from the present 30 W or so. Another issue is the development of a resist with a line-edge roughness (LER) of 3 nm or less, because LER influences the width of an exposed pattern. For resists, there seems to be a trade-off between LER and sensitivity; and it is important to find a material with a small LER that requires a small exposure dose. If a resist that provides the requisite LER and a sensitivity of $1.0\,\mathrm{mJ/cm^2}$ is developed, the intensity of the light source can be reduced to something like 30 W, which dramatically increases the possibility of the realization of practical EUVL. Unlike a conventional optical system, we have to remember that EUVL is a reflection system, and increasing the number of mirrors is fatal. All the possibilities for the apparatus, light source, and resist must be investigated with the goal of mitigating the severity of the specifications so that a practical EUVL system can be realized as quickly as possible.

In conclusion, research and development on EUVL over the past 20 years has led to significant breakthroughs in processing and measurement technology. Many lithographic technologies have been developed and screened during the last 20 years. Although several critical problems still remain with regard to such things as the light source, masks and resist, it appears now that solutions can be found because the two biggest problems — the fabrication of aspherical mirrors and multilayers, have been resolved.

The first international conference with “EUVL” in the title was held near Mt. Fuji in 1993. In the opening address, I said, “As long as we do not lose the desire that has sprung from within us, technology will steadily advance from the micro to the nano to the pico.” And now is the time when “pico” can easily be used when talking about optical technology.

References

1. Kinoshita H, Kaneko T, Takei H, Takeuchi N and Ishii N, Extended Abstracts, *The 47th Autumn Meeting, 1986*; The Japan Society of Applied Physics, pp. 322 (in Japanese).
2. Namioka T, Current research activities in the field of multilayers for soft X-ray in Japan, *Revue Phys Appl* **23**:1711–1726, 1988.
3. Kinoshita H, Kurihara K, Ishii Y and Torii Y, Soft X-ray reduction lithography using multiplayer mirrors, *J Vac Sci Technol B* **7**:1648–1651,1989.
4. Bjorkholm JE, Bokor J, Eichner L, Freeman RR, Gregus J, Jewell TE, Mansfield WM, MacDowell MM, Raab EL, Silfvast WT, Szeto LH, Tennant DM, Waskiewicz WK, Windt DL, Wood II R and Bruning JH, Reduction imaging at 14 nm using multiplayer-coated optics: Printing of features smaller than 0.1 μm, *J Vac Sci Technol B* **8**:1509–1513, 1990.
5. Kurihara K, Kinoshita H, Yakeuchi N, Mizota T, Haga T and Trii Y, Two-mirror telecentric optics for soft X-ray reduction lithography, *J Vac Sci Technol B* **9**:3189–3192, 1991.
6. Williamson, U.S. Patent 5,815,310 (1998).
7. Mailing H, Benschop J, Dinger U and Kurz P, Progress of α-RT, the EUVL Alpha research tool, *Proc SPIE* **4343**:38–50, 2001.
8. Bajuk D and Kestner R, Fabrication and testing of EUVL optics in *JSPE Proceedings of the Second US–Japan Workshop on Soft X-Ray Optics: Technical Challenges*, Mt. Fuji, Nov. 12–14, 1996.
9. Kinoshita H, Kurihara K, Mizota T, Haga T, Takenaka H and Torii Y, Large-area, high-resolution pattern replication by the use of a two-aspherical-mirror system, *Appl Optics* **32, 34**:7079–7083, 1993.
10. Sommargren GE, Phase shifting diffraction interferometry for measuring extreme ultraviolet optics in *OSA Trends in Optics and Photonics*, Vol. 4, IEEE Publisher, pp. 108–112, 1994.
11. Sommargren, GE, Phillion DW and Campbell EW, Sub-nanometer interferometry for aspheric mirror fabrication, *Proc. of the IX ICPE, Precision Science and Technology for Perfect Surfaces*, Japan Society for Precision Engineering, pp. 329–335, 1999.
12. Murphy JB, White DL, MacDowell AA and Wood II OR, Synchrotron radiation sources and condensers for projection X-ray lithography, *Appl Optics* **32, 34**:6920–6929, 1993.
13. Hansson B, Fomenkov I, Bowering N, Ershov A, Partlo W, Myers D, Khodykin O, Bykanov A, Rettig C, Hoffman J, Vargas E, Simmons R, Chavez J, Marx W and Brandt D, LPP EUV source development for HVM, *Proc SPIE* **6151**:61510R1–61510R9, 2006.
14. Stamm U, Kleinschmidt J, Bolshukhin D, Hergenhan G, Korobotchko V, Nikolaus B, Schurmann MC, Schriever G, Ziener C and Borisov VM, Development status of EUV sources for use in Beta-tools and high-volume chip manufacturing tools, *Proc SPIE* **6151**:61510O1–61510O11, 2006.

15. Pankert J, Apetz R, Bergmann K, Damen M, Derra G, Franken O, Janssen M, Jonkers J, Klein J, Kraus H, Krucken T, List A, Loeken M, Mader A, Metzmacher C, Neff W, Probst S, Prummer R, Rosier O, Schwabe S, Seiwert S, Seimons G, Vaudrevange D, Wagemann D, Weber A, Zink P and Zitzen O, EUV sources for the Alpha-tools, *Proc SPIE* **6151**:61510Q1–61510Q9, 2006.
16. Hawryluk AM, Ceglio NM and Gaines DP, Reflection mask technology for X-ray projection lithography, *J Vac Sci Technol B* **7**:1702–1704, 1989.
17. Tennant DM, Bjyokholm JE, D'Souza RM, Eichner L, Freeman RR, Pastalan JZ, Szeto LH, Wood II OR, Jewell TE, Mansfield WM, Waskiewicz WK, White DL, Windt DL and MacDowell AA, Reflective mask technologies and imaging results in soft X-ray projection lithography, *J Vac Sci Technol B* **9**:3176–3183, 1991.
18. Kinoshita H, Watanabe T, Ozawa A and Niibe M, Mask technology of extreme ultraviolet lithography, *Proc SPIE* **3412**:358–368, 1998.
19. Yulin S, Kuhlmann T, Feigl T and Kaiser N, Damage resistant and low stress EUV multilayer mirrors, *Proc SPIE* **4343**:607–614, 2001.
20. Yan PY, Zhang G, Kofron P, Powers J, Tran M, Ling T, Stivers A and Lo FC, EUV mask absorber characterization and selection, *Proc SPIE* **4066**:116–123, 2000.
21. Yan PY, Zhang G, Ma A and Liang T, TaN EUVL mask fabrication and characterization, *Proc SPIE* **4343**:409–414, 2001.
22. Nii H, Kinoshita H, Watanabe T, Hamamoto K, Tsubakino H and Sugie Y, Performance of Cr mask for extreme ultraviolet lithography, *Proc SPIE* **4409**:681–686, 2001.
23. Wasson J, Smith K, Mangat PJS and Hector S, An infinitely selective repair buffer for EUVL reticles, *Proc SPIE* **4343**:402–408, 2001.
24. Wasson JR, Lu B, Mangat PJS, Nordquist K and Resnick DJ, Writing, repairing and inspecting of extreme ultraviolet lithography reticles considering the impact of the materials, *J Vac Sci Technol B* **19**:2635–2640, 2001.
25. Lee BT, Hoshino E, Takahashi M, Yoneda T, Yamanashi H, Hoko H, Ryoo M, Chiba A, Ito M, and Sugawara M, Approach to patterning of extreme ultraviolet lithography masks using Ru buffer Layer, *Jpn J Appl Phys* **40**:6998–7001, 2001.
26. Tenant DM, Fetter LA, Harriott LR, MacDowell AA, Mulgrew PP, Waskiewicz WK, Windt DL and Wood II OR, Detect repair for soft X-ray projection lithography masks, *J Vac Sci Technol B* **10**:3134–3140, 1992.
27. Hawryluk AM and Stewart D, Repair of opaque defects on reflection masks for soft X-ray projection lithography, *J Vac Sci Tecnol B* **10**:3182–3185, 1992
28. Early K, Windt DL, Waskiewicz WK, Wood II IR and Tennant DM, Repair of soft-X-ray optical elements by stripping and redeposition of Mo/Si reflective coatings, *J Vac Sci Technol B* **11**:2926–2929, 1993.
29. Tanaka Y, Fujii K, Suzuki K, Iwamoto T, Tsuboi S and Matsui Y, Fabricatrion of NIST-format X-ray masks with 4-Gbit DRAM test patterns, *Proc SPIE* **4409**:660–668, 2001.
30. Tonh WM, Taylor JS, Hector SD, Shell MK, Mask substrate requirements and development for extreme ultraviolet lithography (EUVL), *Proc SPIE* **3873**:421–428, 1999.
31. Nagata H, Ohtani M, Murakami K, Oshino T, Maejima Y, Tanaka T, Watanabe T, Yamashita Y and Atoda N, Soft X-ray projection imaging using 32:1 Schwarzschild Optics, *OSA Proc on Soft X-Ray Projection Lithography*, Vol. 18, pp. 83–86, 1993.
32. Ito M, Katagiri S, Yamanashi H, Seya E, Ogawa T, Oizumi H and Terasawa T, Optical technology for EUV Lithography, *OSA TOPS on Extreme Ultraviolet Lithography*, Vol. 4, pp. 9–12, Washington, DC, 1996.
33. Silfvast WT and Wood II OR, Tenth micron lithography with a 10 Hz 37.2 nm sodium laser, *Microelectron Eng* **8**:2–10, 1988.

34. Hawryluk AM and Seppala LG, Soft X-ray projection lithography using an X-ray reduction camera, *J Vac Sci Technol B* **6**:2162–2166, 1988.
35. White DL, Bjorkholm JE, Bokor J, Eichner L, Freeman RR, Gregus JA, Jewell TE, Mansfield WM, MacDowell AA, Raab EL, Silfvast WT, Szeto LH, Tennant DM, Waskiewicz WK, Windt DL and Wood II OR, Soft X-ray projection lithography: Experiments and practical printers, *Proc SPIE* **1343**:204–213, 1990.
36. Kubiak GD, Outka DA, Rohlfing CM, Zeigler JM, Windt DL and Waskiewicz WK, Extreme ultraviolet resist and mirror characterization:Studies with a laser plasma source, *J Vac Sci Technol B* **8**:1643–1647, 1990.
37. Berreman DW, Bjorkholm JE, Eichner L, Freeman RR, Jewell TE, Mansfield WM, MacDowell AA, Malley MLO, Raab EL, Silfvast WT, Szeto LH, Tennant DM, Waskiewicz WK, White DL, Windt DL and Wood II OR, Soft-X-ray projection lithography: Printing of 0.2-μm features using a 20:1 reduction, *Optics Lett* **15**:529–531, 1990
38. Ceglio NM, Hawryluk AM, Stearns DG, Gaines DP, Rosen RS and Vernon SP, Soft X-ray projection lithography, *J Vac Sci Technol B* **8**:1325–1328, 1990.
39. MacDowell AA, Bjorkholm JE, Bokor J, Eichner L, Freeman RR, Mansfield WM, Pastalan J, Szeto LH, Tennant DM, Wood II OR, Jewell TE, Waskiewicz WK, White DL, Windt DL, Silfvast WT and Zernike F, Soft X-ray projection lithography using a 1:1 ring field optical system, *J Vac Sci Technol B* **9**:3193–3197, 1991.
40. Haga T and Kinoshita H, Illumination system for extreme ultraviolet lithography, *J Vac Sci Tecnol B* **13**:2914–2918, 1995.
41. Tichenor DA, Ray–Chaudhuri AK, Kubiak GD, Nguyen KB, Haney SJ, Berger KW, Nissen RP, Perras YE, Jin PSJ, Weingarten LI, Keifer PN, Stulen RH, Shagam RN, Sweatt WC, Smith TG, Wood II OR, MacDowell AA, Bjorkholm JE, Jewell TE, Zernike F, Fix BL and Hauschildt HW, Progress in the development of EUV imaging system*, OSA TOPS on Extreme Ultraviolet Lithography*, Vol. 4, pp. 2–8, Washington, DC, 1996.
42. Nguyen KB, Cardinale GF, Tichenor DA, Kubiak GD, Berger K, Ray–Chaudhui AK, Perras Y, Haney SJ, Nissen R, Krenz K, Stulen RH, Hujioka H, Hu C, Bokor J, Tennant DM and Fetter LA, Fabrication of MOS devices with extreme ultraviolet lithography, *OSA TOPS on Extreme Ultraviolet Lithography*, Vol. 4, pp. 208–211, 1996.
43. Kinoshita H, Watanabe T, Ito M, Oizumi H, Yamanashi H, Murakami K, Oshino T, Platonov Y and Grupid N, Three-aspherical mirror system for EUV lithography, *Proc SPIE* **3331**:20–31, 1998.
44. Kinoshita H, Watanabe T, Li Y, Miyafuji A, Oshino T, Sugisaki K, Murakami K, Irie S, Shirayone S and Okazaki S, Recent advances of 3-aspherical mirror system for EUVL, *Proc SPIE* **3997**:70–75, 2000.
45. Watanabe T, Kinoshita H, Mityafuji A, Irie S, Shirayone S, Mori S, Yano E, Hada H, Ohmori K and Komano H, Lithographic performance and optimization of chemically amplified single layer resists for EUV lithography, *Proc SPIE* **3997**:600–607, 2000.
46. Tichenor D, Ray–Chaudhuri A, Repolgle W, Stulen R, Kubiak G, Rocket P, Klebanoff L, Wronosky J, Hale L, Chapman H, Taylor J, Forta J and Montcalm C, System integration and performance of the EUV engineering test stand, *Proc SPIE* **4343**:19–37, 2001.
47. Naulleau PP, Goldberg KA, Anderson E, Cain JP, Denham P, Hoef B, Jackson K, Morlens AS, Rekawa S and Dean K, EUV microexposures at the ALS using the 0.3-NA MET projection optics, *Proc SPIE* **5751**:56–63, 2005.
48. Roberts JM, Bacuita T, Bristol RL, Coo HB, Chandhok M, Lee SH, Panning EM, Shell M, Zhang G and Rice BJ, One small step: World's first integrated EUVL process line, SPIE **5751**:64–77, 2005.

49. Booth M, Brisco O, Brunton A, Cashmore J, Elbourn P, Elliner G, Gower M, Greuters J, Gruenewald G, Gutierrez R, Hill T, Hirsch J, Kling L, McEntee N, Mundair S, Richards P, Truffert V, Wallhead I, Whitfield M and Hudyma R, High-resolution EUV imaging tools for resist exposure and aerial image monitoring, *Proc SPIE* 78–89, 2005.
50. Oizumi H, Tanaka Y, Kumasaka F, Nishiyama I, Kondo H, Shiraishi M, Oshino T, Sugisaki K and Murakami K, Lithographic performance of high-numerical-aperture (NA = 0.3) EUV small-field exposure tool (HINA), *Proc SPIE* **5751**:102–109, 2005.
51. Meiling H, Banine B, Horned N, Blum B, Wilton ASML, Kuerz P and Meijer H, Development of the ASML EUV alpha demo tool, *Proc SPIE* **5751**:90–101, 2005.
52. Meiling H, Meijer H, Banine V, Groeneveld R, Voorma H, Mickan U, Wolschrijn B, Mertens B, Baars G, Kuerz P and Harned N, First performance results of the ASML alpha demo tool, *Proc SPIE* **6151**:6151081–61510811, 2006.

SYNCHROTRON-RADIATION-SUPPORTED HIGH-ASPECT-RATIO NANOFABRICATION

A. CHEN, G. LIU*, L. K. JIAN and HERBERT O. MOSER
Singapore Synchrotron Light Source
National University of Singapore
5 Research Link, Singapore 117603
slsca@nus.edu.sg

X-ray lithography with synchrotron radiation is an important nanolithographic tool which has unique advantages in the production of high aspect ratio nanostructures. The optimum synchrotron radiation spectrum for nanometer scale X-ray lithography is normally in the range of 500 eV to 2 keV. In this paper, we present the main methods, equipment, process parameters and preliminary results of nanofabrication by proximity X-ray lithography within the nanomanufacturing program pursued by Singapore Synchrotron Light Source (SSLS). Nanostructures with feature sizes down to 200 nm and an aspect ratio up to 10 have been successfully achieved by this approach.

Keywords: Nanofabrication; X-ray lithography; synchrotron radiation.

1. Introduction

In recent years, the development in nanolithography has contributed greatly to the progress in nanoscience and nanotechnology. The continuous improvement of lithographic resolution has enabled the density increment of electronic integrated circuits, as well as the development of novel nanodevices. The main nanolithographic techniques fall in two classes, namely,

(i) full wafer exposure lithographies that are intrinsically parallel and fast, but need a mask,
(ii) writing lithographies that are serial and slow, but suitable for primary pattern generation.

The former includes

(a) projection lithographies that employ either the deep ultraviolet spectral range provided by excimer laser sources or the extreme ultraviolet (EUV), in

---

*Also at: *National Synchrotron Radiation Laboratory, University of Science and Technology China, Hefei, China 230029.*

particular, at 13.5 nm wavelength, produced by either plasma sources driven by lasers or electric discharges, or synchrotron light sources,
(b) proximity X-ray lithography with synchrotron radiation,
(c) nanoimprint lithography.

The writing lithographies include electron-beam lithography (EBL) and ion-beam lithography.

Singapore Synchrotron Light Source (SSLS) is pursuing all three mentioned full wafer exposure lithographies as well as EBL. Proximity X-ray lithography is the workhorse for deep X-ray lithography at SSLS whereas projection EUV lithography (EUVL) is being pursued on a planning level. Nanoimprint lithography is used as required by demand.

The synchrotron radiation spectrum delivered by SSLS Helios 2 compact electron storage ring caters for both spectral ranges, X-rays and EUV (Fig. 1). Originally, Helios 2 and its sister machine Helios 1 that had been developed by Oxford Instruments,[1] as well as storage rings AURORA (Sumitomo Heavy Industries),[2] NIJI-3 (Sumitomo Electric Industries in co-operation with the Electrotechnical Laboratory at Tsukuba),[3] MELCO (Mitsubishi Electric Corporation),[4] SuperALIS (NTT),[5] and others were built for X-ray proximity lithography for semiconductor manufacturing towards the 45-nm node with an intended aspect ratio of around 1.[6] Subsequent development using such machines has been attempted for even smaller critical feature sizes of 35 nm, and possibly, 20 nm.[7]

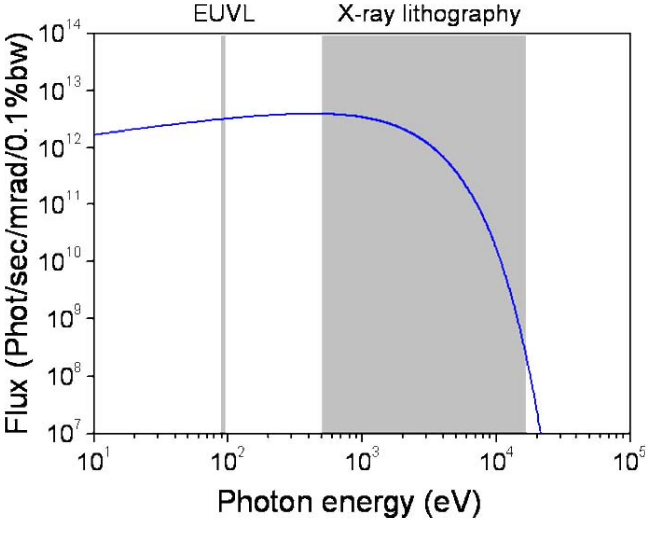

Fig. 1. Spectrum of synchrotron radiation from the dipoles of the Helios 2 superconducting storage ring running at 500 mA electron current. Spectral ranges used for X-ray proximity and EUV lithography are indicated. At the moment, SSLS X-ray proximity range starts at about 2 keV.

Beyond this original application, X-ray proximity lithography was proved to be most advantageous for its capability of high aspect ratio and parallel processing to fabricate tall microstructures as demonstrated by the LIGA process[8] that led to unique applications such as the separation nozzle,[9] optical spectrometers[10] and microgears.[8] Building upon these developments, the full LIGA process equipment, including a beamline and scanner for proximity X-ray lithography, was set up in the LiMiNT facility at SSLS spawning a wealth of micro/nanofabrication work[11] including pioneering work on electromagnetic metamaterials for the THz spectral range extending from far-infrared to the visible.[12,13]

Comparably less advanced, work on EUVL at SSLS still proceeds on a project planning at proposal level only.[14] Therefore, it will not be further discussed in this article. Instead, the interested reader is referred to the article by H. Kinoshita in this issue.

Nanoimprint lithography, finally, based on Ni mold inserts fabricated by EBL has been used in certain cases including the fabrication of 2-dimensional (2D) photonic crystal structures designed for photonic crystal light-emitting diodes.[15]

The X-ray lithography system that is being operated in the SSLS LiMiNT facility is the basis for synchrotron-radiation-supported nanofabrication at SSLS. Moreover, access is also possible in co-operation with China National Synchrotron Radiation Laboratory (NSRL) to its soft X-ray lithography beamline.

In the following, a short description of the method will be given with special attention to the limiting effects in nanoscale X-ray proximity lithography. The lithography equipments in SSLS and NSRL will be shortly introduced and compared. Desirable upgrades will be discussed. First, results will be presented and discussed, followed by the conclusion.

2. Method

The optics of X-ray proximity nanolithography is shown in Fig. 2. The lateral dose intensity distribution on the substrate surface depends on the distance between the substrate and the absorber, the minimum lateral width of the clear mask feature and the source wavelength. It is usually described by means of the dimensionless Fresnel number

$$N_F = \frac{w^2}{4G_p\lambda}, \tag{1}$$

where w is the minimum width of the clear mask feature, G_p the distance from the mask downstream which is called proximity distance, and λ the wavelength of the radiation source.[16,17] At $N_F > 10$, i.e., comparably close to the mask absorber, the shape of the clear mask feature is pretty faithfully reproduced by the intensity distribution pattern. This is called the Fresnel diffraction regime. However, at $N_F < 1$, the lateral intensity distribution becomes more and more like the Fraunhofer diffraction pattern of a small aperture, i.e., characterised by a central maximum and several side maxima and minima. For a good reproduction of the mask

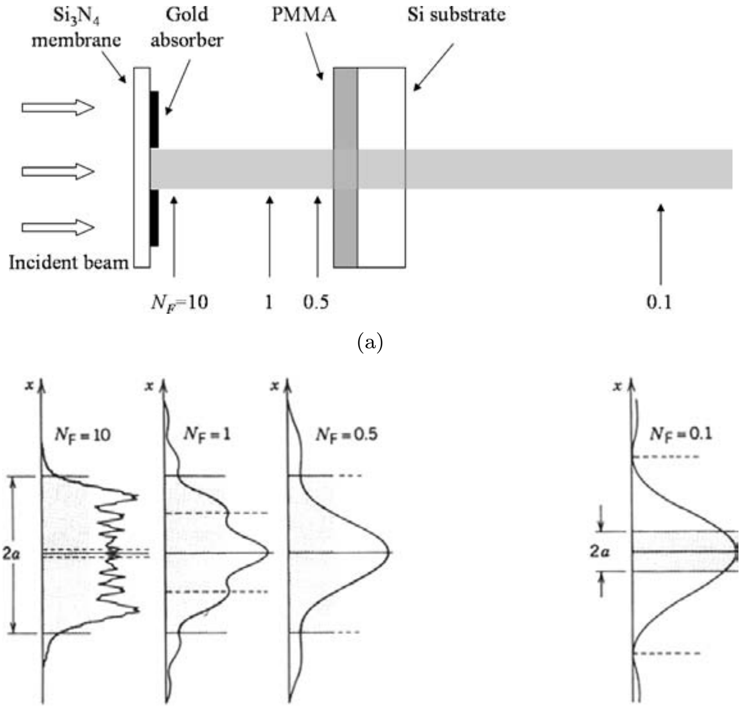

(a)

(b)

Fig. 2. (a) Schematic setup for proximity X-ray lithography. (b) Dose intensity profiles downstream the mask at different proximity gaps/Fresnel numbers[16] (with kind permission by Wiley-Interscience). The shaded area in (b) indicates the geometrical shadow of the clear feature on the mask. For 1:1 pattern replication, the gap must be small enough to ensure a large Fresnel number ($N_F = 10$), and thus a faithful feature reproduction. In the case of a large proximity gap and a small Fresnel number ($N_F = 0.5$), the dose profile is characteristic of a sharp central maximum with shoulders, which can be used to print a feature smaller than the clear mask feature. This is called "super-resolution."

feature, one needs to be sufficiently deep in the Fresnel regime. It is noted that the smaller the clear mask features, the smaller the proximity distance must be for a given wavelength of radiation posing more and more stringent requirements on the proximity gap, as well as the absorber and resist surfaces.

Atoda *et al.*[18] have analysed the pattern transfer quantitatively recasting the Fresnel number Eq. (1) into

$$w = U_0(G_p\lambda/2)^{1/2}. \qquad (2)$$

Comparing Eqs. (1) and (2) leads to

$$U_0 = 2\sqrt{2N_F}.$$

They claim that the value of U_0 should be larger than 3 to reproduce the clear mask feature adequately. This corresponds to a Fresnel number of 1.125. Assuming a source wavelength of 1 nm, the proximity gap required for the precise transfer of sub-100 nm patterns is less than 3 μm. However, the lithographic printing of sub-100 nm patterns was achieved at larger gaps (10 μm) by using low contrast masks and a chemically amplified resist.[19] Simulation studies indicated that narrowband source exposure in conjunction with a resist containing special absorbing elements may also lead to sub-100 nm pattern printing at a 10 μm gap.[20]

Although a small mask–substrate gap is desired for 1:1 pattern transfer, a dose profile with a sharp peak and shoulders is available at a relatively large gap distance ($N_F = 0.5$), as shown in Fig. 2. By selecting a proper development level in this case, a local "demagnification" of clear features from the mask to the substrate can be achieved. This is the so-called "super-resolution" process, which has potential applications for sub-10 nm nanolithography.[21–23] At present, 25-nm line features have been obtained at 15–30 μm proximity gaps.[23]

3. Existing Facilities and Development Program

The SSLS LiMiNT beamline layout is schematically shown in Fig. 3. This beamline was originally designed for deep hard X-ray lithography. The useful spectral flux at the sample covers a bandwidth from 2 keV to > 10 keV delivering a power of 1.5 W to a 4-inch wafer at an electron current of 500 mA. Development work is underway to remove one of the two Be windows to increase power in the soft X-ray range, and to introduce a mirror-based spectral low pass to cut off harder X-rays above a tunable wavelength.

Besides the LiMiNT beamline, the LiMiNT class 1000 cleanroom is equipped with the tools for micro- and nanoscale primary pattern generation, including the EBL system, direct laser writer, electroplating baths, and hot embossing press. Fig. 4 shows an interior view of the cleanroom with the e-beam writer.

The NSRL U1 beamline has been designed for soft X-ray lithography. Its layout is schematically shown in Fig. 5. A mirror reflector is employed to cut off the harder part of the source spectrum, selecting a spectral range from 500 eV to 3 keV. The mirror coating consists of gold, and the grazing incidence angle is 20 mrad.

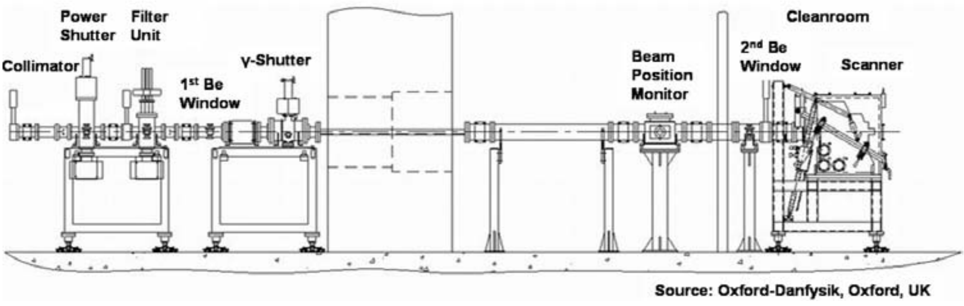

Source: Oxford-Danfysik, Oxford, UK

Fig. 3. Schematic layout of the LiMiNT beamline for micro/nanofabrication at SSLS. The beamline height is 1.2 m above floor. The photon beam enters the beamline from the left and is led into the X-ray scanner that is located in a clean room of class 1000.

Fig. 4. Photo of the class 1000 cleanroom of SSLS showing the e-beam writer, laser writer, plasma cleaner and hot embosser. The X-ray scanner is in the background, hidden by the laser writer.

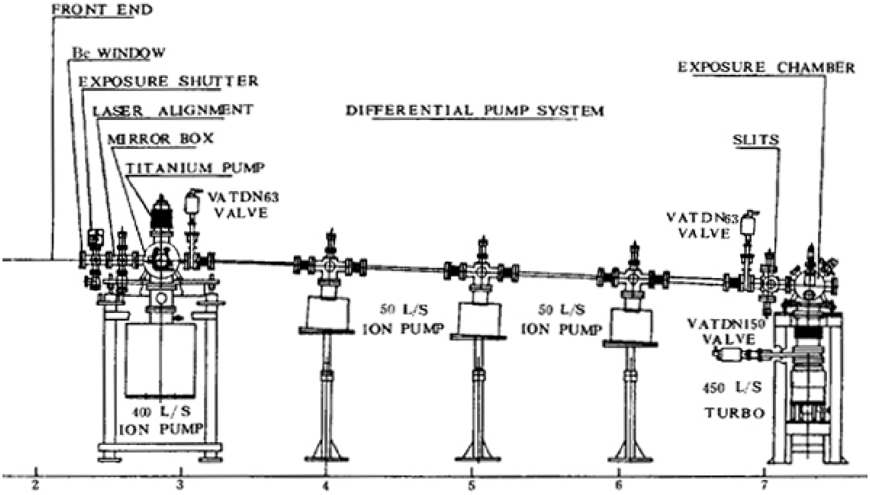

Fig. 5. Schematic layout of the NSRL U1 beamline for soft X-ray lithography. The cross-section of the beam is kept at $30 \times 30\,\mathrm{mm}^2$, low enough to set up a differential pumping system that enables windowless operation while the pressure in the exposure chamber is 4×10^{-4} Pa.

The absorber thickness on the X-ray mask has to be selected such that the residual dose below the absorber is lower than the development threshold of the resist. Considering a bottom dose of $3000\,\mathrm{J/cm}^3$ and a residual dose of $< 100\,\mathrm{J/cm}^3$ for a resist such as polymethylmethacrylate (PMMA), the absorber thickness needs to be larger than $2\,\mu$m for the SSLS LiMiNT beamline source. The fabrication of such thick absorbers is challenging, especially for a feature size down to sub100 nm. Therefore, we chose the NSRL U1 beamline for X-ray lithography at this moment, which has a much softer source spectrum. The required gold absorber thickness is about 250 nm.

4. Results and Forthcoming Work

The X-ray masks were fabricated on 1 μm-thick silicon nitride membranes using SSLS LiMiNT facilities. The fabrication process followed the *additive* scheme. First, a thin Au/Cr seeding layer was deposited on the membrane, followed by the spin-coating of PMMA 950 kDa with a thickness of 400 nm. Various nanopatterns with critical dimensions down to 70 nm were defined in PMMA by EBL at 30 keV. Gold electroplating was then performed up to a thickness of 250 nm. As the total area patterned by EBL is small, shunt areas were introduced to increase the overall current of electroplating. Finally, the mask was soaked in acetone to remove the PMMA. Typical gold patterns fabricated on the mask are shown in Fig. 6. Both positive

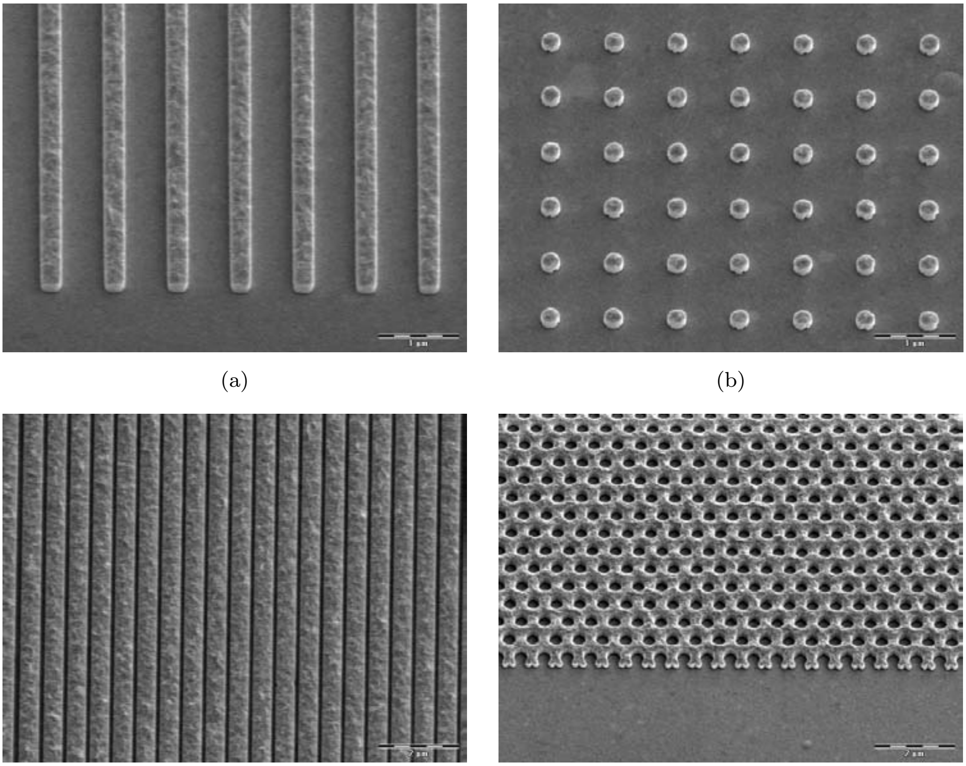

(a) (b)

(c) (d)

Fig. 6. Scanning electron microscopy (SEM) images of gold patterns on the X-ray mask: (a) isolated line array; (b) isolated pillar array; (c) line space array and (d) hexagonal air hole array. The scale bars are 1 μm for (a) and (b), and 2 μm for (c) and (d).

and negative nanopatterns were obtained with good quality. As the electroplating rate varies with the pattern size and geometry, especially when the pattern size is reduced to sub-100 nm regimes, it would be advisable to have the patterns of similar type and dimensions on the same piece of mask. Moreover, pulsed plating may further improve the thickness uniformity of different-sized patterns across the whole mask,[24] and will be investigated in our future work.

Soft X-ray exposure was performed at NSRL. The resist used is PMMA 950 kDa with a thickness of 2–3 μm. The proximity gap was kept at about 13 μm by separating the mask and substrate with a Kapton foil. The mask contrast is estimated to be 15:1, considering a gold seeding layer thickness of 20 nm. After exposure, the development was carried out in an MIBK:IPA (1:3) solution for 30 s. As indicated by Eq. (2), patterns with critical dimensions smaller than 350 nm are subject to prominent diffraction effects and may fail to transfer at a gap distance of 13 μm. However, pattern transfer with a substantially smaller feature size might be achieved by a suitable choice of resist, exposure dose and development level.[19]

The first results of deep X-ray exposure are shown in Fig. 7. Various PMMA nanostructures, including isolated lines/pillars, line gaps and periodic air hole arrays

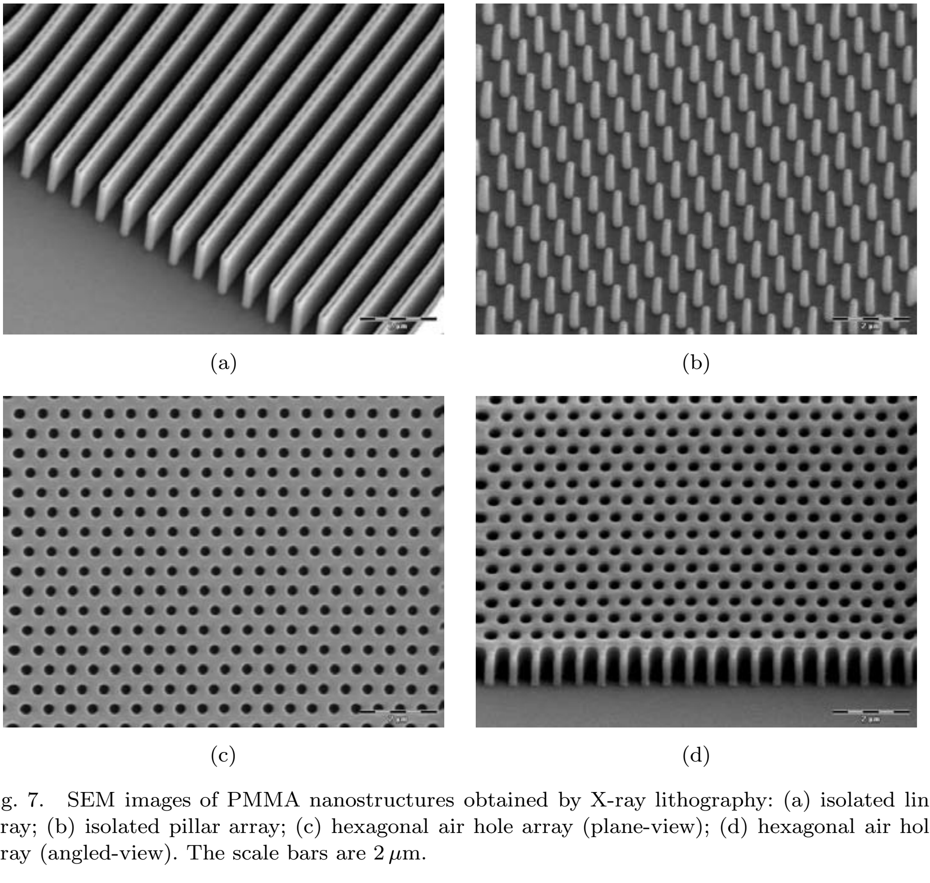
(a) (b) (c) (d)

Fig. 7. SEM images of PMMA nanostructures obtained by X-ray lithography: (a) isolated line array; (b) isolated pillar array; (c) hexagonal air hole array (plane-view); (d) hexagonal air hole array (angled-view). The scale bars are 2 μm.

were obtained with straight and smooth sidewalls. The smallest feature size that has been replicated is 200 nm, with an aspect ratio of 10. The discrepancy between the pattern sizes on the substrate and those on the mask is less than 10%.

Although successful pattern replication was attained, it is observed that there are diffraction effects and distortion of original patterns on some samples, especially when the exposure dose is large. Further work is required to optimize the exposure dose and development time for accurate pattern replication.

Moreover, as the Fresnel number is of the order of 1 for the nanolithography cases of interest, the 3-dimensional (3D) distribution of the wavefield and the corresponding dose must be carefully taken into consideration.

Collapse of isolated nanostructures was observed in some areas of the substrate for an aspect ratio of 10. It is speculated that the height and aspect ratio of the PMMA nanostructures may be severely limited by stiction due to unbalances in the distribution of the surface tension during the drying of rinsing water. Thus, the issue of minimising mechanical forces on the nanostructures during processing is of high priority.

5. Conclusion

We have demonstrated the fabrication of high aspect ratio nanostructures by X-ray proximity lithography. Silicon nitride masks with various gold absorber patterns down to 70 nm have been produced. PMMA patterns with a feature size down to 200 nm and an aspect ratio of 10 have been achieved at a proximity gap of 13 μm. The future work is towards replication of patterns with a smaller feature size and a higher aspect ratio by optimizing the proximity gap, exposure dose and development process. Applications of such high aspect ratio nanostructures including nanofilters and nanosensors will be pursued.

Acknowledgment

Work partly performed at SSLS under NUS Core Support C-380-003-003-001, A*STAR/MOE RP 3979908M and A*STAR 12 105 0038 grants.

References

1. Wilson MN *et al.*, The Helios 1 compact superconducting storage ring X-ray source, *IBM J Res Develop* **37**:351–371, 1993.
2. Takahashi N, Compact superconducting SR ring for X-ray lithography, *Nucl Instr Meth B* **24–25**:425–428, 1987.
3. Tomimasu T, An electron undulating ring dedicated to VLSI lithography, *Jpn J Appl Phys* **26**:741–746, 1987.
4. Nakanishi T *et al.*, Construction and beam experiment of a compact storage ring at MELCO, *Rev Sci Instr* **66**:1968–1970, 1995.
5. Hosokawa T, NTT superconducting storage ring — Super-ALIS, *Rev Sci Instr* **60**:1783–1785, 1989.

6. Heuberger A, X-ray lithography, *J Vac Sci Technol B* **6**:107–121, 1988.
7. Kitayama T *et al.*, Proposal for a 50 nm proximity x-ray lithography system and extension to 35 nm by resist material selection, *J Vac Sci Technol B* **18**:2950–2954, 2000; Itoga K *et al.*, Effect of secondary electron from the substrate in x-ray lithography using harder radiation spectra, *J Vac Sci Technol B* **19**:2439–2443, 2001.
8. Becker EW, Ehrfeld W, Hagmann P, Maner A and Münchmeyer D, Fabrication of microstructures with high aspect ratios and great structural heights by synchrotron radiation lithography, galvanoforming, and plastic moulding (LIGA process), *Microelectron Eng* **4**:35–56, 1986.
9. Becker EW, Ehrfeld W, Münchmeyer D, Betz H, Heuberger A, Pongratz S, Glashauser W, Michel HJ and Siemens RV, Production of separation-nozzle systems for uranium enrichment by a combination of X-ray lithography and Galvanopastics, *Naturwissenschaften* **69**:520–523, 1982.
10. Mohr J, Anderer B and Ehrfeld W, Fabrication of a planar grating spectrograph by deep-etch lithography with synchrotron radiation, *Sens Actuators A* **27**:571–575, 1991.
11. Moser HO, Bahou M, Casse BDF, Jian LK, Yang P, Gao XY and Wee ATS, Making and measuring nanostructures: nanoscience and technology at the Singapore Synchrotron Light Source, *Crystallography Reports* **51**:170–182, 2006.
12. Moser HO, Casse BDF, Wilhelmi O and Saw BT, Terahertz response of a microfabricated rod-split-ring-resonator electromagnetic metamaterial, *Phys Rev Lett* **94**:063901–063904, 2005.
13. Casse BDF, Moser HO, Lee JW, Bahou M, Inglis S and Jian LK, Towards three-dimensional and multilayer rod-split-ring metamaterial structures by means of deep x-ray lithography, *Appl Phys Letts* **90**:254106–254108, 2007.
14. Wilhelmi O, Moser HO, Singh N and Mukherjee-Roy M, *ELFA — an EUV Lithography Facility for Singapore,* Thin Films & Nanotech 2004, 13–17 July 2004, Singapore.
15. Chen A, Wang BZ, Chua SJ, Wilhelmi O, bin Mahmood S, Saw BT, Kong JR and Moser HO, Patterning of two-dimensional photonic crystal structures by nanoimprint lithography, *Int J Nanosci* **5**:559–563, 2006.
16. Saleh EA and Teich MC, *Fundamentals of Photonics*, Wiley, New York, 1991.
17. Spiller E, *Soft X-Ray Optics*, SPIE Optical Engineering Press, Bellingham, WA, 1994.
18. Atoda N, Kawamatsu H, Tanino H, Ichimura S, Harita M and Hoh K, Diffraction effects on pattern replication with synchrotron radiation, *J Vac Sci Technol B* **1**:1267–1270, 1983.
19. Deguchi K, Nakamura J, Kawai Y, Ohno T, Fukuda M, Oda M, Kochiya H, Ushiyama Y, Hamada H and Shimizu T, Lithographic performance of a chemically amplified resist developed for synchrotron radiation lithography in the sub-100-nm region, *Jpn J Appl Phys* **38**:7090–7093, 1999.
20. Watanabe H, Marumoto K, Sumitani H, Yabe H, Kise K, Itoga K and Aya S, 50 nm pattern printing by narrowband proximity X-ray lithography, *Jpn J Appl Phys* **41**:7550–7555, 2002.
21. Guo JZY and Cerrina F, Modeling X-ray proximity lithography, *IBM J Res Develop* **37**:331–349, 1993.
22. Kong JR, Wilhelmi O and Moser HO, Gap optimisation for proximity X-ray lithography using the super-resolution process, *Int J Comp Eng Sci* **4**:585–588, 2003.
23. Bourdillon AJ, Boothroyd CB, Williams GP and Vladimirsky Y, Near field x-ray lithography simulations for printing fine bridges, *J Phys D: Appl Phys* **36**:2471–2482, 2003.
24. Lindblom M, Hertz HM and Holmberg A, Pulse reverse plating for uniform nickel height in zone plates, *J Vac Sci Technol B* **24**:2848–2851, 2006.

Part 3

FUNCTIONAL NANOMATERIALS

This page intentionally left blank

CHEMICAL INTERACTIONS AT NOBLE METAL NANOPARTICLE SURFACES — CATALYSIS, SENSORS AND DEVICES

A. SREEKUMARAN NAIR, RENJIS T. TOM, V. R. RAJEEV KUMAR,
C. SUBRAMANIAM and T. PRADEEP*
DST Unit on Nanoscience, Department of Chemistry
and Sophisticated Analytical Instrument Facility
Indian Institute of Technology, Madras
Chennai-600036, India
**pradeep@iitm.ac.in*

In this paper, a summary of some of the recent research efforts in our laboratory on chemical interactions at noble metal nanoparticle surfaces is presented. The article is divided into five sections, detailing with (i) interactions of simple halocarbons with gold and silver nanoparticle surfaces at room temperature by a new chemistry and the exploitation of this chemistry in the extraction of pesticides from drinking water, (ii) interaction of biologically important proteins such as Cyt *c*, hemoglobin and myoglobin as well as a model system, hemin with gold and silver nanoparticles and nanorods forming nano–bio conjugates and their surface binding chemistry, (iii) formation of polymer–nano composites with tunable optical properties and temperature sensing characteristics by single and multi-step methodologies, (iv) nanomaterials-based flow sensors and (v) composites of noble metal nanoparticles and metallic carbon nanotubes showing visible fluorescence induced by metal–semiconductor transition.

Keywords: Nanomaterials; halocarbons; nano–bio conjugates; microgels; flow sensors; carbon nanotubes.

1. Introduction

Research on nanomaterials has evinced keen interest in recent years because of the new opportunities they present in nanocomposites, catalysis, environmental remediation and sensing.[1–5] Metal nanoparticles have potential applications in catalysis because of their large surface to volume ratio and unusual chemical reactivity.[6] Metal nanoparticles of different shapes could catalyze the reactions with different efficiencies because nanocrystals of different shapes represent various facets.

---

[*] Corresponding author.

Nanoparticles of silver, gold, copper, iron and its oxides, palladium and platinum have found applications in catalyzing reactions,[7–11] which offer immense scope for green chemistry. Iron and its oxide nanoparticles are excellent materials for environmental remediation.[4] Nanoscale materials are used as sorbents for contaminants, in nanofiltration and in reactive membranes.[12] The use of metal nanoparticles in sensing could bring about a revolution in biology, healthcare, military and day-to-day life.[13]

In this paper, we present various aspects of our studies on the chemical interactions at noble metal nanoparticle surfaces, touching upon (i) the investigation of the chemical reactivity of Au and Ag nanoparticles towards simple halocarbons by a new chemistry[14–16] and its extension in achieving the removal of common pesticides from drinking water,[17,18] (ii) the immobilization of biologically important proteins on nanosurfaces and their surface binding chemistry,[19,20] (iii) fabrication of polymer polymer–nano composites by single-step methodologies such as polymerization of molecules on nanosurfaces[21] and multi-step strategies,[22–24] (iv) fabrication of flow sensors from metal nanoparticles[25,26] and (v) formation of composites from single-walled carbon nanotubes (SWNT) and noble metal nanoparticles.[27] Simple halocarbons, which pose severe environmental hazards could be degraded by Au and Ag nanoparticles to metal halides and carbon at room temperature.[14] The same chemistry was used as a methodology for making oxide nanobubbles[15] from core–shell nanoparticles and also to investigate the porosity[16] of core–shell nanosystems. The interaction of biologically important proteins such as cytochrome *c* (Cyt *c*), myoglobin (Mb) and hemoglobin (Hb) with Au and Ag nanostructures leads to the formation of bio–nano conjugates.[19,20] We have succeeded in bringing about the polymerization of certain molecules such as benzylthiocyanate on nanoparticle surfaces[21] resulting in polymer–nano composites. Temperature sensitive poly (N-isopropylacrylamide)-capped *smart Au nanogels* were recently synthesized.[22] Gold nanorods were grown in microgels, which respond to temperature and pH changes in the environment.[23] Poly (*o*-toluidine) capped Au nanoparticles were synthesized by a one-pot methodology and the utility of the material in pH sensing was explored.[24] An array of Au nanoparticles on conducting glass surfaces was fabricated, which showed excellent flow sensing characteristics.[25,26] Also, composites of Au and Ag nanostructures with carbon nanotubes showed new and exciting phenomena.[27] We will illustrate more detail in the following section.

2. Experimental

Syntheses of citrate-capped Au and Ag nanoparticles and Au nanorods; methodologies for getting nano–bio composites of Cyt *c*, myoglobin, hemoglobin and hemin with Au and Ag nanoparticles and Au nanorods, polymer–nano composites by single and multi-step processes, fabrication of nanoparticles on conducting glass surfaces for flow sensors, the formation of nanoparticles-nanotubes composites; and the experimental methodology associated with each one of these studies are described in detail in the cited references. Characterization of the above nanomaterials involved UV–visible spectroscopy (Perkin–Elmer Lambda 25), infrared spectroscopy (Perkin–Elmer Spectrum One), fluorescence spectroscopy (Hitachi F-4500 spectrofluorimeter and Jobin–Vyon fluorolog instrument), Raman spectroscopy (Confocal Raman spectrometer CRM 200 of Witec), matrix assisted laser desorption ionization (MALDI) mass spectrometry (Voyager DE PRO Biospectrometry Workstation of Applied Biosystems), transmission electron microscopy (JEOL 3010 UHR operating at 300 kV), and AFM (CRM 200 of Witec with Alpha SNOM). Samples of extracted metallic SWNT (mSWNT), Au–mSWNT composite and Au–SWNT composites were investigated through point-contact current imaging-atomic force microscopy (PCI-AFM). As-received SWNT samples were thoroughly cleaned to remove impurities. PCI-AFM measurements were done at several places on each of these samples and also across several samples to confirm the authenticity and reliability of the data reported. In case of pure extracted mSWNTs, the sample was drop casted on a freshly cleaved mica surface and allowed to dry in a vacuum desiccator. For composite samples, the material was lifted from the aqueous–air interface (after evaporation of the organic layer) and drop cast on the mica surface. This was also subsequently dried in a vacuum desiccator. Half of the dried samples were masked using a clean cover glass slip and placed inside the thermal evaporation chamber. This chamber consists of a resistive heating wire on which a piece of pure gold metal was placed. The entire chamber was pumped using a turbo–molecular pump to a vacuum of 10^{-6} torr. A quartz crystal plate interfaced to a microbalance unit was held at the same level as the sample, to allow monitoring of the amount and thickness of the gold layer deposited. After pumping the system to vacuum, the evaporation of the gold was carried out by increasing the current through the resistive wire. This causes the gold to evaporate and deposit all around the evaporation chamber, including the unmasked portion of the sample. The evaporation was carried out till a gold pad thickness of 30–40 nm was achieved on the sample, which was monitored using the quartz crystal. The evaporation was then stopped and the chamber was brought slowly to room temperature with constant pumping. Finally, the samples were removed from the chamber, the mask was lifted carefully and the samples were preserved until further use.

PCI-AFM measurements were carried out on a JEOL JSPM-4210 instrument equipped with two function generators (WF 1946, NF Corporation). The I–V characteristics along the long axis of the nanotube composite were measured using Pt-coated conductive cantilevers. From the large area topographic image, it was ensured that the tubes selected for I–V measurements were indeed in contact with the gold electrode. The bias voltage was applied on the gold electrode and the cantilever was grounded. The entire experiment was carried out in a housing purged with N_2 gas to minimize the effects of humidity. The I–V data corresponds to the point of contact which reflects the local symmetry. The PCI-AFM image was constructed for 128 × 128 pixels with topographic and I–V characteristics acquired simultaneously.

3. Results and Discussion

3.1. *Interaction of halocarbons with metal nanoparticle surfaces — a novel chemistry for environmental remediation*

We have invented new reactions between the nanoparticles of Au and Ag (details are described in Ref. 14) and simple halocarbons such as CCl_4, $CHBr_3$, CCl_3F and benzylchloride, whereby the halocarbons are degraded by the nanoparticles to metal halides and amorphous carbon at room temperature.[14] We have systematically investigated the reactions in detail by spectroscopy, microscopy, pH and conductivity measurements to gain an understanding of the mechanistic aspects of the degradation. We have noted that the Au and Ag nanoparticles degrade the halocarbons by different reaction pathways.[14] While the halocarbons directly react at the nanoparticle surfaces in the case of Ag, they adsorb onto the surfaces of Au nanoparticles and degrade completely over a period of time, bringing about interesting features in the surface plasmon characteristics. The chemical reactivity of Au and Ag towards the halocarbons and the corresponding changes to the surface plasmon feature of the nanoparticles were monitored by UV–visible spectroscopy in a time-dependent manner. These are illustrated in Fig. 1. Figure 1(a) is the UV–visible spectra showing the interaction of Ag nanoparticles (70-nm diameter) with CCl_4. The progressive reduction in the intensity of the surface plasmon peak is attributed to the time dependent conversion of Ag into AgCl by CCl_4. Complete conversion of Ag into AgCl occurs in 12 h of interaction. The interaction of halocarbons with Au (~15 nm diameter) follows a different pathway, as is evident from Fig. 1(b). The binding of the halocarbon (benzylchloride) on Au results in time-dependent changes in the surface plasmon feature due to the adsorbate-induced aggregation of the nanoparticles.[14] The adsorbate-induced aggregation of Au nanoparticles was confirmed by TEM studies. The adsorbed halocarbons then react with the Au nanoparticles over a period of 48 h, resulting in their complete degradation to $AuCl_3$ and amorphous carbon. The formation of metal halides (AgCl and $AuCl_3$) was confirmed by X-ray diffraction and absorption spectroscopy respectively, and amorphous carbon by infrared (IR) and Raman spectroscopy.[14] The insets of Figs. 1(a) and 1(b) are the photographs depicting the color changes before (left) and after (right) the reaction with the respective nanoparticles. The pH and conductivity during the course of the reaction were monitored in a time-dependent manner. The pH of the reaction showed a decrease from 9.7 (that of the starting reaction mixture) to 1.2 (after complete degradation) during the course of the reaction and the conductivity of the solution showed a marked increase from $3.32 \times 10^3\,\mu S\ cm^{-1}$ to $3.51 \times 10^4\,\mu S\ cm^{-1}$. The conversion of 2-propanol (in the reaction mixture) to acetone ($CH_3–CHOH–CH_3 \rightarrow CH_3–CO–CH_3+2H^++2e$, the formation was confirmed by gas chromatographic measurements) *via* ketyl radical formation during the reaction is supposed to be the main source of protons. Hence the reason for the drastic reduction in pH. The chemical reactivity was also investigated with other halocarbons such as benzylchloride,

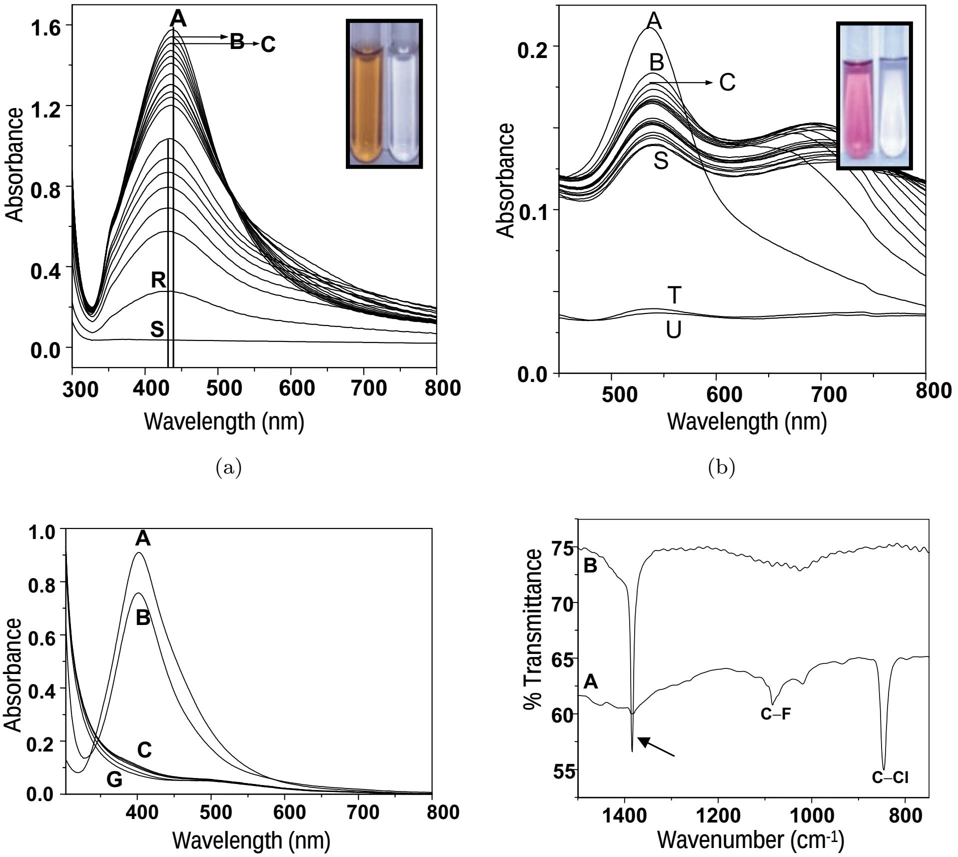

(a) (b)

(c) (d)

Fig. 1. (a) Variation in the UV–visible spectrum of silver nanoparticles upon the interaction with CCl_4. Spectrum of the pure nanoparticles, (A) shows the plasmon excitation at 438 nm, characteristic of silver nanoparticles of 60–80 nm diameter. Trace (B) was recorded just after the addition of 50 μL of CCl_4 to 2.5 mL of the solution. Subsequent traces were taken at 20 mins intervals (C to R) and trace (S) was recorded after 12 h showing the complete disappearance of the plasmon excitation. (b) Changes in the absorption spectra during the reaction between Au@citrate and benzylchloride. Trace (A) is the absorption spectrum of pure Au@citrate. Trace (B) was taken immediately after the addition of benzylchloride. Subsequent traces, (C–S) were taken at 20 mins intervals. The absorption spectrum U was taken after 48 h. (c) UV–visible spectra of the reaction between Ag@citrate and $CHBr_3$ in a time-dependent manner. The traces were taken at intervals of 3 mins. Note the rapid decrease in the intensity of the plasmon excitation of Ag@citrate (A) by the addition of 50 μL of bromoform to 2.5 mL of Ag@citrate (B–G). (d) A comparison of the infrared spectra of CCl_3F (trace A) and its reaction product with Ag@citrate (trace B). Note that the C–Cl and C–F features disappeared in the reaction product and a sharp peak corresponding to amorphous carbon emerged (indicated by an arrow) at 1384 cm^{-1}.

CH_2Cl_2, $CHBr_3$ and CCl_3F. The kinetics of binding and degradation of benzylchloride with Ag and Au were found to be faster compared to the CCl_4 case. The fastest reaction observed was with $CHBr_3$. Figure 1(c) shows the time-dependent UV–visible spectra of the reaction between $CHBr_3$ and Ag. The surface plasmon peak of Ag disappears just after 10 mins of their interaction. In the degradation of CCl_3F, analysis of the reaction product (Fig. 1(d), trace B) by infrared spectroscopy revealed the complete disappearance of the C–F and C–Cl bonds (seen in CCl_3F, Fig. 1(d), trace A) and the appearance of the carbonaceous peak (indicated by arrow). Similarly, no C–H frequency was seen in the reaction products of CH_2Cl_2 and $CHCl_3$ indicating their complete degradation. In view of the mechanistic details of the reaction investigated, the degradation reaction in the case of Ag may be represented as ($4Ag_{(s)} + CCl_{4(l)} \rightarrow 4AgCl_{(s)} + C_{(graphite)}$, $\Delta H = -379.8\,KJ\ mol^{-1}$, considering ΔH^0_{f298} of CCl_4 and AgCl as -128.2 and $-127.0\,kJ\ mol^{-1}$, respectively). The large negative ΔH value accounts for the fast reaction of halocarbons with the Ag nanoparticles. Thermochemistry suggests a less exothermic reaction ($4Au_{(s)}+3\,CCl_{4(l)} \rightarrow 4AuCl_{3(s)}+C_{(graphite)}$, $\Delta H = -85.8\,kJ\ mol^{-1}$) for gold, ($\Delta Hf^o_{298}$ for $AuCl_3 = -117.6\,kJ\ mol^{-1}$) which could be the reason for the slow reaction between Au nanoparticles and the halocarbons. The chemistry of halocarbons with metal nanoparticles was used to selectively leach metal cores from core–shell nanoparticles, namely Ag@ZrO_2, Au@ZrO_2 and Au@SiO_2 (metal cores protected with oxide shell of ZrO_2 and SiO_2, respectively).

The selective removal of Au and Ag nanoparticles resulted in ZrO_2 and SiO_2 nanobubbles/nanoshells.[15,28] The reaction of CCl_4 with Au@SiO_2 nanoparticles resulted in the growth of carbon onions inside the SiO_2 shell.[28] The halocarbon chemistry was also used to investigate the porosity of the shells.[16] This novel chemistry opens up a feasible means to incorporate molecules in nanoshells and investigate their spectroscopy in a confined atmosphere.[29] The methodology also enables us to incorporate drugs in nanoshells and study their controlled delivery.[30]

While searching for a feasible field of application for this new chemistry, the pesticide contamination in drinking water in India and some parts of the world came to our attention. Incidentally, most of the pesticides of interest (those detected in water) are either halocarbons or molecules with sulfur. These pesticides are endosulfan, chlorpyrifos and malathion, their presence in drinking water and soft drinks has become a huge environmental issue in India. Our initial experiments were using bare nanoparticles for their detection and extraction from water. Figure 2(a) shows changes to the absorption spectrum when endosulfan of different concentrations was exposed to Au nanoparticles.[17] The resultant color change is shown in the inset. The decrease in the intensity of the surface plasmon feature at 532 nm and the concomitant emergence of absorption peaks at longer wavelengths is characteristic of adsorbate-induced aggregation of the nanoparticles (and the resultant interplasmon coupling). This is clearer in Fig. 2(b), which shows the time-dependent UV–visible spectral changes of the interaction of endosulfan with Au nanoparticles. Note the reduction in the intensity of the 532 nm peak and the emergence of

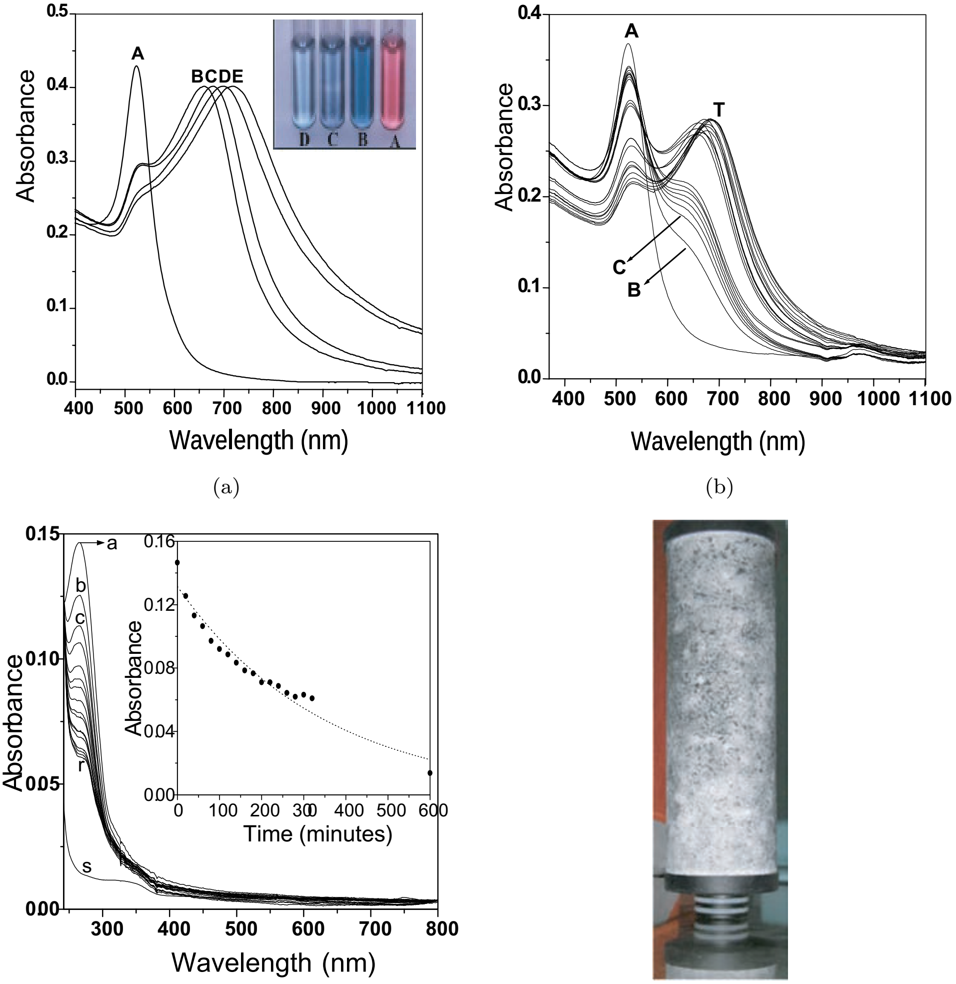

(a) (b)

(c) (d)

Fig. 2. (a) UV–visible spectrum of (A) citrate stabilized gold nanoparticles and the effect of exposure of endosulfan at various concentrations: (B) 2 ppm, (C) 10 ppm, (D) 100 ppm, and (E) 250 ppm. The spectra were recorded 9 h after exposure to endosulfan. The solutions have the same composition, except for endosulfan. A photograph of the solutions is shown in the inset, (A) pure citrate stabilized nanoparticles; (B), (C) and (D) correspond to 2, 10 and 100 ppm, respectively. (b) Time-dependence of the UV–visible absorption spectrum of citrate stabilized gold nanoparticles upon exposure of 10 ppm endosulfan. (A) Original nanoparticle solution, (B) 3 mins after adding endosulfan solution, (C) to (T), at 20 mins intervals thereafter. (c) shows the time-dependent UV–visible spectra showing the adsorption of 1 ppm chlorpyrifos on Al_2O_3@Ag. Trace A is the absorption spectrum of 1 ppm chlorpyrifos and traces (B–R) were taken at 20 mins intervals after the interaction with the nanoparticles. Trace s was taken after 10 h showing the complete disappearance of chlorpyrifos from water. The inset shows decrease in absorbance vs. time from the absorption spectroscopy data for the traces (A–S). The dotted line in the inset shows a fit of the exponential decrease in absorbance with time. (d) Photograph of a pesticide filter devise using supported nanoparticles.

another absorption peak at longer wavelength in a time-dependent manner. The binding of endosulfan on Au and Ag was also confirmed by spectroscopic means. Similarly, we have found that chlorpyrifos and malathion also bind to the nano surfaces effectively.[18] Having established the binding of pesticides on nano surfaces, we thought of making a pesticide filter by the incorporation of nanoparticles on suitable supports for water purification purposes. Activated alumina is a good adsorbent and a known player in water purification area. The activated alumina-supported Ag and Au nanomaterials were used for pesticide removal studies and device fabrication. Figure 2(c) shows the time-dependent UV–visible spectra of the interaction of chlorpyrifos with the supported nanoparticles of Ag.[18] Complete uptake of the pesticide by the supported nanoparticles occurs after 10 h of their interaction. This kind of an approach was used for column studies in which the nanoparticle loaded alumina was loaded in a column. Pesticide-spiked water was passed through at 50 ppb concentration and complete removal was detected using gas chromatography using electron capture detection. Taking data from such studies, we devised a filter (Fig. 2(d)), which is now in the market as part of a domestic water purifier.

3.2. *Interaction of biomolecules with nanoparticles-formation of nano–bio conjugates*

Nano–bio conjugates represent a class of interesting materials having widespread applications in gene and drug delivery. A study of chemical interactions of biomolecules with nanosurfaces is important as the conformations and hence the biological activity of the biomolecules could be modified by the interactions. We have investigated the chemical interactions of biologically important molecules such as Cyt *c*, hemoglobin (Hb) and myoglobin (Mb) on Au and Ag nanostructures resulting in the formation of nano–bio conjugates.[19,20] In order to study the interaction of the protein and the effect of such interactions on the functions of the active site, a model system, namely hemin was used. In the case of Au, experiments were conducted with ∼15 nm particles, whereas for Ag, ∼ 4 nm (hereafter Ag(I)) and ∼ 70 nm (hereafter Ag(II)) particles, synthesized by standard methodologies, were employed. Figure 3 shows UV–visible traces of the nano–bio conjugates of hemin with Au (Fig. 3(a)) and Ag (Fig. 3(b) and Fig. 3(c)). Both the Ag nanoparticles showed more aggregation tendency after hemin binding compared to the Au nanoparticles owing to the presence of carboxyl groups in hemin (Ag has more affinity towards –COOH groups), which make particle interlinking feasible. On the other hand, the surface plasmon feature of Au is well defined even after hemin binding, the corresponding feature of Ag is broadened, indicative of aggregation due to greater interaction between particles. The peak maxima of Ag(I) and Ag(II) particles are shifted to higher and lower values as a result of the interaction. Figure 3(d) shows time-dependent UV–visible traces of the interaction of Ag(I) with hemin, the traces being taken at an interval of 10 mins. Shape changes in the surface plasmon band indicate the formation of aggregates of the nano–bio conjugates.

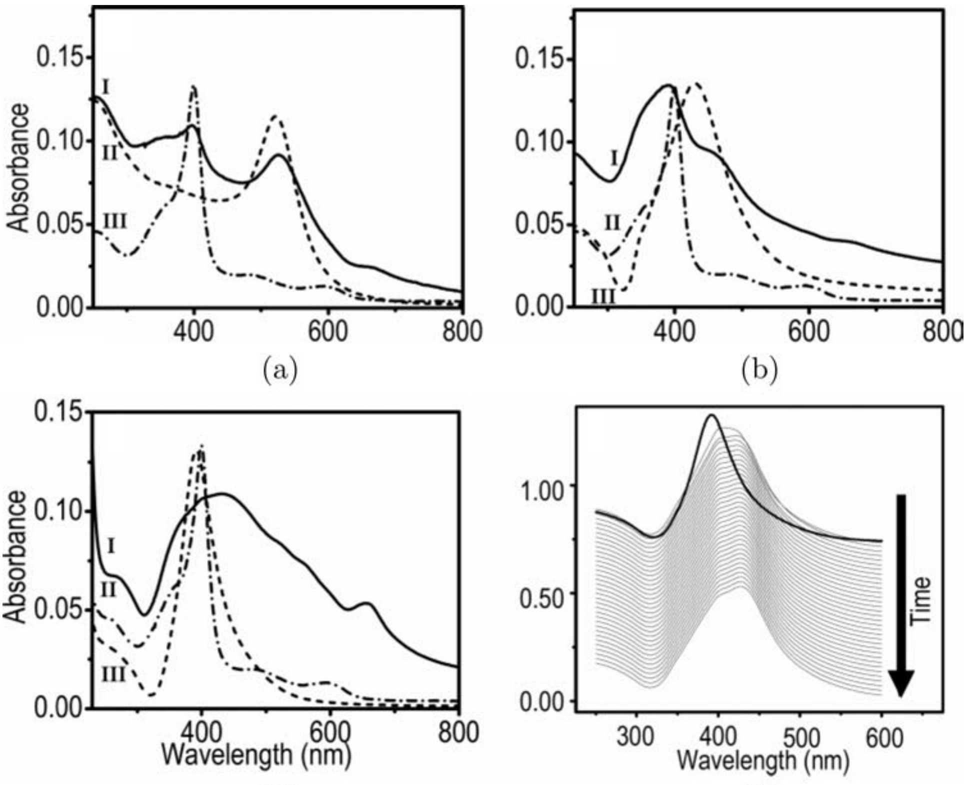

(a) (b)

(c) (d)

Fig. 3. (a–c). UV–visible spectra of Au, Ag (II), and Ag (I) particles, respectively taken in 20% aqueous ethanol. Traces (I), (II), and (III) represent the Hem capped nanoparticles, M@Hem, citrate capped nanoparticles, M@Cit and 0.004 mg/mL hemin chloride, respectively. (d) Time dependent binding of Hem on Ag (4 nm) particle monitored at a time interval of 10 mins for the initial 6 h. Thick curve in (d) corresponds to the parent nanoparticle solution. Traces has been offset for clarity.

Figure 4 illustrates the absorption and emission spectra of Cyt *c* bound Au (Au@Cyt *c*, Figs. 4(a) and 4(b), respectively) and Ag (Ag@Cyt *c*, Figs. 4(c) and 4(d), respectively) nanoparticles. Traces I, II and III in Figs. 4(a) and 4(c) denote the absorption spectra of Cyt *c* bound nanoparticles, citrate capped nanoparticles (showing the surface plasmon resonance) and, pure Cyt *c* (showing a strong Soret band at 408 nm and a weak Q-band at 540 nm), respectively. The binding of Cyt *c* to the nanoparticles results in changes in the dielectric constant of the neighboring environment and hence the red-shift in the surface plasmon band. Figure 4(c) details the broadening and shift in the surface plasmon band of Ag as a result of Cyt *c* binding. Figure 4(d) shows an enlarged view of Fig. 4(c) in the region 350–480 nm, showing the shift in the peak maximum clearly. Figure 4(b) shows the fluorescence spectra of Cyt *c* and Au@Cyt *c* conjugates, respectively. The emission maxima for

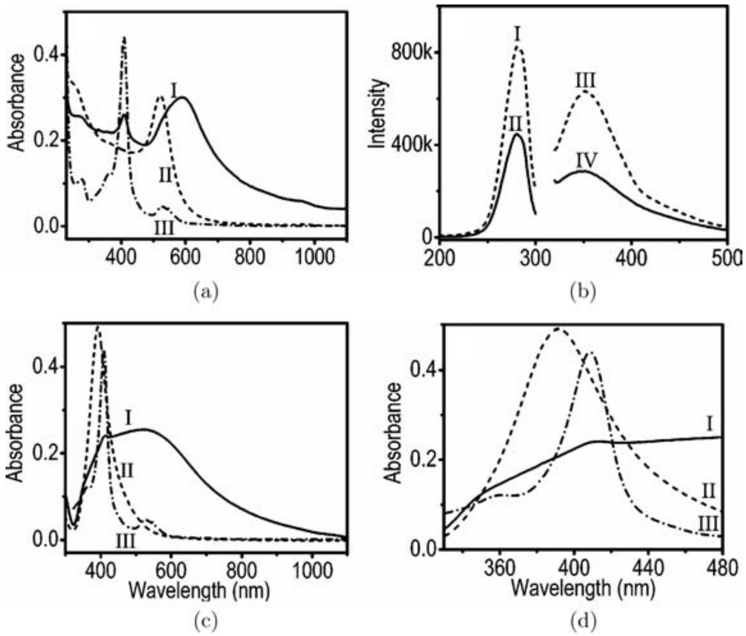

(a) (b)

(c) (d)

Fig. 4. (a) and (b) Absorption and emission spectra, respectively of the Au@Cyc system. Traces (I), (II), and (III) correspond to 0.2 mg/mL Au@Cyt *c*, 0.1 mg/mL Au@Cit and 0.1 mg/mL Cyt *c*, respectively. (B) Excitation and emission spectra of [(I) and (III)] free Cyt *c* (0.01 mg/mL) and [(II) and (IV)] Au@Cyt *c* (0.05 mg/mL) taken in water. (c) is the absorption data of the Ag(I) nanoparticle system. The traces (I), (II), and (III) correspond to similar systems as in A. (d) An enlarged view of panel C in the region, 350–480 nm.

both Cyt *c* (trace III) and Au@Cyt *c* (trace IV) are at 532 nm, and the absence of shifts in the excitation and emission features of free Cyt *c* and the conjugate indicates that the fluorophore is away from the surface of the nanoparticles. The decreased fluorescence is because of quenching of the excited flourophore by the nanoparticles. The nano–bio conjugates were characterized by TEM, IR, Raman spectroscopy and matrix assisted laser desorption ionization (MALDI) mass spectroscopy. TEM images indicated well-separated nanoparticles in the case of Au, whereas aggregated structures in the case of Ag. Infrared and Raman spectra gave spectroscopic signatures of the binding of the biomolecules on Au and Ag. Similarly, we have investigated the formation of bioconjugates from myoglobin (Mb) and hemoglobin (Hb) with Au (Au@Mb) and Ag (Ag@Mb) nanostructures. The conjugates were characterized by absorption spectroscopy. The UV–visible spectra of the bioconjugates showed the Soret band of Mb and Hb at 408 and 407 nm, respectively. The surface plasmon band of Au red-shifted from 520 nm to 543 nm and 527 nm, respectively after the binding with Mb and Hb. UV–visible spectra of Ag@Mb and Ag@Hb showed broad peaks due to aggregation of the conjugates. The nano–bio conjugates formed were further characterized by TEM, IR, Raman, and MALDI techniques. TEM images showed well-separated particles in the case

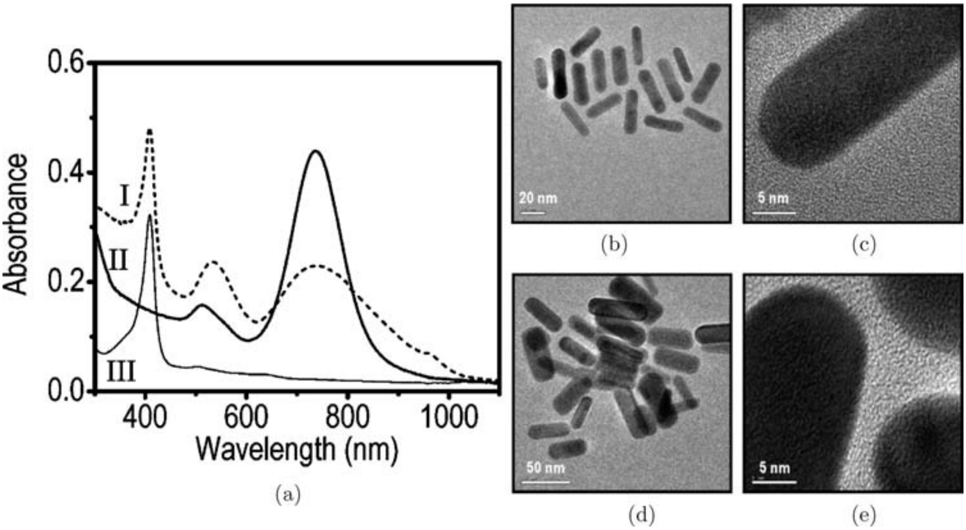

(a) (b) (c) (d) (e)

Fig. 5. (a) UV–visible spectra of AuNR@Mb (I), pure AuNR (II), and Mb(III) 0.1 mg/mL in PBS. HRTEM images of neat AuNR (b, c) and AuNR@Mb (d, e). Images (c) and (e) are lattice resolved.

of Au and aggregated structures in the case of Ag. Infrared and Raman spectra showed the spectral features of the biomolecules on the nanosurfaces. The spectral features of the biomolecules in the nano–bio conjugates were broadened and red-shifted compared to the pure biomolecules, indicative of their surface binding.

We have also studied the conjugate formation of Mb with Au nanorods (AuNR@Mb). This is shown in Fig. 5. Traces I and II correspond to the absorption spectra of AuNR@Mb and pure AuNR solution, respectively (Fig. 5(a)). The AuNRs show two absorption bands at 510 and 736 nm, respectively, corresponding to the transverse and longitudinal plasmons (trace II). After binding to Au, the surface plasmon bands are shifted to 534 and 740 nm, respectively. The dampening and broadening of the longitudinal plasmon is due to aggregation of the nanorods as a result of biomolecule binding. This is further illustrated in the HRTEM images (Figs. 5(b)–5(e)). Figures (5(b), 5(c)) and (5(d), 5(e)) show the TEM images of pure Au nanorods and AuNR@Mb bioconjugates, respectively. As can be seen, the conjugate showed aggregate structures, further confirming the observations in the UV–visible spectra. The protein binding did not cause any change in the morphology of the nanorods, as can be seen from the high-resolution images in Figs. 5(c) (before binding) and 5(e) (after binding).

3.3. *Formation of nanomaterials-polymer composites*

Nanomaterials–polymer composites provide enormous flexibility in devising smart materials with advantageous optical, electrical and mechanical properties. We have explored the possibility of making nanoparticle–polymer composites by single and multi-step methodologies. Our investigations revealed that benzylthiocyanate polymerizes on Ag nanoparticle surfaces to give a nanoparticle–polymer composite (hereafter Ag@PBT) at room temperature.[21] The Lewis acidity of the Ag^+ ion was used to initiate the polymerization reaction. The composite formed was characterized by spectroscopy and microscopy. We also tried to tune the optical properties of the core–shell material by increasing the shell thickness. This was achieved by starting the reaction with a larger concentration of benzylthiocyanate. As expected, the plasmon position showed a red-shift with increasing the thickness of the shell. The surface plasmon is very sensitive to the core radius and shell thickness. Since the core size remains invariant, the growth of the shell around the silver core is the main reason for the red-shift observed in the UV–Vis spectrum. The robustness of the polymeric shell for ion permeability was checked by treating the core–shell material with cyanide ions. The shell did not allow the ions to permeate and react with the metal core. This is shown in Fig. 6(a). Up to 2 mM CN^-, the core was stable. However, at larger ionic concentration, the core is completely destroyed within several minutes. The gradual build up of a thick polymeric shell around the nanoparticles' surfaces caused a red-shift in the surface plasmon peak to higher values. The new position of the surface plasmon peak coincides with the wavelength of the laser line used to measure the Raman spectrum leading to a resonance enhancement in the Raman signal. The Raman spectrum of the composite measured using the resonance enhancement is shown in Fig. 6(b). The intense Raman line at 1600 cm^{-1} due to –C=N– was used to image the material. The Raman image generated using the 1600 cm^{-1} line is shown in the inset of Fig. 6(b). Since the Raman imaging is a

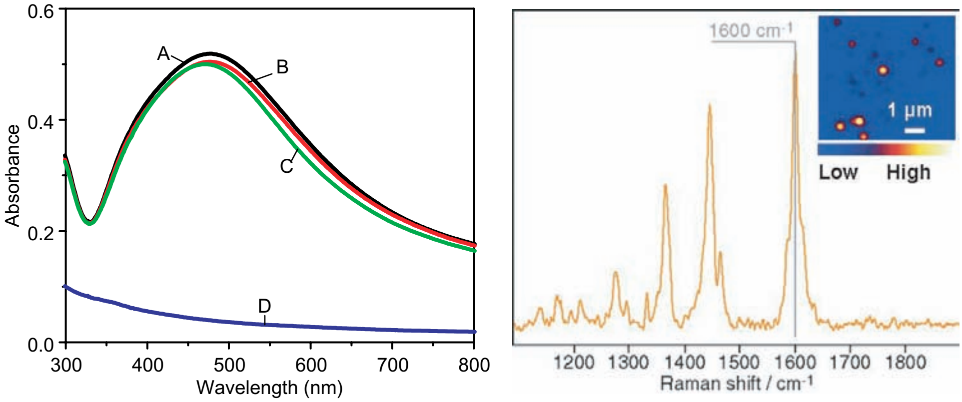

(a) (b)

Fig. 6. (a) UV-vis spectrum of Ag@PBT treated with cyanide in water- isopropyl alcohol mixture. The silver core remained stable even for a day in 2 mM NaCN. Curve A indicates the UV–vis spectrum of Ag@PBT in water-isopropyl alcohol mixture. Curve B is the UV–vis spectrum of Ag@PBT measured 1 h after the addition of 2 mM CN and curve C is after 24 h. Curve D is after adding 10 mM $NaCN^-$. (b) shows the Raman spectrum of Ag@PBT. Inset shows Raman image of the material generated by summing up the intensity at 1600 cm^{-1}.

low-resolution technique, it was not possible to image the core–shell geometry of a single particle. However, the image showed aggregates of core–shell structures. The intensity was maximum at the center of the aggregate and fading away as we move to the periphery of the aggregate, which is expected for a collection of particles. Protons generated from the conversion of isopropyl alcohol to acetone via the formation of ketyl radicals are supposed to bring about the polymerization of benzyl thiocaynate.

Functional polymers such as poly(N-isopropyl)acrylamide (PNIPAm) can be used to incorporate metal nanoparticles inside them. Such polymers can form large particles of well defined shape. We have succeeded in making gold nanorod patterns using PNIPAm microgels by a template assisted method.[23] CTAB-capped Au nanoparticles were used as seed particles to grow nanorods over the microgel particles. 2 mL of the purified microgel dispersion was mixed with the same volume of the nanoparticle seed solution and left undisturbed for adsorption for sufficient time. The nanoparticle-adsorbed microgel, removed by centrifugation, was analyzed by absorption spectroscopy and TEM. The seed loaded microgel was kept in a growth solution containing 40 mL of 100 mM CTAB, 1.7 mL of 10 mM $HAuCl_4 \cdot 3H_2O$, 250 μL of 10 mM $AgNO_3$ and 270 μL of 100 mM ascorbic acid. This results in the growth of nanorods on the surface of the microgels. The nanorod-coated microgel was separated by centrifugation and analyzed by spectroscopy and microscopy. The microgel structures showed a larger population of nanorods at the periphery as the TEM image is a two-dimensional projection. A large area image of the nanorod-loaded microgel is shown in image (I) of Fig. 7(a). Image (II) shows a single microgel decorated with nanorods. A high-resolution image of an adsorbed nanorod is shown in (III). We allowed the microgel to self assemble by keeping the same in water for two days. The UV–visible spectrum of the material showed transverse and longitudinal plasmon bands of nanorods, which are red-shifted compared to the nanorod-coated microgel due to greater interaction between the nanorods in the self-assembled structure. A large area image of the hexagonal pattern is shown in the image (I) in Fig. 7(b). In the self-assembled pattern, each microgel particle was surrounded by six others. A large area image of the hexagonal pattern with the defect sites marked with white circles is shown in the image (iii) in Fig. 7(b). A schematic of the self-assembly is shown in Fig. 7(c). The spherical microgel particles change to hexagonal in shape during self-assembly to fill the voids. The material showed regions with the absence of nanorod marking. The polydispersity of the prepared microgel contributed to defects.

We have found that redispersible nanocomposites of gold nanoparticles and nanorods could be made by using PNIPAm.[22] Trace *a* in Fig. 8(a) shows the UV–Vis spectrum of gold nanoparticle-PNIPAm hydrogel in water below the transition temperature and trace B corresponds to that of the dispersion above the phase transition temperature. Trace C is after bringing the solution back to the initial temperature. The UV–Vis spectrum of the material showed surface plasmon resonance peak around 520 nm, characteristic of gold nanoparticles. The sample above

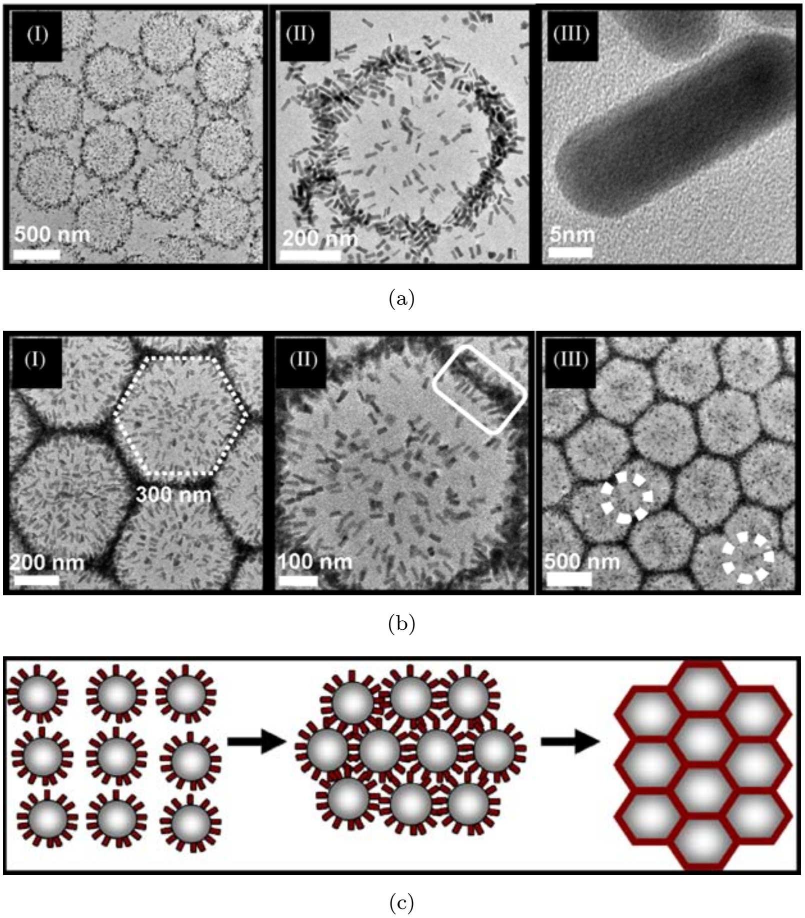

Fig. 7. (a) Image (I) shows the large area image of the nanorod-coated microgels. The decoration of microgels by nanorods at the periphery is clear in image (II). A high resolution TEM image of nanorod part of microgel is given in image (III). (b) Image (I) shows the large area image of a hexagonal pattern. The rectangle in (II) shows the largely parallel arrangement of nanorods at the junction. A large area image of the hexagonal pattern with defects is given in (III). The defect sites are shown by dashed circles. Schematic showing the formation of a hexagonal pattern by the fusion of nanorod-coated microgels is shown in (c).

the transition temperature (32°C) showed increased absorption. This is attributed to scattering due to the precipitation of the polymer from the solution. The solution after switching (25°C) came back to the initial condition, indicating the reversible nature of the switching. Photograph in the inset of Fig. 8(a) shows the color change of the solution during switching. The color of the solution changed from wine red to opaque red during the phase transition. Interestingly, the solution does not show any drastic color change, which is expected when nanoparticles aggregate. This indicates that shrinking of the gel does not reduce the inter-particle distance below the limit necessary for plasmon coupling. The switching can be repeated any number of times.

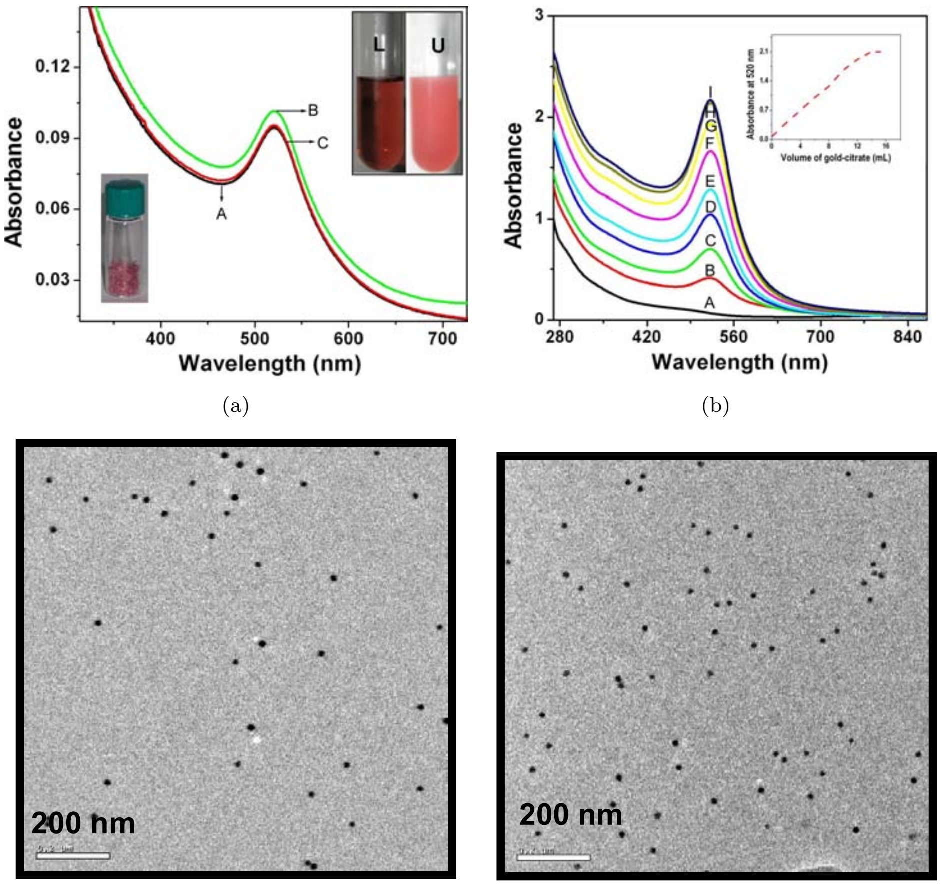

(a) (b)

(c) (d)

Fig. 8. (a) The UV–Vis spectrum of gold nanoparticle–PNIPAm composite. Trace A is before switching. Trace B is above the phase transition temperature, showing significant scattering. Trace C is after cooling the solution to room temperature, showing complete reversibility. The inset shows the photograph of the material below (L) and above (U) the phase transition temperature. Inset in (a) at the bottom left shows the photograph of the dried composite after one time loading of the nanoparticles. (b) shows the UV–Vis spectrum of the gold nanoparticle–PNIPAm composite showing the effect of loading. Traces (A–I) correspond to repeated loading of the same amount of nanoparticle with the same gel. Inset shows the intensity of the surface plasmon peak as a function of nanoparticle loading, (c) shows the TEM image of the gold nanoparticle–PNIPAm composite after first loading and (d) after saturation loading.

The bottom inset in Fig. 8(a) shows a photograph of the vacuum dried sample. To get an idea about the empty space inside the gel and to see whether the material shows any change in the electronic properties with the nanoparticle concentration, the material was loaded repeatedly with gold nanoparticles. Figure 8(b) shows the UV–Vis spectrum of the material during each loading. 2 mL of the gel was found to take up 14 mL of gold citrate solution. This material will have approximately

17.734×10^9 gold nanoparticles inside the voids. The uptake of nanoparticles into the gel (Fig. 8(c) is the TEM image of the gel after first loading of the nanoparticles) was linear and the gel showed a saturation loading as seen from the leveling of the absorbance at the plasmon peak position. As we can see from the TEM image of the gel after saturation loading (Fig. 8(d)), particles do not interact with each other. As a result, the absorption spectrum shows no shifts upon repeated loading. The same experiment was repeated with the gold nanorods. The position of both longitudinal as well as transverse peak remained the same throughout the switching even though the intensity increased, which indicates that the inter-particle interaction is very weak in the case of gold nanorod–PNIPAm composite. The switching was reversible as concluded from the position as well as the intensity of both the longitudinal and the transverse peaks. For the composite made from CTAB capped gold nanorods, saturation-loading experiments were performed. $250\,\mu$L of the as prepared gel was found to absorb $25\,\mu$L of the gold nanorod solution. This amounts to a loading of 3.07×10^{10} gold nanorods into $250\,\mu$L of the gel.

3.4. *Nanoparticle-based flow sensors-transverse electrokinetic effect*

We report the generation of a potential difference due to flow of a liquid across a metal nanoparticle multilayer assembly. The nanoparticles are self-assembled on an indium doped tin oxide conducting glass plate (ITO) by covalent interactions and characterized by UV–visible absorption spectrophotometry. A device is fabricated by arranging two ITO plates, one containing the nanoparticle assembly and the other without it, with their conducting surface facing each other. The edges are separated by a thin inert spacer so that the two conducting surfaces are not in direct contact. Electrical leads taken from the conducting surfaces are connected to the terminals of a Keithley 2700 digital multimeter for online data acquisition and storage. The schematic of the experimental setup is shown in inset (I) of Fig. 9. We find that a potential difference is generated when a liquid flows across the nanoparticle assembly. This potential difference is generated in a direction transverse to the direction of the flow. The magnitude of the potential difference is found to depend on various factors such as the flow rate, dipole moment, viscosity and ionic concentration of the flowing analyte liquid. It is also found to be dependent on the surface coverage of the nanoparticles on the ITO plate. A plot of potential difference generated for various flow rates, with water as the analyte liquid, is shown in Fig. 9. Similar calibration plots could be generated for other parameters like dipole moment, viscosity, ionic concentration and surface coverage. Interestingly, the phenomenon could be observed with other metal nanoparticle assemblies like that of silver (mean diameter 60 nm) and gold nanorods (diameter 11 nm, aspect ratio 2.8). However, nonmetallic systems such as SiO_2 assemblies failed to show this effect. Control experiments done with two ITO plates neither of them containing the

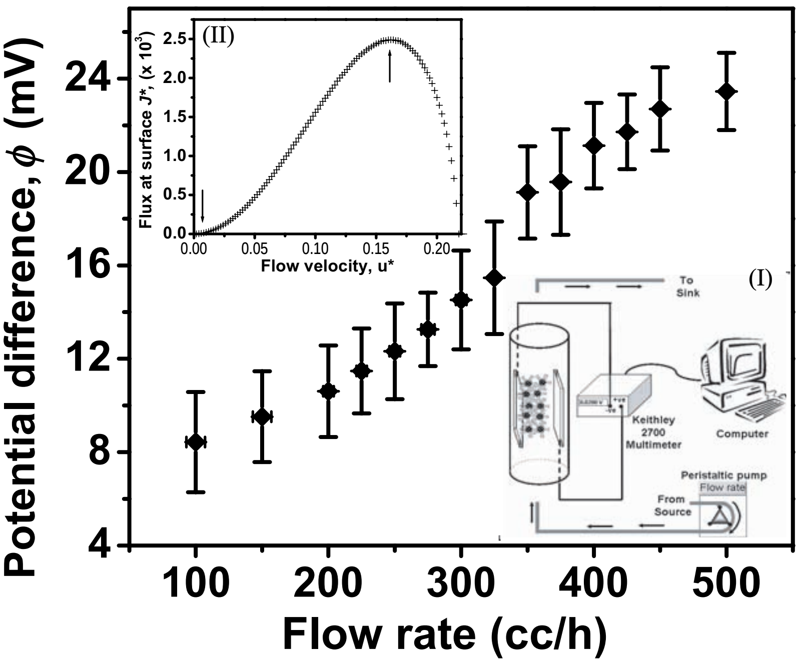

Fig. 9. Variation of potential difference as a function of flow rate for triply distilled water. Inset (I): A schematic of the experimental setup. The device is suspended inside a cylindrical glass column through which the analyte liquid is circulated from the bottom using a peristaltic pump. Inset (II): A plot of flux generated at the surface as a function of flow velocity. The arrows represent the experimentally relevant flow regime. The calculations are done in a numerical manner with dimensionless quantities.

nanoparticles, failed to produce potential difference. Efforts to measure the potential difference in a longitudinal direction (to the flow) also yielded negligible values. Potential difference could not be observed for the device suspended in still water. Through all these control experiments, we attribute this effect solely to the liquid flow across the metal nanoparticle assembly. Based on an elaborate set of experiments, a semi-classical qualitative theoretical understanding of the phenomenon is achieved.

The model considers a single isolated nanoparticle grafted on the ITO surface. The dipole of the flowing liquid interacts with the surface charges of the nanoparticle resulting in a momentum impulse and the subsequent transfer of energy from the flowing dipole to the surface charge on the nanoparticle.[31] Several such Columbic collisions cause the charge to be ejected from the nanoparticle surface with a definite kinetic energy. The ejected charges experience the effect of (a) the viscous drag of the flowing liquid, (b) the electrostatic attraction by the charged nanoparticles and (c) a steeply repulsive interaction preventing the charge from reaching the nanoparticle surface. The combined effect of all these would lead to the charge (which is solvated by the analyte liquid) reaching the surface of the ITO plate with a velocity. This velocity is used to calculate the flux of charges at the surfaces, which is proportional to the potential difference observed. The validity of this theoretical model is seen when the flux of the charges at the ITO surface is plotted as a function of the flow rate of the analyte liquid, as shown in inset (II) of Fig. 9. Excellent agreement with the experimental observation is seen, for the region marked within the arrows in inset (II) of Fig. 9. Similar agreement is observed with dipole moment and viscosity, thereby validating the theoretical model.

3.5. *Visible fluorescence from metal nanoparticle–single walled carbon nanotube composites*

We have reported that as a result of interaction between nanoparticles and SWNT to form a composite, the latter emits in the visible region of the electromagnetic spectrum. The composites, prepared by the interaction of purified SWNTs and metal nanoparticles at the liquid–liquid interface, were probed using micro Raman spectroscopy. The usual Raman modes of SWNTs like the RBM, D, G and G‘ bands were observed along with a sharp visible emission, as shown in Fig. 10. Further studies, using varying excitation sources, established the emission to be fluorescent in nature. The strong fluorescent signal allowed the spectroscopic mapping of the SWNTs present in the composite through microRaman microscopy. Transmission SNOM at sub-diffraction limits was also achieved on the composite, using the strong fluorescence signal. The fluorescence was observed for all metal nanoparticle composites such as gold nanoparticle (mean diameter 12 nm), silver nanoparticles (mean diameter 60 nm) and gold nanorods (mean diameter 11 nm, aspect ratio 2.8). However, it was not observed in pristine nanoparticles, nanorods or SWNTs. Thus, the fluorescence is attributed to the inherent states of modified SWNTs present in

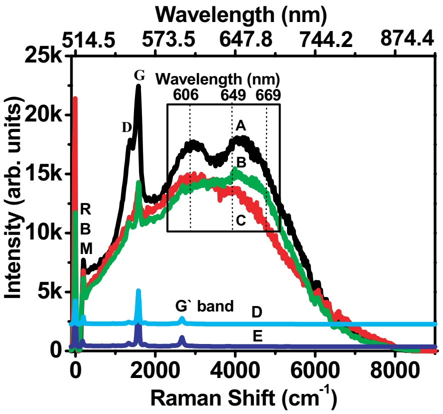

Fig. 10. Raman spectra of Ag–SWNT composite (trace A), AuNR-SWNT (trace B) and Au-SWNT (trace C) composites. Trace D and E pertain to control experiments with pristine SWNTs and SWNTs heated with tridsodium citrate, respectively. The corresponding emission wavelengths are marked. The emission maxima occur at 606 and 652 nm. The RBM, D and G bands are marked.

the composite. The discovery poses important questions about the metallic states of SWNTs, which are bound to be present in the composite.

The presence of metallic states offer nano-radiative decay channels[32] and thus the near-infrared fluorescence, normally observed in isolated SWNTs is not usually observed in SWNT bundles.[32] Therefore, a thorough investigation of the electrical properties of the SWNTs in the composite was carried out using point-contact current-imaging atomic force microscopy (PCI-AFM) and microRaman spectroscopy. Metallic SWNTs (mSWNTs) isolated from an ensemble according to established procedures[33] were used to form the composite with metal nanoparticles. The PCI-AFM images of pristine mSWNTs and the composite are shown in Figs. 11(a) and 11(b), respectively. Differential conductance plots, reflecting the

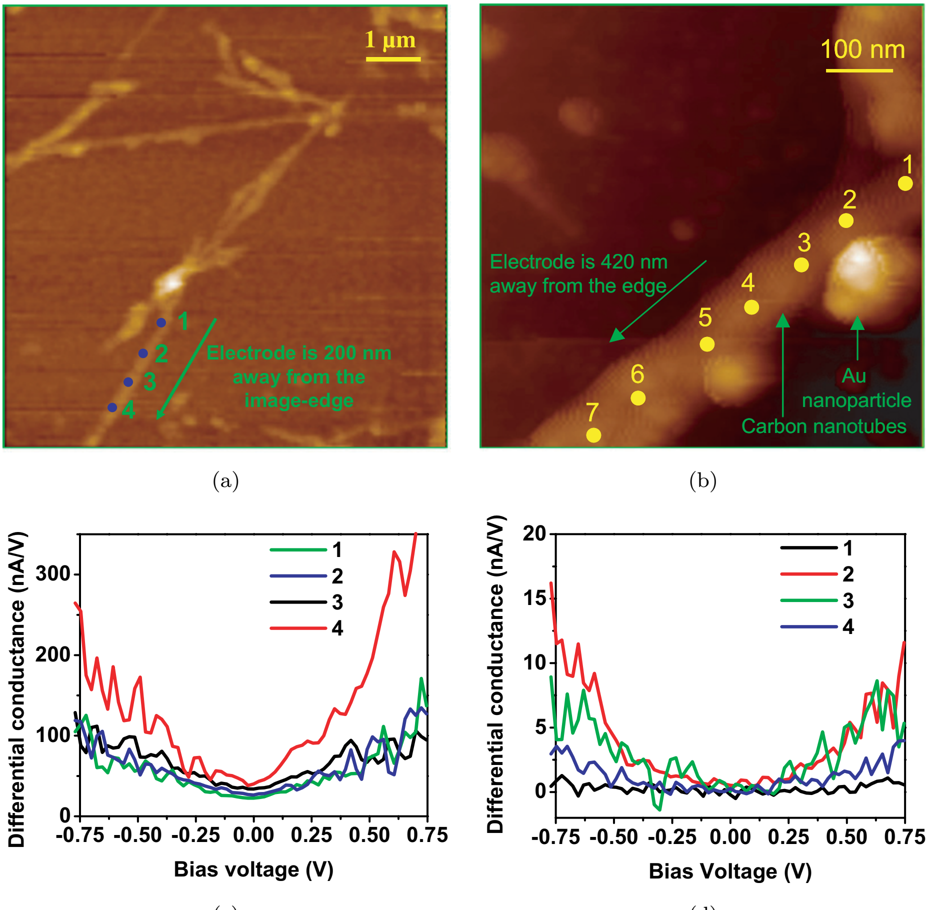

(a) (b)

(c) (d)

Fig. 11. PCI-AFM images of (a) pure mSWNT and (b) Au-mSWNT composite. The corresponding differential conductances measured at specific locations labeled 1 to 4 are shown in (c) and (d), respectively. Non-zero conductance values are seen in (c) at the Fermi point in comparison to (d) where zero conductance is seen.

density of states of SWNTs for mSWNTs and SWNT composite are shown in Figs. 11(c) and 11(d), respectively.

The conductance in the Fermi region for SWNT composite being zero, reflects the semiconducting states of the SWNTs in the composite. This is in contrast to the non-zero conductance near the Fermi region for mSWNTs, which is the starting material. Thus mSWNTs are converted to semiconducting SWNTs upon formation of the composite. Thus, a metal–semiconductor transition was observed in SWNTs due to interaction with metal nanoparticles. The nature of this interaction has been probed and established to be electrostatic in nature.

4. Conclusions

In this paper, we have reviewed our research on chemical interactions at noble metal surfaces in some detail. Simple halocarbons degrade at the surfaces of metal nanoparticles to metal halides and amorphous carbon at room temperature by a new chemistry, which offers a simple and effective methodology for environmental remediation. The new chemistry was exploited for devising a filter for the effective removal of common pesticide contaminants from drinking water. Immobilization of biologically important molecules such as hemin, Cyt *c*, hemoglobin and myoglobin on Au and Ag nanostructures lead to nano–bio conjugates and their surface binding chemistry was explored in detail. The nano–bio conjugates were characterized by spectroscopy and microscopy. Polymer–nano composites with tunable optical properties were prepared by single and multi-step methodologies and the utility of them in sensing was investigated. Smart nanogel–nanoparticle composites and nanogel–nanorod patterns were made from PNIPAM based on a template-assisted method. An array of noble metal nanostructures fabricated on conducting glass substrates showed excellent flow sensing characteristics by the transverse electrokinetic effect. Composites made from noble metal nanostructures and metallic single walled carbon nanotubes showed concomitant visible fluorescence and metal to semiconductor transition, as shown by Raman and PCI-AFM measurements.

Acknowledgements

TP acknowledges financial support from the Department of Science and Technology, Government of India for supporting his research program on nanomaterials. Renjis T. Tom and C. Subramaniam thank the Council of Scientific and Industrial Research for research fellowships.

References

1. Lu Y and Liu J, Smart nanomaterials inspired by biology: Dynamic assembly of error-free nanomaterials in response to multiple chemical and biological stimuli, *Acc Chem Res* **40**:315–323, 2007.
2. Lee BI, Qi L and Copeland T, Nanoparticles for materials design: Present & future, *J Ceram Process Res* **6**:31–40, 2005.

3. Daniel MC and Astruc D, Gold nanoparticles: Assembly, supramolecular chemistry, quantum-size-related properties and applications toward biology, catalysis, and nanotechnology, *Chem Rev* **104**:293–346, 2004.
4. Zhang WX, Nanoscale iron particles for environmental remediation: An overview, *J Nanopart Res* **5**:323–332, 2003.
5. Fan J and Gao Y, Nanoparticle-supported catalysts and catalytic reactions — A mini-review, *J Exp Nanosci* **1**:457–475, 2006.
6. Mayer ABR, Colloidal metal nanoparticles dispersed in amphiphilic polymers, *Polym Adv Technol* **12**:96–106, 2001.
7. Son S, Park IK, Park J and Hyeon T, Synthesis of Cu_2O coated Cu nanoparticles and their successful applications to Ullmann-type amination coupling reactions of aryl chlorides, *Chem Commun* 778–779, 2004.
8. Crooks RM, Zhao M, Sun L, Chechik V and Yeung LK, Dendrimer-encapsulated metal nanoparticles: Synthesis, characterization and applications to catalysis, *Acc Chem Res* **34**:181–190, 2001.
9. Rahim EH, Kamounah FS, Frederiksen J and Christensen JB, Heck reactions catalyzed by PAMAM-dendrimer encapsulated Pd(0) nanoparticles, *Nano Lett* **1**:499–501, 2001.
10. Moreno-Manas M and Pleixats R, Formation of carbon–carbon bonds under catalysis by transition-metal nanoparticles, *Acc Chem Res* **36**:638–643, 2003.
11. Stevens PD, Fan J, Gardimalla HMR, Yen M and Gao Y, Superparamagnetic nanoparticle-supported catalysis of Suzuki cross-coupling reactions, *Org Lett* **7**:2085–2088, 2005.
12. Savage N and Diallo MS, Nanomaterials and water purification: Opportunities and challenges, *J Nanopart Res* **7**:331–342, 2005.
13. Coyle S, Wu SY, Lau KT, Rossi DD, Wallace G and Diamond D, Smart nanotextiles: A review of materials and applications, *Mater Res Bullt* **32**:434–442, 2007.
14. Nair AS and Pradeep T, Halocarbon mineralization and catalytic destruction by metal nanoparticles, *Curr Sci* **84**:1560–1564, 2003.
15. Nair AS, Tom RT, Suryanarayanan V and Pradeep T, ZrO_2 bubbles from core–shell nanoparticles, *J Mater Chem* **13**:297–300, 2003.
16. Suryanarayanan V, Nair AS, Tom RT and Pradeep T, Porosity of core–shell nanoparticles, *J Mater Chem* **14**:2661–2666, 2004.
17. Nair AS, Tom RT and Pradeep T, Detection and extraction of endosulfan by metal nanoparticles, *J Environ Monitor* **5**:363–365, 2003.
18. Nair AS and Pradeep T, Quantitative extraction of chlorpyrifos and malathion from water by metal nanoparticles, *J Nanosci Nanotechnol* **7**:1871–1877, 2007.
19. Tom RT and Pradeep T, Interaction of azide ion with hemin and Cyt *c* immobilized on Au and Ag nanoparticles, *Langmuir* **21**:11896–11902, 2005.
20. Tom RT, Samal AK, Sreeprasad TS and Pradeep T, Hemoprotein bioconjugates of Au and Ag nanoparticles and Au nanorods: Structure–function correlations, *Langmuir* **23**:1320–1325, 2007.
21. Rajeevkumar VR and Pradeep T, Polymerization of benzyl thiocyanate on silver nanoparticles and the formation of polymer coated nanoparticles, *J Mater Chem* **16**:837–841, 2006.
22. Rajeevkumar VR and Pradeep T (unpublished results).
23. Rajeevkumar VR and Pradeep T, Gold nanorods grown on microgels leading to hexagonal nanostructures, *Langmuir* **23**:8667–8669, 2007.
24. Subramaniam C, Tom RT and Pradeep T, On the formation of protected gold nanoparticles from $AuCl_4^-$ by the reduction using aromatic amines, *J Nanopart Res* **7**:209–217, 2005.

25. Subramaniam C, Pradeep T and Chakrabarti J, Flow induced transverse electrical potential across an assembly of gold nanoparticles, *Phys Rev Lett* **95**:164501–164504, 2005.
26. Subramaniam C, Pradeep T and Chakrabarti J, Transverse electrokinetic effect: A potential flow sensor, *J Phys Chem C* (in press).
27. Subramaniam C, Sreeprasad, TS, Pradeep T, Pavan Kumar GV, Narayana C, Yajima T, Sugawara Y, Tanaka H, Ogawa T and Chakrabarti J, Metal–semiconductor transition induced visible fluorescence in single walled carbon nanotubes–noble metal nanoparticle composites, *Phys Rev Lett* **99**:167404–167407, 2007.
28. Rose MJ, Mac Laren I and Pradeep T, Carbon onions within silica nanoshells, *Carbon* **42**:2352–2356, 2004.
29. Rosemary MJ, Suryanarayanan V, MacLaren I and Pradeep T, Aniline incorporated silica nanobubbles, *J Chem Sci* **118**:375–384, 2006.
30. Rosemary MJ, MacLaren I and Pradeep T, Investigations of the antibacterial properties of ciprofloxacin@SiO_2, *Langmuir* **22**:10125–10129, 2006.
31. Jackson JD, *Classical Electrodynamics*, Wiley Press, New York, 1998.
32. O'Connell MJ, Bachilo SM, Huffman CB, Moore VC, Strano MS, Haroz EH, Rialon KL, Boul PJ, Noon WH, Kittrell C, Ma J, Hauge RH, Weisman RB and Smalley RE, Band gap fluorescence from individual single-walled carbon nanotubes, *Science* **297**:593–596, 2002.
33. Maeda Y, Kimura SI, Kanda M, Hirashima Y, Hasegawa T, Wakahara T, Lian Y, Nakahodo T, Tsuchiya T, Akasaka T, Lu J, Zhang X, Gao G, Yu Y, Nagase S, Kazaoui S, Minami N, Shimizu T, Tokumoto H and Saito R, Large-scale separation of metallic and semiconducting single-walled carbon nanotubes, *J Am Chem Soc* **127**:10287–10290, 2005.

DIAMOND-LIKE CARBON: A NEW MATERIAL BASE FOR NANO-ARCHITECTURES

XIJUN LI and DANIEL H. C. CHUA*

Department of Materials Science and Engineering
National University of Singapore, Block E3A, #04-10
7 Engineering Drive 1, Singapore 117574
**msechcd@nus.edu.sg*

Diamond-like carbon (DLC) is a form of amorphous carbon which has high fraction of sp^3 hybridization. Due to its nature of sp^3 bonding, diamond-like carbon has been shown to have excellent properties similar to that of diamond. This includes high hardness, excellent wear-resistance, large modulus and chemically inert. Traditional applications include wear resistant coatings and protective film. This article intends to review the synthesis and material properties of diamond-like carbon as well as its potential as a novel material for applications in nano-architecture and nano-mechanical devices. An introduction into metal-dopants in diamond-like carbon film will be briefly mentioned as well as techniques on the design and fabrication of this material.

Keywords: Diamond-like carbon; filtered cathodic vacuum arc; nano-architectures; micromechanical resonator; nanomechanical resonator; nanotechnology.

1. Introduction

Diamond-like carbon is a kind of carbon-based material, in which most of its carbon atoms are bonded in sp^3 hybridization. In the case of non-hydrogenated diamond-like carbon films, it has been widely studied in the past decades and is sometimes known as amorphous diamond (a-D), tetrahedral amorphous carbon (ta-C) and/or diamond-like amorphous carbon (DL-aC). There are several review publications on the synthesis of diamond-like carbon films,[1–6] among which the most common are pulsed laser deposition,[4–6] filtered cathodic vacuum arc (FCVA),[4–6] r.f. magnetron sputtering[7] and mass-selected ion-beam techniques.[4–6,8] The diamond-like carbon films deposited by these techniques tend to have little hydrogen (hence non-hydrogenated), amorphous with high sp^3 fraction. The films grown by FCVA are very smooth, and sometimes considered as atomically flat.[9] Through these different techniques, diamond-like carbon films can be easily deposited on the surface of many materials. In this article, we review the diamond-like carbon film deposited using the filtered cathodic vacuum arc technique.

Due to its high fraction of sp^3 bonding, diamond-like carbon has high abrasive resistance, high Young's Modulus and very high hardness, which is close to that

Table 1. A comparison of the various properties of diamond-like carbon films, amorphous-silicon and microcrystalline diamond films.

Properties	Ta-C	a-Si	Diamond
Max Mass Density (g/cm^3)	~ 3.4	~ 2.2	~ 3.5
Hardness (GPa)	~ 60	~10	110
Young's Modulus (GPa)	~ 800	~ 5.9	>1000
Optical Bandgap (eV)	>3.5	1.8	5.4
Refractive Index	2.5–2.8	4	~ 2.4
Extinction Coefficient	0.01–0.2	0.01	0.1–0.001

of diamond[1] and has excellent wear-resistance properties. Furthermore, it has an ultrasmooth surface and low coefficient of friction, thus finding niche applications as a coating material[2] especially for tribological tools, such as razor blades.[3] In addition to attractive mechanical and tribological properties, it is also chemically inert, making it a very effective high performance material for harsh environmental applications. Table 1 gives a brief review on the material and physical properties of the diamond-like carbon films.

Some of the engineering applications for these diamond-like carbon films include microelectromechanical systems (MEMS) and electron emission devices. For the former, diamond-like carbon films deposited using the filtered cathodic vacuum arc techniques gives the highest sp^3 fraction, with a density of $\sim 3.2\,\mathrm{g/cm^3}$ and Young's modulus as high as 800 GPa.[5,6] These properties indicate that micro-resonator devices made of diamond-like carbon has superior working frequency response compared to devices of similar size fabricated from other materials such as silicon,[7] silicon carbide or silicon nitride. In addition, diamond-like carbon films have been shown to be hydrophobic (more described in Sec. 3), which further gives an edge for diamond-like carbon MEMS. Frequent close contact in MEMS will create wear and tear as well as stiction. This limits the lifetime for some of the silicon-based MEMs. A comprehensive review on MEMS application can be found in Refs. 10 and 11. Other applications for diamond-like carbon devices include cold cathode material or field emission device,[12] a preservative material for beer storage,[3] coatings for biomedical tools[13] and other electronic devices.[14] In this review, some of the previous and well-known applications will be avoided. Instead, the main emphasis will be on bottom-up synthesis of diamond-like carbon based nano-architectures, and some top-down fabrications of diamond-like carbon based architectures and their applications.

2. Diamond-Like Carbon: Synthesis and Characterization

2.1. *Diamond-like carbon films by filtered cathodic vacuum arc technique*

The filtered cathodic vacuum arc (FCVA) is among the best tool used for the deposition of diamond-like carbon films.[5] The schematic diagram of the FCVA system is illustrated in Fig. 1.

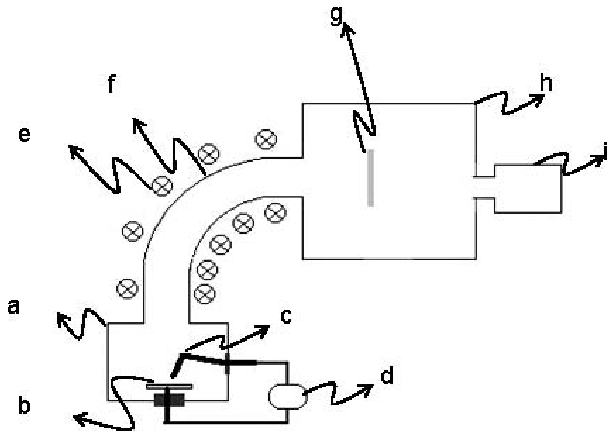

Fig. 1. Schematics of FCVA. (a) Arc chamber, (b) target on cathode, (c) anode striker, (d) arc power supply, (e) solenoid, (f) filer bend, (g) substrate, (h) substrate chamber and (i) vacuum pump.

The process to deposit diamond-like carbon films using the FCVA usually requires a pure carbon target, which is loaded in the arc chamber (see Fig. 1). The target is loaded onto a cathode and is triggered for arcing by an anode striker.

After the chambers are evacuated to a vacuum of background pressure of 10^{-5} Pa, a high current (whether direct current or pulse) is applied to the target through the striker. Both carbon ions and micro/macro carbon particles are generated in the arc. The carbon ions are directed by a magnetic field generated by a solenoid around the bend onto the substrate in another vacuum chamber where the thin film is deposited while the mico/macro particles follow a line-of-sight direction and are usually filtered off in the filter bend. For more information on the history and development of the FCVA as well as various thin film applications, good reviews were previously reported in Refs. 6 and 15.

2.2. *Material properties of diamond-like carbon films*

This section shows various characterization techniques of how the general material properties were obtained. Among the common properties include the composition i.e. sp^3 and sp^2 bonding fraction, its surface morphology, cross section morphology, microstructural and various mechanical properties, such as modulus, hardness, density and coefficient of friction. These properties are needed as part of the nano–mechanical device design and system improvement. Common material characterization facilities, such as scanning electron microscope, transmission electron microscope, Raman spectroscopy, X-ray photoemission spectroscopy, atomic force microscope and mechanical properties test tools, such as micro scratch test, nanoindenter can be used to study the film.

2.2.1. *Composition and determining the sp^3 content*

sp^3 and sp^2 bonding fractions in the diamond-like carbon film determine the main material properties which leads to important applications. To quantify the sp^2 and sp^3 bond fraction in the film, three main techniques used are electron energy loss spectrum (EELS),[16] X-ray photoelectron spectroscopy (XPS) and Raman spectroscopy (Raman). Other techniques such as energy dispersive X-ray scattering (EDX),[17] can be used but limited to elemental analysis. Usually, EDX is incorporated in a scanning electron microscope while EELS is incorporated in a transmission electron microscope.

In EELS in a TEM, a sample is exposed to a beam of high energy electrons. Some of the electrons will undergo inelastic scattering, which means that they lose energy and have their paths slightly deflected. The energy loss will be carefully measured using an electron spectrometer and interpreted in terms of what caused the energy loss. Inelastic interactions give rise to phonon excitations, inter and intra band transitions, plasmon excitations, inner shell ionizations etc. The inner-shell ionizations are most particularly useful for detecting the elemental components of a material. For example, in the case of carbon, a larger number of electrons with energy less than 285 eV come through the material than those with energy higher than 285 eV because 285 eV is the energy required to remove an inner-shell electron from a carbon atom. In addition to chemical composition, EELS is capable of measuring chemical bonding, valence and conduction band electronic properties, surface properties and element-specific pair distance distribution functions.[17] One advantage of EELS lies in its ability to clearly detect the differences among diamond, graphite and amorphous carbon through the anti-π bonding orbital. An example of EELS spectrum of a high-sp^3 fraction diamond-like carbon is shown in Fig. 2. The way to analyze the EELS data was by taking the area of the $1s$-π^* peak and comparing it with the total area of the carbon K-edge.[18,19] The peak at 285 eV is due to electronic excitations from the ground state $1s$ core level to the vacant π^*-like states. Excitations to higher lying σ^* states occur above 290 eV. To estimate the sp^3 fraction, it is assumed that the ratio of the integrated areas under the energy windows around the π^* peak and around the σ^* edge is proportional to N_π/N_σ. This gives the fraction of sp^3 bonding of the films and has approximately $\sim 85\%$ or more of sp^3 fraction. In general, XANES (X-ray absorption near-edge spectroscopy) gives similar information as that of EELS and they are comparable to each other.

Raman spectroscopy is based on the Raman effect. The Raman effect comes about when a monochromatic light incident onto a material specimen scattering the light at frequencies that are different from the incident frequency. This phenomenon results from an interaction between the incident photons and the vibration energy levels of the molecules. Usually for diamond-like carbon films, the Raman spectra can be fitted with two Gaussian-like peaks[16,20] as shown in Fig. 3(a). The positions and line widths of the deconvoluted D and G bands give an approximation for

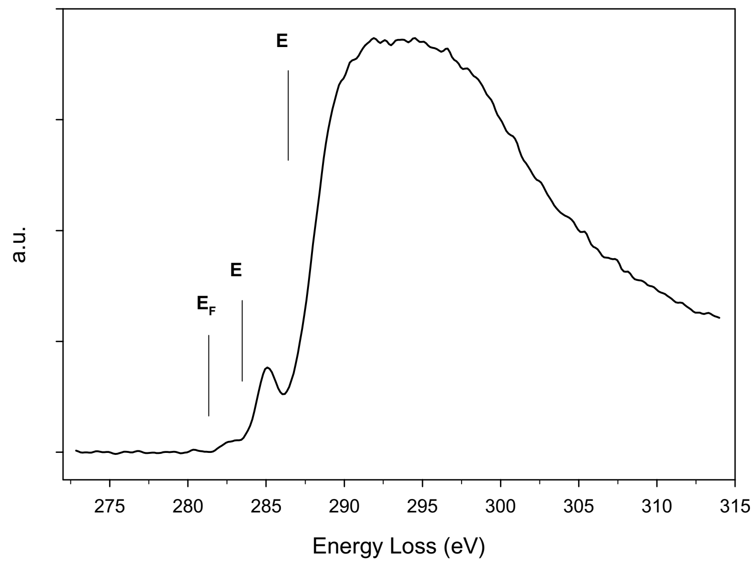

Fig. 2. EELS spectra of a diamond-like carbon sample. The low intensity of the $1s$-π^* peak confirms that the DLC film has high sp^3 content.

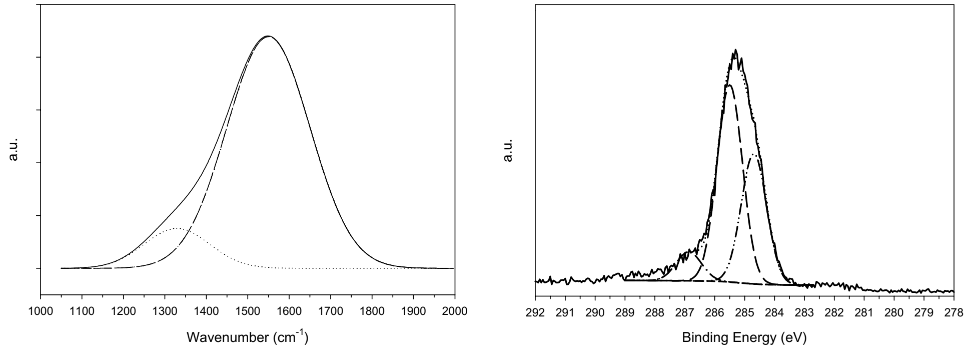

(a)

(b)

Fig. 3. (a) Raman shift and (b) deconvoluted XPS of diamond-like carbon sample.

the sp^3 fraction in the thin films. The G-peak was assigned to $\sim 1550\,\text{cm}^{-1}$ while the D-peak was assigned to $1330\,\text{cm}^{-1}$. Usually, the D-peak was nearly negligible indicating a low degree of sp^2 clustering and no short sp^2 chains existed in the films.

X-ray photoelectron spectroscopy (XPS) is among the most essential technique for detecting the elements and the bonding states on the surface of the materials. This method uses X-rays to excite core-shell electrons and the energy of the core-shell will shift depending on chemical state of the atom. In Fig. 3(b), the XPS spectra of diamond-like carbon film is shown and deconvoluted according to its sp^3/sp^2 content. It has further been shown that the ratio of peak areas at 285.39 eV and 284.29 eV, which correspond to sp^3 and sp^2 ratio, can be used to determine the sp^3 fraction.[21]

Various researchers have shown that there is a good correlation between all these three main techniques, XPS, Raman and EELS.[5,18,21] This indicates that it can analyze and give a good indication of the sp^3 fraction in any diamond-like carbon films with negligible uncertainty by one of these techniques only. In the example shown above, Figs. 2 and 3 showed a sp^3 fraction high than 85% DLC films.

2.2.2. *Intrinsic stress of diamond-like carbon films*

It is believed that the high sp^3 fraction of the diamond-like carbon films grown by FCVA gives the films high intrinsic residual stress. This intrinsic residual stress can be higher than 10 GPa[22] and can limit the film thickness to a hundred nanometers or so when growing on a silicon substrate. In the fabrication of nano-architectures of diamond-like carbon, it is essential to have stress-free films. Without controlling the residual stress, the film thickness on silicon substrate is only limited to several tens of nanometers which is not thick enough for designing a practical nano-architecture.

There are several ways to control the residual stress of diamond-like carbon film on silicon substrate, such as doping the target carbon material with metals,[23–26] or rare-earth metal oxides,[27,28] or proper voltage bias[29–31] to the substrate (substrate biasing) during arc deposition. It is also known that metal doped targets for the cathodic arc usually gives a nanocomposite film of metal nanoparticles dispersed into diamond-like carbon medium instead of pure diamond-like carbon film. More will be explored and discussed in Sec. 3 of this review.

Another way of controlling residual stress is through applying a substrate bias during film deposition process. There are two kinds of voltage applied to substrate to reduce the residual stress of diamond-like carbon film on silicon substrate. One is to apply a short pulse of high voltage higher than thousand volts to the substrate during arc. This method increases the energy of the carbon ions which in turn, increases its penetration depth for a subsurface growth mechanism or sub-plantation model.[32] This technique is sometimes called plasma ion immersion implantation (PIII). The other is to apply a dc voltage to the substrate during arc growth of the diamond-like carbon film. Usually, voltages as low as 500 V are sufficient enough to grow a residual stress-free diamond-like carbon films by this method. However, this method also reduces the sp^3 fraction of the film. Though the exact stress suppression mechanism is not well known, it was found that a high dc voltage could change the residual stress of diamond-like carbon of compressive stress at 0 V to tensile stress at voltages over 300 V.[33]

Diamond-like carbon with low compressive stress can be grown to a thickness of 2 μm in 30 minutes which is one of the requirements in micro–nano-fabrication process. In our research, we did not find the evidence of layer growth[33,34] in our thick diamond-like carbon films. The films thickness obtained using the dc biasing technique can satisfy the requirement of fabricating both micromechanical and nanomechanical devices.

2.2.3. *Surface morphology and surface energy*

When diamond-like carbon film with desired sp^3 fraction is applied to nanomechanical and micromechanical devices, surface morphology is a highly critical parameter which determines the device performance. The surface topography and roughness can be studied by using an atomic force microscopy (AFM). Usually for non-destructive testing, a non-contact or tapping mode at a proper scan frequency is used. The contact mode is not desirable as it may introduce scratches onto the sample surface and distort the topography.

As the films are generally very smooth, the AFM has to be suspended on an anti-vibration swing to enhance the tracking. Good tracking is important to ensure accurate images of the surfaces are captured. A surface area of 1 μm^2 free of particles is usually chosen and scanned (see Fig. 4).

The root mean square (rms) roughness of the films was recorded. A typical surface morphology of diamond-like carbon measured with AFM is shown in Fig. 4. It is clear that the surface roughness of the film is within 0.2 nm. "Pure" diamond-like carbon films have been reported to possess an rms roughness of 0.12 nm.[35] The value of 0.20 nm obtained was found to be comparable to that reported in literature. However, incorporation of metals into diamond-like carbon films is generally giving a rougher film. In fact, an increase in the metal fraction generally leads to an increase in the rms roughness of deposited films. It is believed that this trend could be explained by using the thermal spike model which describes the *in situ* deposition condition at the surface of the as-growing film when two different ions

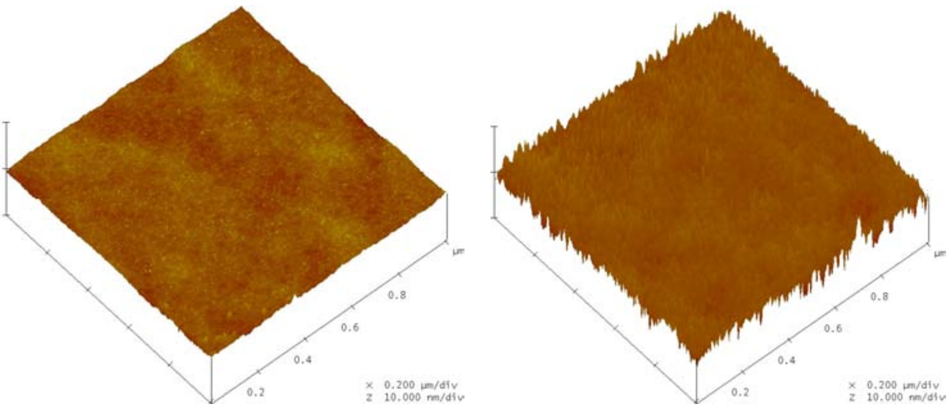

(a) (b)

Fig. 4. Surface morphology of (a) a near atomically smooth high sp^3 content diamond-like carbon film deposited at floating voltage and (b) a 1 μm thick diamond-like carbon film with 50% sp^3 fraction deposited at -800 V. The roughness is negligible.

impinge onto the surface.[36] During deposition, a small area with enhanced temperature was created on the surface as ions from the plasma impinged on it. There was no single value of temperature that could be quoted for deposition. Instead, temperature could only be understood in a local, time-dependent sense. The size of the area was determined by the collision cascades which were known to quench in some picoseconds. In the case of where biasing was added to the substrate, the surface was observed to have an increase of roughness. In the case of FVCA, the area was usually limited to a small number of atoms. The atoms were not able to move to many configurations at times within such a short thermal spike quenching time.

Studies conducted by Shi[36,37] tried to correlate the surface morphology properties to the sp^3 fraction in the diamond-like carbon films and concluded that there was an inverse relationship between rms roughness of the surface and sp^3 fraction in the films. In other words, a higher rms roughness corresponds to lower sp^2 fraction. As with the previous results from Raman spectroscopy, XPS and nano-indentation, indeed, the incorporation of metals does decrease the sp^3 fraction as the amount of metal increased.

Surface energy of the films is another important factor due to the fact that it can give some clues to the surface properties of the thin film. The correlation between contact angle and surface free energy of solid surface and liquid was provided by Young when a drop of liquid lies on a solid surface. Young's equation[38,39] is

$$\gamma_{\mathrm{sv}} = \gamma_{\mathrm{sl}} + \gamma_{\mathrm{lv}} \cos\theta, \tag{1}$$

where γ_{sv} and γ_{lv} are the solid and liquid surface energy respectively; γ_{sl} is the solid/liquid interfacial energy and θ the contact angle. The contact angle θ and the liquid surface energy γ_{lv} are measurable parameters. In order to determine the surface energy of the solid through the measurement of the contact angle, various theoretical statements describing the interfacial energy γ_{sl} as $\gamma_{\mathrm{sl}} = f(\gamma_{\mathrm{sv}}, \gamma_{\mathrm{lv}})$ were used. In this work, the harmonic-mean model was used.[40]

$$(1+\cos\theta)\gamma_{\mathrm{lv}} = 4\left(\frac{\gamma_{\mathrm{sv}}^{\mathrm{d}}\gamma_{\mathrm{lv}}^{\mathrm{d}}}{\gamma_{\mathrm{sv}}^{\mathrm{d}}+\gamma_{\mathrm{lv}}^{\mathrm{d}}} + \frac{\gamma_{\mathrm{sv}}^{\mathrm{p}}\gamma_{\mathrm{lv}}^{\mathrm{p}}}{\gamma_{\mathrm{sv}}^{\mathrm{p}}+\gamma_{\mathrm{lv}}^{\mathrm{p}}}\right) \tag{2}$$

Here $\gamma_{\mathrm{lv}} = \gamma_{\mathrm{lv}}^{\mathrm{d}} + \gamma_{\mathrm{lv}}^{\mathrm{p}}$ and the superscripts d and p refer to the dispersive and polar components respectively. When two liquids are used, and the values of $\gamma_{\mathrm{lv}}^{\mathrm{d}}$ and $\gamma_{\mathrm{lv}}^{\mathrm{p}}$ for these liquids are known, the dispersive and polar components of the solid surface energy ($\gamma_{\mathrm{sv}}^{\mathrm{d}}$ and $\gamma_{\mathrm{sv}}^{\mathrm{p}}$) can be obtained by solving the two simultaneous equations. The surface energy is a combination of these two separate components, the dispersive and polar component.

In general, the contact angle for diamond-like carbon films can range from 75° to a high of 80°, with the theoretical limit for amorphous carbon films reported to be ~80°.[19] It has been further reported that the contact angle for typical diamond-like carbon films deposited by FCVA is around 77° depending on deposition conditions.[19] The surface energy of these diamond-like carbon films has been reported to be as low as $\sim 4.0 \times 10^{-6}\,\text{Nm}^{-1}$ using multiple liquid testing.[41] The main component that affects the surface energy is the polar component, which can vary from 1.3×10^{-6} to $0.9 \times 10^{-6}\,\text{Nm}^{-1}$. It was noted that the dispersive component tends not to change. The polar component results from three different intermolecular forces due to permanent and induced dipoles and hydrogen bonding, whereas the dispersive component of the surface energy is due to instantaneous dipole moments. As diamond-like carbon films grown by the FCVA technique have little hydrogen present in the films, the polar component is due to the change of the sp^2 carbon formation and dangling bonds in the amorphous carbon network.[19] As such, the process conditions required to obtain high sp^3 fraction diamond-like carbon films probably require highly dense plasma, which in turn, will inevitably affect the surface energy as the confinement within the same unit volume may cause a significant reduction in the dangling bonds or other defect sites due to the decrease in surface energy.

2.2.4. *Mechanical property measurement*

There are several ways to measure the Young's modulus of these films. One conventional technique is by nano-indentation techniques. Another technique is by laser induced surface acoustic wave (L-SAW). This laser-acoustic technique uses short pulses of a laser to generate wide-band surface wave impulses. The surface wave impulse is detected by a wide-band piezoelectric transducer. Both specimen and transducer are fixed to a translation stage that moves perpendicular to the laser beam position. The surface acoustic waveform is detected at different distances between the laser focus line and the transducer. The experimental dispersion curve is fitted with the theoretical curve to obtain the film parameters. The fit yields the Young's modulus of the film.[40,41]

The density of the films, ρ, can be indirectly deduced from the Young's modulus, E, as reported by an empirical method.[41]

$$\rho = 1.79\,[\text{g/cm}^3](1 + E/780[\text{GPa}] - (E/1620[\text{GPa}])^2). \tag{3}$$

Using this relation, the density of the thin films could be determined. This equation was derived using some test samples for which the density of the films was determined using XRR, RBS and EELS.[41]

In the case of high sp^3 fraction diamond-like carbon films, a high of $\sim 800\,\text{GPa}$ Young's modulus can be obtained. Using the empirical method described above in Eq. (3), the density of the film can be as high as $\sim 3.4\,\text{g/cm}^3$.[19] This estimated value was very close to the current reported values of polycrystalline diamond, of $\sim 3.5\,\text{g/cm}^3$. As such, it had been observed that the diamond-like carbon films possibly are very compact and stiffer with high sp^3 bond fraction.

The dynamic friction coefficient is shown in Fig. 5. The coefficient of friction for diamond-like carbon films is generally very low, with an average value of < 0.1.

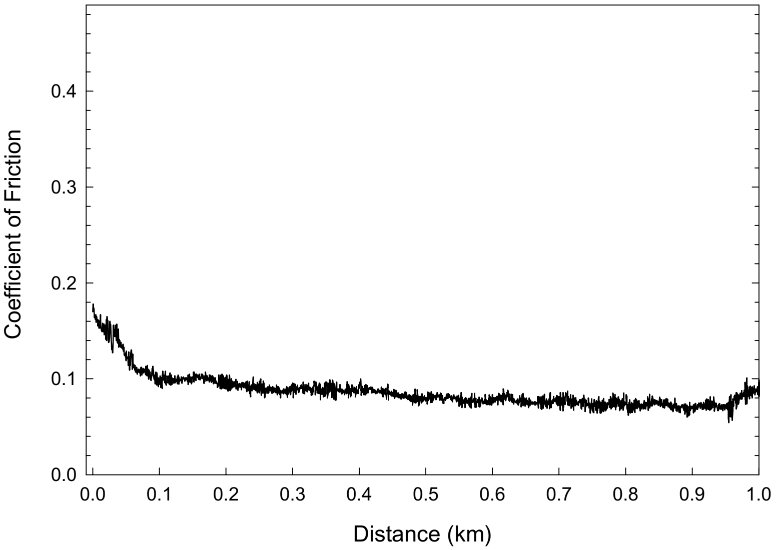

Fig. 5. COF of diamond-like carbon measured by a tribometer.

This value is very close to the coefficient of friction of graphitic (soft) films. During the process where there is mechanical contact on the surface of the diamond-like carbon films, the force (and possibly localized heat) causes the sp^3 bonds to be graphitize. As such, Fig. 5 further shows that the coefficient of friction decreases with a longer sliding distance.

The micro-scratch tests are usually carried out under a progressively increasing load from 0 to 5 N. Figure 6 shows a typical scratch test result for diamond-like carbon films deposited where a critical load of 2.1 N was obtained.[19] On the average, the critical load for diamond-like carbon films on silicon can range from ~1 to ~2 N depending on film thickness and adhesion strength. It had been previously shown that the adhesion strength depends heavily on the type of substrate used. In the case where silicon was used, a thin silicon carbide interface was formed and this enhances the interface strength. As such, diamond-like carbon film tends to form carbide bonds with metals thus making it a very suitable material for wear coating.

The wear rate of high sp^3 content diamond-like carbon films can be calculated using the relation in Eq. (4). Wear rate (k),

$$k = V/(W \times S), \tag{4}$$

where V is the wear volume (mm^3); W, the normal applied load (N); and S, the sliding distance (m). The wear rate was approximately $1.2\,(\pm 0.5) \times 10^{-8}\,\text{mm}^3/\text{N}\cdot\text{m}$ for diamond-like carbon thin films. For a thin 30 nm film, high quality diamond-like carbon films can withstand slide cycles as much as 20,000 times (~0.2 km) against a sapphire ball under a 10 N applied load in normal ambient air conditions.[19]

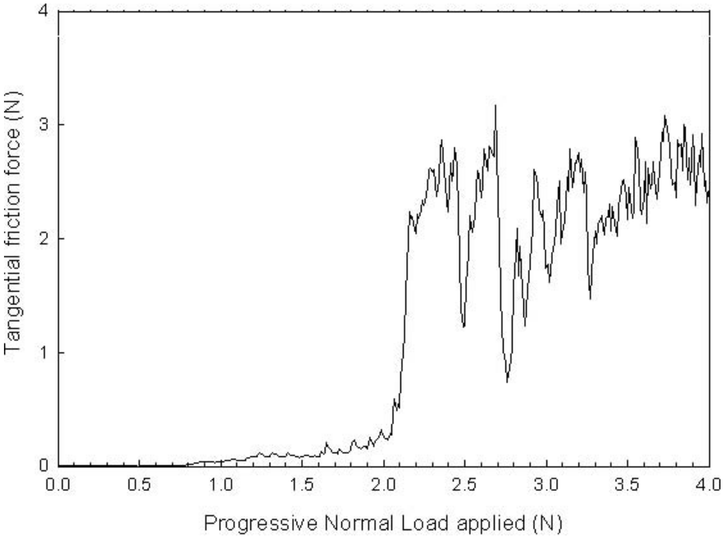

Fig. 6. Scratch test results of a typical high sp^3 content diamond-like carbon film on silicon substrate. The test was performed at room temperature, in ambient air.

3. Bottom-Up Nano-Architectures of Diamond-Like Carbon

To obtain diamond-like carbon based nano-architectures for practical applications, there are two main technological routes. One is to build architecture directly from material growth during which the architectures are defined with either little or minor treatments required. This route is usually called a bottom-up approach. The other is to start with an already-prepared material, by using the technology well-developed for microelectronics to subtract the undesired part for target architectures at nanoscale. This route is always called a top-down method. These two routes can be well described in Fig. 7. The bottom-up method applied to diamond-like carbon will be reviewed in this section while the top-down will be reviewed in Sec. 4.

Nano-architectures of diamond-like carbon fabricated with bottom-up method can be classified into different types, such as nano-architecture containing zero-dimension (0D) nano-object embedded in a diamond-like carbon sheet, nano-architecture containing one dimension (1D) nano-object embedded in a diamond-like carbon sheet or three dimension (3D) diamond-like carbon architectures at nano-scale. All these nano-architectures will be described in this section.

3.1. *Diamond-like carbon nano-architectures containing 0D objects*

Nano-architecture of diamond-like carbon containing 0D nano-objects refers to a thin diamond-like carbon sheet embedded with nano-particles of hetero-materials, such as metal, inorganic and even organic and biomaterials. Diamond-like carbon sheet embedded with 0D objects originates from metal-doped diamond-like carbon.[18,20,42] The initial intention is to reduce residual stress in diamond-like

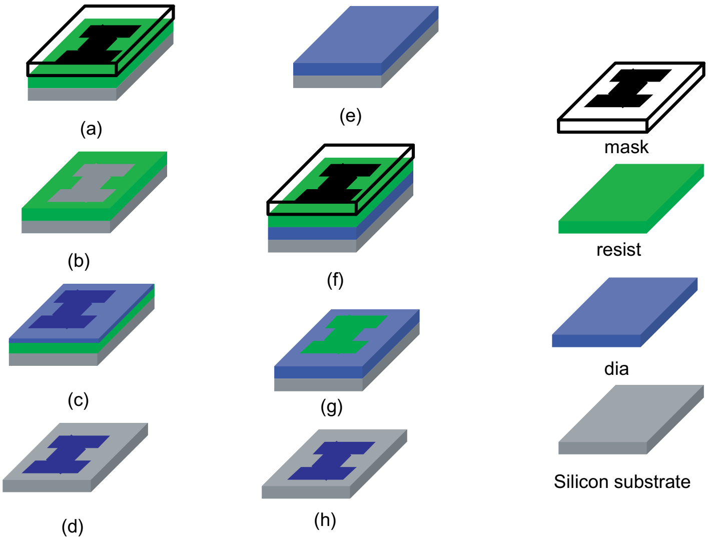

Fig. 7. Schematic diagram of (a)–(d) top-down and (e)–(h) bottom-up process for fabricating diamond-like carbon based nano-architectures.

carbon grown on silicon substrate.[42] For example, Al doping and other metal doping are found to be able to reduce this residual stress, which is harmful for fabricating free standing diamond-like carbon structures on silicon substrate. The main purpose of nano-architectures of diamond-like carbon embedded with 0D object in this review is to utilize the chemical inertness of diamond-like carbon which can be used to preserve most of nanoparticles embedded from performance degradation. Diamond-like carbon is an amorphous material, hence it has negligible or no grain boundaries in the bulk. The inter-woven network of sp^3 carbon atoms in diamond-like carbon thus prevents other atom diffusion such as gas atoms or water molecules in air moisture into grain boundaries which was found to be one of the most important hetero-atom diffusion in multi-crystalline materials. Additionally, as diamond-like carbon is a mixture of sp^3 and sp^2 hybrid carbon atoms. The sp^3 bonding in diamond-like carbon tends to open an energy band gap of diamond-like carbon while sp^2 bonded atoms tend to reduce the dangling bond in the material. A nano-object embedded in this diamond-like carbon system has less surface state which may degrade the photon emission properties.

An example of Ni nanoparticles embedded in diamond-like carbon is illustrated in Fig. 8. Particles of Ni with sizes ranging from 2 to 5 nm are clearly seen in the TEM image. These particles may have super-paramagnetic property as reported in Ref. 43. Due to the resistance of diamond-like carbon to gas diffusion into it, Ni nanoparticles can be well preserved from oxidization when exposed to atmosphere.

Nanoparticles other than metallic, like nitride, oxides and other materials can also be embedded into a diamond-like carbon sheet. Recently, Hsieh *et al.* succeeded in embedding zinc oxide nanoparticles in such a diamond-like carbon sheet by FCVA

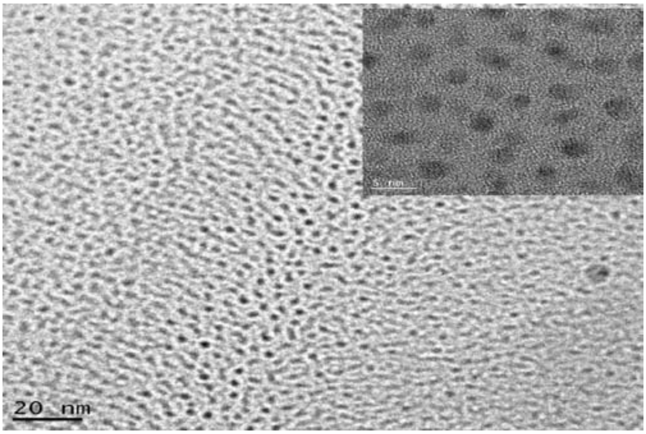

Fig. 8. TEM image of Ni particles embedded in diamond-like carbon. Reprinted with permission from Ref. 29, © 2007, Interscience.

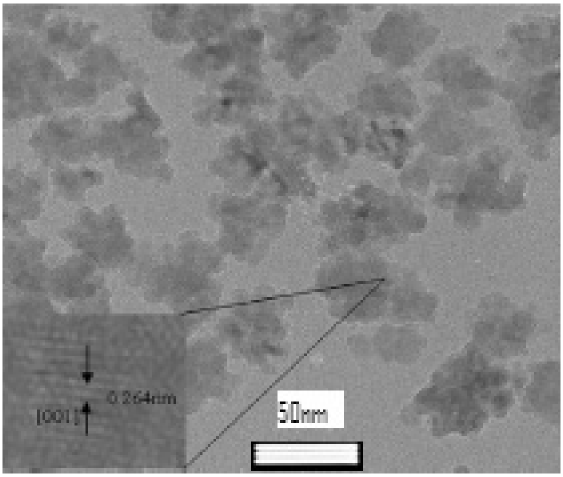

Fig. 9. ZnO embedded in diamond-like carbon. Reprinted with permission from Ref. 44, © 2008, Elsevier.

technique using a carbon target mixed with zinc powder.[44] Figure 9 shows the distribution of the particles in the diamond-like carbon medium. As described above, due to the inter-woven properties of sp^3 and sp^2 carbon atom networks, the surface state of zinc oxide can be largely suppressed and the total architecture provides better photon emission properties of zinc oxide.

Reference 44 further showed that only a narrow, near band edge emission is detected in the photoluminescence measurement. This suggests that photo-emission particles embedded in diamond-like carbon can be applied to an electroluminescent device as the active layer. An ideal device structure was schematically shown in Fig. 10, where nanoparticles of an intrinsic semiconductor material embedded in a

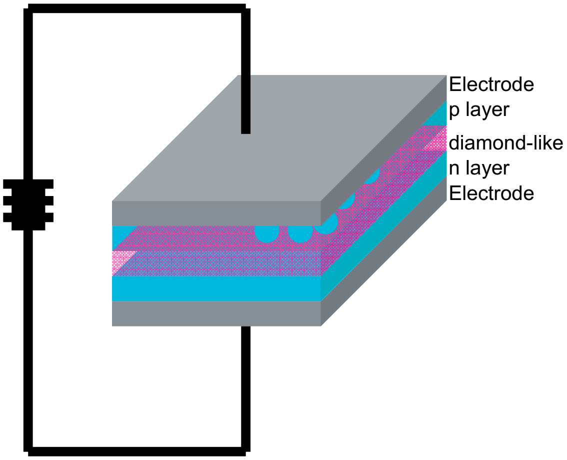

Fig. 10. A schematic view of a LED utilizing diamond-like carbon architecture as active layer.

diamond-like carbon sheet is used as the active layer. As the surface state of the semiconductor nanoparticles can be largely reduced, narrower spectrum emission or pure color can be expected from these emission devices. As the band gap of diamond-like carbon matrix can be increased to 5 eV[45] by nitrogen doping, thus this device configuration can be applied to UV light emission electroluminescent devices.

One of the open issues that needs to be addressed is that, at present, the embedded 0D nanoparticles are produced by mixing fine metal powder with carbon to make a target for nano-architecture growth. This method is acceptable when the metal powder is inexpensive. The material usage rate in FCVA arc is usually less than 1%. That means most of the metal will be lost in the process of FCVA growth of diamond-like carbon architecture. It may be a serious issue when more expensive metal powder is used. For each carbon target mixed with metal powder, the nanoparticle concentrate in the diamond-like carbon nano-architecture is also fixed. Many different targets are required to study the particle concentration effect reliably in nano-architectures.

3.2. *Diamond-like carbon nano-architectures containing 1D nano-objects*

Another diamond-like carbon based nano-architecture is to utilize 1D nano-objects, such as nanotubes, nanowires, nanorods. An example is shown in Fig. 11. From the figure, it is clear that a diamond-like carbon sheet of around 5 μm is grown on the top of a carbon nanotube layer. This nano-architecture shows tunable damping properties depending on the density and height of the carbon nanotubes. The system in Ref. 46 may be used in future nanomechanical system. The fabrication process is to grow a layer of vertically arranged carbon nanotubes with plasma assisted

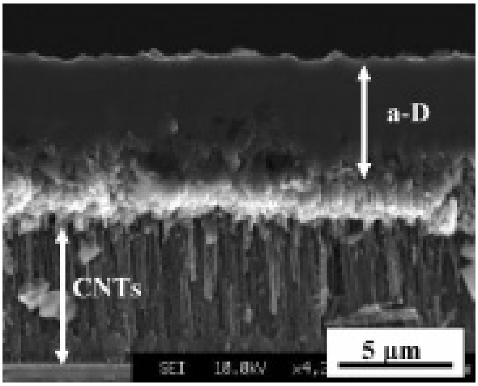

Fig. 11. Diamond-like carbon nano-architecture containing a carbon nanotube layer. Reprinted with permission from Ref. 46, © 2007, Wiley.

chemical vapor deposition (PA-CVD) followed by depositing a layer of diamond-like carbon with filtered cathodic vacuum arc (FCVA). The details of the process can be found in Ref. 46.

In this nano-architecture, as the diamond-like carbon layer is grown on the top of carbon nanotube, the diamond-like carbon layer is expected to have negligible residual stress, and thicker diamond-like carbon films can be grown without caring about the residual stress. Contrary to this multi-layered nano-architecture containing 1D nano-objects, 1D nano-objects can be embedded in the diamond-like carbon sheet too. The proposed diamond-like carbon nano-architecture is illustrated in Fig. 12(a).

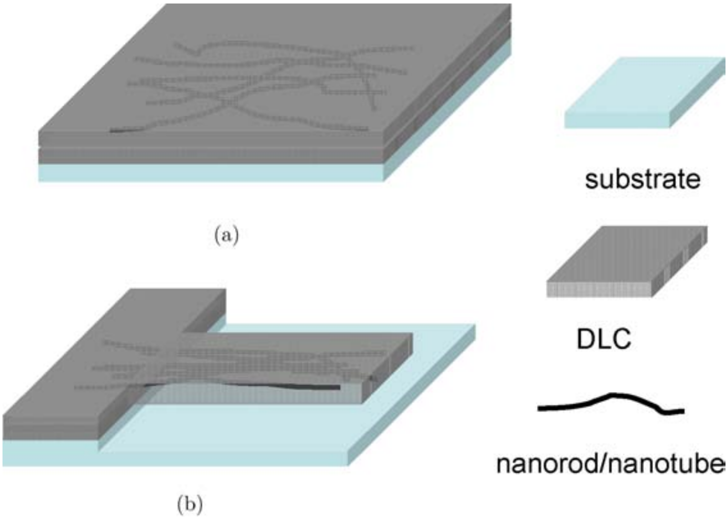

Fig. 12. Nano-concrete of diamond-like carbon.

By first growing a thin diamond-like carbon layer on a substrate, 1D nano-objects, such as nanotubes are then dispersed on the diamond-like carbon plane. This dispersion process can be spin coating or others and is then followed by growing of another layer of diamond-like carbon. This nano-architecture gives us an image of concrete at nano-scale. A diamond-like carbon sheet is usually deposited on a silicon substrate and has a high residual stress due to the lattice mismatch between silicon and carbon. This residual stress sometimes breaks the nano-architectures fabricated on a silicon substrate when the architecture is to be relieved from the substrate.[10,11] A resonator device, as illustrated in Fig. 12(b), made up of the proposed diamond-like carbon nano-architecture as shown in Fig. 12(a) can be fabricated with the top-down technologies. High working frequency for the resonator made of this kind is expected to be made of nanotubes which have higher vibration modes. Additionally, devices made of this nano-concrete may possess higher mechanical toughness as expected from the toughness enhanced in concrete used in our buildings.

3.3. *Diamond-like carbon nano-architecture grown with focused ion beam*

Focused ion beam assisted growth of diamond-like carbon from an organic precursor is an offspring of ion beam assisted chemical vapor deposition technology. Due to the tiny beam diameter of a focused ion beam, direct growth of diamond-like carbon nano-architectures is possible. As the beam can be well controlled in a two dimensional mode while the sample stage can move in the third one independently, full three dimensional nano-architectures can be well fabricated. The main fabrication process is illustrated in Fig. 13. First, the ion beam is well focused on the sample hold onto a stage while a metal nozzle delivers gusts of carbon-rich organic gas, usually, methane (CH_4) or phenanthrene (C_4H_{10}), onto focused area. Once a carbon-rich organic molecule meets the energetic ions near the focus point, it is

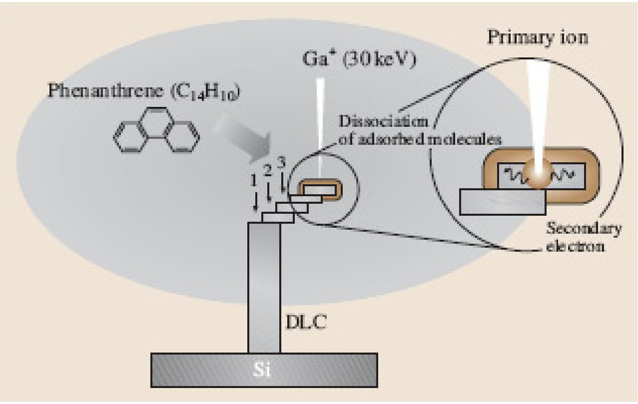

Fig. 13. Schematics of diamond-like carbon deposition by focused ion beam. Reprinted with permission from Ref. 47, © 2006, National Institute for Materials.

decomposed into volatile gases such as hydrogen and carbon ions, which will be deposited on the sample surface. This is due to the momentum of the energetic beam moving towards the sample surface is partially transferred to the decomposed carbon atom, which deflects carbon ions'/atoms' initial motion direction onto the sample surface and diamond-like carbon nano-architectures begin to nucleate and grows.

One example of the vertically standing diamond-like carbon nano-architectures grown by this method is illustrated in Fig. 14. From this figure, we can see that diamond-like carbon nano-pillars (1D diamond-like carbon architectures) can be well fabricated with a dimension down to less than 100 nm. At present, a beam size less than 10 nm in a focused ion beam can be well controlled. Thus this method is fit for fabricating fine nano-architectures. In the same figure, a scanning electron microscope modified to measure the mechanical properties is also included. By using this characterization system, a mechanical property of diamond-like carbon pillars depending on aspect ratio of the pillar is verified. This aspect ratio dependence is however not due to the intrinsic property of the diamond-like carbon nano-architectures, but instead, a novel technology.

As the beam ion used in Ref. 47 is a gallium ion, which is not volatile, upon the diamond-like carbon nano-architecture depositing on the substrate, gallium (reduced from the gallium ions) will also deposit in the pillar structure. Usually, the deposited gallium is at the center of the pillar. This metal bone usually influences the total mechanical properties of the nano-architectures.

As the present-day FIB system has very fine controllability over full space, true 3D nano-architectures of diamond-like carbon can be well fabricated. Figure 15 shows the versatility of this FIB assisted deposition of diamond-like carbon. It is

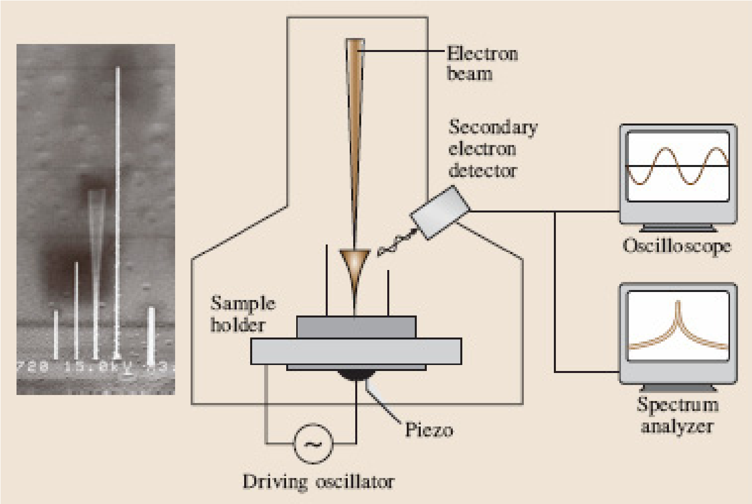

Fig. 14. Bottom-up nano-mechanical resonator and its motion detection method by SEM. Reprinted with permission from Ref. 50, © 2003, Materials Research Society.

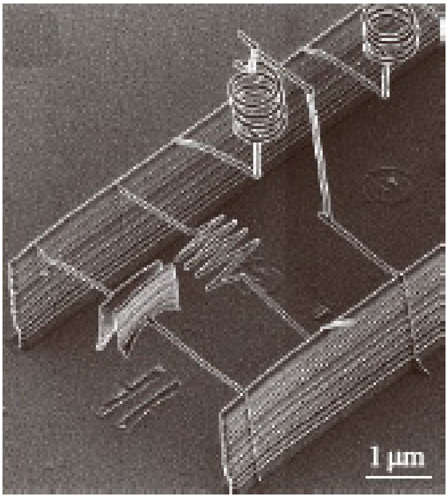

Fig. 15. More sophisticated diamond-like carbon based nano-architecture fabricated by FIB-CVD. Reprinted with permission from Ref. 47, © 2006, National Institute for Material Science.

interesting that complex three dimensional nano-architectures for capacitance, inductance and resistance woven together can be easily fabricated using this method.

Another advantage of the FIB technique is that it is a mask-less process and true bottom-up. Devices are fabricated with the help of design software in the computer which makes both design and demonstration of new ideas very efficient and economical.

Though the bottom-up nano-architecture process of diamond-like carbon by this FIB based method is a series process, which limited the technology just to a lab demonstration other than an industrial batch production, it can provide an easy design and demonstration for proposed nano-architecture. For a lab demonstration of diamond-like carbon nano-architectures, one must improve the quality of diamond-like carbon fabricated. As mentioned above, to remove residual gallium in the diamond-like carbon nano-architectures is the key issue. To solve this issue, other ion source, especially those ones which are volatile, for example, argon ion, can be used. In this case, the fabricated diamond-like carbon nano-architecture can be well free of metal doping and will provide size independent mechanical properties.

Another issue needing clarification is the reported increase of sp^3 fraction of such diamond-like carbon architectures. So far, the diamond-like carbon nano-architecture fabricated with this method has limited sp^3 fraction, as indicated by the mechanical properties reported in Ref. 19. Further discussions in Ref. 5 showed that the sp^3 fraction in diamond-like carbon films is dependent on the energy of carbon ions. In FIB–CVD deposition of diamond-like carbon of Ref. 47, the gallium ions are limited to 30 kV. By changing the acceleration voltage of the beam, the kinetic energy of the decomposed carbon can be controlled in the range where reasonable sp^3 fraction is obtainable. However, the maximum amount of sp^3 fraction is still unknown.

3.4. *Diamond-like carbon nano-architecture grown from patterned substrate*

In addition to the above-mentioned method of nano-architecture building technologies, there is another technique called architecture building from a patterned substrate. This method makes use of a different nucleation probability of carbon on different substrate to build a nano-architecture, or a different growth mechanism of diamond-like carbon on differently treated area of the same substrate. Using a structured aluminum oxide surface with different diamond-like carbon growth mechanisms, Hashimoto *et al.* reported that different diamond-like carbon nano-architectures can be obtained only by changing the substrate property.[48] As shown

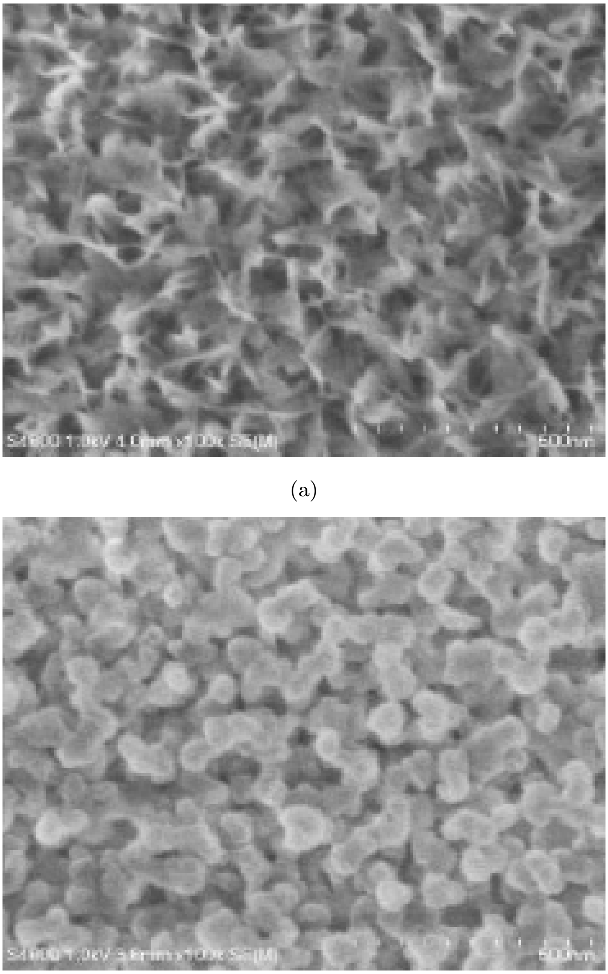

(a)

(b)

Fig. 16. Different diamond-like carbon nano-architectures obtained on aluminum oxide with different surface treatment. Reprinted with permission from Ref. 48, © 2007, Institute of Pure and Applied Physics.

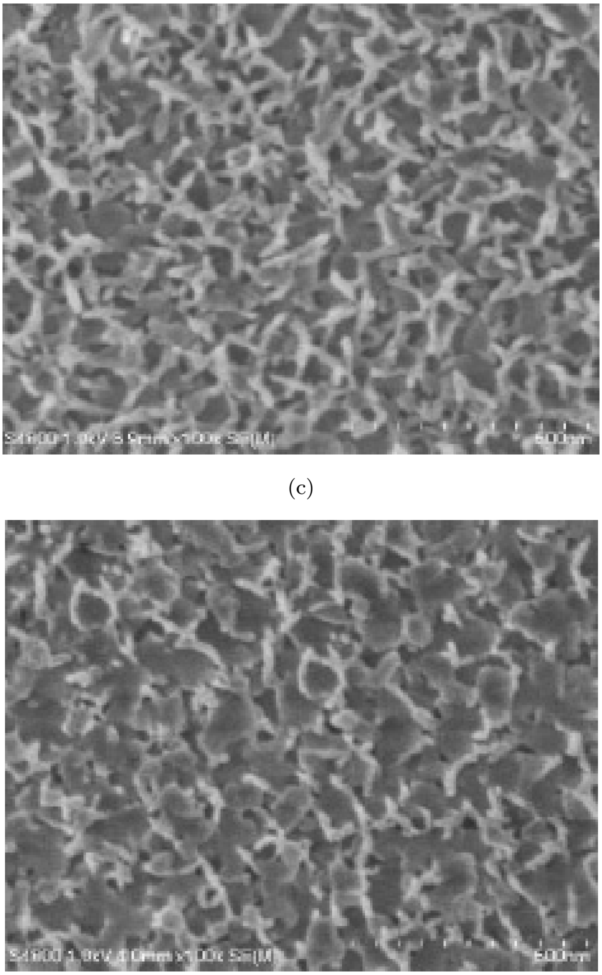

(c)

(d)

Fig. 16. (*Continued*)

in Fig. 16, different diamond-like carbon nano-architectures can be fabricated. As carbon is a good candidate material for field emission source,^{49} different field emission properties can be expected for these nano-architectures with different surface morphology. That is through micro-structuring aluminum oxide into different pattern to form patterned unit, morphology-controlled diamond-like carbon unit can be grown directly from the bottom-up method. One of this proposed unit is illustrated in Fig. 17 which is taken from Ref. 48 and synthesized.

Another bottom-up method is to cover silicon substrates with patterned lithography resist. As illustrated in Figs. 7(e)–7(h), the initial process in nanolithography (either photolithography or e-beam lithography) are defining nano-size resist patterns on the surface of silicon. Pattern developing of the resist is followed by

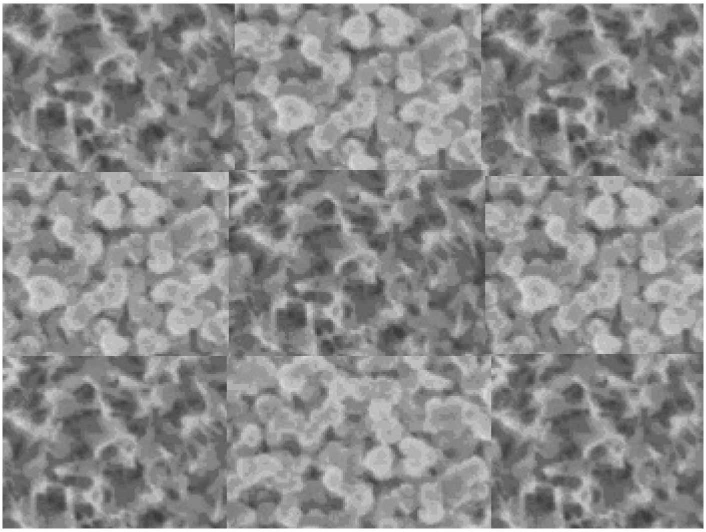

Fig. 17. A 3 × 3 unit of patterned diamond-like carbon nano-architectures composed of the DLC texture from Fig. 16. Reprinted with permission from Ref. 48, © 2007, Institute of Pure and Applied Physics.

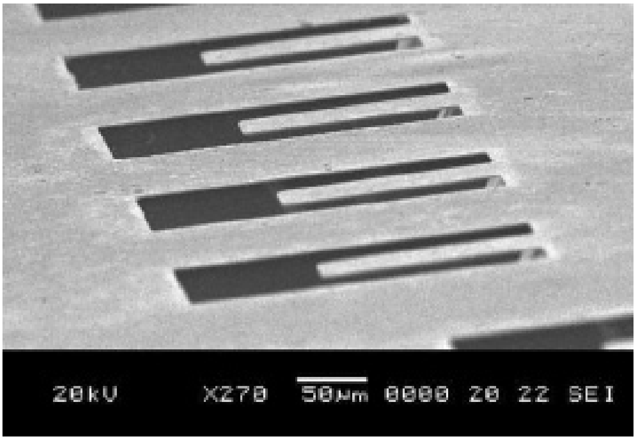

Fig. 18. Free standing cantilever with resist lift off. Reprinted with permission from Ref. 51, © 2004, American Vacuum Society.

diamond-like carbon growth.[50] Finally, lift off technique is applied to the photoresist to remove the undesired parts of diamond-like carbon on the resist from those on the silicon. One of the cantilever structures at microscale fabricated with this method is illustrated in Fig. 18.[51,52] One of the limitations of this method to fabricate diamond-like carbon nano-architectures is that the aspect ratio of the architecture is largely limited. As nano-size pattern of resist is to be developed, usually, the resist thickness is limited to less than 1 μm. The upper limit of the aspect ratio is limited to be only several. As described above, FIB–CVD is much better for developing high aspect-ratio nano-architectures of diamond-like carbon.

4. Diamond-Like Carbon Nano-Architectures from Top-Down

4.1. *Fabrication method*

The top-down method for fabrication diamond-like carbon nano-architectures (or sometimes known as subtraction method) to fabricate nano-architecture are also widely used, especially popular in the fabrication of silicon microelectronics. When applied to diamond-like carbon films, the difficulty of this method is not in the patterning but in the etching process. As diamond-like carbon is quite chemically inert, it is difficult to fabricate diamond-like carbon architectures using wet etching. Diamond-like carbon nano-architectures are only possible when dry etching process has been successfully developed for diamond-like carbon material.[53]

The top-down route for fabricating nano-architectures of electronics is shown in Figs. 7(a)–7(d); it can be well applied to diamond-like carbon. The first step is to cover the diamond-like carbon film on a substrate with a resist of proper thickness. After lithographically patterning the resist, pattern developing, dry etching and resist lift off are sequentially applied. With the recently developed oxygen ion dry etching of DLC,[53] freestanding bridges of diamond-like carbon at micrometer scale has been demonstrated as shown in Fig. 19. It is noted that the etching parameters for diamond-like carbon doped with different metals may change drastically. For

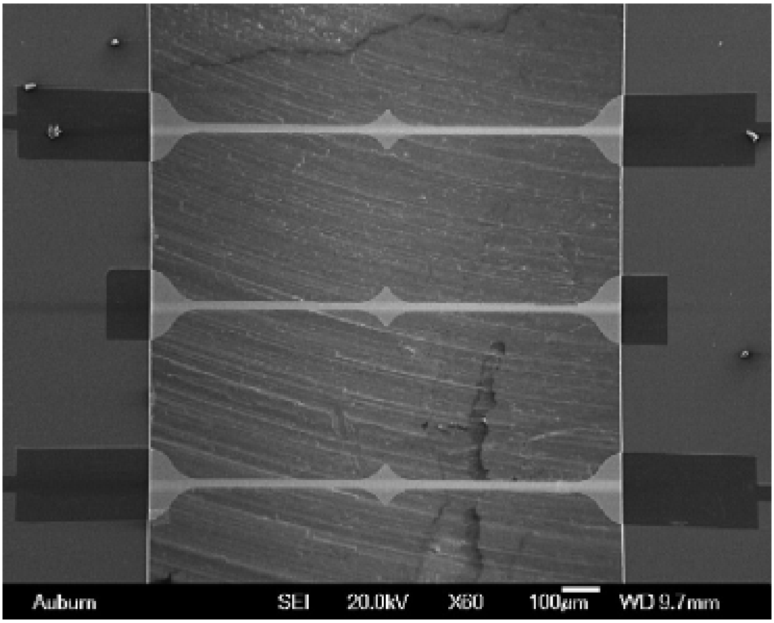

Fig. 19. Free-standing diamond-like carbon micro-bridge, from Ref. 54.

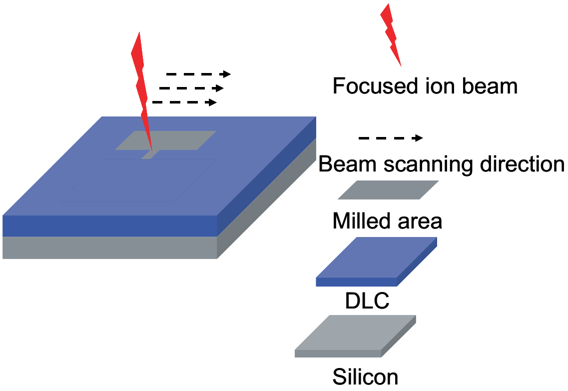

Fig. 20. Schematics diagram of FIB fabricating a nano-architecture in diamond-like carbon.

example, copper doped diamond-like carbon is harder to be etched off than Ti doped DLC.[54]

Focused ion beam milling is widely used in the field of material science[55,56] as a tool for preparing high quality transmission electron microscope (TEM) sample lamellae. This technique utilizes a focused ion beam to mill material other than to deposit in a FIB–CVD method. FIB can also be applied in fabricating diamond-like carbon nano-architectures by using its milling ability, as illustrated in Fig. 20. By scanning a highly focused ion beam on a diamond-like carbon thin film or diamond-like carbon thin film covered by a metal film which is used to reduce the surface charge effect to provide better fabrication quality, diamond-like carbon nano-architectures as fine as the focusing limit of a FIB facility can be fabricated. This coating metal film may be Cr, which can be easily removed after FIB milling.

One of the most striking properties is that focused ion beam milling ability is almost material independent for the diamond-like carbon based materials. It can be applied to any diamond-like carbon thin films, whether doped or not. The fabrication rates for the variance of the same materials are almost the same. Another property is that focused ion beam milling is a mask-less process; this reduces the fabrication period and cost and at the same time add more design flexibility.

4.2. *Diamond-like carbon micro-architectures*

Directly applying top-down approach to pattern diamond-like carbon film was used as moving mechanical parts in the design of micro-architectures. Those already mature fabrication tools with fabrication accuracy of micron-scale initially developed for microelectronic devices are now widely available. Using a simple contact photolithography system patterns with line resolution of $< 1\,\mu$m with desk-top RIE system, diamond-like carbon cantilevers could be fabricated as shown in Fig. 18. Chua *et al.*[51–53,57] applied this kind of micro-architectures of diamond-like carbon as

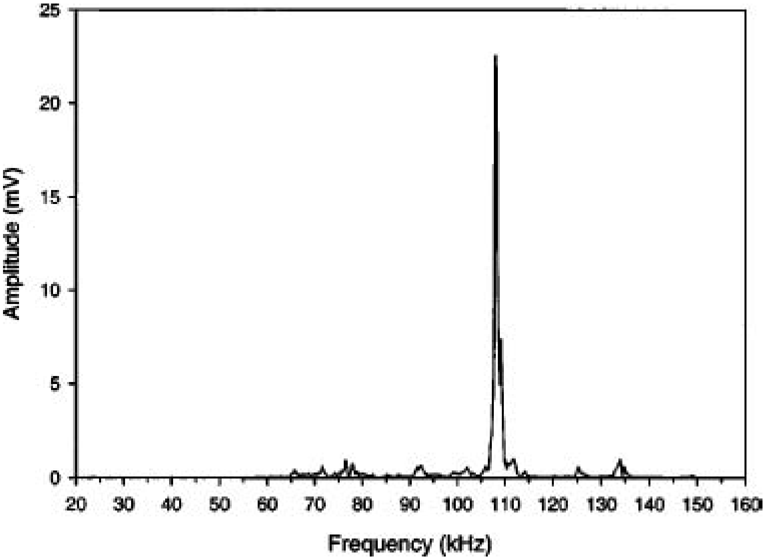

Fig. 21. Diamond-like carbon vibration resonator. Reprinted with permission from Ref. 51, © 2004, American Vacuum Society.

micromechanical resonator. They measured the resonator performance using optical method, and the measured vibration property was summarized in Fig. 21. They found that the resonance frequency of diamond-like carbon micro-architectures is twice that of a silicon resonator of the same size. This confirmed the theoretical prediction that diamond-like carbon micro-architectures have better resonator performance than silicon. In the same paper, residual stress of diamond-like carbon film has also been demonstrated to be able to increase the resonator's frequency.

Luo *et al.* used this top-down route to fabricate diamond-like carbon micro-architectures.[10] Due to the strong residual stress in the diamond-like carbon film, these micro-architectures curled up while relieving from the silicon substrate by wet etching in KOH solution, as indicated in Fig. 22.

Instead of reducing the residual stress in diamond-like carbon film, Luo *et al.*[10] utilized the stress and through a second metal layer on diamond-like carbon film, they successfully fabricated micro-architectures of a plurality layers containing a diamond-like carbon layer, a SU8 resist and a metal layer. The whole micro-architecture was used as a thermal driven clamper. When relieving from the silicon substrate, the fingers of the clamper curl up and hold as a balance between the residual stress of diamond-like carbon and the stiffness of the metal, as shown in Fig. 23(a).

When an electrical pulse applies to the architectures, heating up of the micro-architectures will stretch the fingers to be ready to welcome a micro-object due to the thermal stress of origin from mismatch of the thermal expansion coefficients of

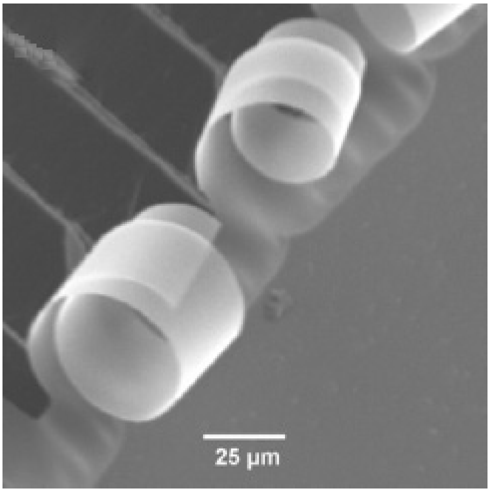

Fig. 22. Curl up due to the residual stress of diamond-like carbon. Reprinted with permission from Ref. 10, © 2007, Institute of Physics.

the diamond-like carbon and the metal. This micro-architecture can be applied to carry micro-particles as shown in Fig. 23(b).

4.3. *Diamond-like carbon nano-architectures*

For practical applications of diamond-like carbon micro-cantilevers as sensors or filters, one needs to increase their intrinsic frequency to GHz range other than those in MHz range held by the micro-cantilevers. This can be accomplished by shrinking the size of the cantilever from micrometer scale into the nanometer scale. By reducing the size to that of nano-cantilevers, intrinsic frequency of the device can enter the GHz range. Recently, nanocrystalline diamond based nano-resonator has been fabricated.[58] One of the serious issues of size scaling of cantilever based nano-mechanical resonators working at GHz is that quality of factor of the nano-cantilever is usually too small to be practical. For example, mechanical resonator at micro-scale can hold a QF as high as 10^6, but for nano-scale architecture, the value quickly drops to less than 1000. One of the ways to build a nano-mechanical system with a working mode at high frequency yet with a reasonable QF is preferable to nano-architecture other than a simple cantilever based nano-mechanical resonators. The nano-architecture explores nano-cantilever based resonators coupled to a micro-size stander. The total architecture could hold a collective vibration mode in the GHz range yet hold a QF near a practical level.

A silicon nitride with tensile stress[59] has also been applied to fabricate a different-shape nano-architecture, as illustrated in Fig. 24(a). This nano-architecture demonstrates an ultrahigh QF over 1 million above a vibration frequency of 1 MHz. In order to obtain true gigahertz architecture, material of less density and higher modulus are more profitable. Among these material, aluminum

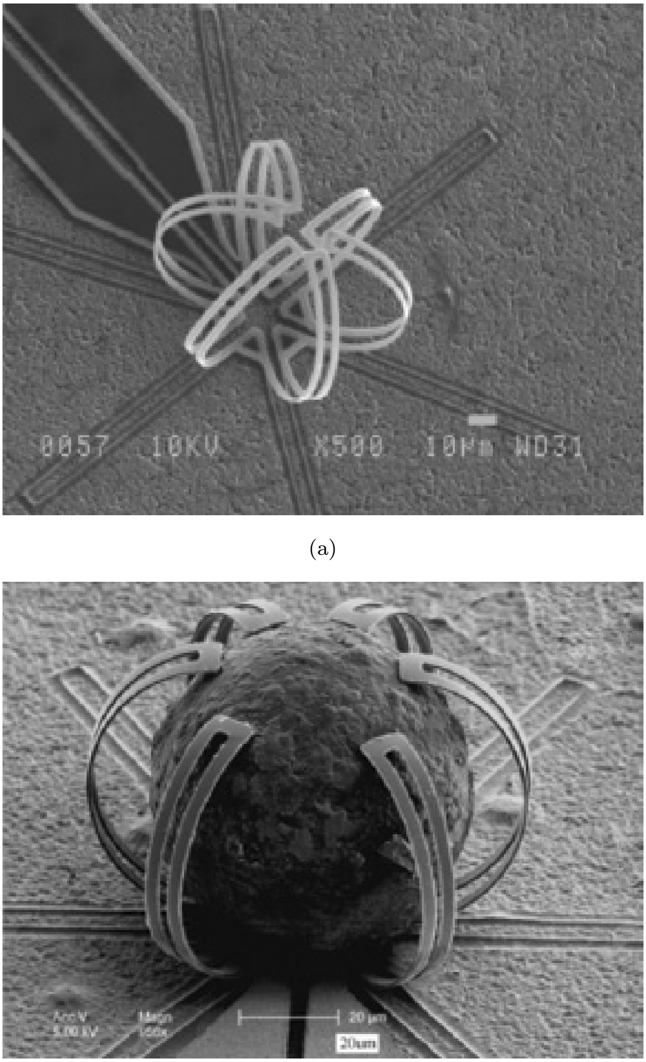

(a)

(b)

Fig. 23. Stress engineered diamond-like carbon micro-architectures for MEMs applications. Reprinted with permission from Ref. 10, © 2007, Institute of Physics.

nitride, diamond and diamond-like carbon are the best candidate. Mostly notable are the latter two. One of the nano-architectures is illustrated in Fig. 24(b). This device is fabricated in nanocrystalline diamond.[60] In this paper, high order vibration of 1.441 GHz has been demonstrated, while its QF remains 20,000 above 500 MHz.

Though diamond based nano-architecture has been demonstrated to work in GHz frequency, diamond suffers from a relatively rough surface. Additionally, its etching condition is not easy to control as residual diamond crusts are difficult to

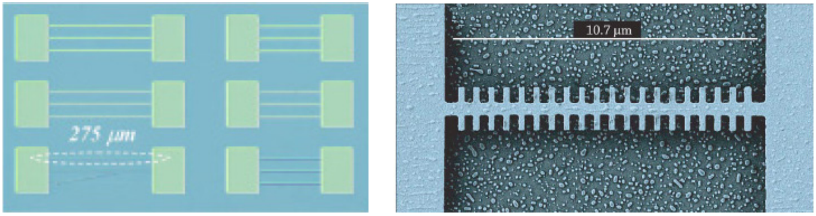

(a) (b)

Fig. 24. Nano-architecture for GHz, high QF mechanical devices. Figure (a) is reprinted with permission from Ref. 59, © 2008, American Institute of Physics. Figure (b) is reprinted with permission from Ref. 60, © 2007, American Institute of Physics.

etch and remove. In contrast, diamond-like carbon films deposited by FCVA have an ultra-smooth surface and do not have problem of residual crusts on the etched surface. According to Verbridge *et al.*, the residual tensile stress of a diamond-like carbon film can be controlled and utilized to increase both its working frequency[50] and the quality factor. Thus, diamond-like carbon based nano-architectures are expected to be a good candidate for mechanical nano-architectures. In addition, diamond-like carbon based nano-architecture can make use of the hydrophobic properties of DLC[61] as previously shown in Sec. 2. Such nano-architectures can work much better than those made of silicon or other materials in solution environment.

A potential research field in nano-mechanical system is shock wave region where mechanical load is so strong that a shock wave may be generated in the nano-mechanical systems. Beil *et al.*[63] recently pioneered this research. By using a surface acoustic wave generated by an interdigitated transducers (IDTs) fabricated on a nano-mechanical resonator, as illustrated in Fig. 25, they detected shock wave propagation in the resonator by measuring the anomalous acoustoelectric current of a suspended 2D electron gas embedded in the resonator. As shock wave is a highly nonlinear wave, this research will excite studies on highly nonlinear response of nano-architecture to intensive mechanical load.

Shock wave is not a new research field for macro world where its motion is mainly determined by Hugoniut of the materials which it propagates in. Generally speaking, during shock wave propagation in the nano-architecture based resonator, there is a strong release wave which is refracted by the interaction of the shock wave with the surroundings of the nano-architecture at the interface. In the nano-architecture resonator of Ref. 62, the longitudinal dimension of 1.2 μm of the 2DEGs is much larger than sideway dimension (200 nm). There aspect ratio is far larger than that used in macro-object for which the transverse dimension is usually much larger than the longitudinal one of the wave propagation. It is reported that shock wave propagation can be well recorded,[62] while for a macro-object of the same aspect ratio, this detection is impossible. This indicates that shock wave propagates in a nano-architecture may differ from that for a macro-object.

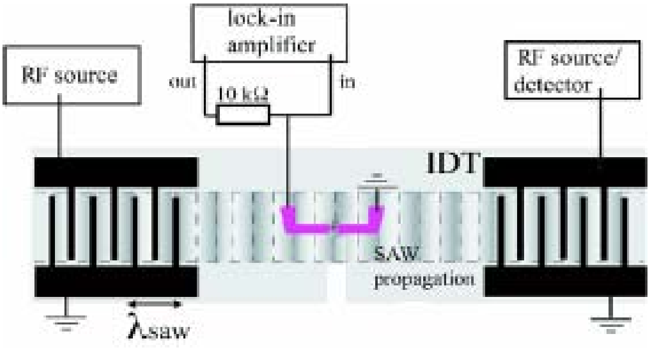

Fig. 25. Surface acoustic wave nano-mechanical system. Reprinted from Ref. 62 with permission, © 2008, The American Physical Society.

At the same time, there is no indication of the strength of the shock wave in Ref. 62. Usually, shock wave strength is beyond the fracture strength of macro-objects while in the reference, the resonator exists without damage after multiple shock wave propagation through it. Additionally, shock wave will induce a sharp temperature rise which is also not mentioned in the paper. There are several applications of shock wave in nano-architectures. One of the applications of shock wave in nano-mechanical resonator is to compress an embedded nano-object, say carbon to study the phase transition mechanism from graphite to diamond. Shock wave or other high pressure techniques have been widely applied to synthesizing diamond for industrial application. But the particle size of artificial diamond is much less than that of large natural gem. Nano-architecture based resonator provides accurate study of this phase transition with a system embedded in the resonator. A diamond-like carbon nano-architecture based resonator loaded with shock, especially those with lower sp^3 content but doped with metal particles as catalyst may transit into ones with high sp^3 content or even nanocrystalline diamonds.

5. Future for Diamond-Like Carbon Nano-Architectures

Based on the above review on both micro-architectures and nano-architectures of diamond-like carbon, it is clear that the nano-architecture based mechanical device is a field not well explored for practical applications. Many designs and processes are still not well understood, for example, the etching process to fabricate nano-architectures and nano-architecture design most optimal for obtaining a high vibration frequency with a high quality factor.

For many components and devices based on these nano-architectures, a material highly stable against degradation in moisture condition and other harsh environment conditions is among the best candidates. For chemical and bio applications, the vibrating device based on the architecture needs to work in a solution condition. Both silicon and silicon nitride devices will suffer serious performance degradation as they are strongly hydrophilic to the water or other liquids. Diamond-like carbon, however, is hydrophobic. Nano-architectures developed from diamond-like carbon will have better vibrating performance in these severe environments. It is expected that diamond-like carbon nano-architectures are much better for applying to an atmosphere and solution environment than those made up of silicon or silicon nitrides. In addition, diamond-like carbon is also bio-compatible, and has already been applied to bio-systems. We can also expect that diamond-like carbon nano-architectures can be developed into other nano-fluidic systems for virtual single-molecular sensing and detection. Yet, combination of both bottom-up and top-down methods can provide more sophisticated nano-architectures and better performance for diamond-like carbon based mechanical devices.

Another important property of top-down fabrication is that different nano-architectures can be fabricated simultaneously. If many nano-architectures, whether identical or different, are left coupled to each other, this coupled system may leave more space for basic researches as a mechanical version of condensed matter physics. Most of the coupling mechanisms well studied in solid state physics are in the linear region. Things are usually too complicated to be well understood when we go down to the nonlinear coupling region because a gradually increasing coupling region in solid state is not available. The nano-architectures otherwise can provide such an idea system for study both individual nonlinear movement, for example, shock wave developing and propagation in a single nano-architecture, and collective motion of nonlinearly coupled architectures, for example, mechanical coupling between individual nano-architectures can well be tailored by the mechanical parts between them.

This review concentrates on the diamond-like carbon nano-architecture and its application as mechanical devices. Its design and ideas can be easily extended to other material systems. Mostly, its application here refers to mechanical movement. Other applications of these nano-architectures can be explored to other fields, say field emission device for display etc.

Acknowledgment

The authors would like to acknowledge NUS WBS: R-284-000-046-123 for the financial support.

References

1. Martin PJ, Filipczuk SW, Netterfield RP, Field JS, Whitenall DF and McKenzie DR, Structure and hardness of diamond-like carbon films prepared by arc evaporation, *J Mater Sci Lett* **7**:410–412, 1988.
2. Hauert R, An overview on the tribological behavior of diamond-like carbon in technical and medical applications, *Tribol Int* **37**:991–1003, 2004.
3. Casiraghi C, Robertson J and Feraari AC, Diamond-like carbon for data and beer storage, *Materials Today* **10**:44–53, 2007.
4. Milne WI, Robertson J and Amaratunga GAJ, *Diamond-like Carbon*, World Scientific, 1996.

5. Robertson J, Diamond-like amorphous carbon, *Mater Sci Eng Rep* **37**:129–281, 2002.
6. Martin PJ and Bendavid A, Review of the filtered cacuum arc process and material deposition, *Thin Solid Films* **394**:1–15, 2001.
7. Saw KG, Idrus RM and Ibrahim K, Diamond-like amorphous carbon film by d.c. magnetron sputtering, *J Mater Sci Lett* **19**:735–737, 2000.
8. Funada Y, Awazu K and Shimamura K, Diamond-like carbon thin-film formation by ion-beam-assisted deposition, *Surf Coat Technol* **66**:514–518, 1994.
9. Casiraghi C, Ferrari AC and Robertson J, The smoothness of tetrahedral amorphous carbon, *Diamond and Related Materials* **14**:913–920, 2005.
10. Luo J, Fu YQ, Le HR, Williams JA, Spearing SM and Milne WI, Diamond-like carbon MEMs, *J Micromech Microeng* **17**:S146–S163, 2007.
11. Peiner E, Tibrewala A, Bandorf R, Luthje H, Doering L and Limmer W, Diamond-like carbon for MEMs, *J Micromech Microoeng* **17**:S83–S90, 2007.
12. Milne WI, Diamond like carbon field emission displays, in *Future Directions in Thin Film Science and Technology: Proceedings of the Ninth International School on Condensed Matter Physics* (Marshall JM *et al.*, eds.), World Scientific Pub Co Inc, 1997.
13. Roy RK and Lee KR, Biomedical applications of diamond-like carbon coatings: A review, *J Biomed Mater Res Part B: Appl Biomater B* **83**:72–84, 2007.
14. Milne WI, Electronic devices from diamond-like carbon, *Semicond Sci Technol* **18**:S81–S85, 2003.
15. Tay BK, Zhao ZW and Chua DHC, Review of metal oxide films deposited by filtered cathodic vacuum arc technique, *Mater Sci Eng Rep* **52**:1–48, 2006.
16. Schwan J, Ulrich S, Batori V, Ehrhardt H and Silva SRP, *J Appl Phys* **80**:440–447, 1996.
17. Egerton RF, *Electron Energy-Loss Spectroscopy in the Electron Microscope*, Plenum Press, 1996.
18. Berger SD, McKenzie DR and Martin PJ, EELS analysis of vacuum arc-deposited diamond-like films, *Phil Mag Lett* **57**:285–290, 1988.
19. Chua DHC, Teo KBK, Tsai TH, Milne WI, Sheeja D, Tay BK and Schneider D, Correlation of surface, mechanical and microproperties of tetrahedral amorphous carbon films deposited under different magnetic confinement conditions, *Appl Surf Sci* **221**:455–466, 2004.
20. Ferrari AC and Robertson J, Interpretation of Raman spectra of disordered and amorphous carbon, *Phys Rev B* **61**:14095–14107, 2000.
21. Tay BK, Shi X, Tan SH and Chua HCD, Investigation of tetrahedral amorphous carbon films using X-ray photoelectron and Raman spectroscopy, *Surf Interface Anal* **28**:231–234, 1999.
22. Zhang S, Xie H, Zeng XT and Hing P, Residual stress characterization of diamond-like carbon coatings by X-ray diffraction method, *Surf Coat Technol* **122**:219–224, 1999.
23. Wang DY, Weng KW and Hwang SY, Study on metal doped diamond-like carbon films synthesized by cathodic arc evaporation, *Diam Rel Mater* **9**:1762–1766, 2000.
24. Hsieh WP, Wang DY and Shieu FS, Characterization of the Ti-doped diamond-like carbon coatings on a type 304 stainless steel, *J Vac Sci Technol* **17**:1053–1058, 1999.
25. Weng KW, Chen YC, Lin TN and Wang DY, Metal-doped diamond carbon film synthesized by filter-arc deposition, *Thin Solid Films* **515**:1053–1057, 2006.
26. Chiu MC, Hsieh WP, Ho WY, Wang DY and Shieu FS, Thermal stability of Cr-doped diamond-like carbon films synthesized by cathodic arc evaporation, *Thin Solid Films* **476**:258–264, 2005.

27. Zhang ZY, Lu XC, Luo JB, Liu Y and Zhang CH, Mechanical properties of La2O3 doped diamond-like carbon films, *Surf Coat Technol* **202**:1621–1627, 2008.
28. Zhang ZY, Lu XC and Luo JB, Unusual stress behaviour of CeO2-doped diamond-like carbon nanofilms, *Phil Mag Lett* **88**:145–151, 2008.
29. Hsu CY, Chen LY and Hong FCN, Properties of diamond-like carbon films deposited by ion plating with a pulsed substrate bias, *Diamond and Related Materials* **7**:884–891, 1998.
30. Zhang W, Tanaka A, Wazumi K and Koga Y, Structural, mechanical and tribological properties of diamond-like carbon films prepared under different substrate bias voltage, *Diamond and Related Materials* **11**:1837–1844, 2002.
31. Cheng YH, Tay BK, Lau SR and Shi X, Influence of substrate bias on the structure and mechanical properties of Ta-C:W films deposited by filtered cathodic vacuum arc, *Surface & Coating Technol* **146**:398–404, 2001.
32. Davis CA, Amaratunga GAJ and Knowles KM, Growth mechanism and cross-sectional structure of tetrahedral armorphous carbon thin films, *Phys Rev Lett* **80**:3280–3282, 1998.
33. Li XJ, Foong YM and Chua DHC, unpublished results.
34. Uhlmann S, Frauenheim T and Lifshitz Y, Molecular-dynamics study of the fundamental processes involved in subplantation of diamond-like carbon, *Phys Rev Lett* **81**:641–644, 1998.
35. Shi X, Tay BK and Lau SP, The double bend filtered cathodic arc technology and its applications, *Int J Mod Phys B* **14**:136–153, 2000.
36. Zhang P, Fabrication & Characterization of composite diamond-like carbon films for some applications, PhD. Thesis, Nanyang Technological University, 2004.
37. Shi X, Tay BK, Tan HS, Zhong L, Tu YQ, Silva SRP and Milne WI, Properties of carbon ion deposited tetrahedral amorphous carbon films as a function of ion energy, *J Appl Phys* **79**:7234–7240, 1996.
38. Young T, An essay on cohesion of fluids, *Philos Trans R Soc London* **95**:65–87, 1805.
39. Wu S, *Polymer Interface and Adhesion*, Marcel Dekker, New York, 1982.
40. Weiler M, Sattel S, Jung K, Ehrhardt H, Veerasamy VS and Robertson J, Highly tetrahedral, diamond-like amorphous hydrogenated carbon prepared from a plasma beam source, *Appl Phys Lett* **64**:2797–2799, 1994.
41. Pivin JC, Allouard M and Rotureau G, Determination of the optimal energy-range for obtaining diamond-like films by ion-implantation, *Surf Coat Technol* **47**:433–444, 1991.
42. Sheeja D, Tay BK, Sze JY, Yu JK and Lau SP, A comparative study between pure and Al-containing amorphous carbon films prepared by FCVA technique together with high substrate pulse biasing, *Diam Rel Mater* **12**:2032–2036, 2003.
43. Teo EHT, Zhang P, Tay BK and Chua DHC, Self-assembled, Ni nanoclusters in a diamond-like carbon matrix, *Int J Nanotech* **4**:424–430, 2007.
44. Hsieh J, Chua DHC, Tay BK, Teo EHT and Tanemura M, Monochromatic photoluminescence obtained from embedded ZnO nanodots in an ultrahard diamond-like carbon matrix, *Diam Rel Mater* **17**:167–170, 2008.
45. Ferrari AC, Rodil SE and Robertson J, Interpretation of infrared and Raman spectra of amorphous carbon nitrides, *Phys Rev B* **67**:115305, 2003.
46. Teo EHT, Yung WKP, Chua HCD and Teo BK, A carbon nanomattress: A new nanosystem with intrinsic, tunable, damping properties, *Adv Mater* **19**:2941–2945, 2007.
47. Matsui S, Three-dimensional nanostructure fabrication by focused ion beam chemical vapour deposition, in *Springer Handbook of Nanotechnology* (2nd edition), Baharat Bhushan ed., Springer, New York, 2007, pp. 179–195.

48. Hashimoto Y, Kotani Y, Yamada M, Yamashita D, Nakajima Y and Manabu H, Structure of diamond like carbon deposited on aluminum oxide surface with microstructure, *Jpn J Appl Phys* **46**:362–366, 2007.
49. Robertson J, Mechanisms of electron field emission from diamond, diamond-like carbon and nanostructured carbon, *J Vac Sci Technol B* **17**:659–665, 1999.
50. Chua HCD, Milne WI, Yu LJ, Sheeja D and Tay BK, Fabrication and simulation of amorphous carbon cantilever structures, *Mat Res Soc Symp Proc* **773**:N3.2.1–N3.2.8, 2003.
51. Chua HCD, Milne WI, Sheeja D, Tay BK and Schneider D, Fabrication of diamond-like amorphous carbon cantilever resonators, *J Vac Sci Technol B* **22**:2680–2684, 2004.
52. Chua HCD, Tay BK, Zhang P, Teo EHT, Lim LTW, O'Shea S, Miao J and Milne WI, Vibratory response of diamond like amorphous carbon cantilevers under different temperature, *Diam Rel Mater* **13**:1980–1983, 2004.
53. Zhou B, Prorok BC, Erdemir A and Eryilmaz O, Microfabrication issues in constructing freestanding membranes of near frictionless carbon and diamond-like films, *Diamond and Related Materials* **16**:341–349, 2007.
54. Li XJ, Foong YM and Chua DHC, unpublished results.
55. Yao N (ed.), Focused ion beam systems: Basics and applications, Cambridge University Press, Cambridge, UK, 2007.
56. Mayer J, Giannuzzi LA, Kamino T and Michael J, TEM sample preparation and FIB-induced damage, *MRS Bulletin* **32**:400–407, 2007.
57. Chua HCD, Milne WI, Sheeja D and Tay BK, Stress and strength of free-standing 2-dimensional tetrahedral amorphous carbon bridge arrays, *Mat Res Soc Symp Proc* **775**:U8.27.2–U8.27.6, 2003.
58. Sekaric L, Parpia JM, Craighead HG, Feygelson T, Houston BH and Butler JE, Nanomechanical resonator structures in nanocrystalline diamond, *Appl Phys Lett* **81**:4455–4457, 2002.
59. Verbridge SS, Craighead HG and Parpoa JM, A megahertz nanomechanical resonator with room temperature quality factor over a million, *Appl Phys Lett* **92**:013112, 2008.
60. Gaidarzhy A, Imboden M, Mohanty P, Rankin J and Sheldon W, High quality factor gigahertz frequencies in nanomechanical diamond resonators, *Appl Phys Lett* **91**:203503, 2007.
61. Harada R and Baba K, Preparation of hydrophobic diamond like carbon film by plasma source ion implantation, *Nucl Instrum Methods in Phys Res B* **148**:655–658, 1999.
62. Beil FW, Wixforth A, Wegscheider W, Schuh D and Blick R, Shock waves in nanomechnanical resonators, *Phys Rev Lett* **100**:026801, 2008.

HOTPLATE TECHNIQUE FOR NANOMATERIALS

YANWU ZHU and CHORNG HAUR SOW*
National University of Singapore Nanoscience &
Nanotechnology Initiative
Department of Physics, National University of Singapore
**physowch@nus.edu.sg*

As an efficient and cost-effective method to synthesize nanomaterials, the hotplate technique has been reviewed in this article. Systematic studies have been carried out on the characterizations of the materials synthesized. In addition to the direct preparation of nanomaterials on metals, this method has been extended to the substrate-friendly and plasma-assisted hotplate synthesis. Apart from chemically pure nanostructures, a few nanohybrids were synthesized, further demonstrating the flexibility of this technique. The investigations on their applications indicate that they are promising material systems with potential applications in field emission devices, gas sensors, Li-ion batteries and ultrafast optical devices.

Keywords: Hotplate; nanomaterials; field emission; electron microscopy.

1. Introduction

In the last decade, nanoscience and nanotechnology has initiated much interest in fundamental research and industrial applications. As the foundation of nanoscience and nanotechnology, nanostructured materials have become one of the most studied materials across multiple research fields.[1] Normally, nanostructures are defined as those structures with at least one dimension less than 100 nm. In this dimension, the number of atoms is countable, making the properties of nanostructures different from those of their bulk counterparts or single atoms, despite the fact that they share the same chemical compositions. Within the structure of countable atoms, the combination of quantum effects and multi-body interaction may lead to novel mechanical, electrical, optical, chemical and biological properties. Based on these properties, various potential applications of nanostructures can be expected, such as their use in logic circuit, chemical and biological sensors, optical devices and so on.[2] Driven by these applications, current research activities mainly focus on the synthesis of nanostructures, assembly and manipulation of nanostructural blocks, characterizations, processing and investigation of their properties.

Generally, two approaches are adopted to fabricate nanostructures: top-down and bottom-up methods. In the former method, the size of bulk materials is gradually reduced to the nanometer scale by using etching techniques with the help of various lithography techniques. The top-down method has proven to be a great success in the highly developed semiconductor industry in the last half century. However, with the requirement of device size miniaturization, the top-down route is facing some major challenges. For example, to break through the wavelength limitation of conventional lithography, the technique is becoming more and more complex to obtain nanostructures with smaller size, leading to increasing costs.[3] The complicated steps in the top-town technique also make the precise control of these properties extremely difficult. Furthermore, device size fluctuations may result in a large spread in device characteristics at the nanoscale, affecting key parameters for the operation of the devices.[4] Future applications require more rational synthesis of nanostructures, e.g. precisely controlling the position, size, surface and structures of the final nanostructures. To realize the goal, bottom-up methods appear to be more promising because they mainly utilize the self-assembly of some basic blocks into nanostructures and such a process can be rationally controlled by the growth dynamics. Depending on the existing form of the growth blocks, the bottom-up method can be solution-based or vapor-based and they are two of the most commonly used methods to fabricate nanowires.[5] In both methods, the growth blocks such as clusters or vapors are generated in many ways including thermal evaporation, chemical reaction, laser ablation, arc discharge, sputtering, etc. Then the precursor is transported in a solution or by a gas flow from source to the deposition spots under certain conditions. Many parameters are varied to optimize the growth for the production of nanostructures. In a vapor-based growth, the parameters mainly include temperature, gas flow rate, pressure, etc. In a solution-based growth, the concentration, temperature, pH values are very important. For growth anisotropy, catalysts or growth reagents are commonly used.

As another simpler alternative, the hotplate technique provides a cost-effective and straightforward way for the growth of nanostructures by directly oxidizing metals in ambient conditions. As early as the 1950s, Pfefferkron[6] and Arnold[7] described a method to obtain metal oxide filaments by annealing the corresponding metals in air at elevated temperatures. In this way, oxides of Pt, Zn, Ni, Pd, Fe and Mg were synthesized in the form of microrods or nanorods. However, during the early stages of development of this method, the coverage of nanostructures on the metal surface was very low and the morphological control of the products remained a challenge. Furthermore, due to technical limitations, the studies on their characterization and applications were inadequate. Recently, this method has attracted much attention due to its simplicity and low cost. Since the synthesis can be carried out on a hotplate without any gas flow and pressure control, the growth parameters investigated are simplified to just temperature and duration. Furthermore, the growth temperature is relatively lower than that used in normal vapor-based method, making it more energy efficient. Moreover, the chamber free approach is suitable for mass production in future large-scale applications.

In this article, recent efforts from our research group on this efficient and cost-effective method will be reviewed. This review focuses on the materials synthesized, their characterizations and related applications studies. In addition, extensions to this method including substrate-friendly and plasma-assisted hotplate synthesis are also briefly discussed. Apart from chemically pure nanostructures, a few nanohybrids are included for demonstrating the flexibility of this method. Finally, investigations on some applications of the nanomaterials synthesized such as field emission devices, gas sensors, Li-ion batteries and ultrafast optical devices are reviewed.

2. Synthesis and Characterizations of Nanomaterials

2.1. *Direct synthesis on metals*

On a hotplate, the simplest method is heating a metal plate at elevated temperatures in ambience. During the oxidation process, nanostructures of the corresponding metal oxides are grown on the surface of the metal plates. In this case, the metal acts as both the substrate and source of material. The synthesis of such nanostructure oxides directly on conductive substrates is useful in some electric applications such as field emission, since no extra electric contact is needed for as-grown oxide/metal samples. This method has shown success in the syntheses of CuO, Fe_2O_3, Co_3O_4 and ZnO nanostructures.

As a typical example, aligned CuO nanowire arrays have been synthesized by heating Cu plates on a hotplate at a heating temperature of 300–450°C.[8,9] The typical synthesis procedures and scanning electron microscopy (SEM) image of CuO nanowires are shown in Fig. 1. The height, diameter and density of nanowire arrays can be controlled by changing the heating temperature and durations. After synthesis at a temperature of 390°C for three days, the resultant nanowires show an average density of about 10^8 nanowires cm^{-2} with an average length of $30 \pm 3\,\mu m$ and a diameter of $60 \pm 15\,nm$ at the tips. After one day of heating at 430°C, the resultant nanowires show an average density of about 4×10^7 nanowires cm^{-2} with an average length of $4 \pm 0.7\,\mu m$ and a typical tip diameter of $90 \pm 10\,nm$. Transmission electron microscopy (TEM) and high-resolution TEM (HRTEM) studies have shown that these nanowires are single crystalline CuO, with preferential monoclinic growth orientation in the $[-111]$ direction (data not shown). Some nanowires are coated with a thin layer of amorphous coating with thickness of a few nanometers. Such a coating is believed to lead to a diameter dependent behavior of the elastic modulus of CuO through three-point bending studies.[10] Similar to CNTs,[11] CuO nanowires can be melted and removed by a focused laser beam.[12] Based on this technique, patterns of CuO nanowires have been created by selectively removing nanowires. It was found that the tip of CuO nanowires could be melted to microspheres upon laser burning, which demonstrated a lower O:Cu ratio compared with untreated nanowires.[13] Such a laser reduction may be used to fabricate CuO nanowire based heterojunctions.

As the most stable form of iron oxide, hematite (α-Fe_2O_3) nanoflakes were synthesized by heating an Fe foil on a hotplate.[14] The heating temperature can be as low as 300°C. The growth occurs very rapidly and can be realized on a large

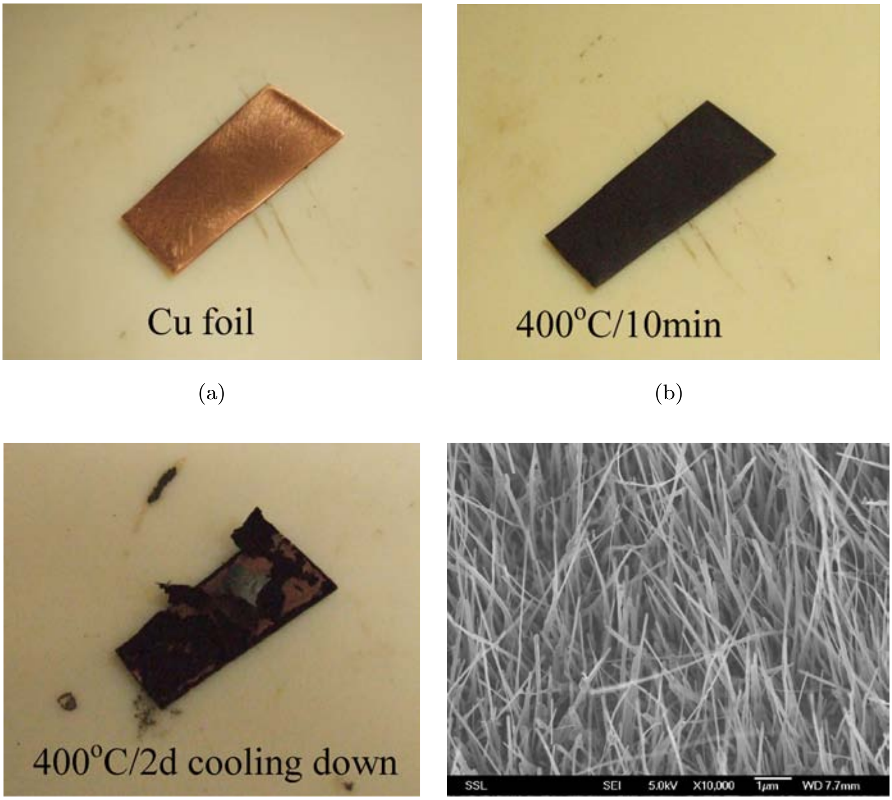

(a) (b)

(c) (d)

Fig. 1. (a)–(c) Synthesis of CuO nanowires by hotplate technique; (d) Typical SEM image of CuO nanowires.

scale using a 10 × 10 cm^2 substrate. All nanoflakes are grown perpendicular to the local surface of the substrate. From the TEM image in Fig. 2(a), we can see that the nanoflakes have very sharp tips with an average diameter of 17 ± 5 nm. At the root of the nanoflakes, the width reaches about 100 nm. The thickness of nanoflakes varies within 10–20 nm from the tip to the root. The sharp tip of the nanoflakes can be observed from the HRTEM image (Fig. 2(b)). Most nanoflakes are single crystalline (rhombohedral) with growth direction of [110] and some along [006]. Raman and X-ray diffraction (XRD) studies have identified an Fe_3O_4 film on the substrate, which should be the precursor for the growth of Fe_2O_3 nanoflakes.

Contrary to the cases of CuO and Fe_2O_3, heating Co plates on a hotplate produced 2D nanostructures–nanowalls.[15] The Co_3O_4 nanowalls can be synthesized at the very low temperature range of 200–350°C. After cooling down, as-grown samples were covered by a high density of 2D nanostructures, with most of them perpendicular to the substrate. The edges of the nanowalls are irregular and the sides are very rough. The thickness can be as thin as 25 nm, as revealed by high resolution

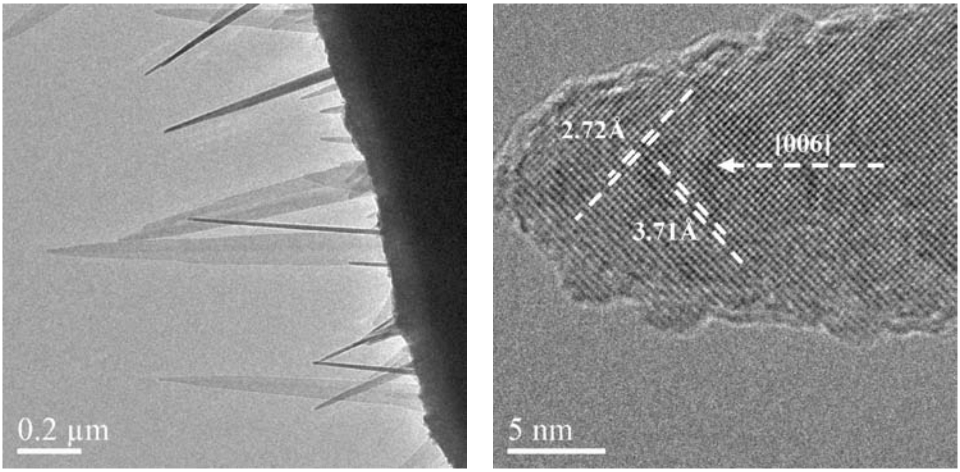

(a) (b)

Fig. 2. (a) TEM and (b) HRTEM images of α-Fe_2O_3 nanoflakes.

SEM studies. TEM and HRTEM demonstrated that Co_3O_4 nanowalls have a layered morphology, with each layer comprising single crystalline spinel structures. The length and thickness of nanowalls could be controlled by simply changing the heating durations. Similarly, CoO was observed from the glancing angle XRD study, suggesting that the existence of sub-oxide is a common feature for the growth of some oxide nanostructures such as CuO, α-Fe_2O_3 and Co_3O_4.

The mechanism responsible for the synthesis of nanomaterials on hotplate was investigated. Compared with the metal melting points, the growth temperatures used in the hotplate technique are very low and the vapor is unlikely to play an important role. To test this supposition, a flow of air at a rate of 10^6 sccm was passed across the Co sample during the heating process. This flow rate is much larger than those commonly used in the fabrication of nanostructures, ensuring that there is not much static fluid vapor near the surface during heating. The SEM images of the products under this condition still show a similar morphology to those fabricated without air flow. In addition, the observation of the presence of sub-oxides renders us to consider different growth mechanisms responsible for the formation of these nanostructures. A solid–liquid–solid (SLS) mechanism is proposed to explain the growth of CuO, Fe_2O_3 and Co_3O_4 nanostructures on hotplate. Figure 3 schematically demonstrates the SLS growth process. In this mechanism, surface melting occurs on the metal, providing a liquid or quasi-liquid media. At the same time, the metal is oxidized to sub-oxide, acting as the precursor for the growth of final products. The sub-oxides on the surface are further oxidized, become supersaturated and start to nucleate and crystallize from the media, forming different nanostructures depending on the growth kinetics.

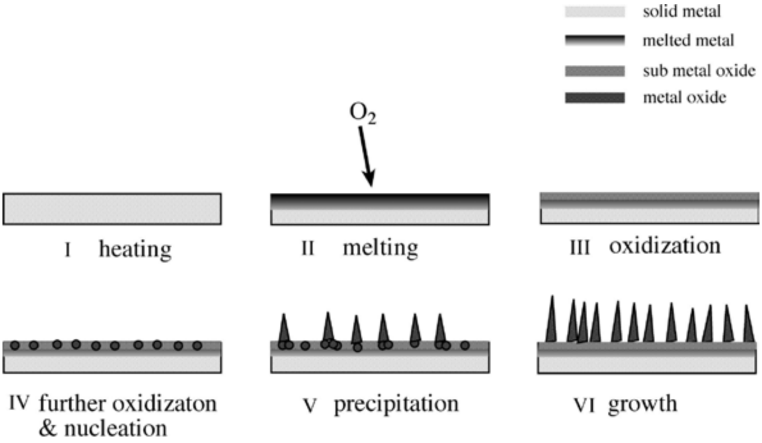

Fig. 3. Schematic of SLS growth of oxide nanostructures on hotplate.

2.2. *Substrate friendly synthesis*

Since surface melting usually occurs within a very thin layer on the surface of the metal, it is expected that heating the metal coating may produce similar results. In fact, the studies have shown that CuO nanowires and Fe_2O_3 nanoflakes can be successfully grown by heating metal coatings on other substrates. This substrate friendly synthesis of metal oxide nanostructures will further improve the flexibility and versatility of the hotplate technique.

Aligned CuO nanowires have been grown on Cu coated Si substrates at the temperature range of 300–450°C.[16] Such growth can effectively avoid the cracking of nanowire films, which is often observed from heated Cu plates. This improvement can be attributed to the fact that the thin surface coating reduces the surface stress during cooling. Furthermore, CuO nanowires have been grown on Cu coated rough substrates such as carbon cloth, consisting of crossed carbon fibers.[17] α-Fe_2O_3 nanoflakes were also successfully fabricated on a wide variety of substrates including Si wafer, glass sides, quartz, silica microspheres, atomic force microscope (AFM) tips, chemically etched tungsten tips, etc. by simply heating Fe coated substrates.[14] The coating thickness of Fe varied from a few hundred nanometers to one micrometer. Electron microscopy studies have shown that the morphology and structure are similar to the products grown by heating pure Fe foil, further suggesting that the surface process dominates the growth of nanomaterials on hotplate. On the other hand, α-Fe_2O_3 nanowalls were grown by annealing electrochemically deposited Fe based films in air.[18] In the experiments, FeMn films containing a low atomic ratio of manganese were deposited on the substrates including Cu, Si and SiO_2. In this case, nanowalls with wall thicknesses of down to 8 nm, lengths up to 2 μm and heights reaching 6 μm were obtained at the temperature range of 300–450°C. It was found that compared with pure Fe film, annealing of FeMn produces more uniform nanowalls with high density. This is attributed to the pinholes left due to the lower evaporation temperature of Mn,[19] thus iron oxides could evaporate easily onto the film surface.

Recently, another strategy has been used to grow metal oxide on other substrates in our group. In this method, the target substrate was positioned on the top and covering the surface of the source metal, which was heated on a hotplate in ambient conditions. For example, tungsten oxide nanorods have been synthesized on the cover glass by heating a tungsten foil.[20] In this method, a pure 99.9% tungsten foil was heated at $485 \pm 5°\mathrm{C}$ with a piece of $150\,\mu\mathrm{m}$ thick glass cover slide pressing on the tungsten foil. After cooling, nanorods were found to deposit directly as a thin film on the transparent cover glass slide. As shown in the images in Fig. 4, most nanorods were micrometers long and with diameters ranging between 100–300 nm. The density of the nanorods was approximately 7×10^5 nanorods/mm^2 after 25 h of heating. HRTEM (Fig. 4(b)) and electron diffraction (ED) analysis revealed that the nanorods exhibited a single crystalline monoclinic $WO_{3\text{-}x}$ structure. The observed preferential growth direction of the nanorods is perpendicular to the (001) plane and stacking faults parallel to the (001) direction were observed. Absorption studies show that as-grown $WO_{3\text{-}x}$ nanorods had an optical band gap of around 4.0 ± 0.2 eV. In comparison, smaller band gap values ranging from 2.6 to 3.4 eV were previously reported from polycrystalline and amorphous tungsten oxide thin films.[21]

By replacing the tungsten foil with molybdenum or vanadium foils, this method has been extended to the synthesis of MoO_3 or V_2O_5 nanostructures on glass slides or silicon wafers. The MoO_3 products show the morphology of nanobelts or nanosheets with typical thicknesses of few tens of nanometers. The widths of the nanobelts vary from 100 nm to $1\,\mu$m, and the lengths can be more than $10\,\mu$m. HRTEM and ED studies showed that the nanobelts or nanosheets are single crystalline structures, consistent with orthorhombic MoO_3 structures. The usual growth direction of MoO_3 nanobelts is along [001]. SEM studies also show that most

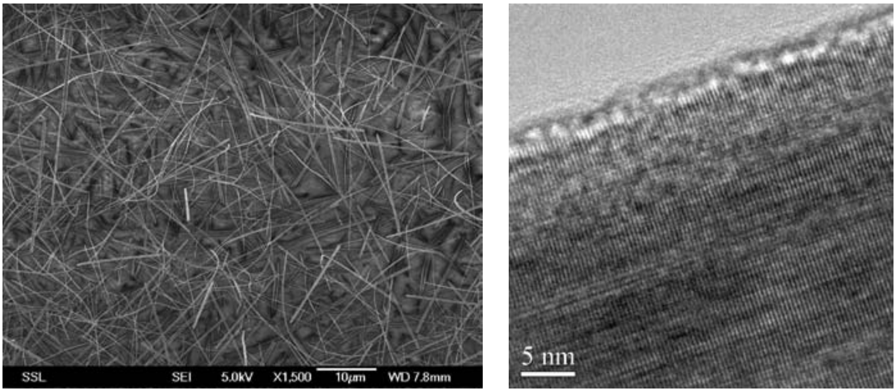

(a) (b)

Fig. 4. Typical (a) SEM and (b) HRTEM image of $WO_{3\text{-}x}$ nanowires.

nanobelts or nanosheets are layered structures, with obvious steps on the surface. V_2O_5 products are in the form of nanobelts. The widths of the nanobelts vary between 20 and 200 nm, with thicknesses of 30–60 nm and lengths up to 200 μm. TEM study shows the nanobelts are layered in structure, with water molecules in between the layers. Such a structure is unstable, especially at high temperature or under electron beam irradiation. A structural transformation was observed *in situ* during the HRTEM studies, possibly due to the loss of water molecules in the nanobelts.

2.3. *Effects of plasma*

Although the hotplate technique has shown preliminary success in the synthesis of a wide range of metal oxide nanostructures, there remain some challenges. For example, the nanostructures of some low-melting point materials still cannot be created by simply heating the corresponding metals in ambient. In addition, the morphology of as-grown products cannot be controlled satisfactorily. To improve the controllability of the hotplate technique, plasma-assisted growth is used to fabricate Co_3O_4 nanostructures.[22] The experiments were carried out in a chamber with base pressure of 10^{-6} Torr. With a heating coil, the temperature was set at 450°C and the growth pressure was 1 Torr. Oxygen gas with a flow rate of 30 sccm was introduced to oxidize the surface of the Co foils. The oxygen partial pressure is much lower than that in ambient. It was found that nanowires were obtained by heating Co in pure oxygen flow. As-grown nanowires have diameters in the range of 10–50 nm and are 2–10 μm in length. TEM study shows the growth of nanowires is along the [220] direction. In contrast, 2D Co_3O_4 nanowalls were grown when a 200 W radio frequency (RF) power supply was used during the heating process. The RF power served to excite the oxygen plasma in the chamber. Similar to the results from heating Co foil on a hotplate in ambient, these 2D nanowall-type structures are also vertically aligned. Typical SEM images of both morphologies are shown in Fig. 5.

It can be seen that the morphology of Co_3O_4 nanostructures can be controlled with or without using an oxygen plasma. In a plasma environment, the oxygen species are more reactive. Consequently, the formation events of nucleation sites for cobalt oxide will be higher than in the absence of a plasma. In addition, the high diffusion rate of the oxidizing species in the presence of plasma increases the growth rate of nanostructures. The high reactivity and diffusivity may cause rapid growth in different lattice directions leading to the formation of 2D structures. Hence, the morphology switching from 1D (nanowire) to 2D (nanowall) nanostructures is primarily attributed to the reactivity and diffusivity enhancement of the oxygen species in the plasma.

With the assistance of a plasma, NiO nanowalls, which cannot be obtained by directly heating Ni foils in ambient, were synthesized on a large scale.[23] The most favorable growth conditions were a substrate temperature of 700 ± 20°C, RF power of 200 W, oxygen flow rate of 30 sccm and processing pressure of 1500 mTorr.

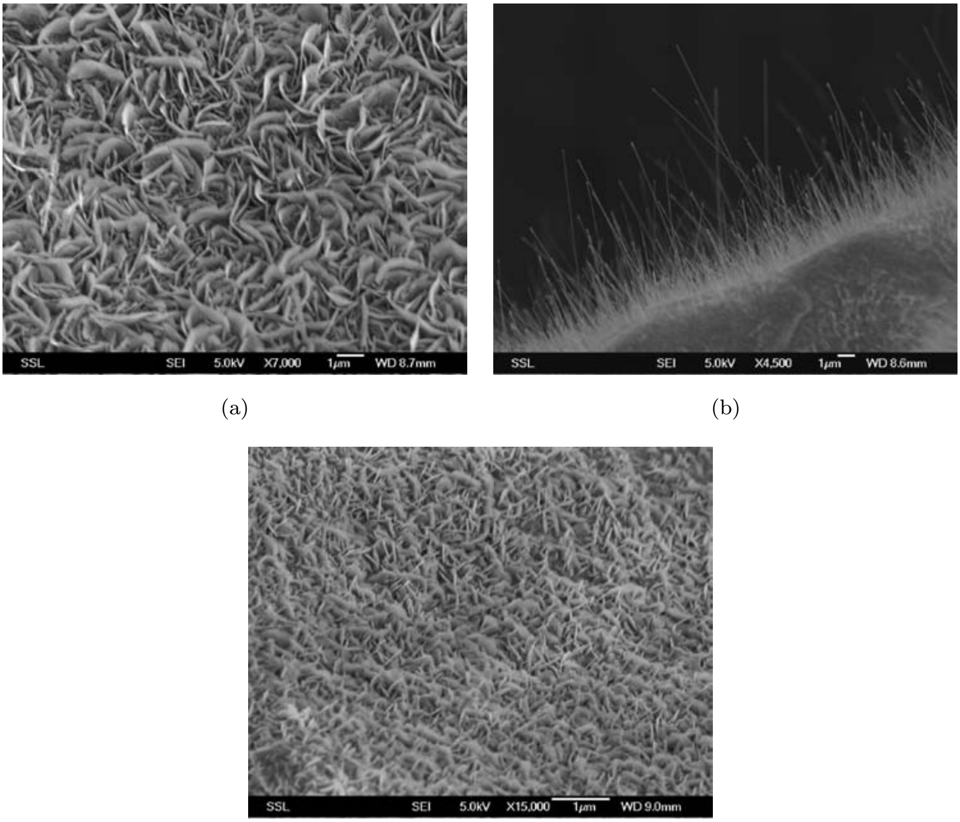

(a) (b)

(c)

Fig. 5. Typical SEM images of (a) Co_3O_4 nanowalls, (b) Co_3O_4 nanowires and (c) NiO nanowalls.

After growth, the shiny metallic surface of the nickel foil turned yellow, indicating the presence of NiO nanostructures. SEM study (Fig. 5(c)) shows that the entire surface of Ni is uniformly covered with a thin film of freestanding 2D nanowalls. The as-synthesized NiO nanowalls are over 200 nm in height and the wall thickness is typically less than 40 nm. The nanowalls are vertically aligned to the substrate and are interconnected to each other resulting in the formation of extended network structures. It should be noted that in the absence of the plasma, no nanowall structures were observed on the heated foil surface. TEM, XRD and Raman investigations have shown that the products are single crystalline NiO structures without any sub-oxide formed on the substrates.

2.4. *Nanohybrids*

The hotplate technique has been used to fabricate hybrid nanostructures, which consist of two or more materials in one system. Such a hybrid system could provide opportunities for multi-functional devices. According to the sequence of fabrication of components in hybrids, the growth can be parallel or sequential. In the former, all the materials/structures in hybrids are formed simultaneously and the mixture of different materials is often used as source of growth. In the sequential fabrication, one structure is synthesized, followed by the growth of another structure.

As a typical example of parallel growth, ZnO/CuO hybrid nanostructures have been simultaneously synthesized by directly heating CuZn alloy (brass) on a hotplate in ambient conditions.[24] With the increase in Zn concentration in brass, the dominant products transition from CuO nanowires to ZnO nanostructures. Both CuO nanowires and ZnO nanoflakes are obtained from the brass substrates with intermediate ZnO content. By changing the growth temperature from 300 to 540°C and the local Zn content, 1D ZnO nanowires/nanoflakes, 2D ZnO nanosheets and complicated 3D ZnO networks are obtained. Electron microscopy studies show the as-synthesized ZnO nanoflakes and nanosheets are single crystalline. It is worth noting that although CuO and ZnO are formed simultaneously on the same substrate, no doping of Cu in ZnO or Zn in CuO was observed. The study of growth mechanisms shows that the formation of CuO and ZnO nanostructures is a kind of isolated growth, but with competition. Specifically, the morphology of ZnO is affected by the local Zn content and temperature. This is because of its relatively low melting point and high vapor pressure, compared with Cu at the same conditions. On the other hand, the growth of CuO 1D structures was suppressed by the formation of ZnO. Cu clusters in brass may act as many tiny templates, confining the dimension of ZnO nanostructures on the brass surface. Thus, the distribution of Cu in brass provides a natural way to control the formation of ZnO nanostructures. A similar function of one metal in an alloy was also observed in the synthesis of iron oxide nanowalls from FeMn films.[18]

In another case, the fabrication of carbon nanotubes (CNTs)/ZnO nanohybrids follows the sequential route.[25] In these experiments, aligned CNT arrays were first grown on Si or quartz substrates by conventional chemical vapor deposition (CVD) technique.[26] After that, the Zn metal was sputtered on the as-grown CNTs and the sample was then subject to heating on a hotplate. Upon cooling, chain-like ZnO nanoparticles were formed on the CNT side walls, as shown in the SEM image in Fig. 6. It was found that the average diameter of ZnO nanoparticles increases from 19.2 to 26.2 and 36.6 nm, with the increase of Zn coating duration from 1 min to 3 min and 5 min. Correspondingly, the average distance between particles was reduced. Raman and photoluminescence (PL) studies were used to confirm the existence of ZnO structures. From TEM investigations (Fig. 6(b)), it can be seen that from 1–3 min coating, hollow ZnO beads are formed along the multiwalled nanotubes (MWNTs). For 5 min coating, most of the particles are solid. Furthermore, the ZnO nanoparticles are single crystalline and the MWNT structure remains intact. A thin amorphous layer was observed to surround the particle and connect the wall of the MWNT at the same time. Such compact connections between the MWNT and ZnO nanoparticle could be due to the good wettability of melted Zn on the surface of CNTs. X-ray photoelectron spectroscopy (XPS) studies have clarified

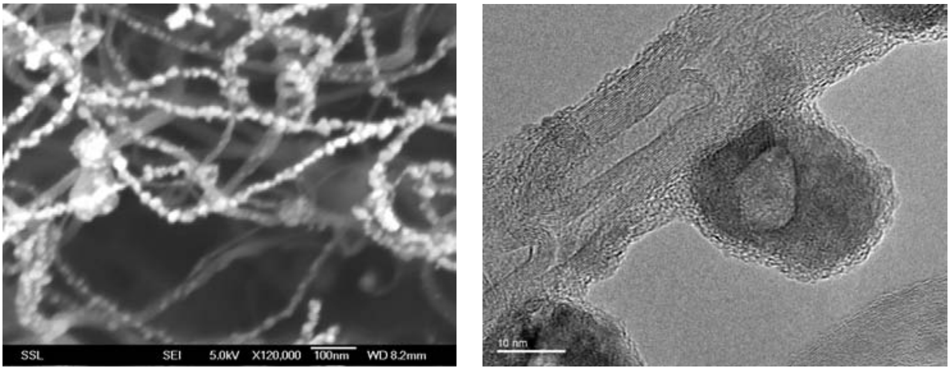

(a)

(b)

Fig. 6. Typical (a) SEM and (b) TEM images of ZnO beaded CNTs.

the presence of Zn–O bonding, but no Zn–C is formed during the heating. As two important building blocks in nanotechnology, ZnO nanoparticles and CNTs are successfully assembled as hybrid structures, and have potential applications in future multi-functional nanodevices.

3. Applications

3.1. *Field emission*

Field emission is the process whereby electrons exit a solid by tunneling through the surface potential barrier. Based on Fowler–Nordheim (FN) theory,[27,28] the emission current density J can be expressed as function of local electrical field F

$$J = \frac{AF^2}{\phi}\exp\left(-\frac{B\phi^{3/2}}{F}\right), \tag{1}$$

where A and B are constants, ϕ is the work function of the emitter. In most experimental measurements, a macroscopic electric field E is applied with little knowledge of the local electric field near the emitter, F. The exact local emission current density J is not readily measured, especially for emitters with multiple emission sites. Thus, the effective emission area γ and enhancement factor β are often defined to connect the experimental data with Eq. (1) by the relationships

$$J = I/\gamma \tag{2}$$

and

$$F = E\beta, \tag{3}$$

in which I is the total current from the measurement. On the other hand, by plotting the FN curve ($I/E^2 \sim 1/E$), information on the work function or enhancement factor can be obtained from the slope, and the intercept gives the effective emission area after the enhancement factor has been determined.

With high aspect ratios, nanostructures may demonstrate exceptional field emission performance.[29] In particular, a good electrical contact can be created between the nanostructures and the substrates when they are directly synthesized on the metals with the hotplate technique. The field emission properties of the nanostructures mentioned above have been systematically investigated for potential applications as field emitters. For example, CuO nanowire films were used as field emission cathodes in a two-plate and transparent anode setup.[9] A typical field emission current density–electric field (J–E) curve is shown in Fig. 7(a). A low turn-on field of 3.5–$4.5\,\mathrm{V}\,\mu\mathrm{m}^{-1}$ and a large current density of $0.45\,\mathrm{mA}\,\mathrm{cm}^{-2}$ under an applied field of about $7\,\mathrm{V}\,\mu\mathrm{m}^{-1}$ have been observed. From the fluorescence image in the inset of Fig. 7(a), we can see the field emission is uniform and no significant screening or edge effect was detected. Furthermore, by comparing the field emission properties of two types of samples with different average lengths and densities ($30\,\mu\mathrm{m}$, $10^8\,\mathrm{cm}^{-2}$ and $4\,\mu\mathrm{m}$, $4\times10^7\,\mathrm{cm}^{-2}$, respectively), it was found that the large length-to-radius ratio of CuO nanowires effectively improved the local field, and the side wall nearby the tip remarkably contributed to high emission current. Verified with finite element calculation, the work function of oriented CuO nanowire films was estimated to be 2.5–2.8 eV, consistent with the estimation from a previous report.[30] Using a similar configuration, the field emission of Co_3O_4 nanowalls was studied.[15] Due to their rough edges, the vertical aligned nanowalls demonstrated low turn-on field of $6\,\mathrm{V}\mu\mathrm{m}^{-1}$ and a maximal current density of $25\,\mu\mathrm{A}\,\mathrm{cm}^{-2}$ under an electrical field of $11\,\mathrm{V}\mu\mathrm{m}^{-1}$. Repeated measurements on different samples showed that the turn-on field varied between 5 to $7\,\mathrm{V}\mu\mathrm{m}^{-1}$, and no sign of saturation was observed up to the maximal field of our system. Reasonably uniform field emission image was recorded under a fixed field of $11\,\mathrm{V}\mu\mathrm{m}^{-1}$. From the FN plots of Co_3O_4 nanowalls field emission, two linear regions were obtained, corresponding to the enhancement factors of 302 and 1118 at low and high electric fields, respectively.

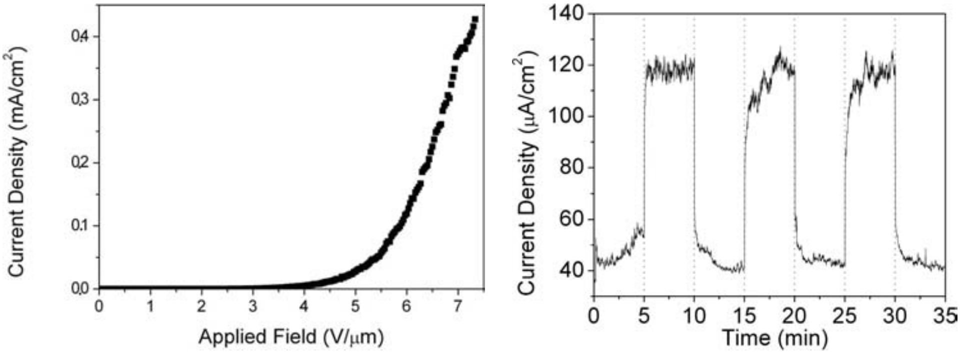

(a) (b)

Fig. 7. (a) Typical field emission J–E curve of CuO nanowires; inset shows uniform emission image. (b) Shows current changes under a fixed voltage upon infrared (1064 nm) laser irradiation.

Fabrication of α-Fe_2O_3 nanoflakes on sharp tips allows us to study the field emission from a small number of emitters. The field emission measurements were carried out on α-Fe_2O_3 nanoflakes grown on AFM[31] and etched W tips.[14] Repeated experiments demonstrated that the turn-on voltage of the α-Fe_2O_3 nanoflakes on AFM tips varied between 400–600 V with an electrode distance of 150 μm. At an applied voltage of 900 V, the emission current reaches 160 nA. Estimating the emission area to be 10 μm^2, which includes several tens to one hundred emitters according to the SEM image, a current density of as high as 1.6 Acm^{-2} under 900 V on the apex of the AFM tip is obtained. Two linear regions were also observed from the FN plots of Fe_2O_3 nanoflakes. According to FN theory, the effective emission areas were estimated to be 0.012 nm^2 at lower voltages and 60 nm^2 at higher voltages. Comparing with the latter, the extreme small value at low field strongly suggests the participation of only a few emitters. It is proposed that the different turn-on voltages for different nanoflakes result in the nonlinear feature in FN plots.

The field emission property of Fe_2O_3 nanoflakes grown on etched W tips was also studied in a field emission microscope (FEM) setup. With FEM under ultrahigh vacuum, the emission point sources can be traced on a fluorescence display. Three voltages, namely 500, 700 and 900 V were applied to the anode ring to obtain average emission currents of 1.3 nA, 66.4 nA and 0.6 mA, respectively. It was observed that at low current of nA level, the current fluctuation was about 16%. However, for the emission under 700 and 900 V, a small fluctuation of less than 4% was obtained. This result is indicative of the stability of MWNT tips and films.[32] It is believed that the large current fluctuation at low current can be ascribed to the shifting of emitting sites within nanoflakes or the mobility of adsorbates.[33] Under high current values, multiple-point emission may average out the current fluctuations induced by individual nanoflakes. From the corresponding FEM images shown in Fig. 8, a significant increase in the number of bright spots was observed, suggesting an increase in the number of active emitters or emission sites. Furthermore, with the increase in the voltage, several spots became much brighter, indicating a larger emission current. However, when the voltage increased from 700 to 900 V, some spots weakened or disappeared, due to the failure of some emitters under high currents.

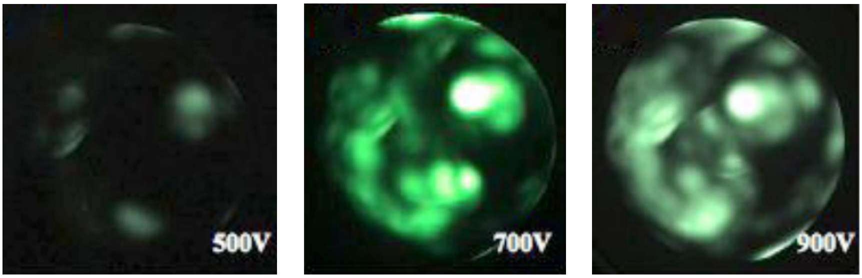

(a) (b) (c)

Fig. 8. FEM images of α-Fe_2O_3 nanoflakes grown on a W tip.

Using a piezoelectric stage with nanometer resolution, individual $WO_{3\text{-}x}$ nanowires mounted on chemically etched tungsten tips were subject to field emission studies.[20] In order to pick up one nanowire from the as-grown sample on the glass slide, the tungsten tip coated with some carbon paste, which was used to pick up nanowires selectively with the assistance of a microprobe station. A typical nanowire has a length of about $20\,\mu$m and a diameter of about 140 nm. With a vacuum distance of about $350\,\mu$m, the turn-on voltage is around 640 V and the field emission current reaches a maximum of about 250 nA at a voltage of 900 V. After 720 V, the field emission curve shows large fluctuations. Compared with the field emission result from $WO_{3\text{-}x}$ nanowire films,[34] and considering the low vacuum of the field emission chamber, this fluctuation could be attributed to residual gas adsorption or other environmental vibration or stress under high voltage. From the FN formula, the enhancement factor is estimated to be $9.8 \times 10^4\,\text{cm}^{-1}$, which is comparable to the results from single carbon nanotubes,[35] and small number of α-Fe_2O_3 nanoflakes on an AFM tip.

3.2. *Field emission enhancement*

The transparent anode technique in our field emission setup allows us to investigate the effect of external light illumination on the field emission of nanowires, especially those with narrow bandgaps such as CuO nanowires. As can be seen from Fig. 7(b), laser irradiation was able to effectively enhance the field emission current of CuO nanowire arrays.[36] The laser intensity, wavelength, emission current and working vacuum have significant influence on the enhancement. With systematical studies of these parameters, the observed laser induced enhancement in field emission current is attributed to the interplay of two factors, namely, laser induced electron transition to excited states and surface oxygen desorption. Among these factors, the contribution from extra excited electrons, which increases the number of electrons in the conduction band of CuO for subsequent tunneling, is dominant. A physical process of laser induced enhancement has been proposed for the observed enhancement. This laser irradiation tuned field emission property of CuO nanowires could be useful for designing future vacuum nanodevices, such as photodetectors or switches, based on field emission of nanowires.

In another effort to create a better control of the field emission property, CF_4 and O_2 plasma from reactive ions etching (RIE) were found to be able to improve the field emission of CuO nanowire films.[37,38] Comparing the same nanowire before and after treatments showed that 10 min of plasma treatment reduces the tip diameter of nanowires by an average of 9 nm. Furthermore, the nanowire tips sharpened and/or bent resulting in a larger effective field emission area. O_2 plasma removed the amorphous layer on the surface of as-grown nanowires, and CF_4 plasma induced fluorinated carbon on the surface of nanowires and reduced the work function by about 0.5 eV. All these factors contribute to the improved field emission current density and lower the turn-on field. It is suggested that this plasma technique can also be extended to other nanomaterials, thus providing a direct means to control the tip diameters and to functionalize the surface morphologies of nanowires for various applications.

3.3. *Li-ion battery*

Nanostructured metal oxides have attracted a lot of attention in recent years as electrodes for lithium-ion batteries because of their potential attributes of better chemical suitability and enlarged effective surface area.[39,40] The hotplate technique provides a simple and cost-effective way to fabricate electrodes used in Li-ion batteries. In a typical example, excellent electrochemical properties have been obtained from α-Fe_2O_3 nanoflakes prepared on Cu foil by directly heating Fe coatings on Cu.[41] The reversible Li-cycling properties have been evaluated by cyclic voltammery, galvanostatic discharge–charge cycling, and impedance spectral measurements on cells with Li metal as the counter and reference electrodes, at ambient temperature. Results show that Fe_2O_3 nanoflakes exhibit a stable capacity of $680 \pm 20\,\mathrm{mAhg}^{-1}$, corresponding to 4.05 ± 0.05 moles of Li per mole of Fe_2O_3 with no noticeable capacity fading up to 80 cycles when cycled in the voltage range 0.005–3.0 V at $65\,\mathrm{mAg}^{-1}$ (0.1 C rate), and with a Coulomb efficiency of $> 98\%$ during cycling (after the 15th cycle). The average discharge and charge voltages are 1.2 and 2.1 V, respectively. The observed cyclic voltammograms and impedance spectra have been analyzed and interpreted in terms of a "conversion reaction" involving nanophase Fe^0–Li_2O. The superior performance of Fe_2O_3 nanoflakes is clearly established by a comparison of the results with those for Fe_2O_3 nanoparticles and nanotubes reported in the literature.

Similarly, the potential use of the NiO nanowalls grown using the plasma assisted hotplate technique in Li-ion batteries was investigated in detail.[23] Remarkably, NiO nanowalls showed excellent capacity retention and high rate capability on cycling. Figure 9 demonstrates the typical galvanostatic curves using NiO nanowalls as electrodes. It was able to achieve a discharge capacity of $\sim 638\,\mathrm{mAhg}^{-1}$ (1.25 C rate) at the end of 85 cycles when cycled between 3.0 V and 5 mV (vs. Li). The superior electrochemical performance of NiO nanowalls in comparison to the previously reported results on nanosized NiO particles can be attributed to its large surface area and shorter diffusion length for mass and charge transport. In addition, an attribute of this synthesis approach is the feasibility of straightforward electrochemical studies of the as-made nanostructures without further post-growth assembly and manipulation.

3.4. *Gas sensing*

As an *n*-type semiconductor, the presence of oxygen deficiencies in $WO_{3\text{-}x}$ could make it sensitive to gas adsorption. For example, oxygen adsorption may trap electrons and form a depletion layer, leading to a decrease in the carrier density. In contrast, the presence of reducing gases such as NH_3 gives rise to an increase in

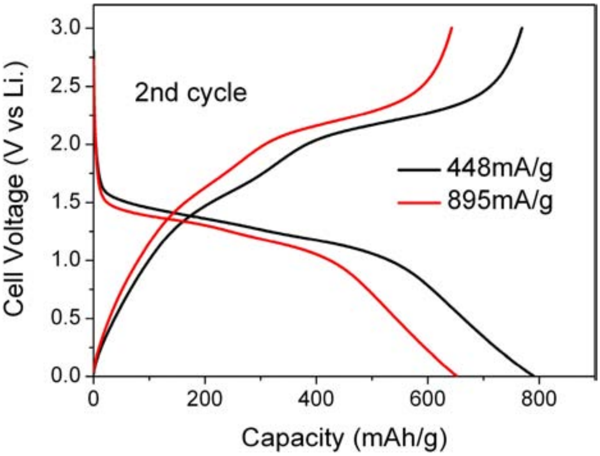

Fig. 9. Galvanostatic cycling plots (voltage vs. capacity) of NiO nanowalls. Current density and cycle number are indicated.

conductivity due to its reaction with adsorbed oxygen.[42] With large aspect ratio and higher ratio of surface area to volume, $WO_{3\text{-}x}$ nanowires may demonstrate more excellent gas sensing properties with high selectivity.[43] Such an investigation has been implemented by measuring the conductance of individual nanowires under controllable gas atmospheres.[44] It was found that the current through the nanowires had a remarkable increase upon introducing NH_3 gas into the chamber. However, the response is still slow at the current stage of study and the resolution needs to be improved with more delicate design of device and measurement skills. On the other hand, when the nanowires are exposed to laser emitting blue light, both the absorbed oxygen species such as the O_2, O_2^-, O^{2-} and the water species such as the H_2O and OH^- that cause the depletion layer may become removed, generating electron–hole pairs, thereby increasing the nanowire conductivity. Such an increase has been observed from $WO_{3\text{-}x}$ nanowires upon laser irradiation under ambient conditions. At high vacuum condition, the blue light irradiation shows an irreversible effect on the nanowires since the number of water and oxygen molecules decreases drastically in vacuum. Such behavior could be used to fabricate nanowire based laser sensors.

3.5. *Ultrafast optical device*

With a wide bandgap and large exciton binding energy, ZnO has attracted intensive research interest for its potential applications in opto-electronic devices.[45] Based on ZnO nanowires, a large second-order nonlinearity has been obtained from nonlinear absorption (NLO) measurements using a near field scanning optical microscope (NSOM) setup,[46] suggesting that ZnO nanowires could be useful as an effective frequency converter in the UV region. Interesting absorptive and refractive nonlinearities have also been observed from a film of MWNTs grown mainly along the direction perpendicular to the surface of quartz substrate.[47] In contrast to ZnO, which could demonstrate strong nonlinear multi-photon absorption,[48] CNTs show negative absorption or optical bleaching. On the basis of the different nonlinear optical properties of CNTs and ZnO, a tunable nonlinear optical property has been observed from ZnO/CNTs hybrids prepared by the hotplate technique.[25] By changing the concentration of ZnO nanoparticles in the ZnO/MWNTs hybrid system, the resultant nonlinear absorption can be controlled due to the interplay between the three-photon absorption in ZnO nanoparticles and the saturable absorption in CNTs. Furthermore, with 220 fs-780 nm laser pulses as probes, degenerate pump–probe experiments have demonstrated fs scale ultrafast recovery from ZnO/CNTs hybrids. Such absorption suggests that the samples can be used as saturable absorber devices. These devices can offer a potentially simple and cost-effective solution for passive optical regeneration, error-free transmission distances for periodically amplified optical transmission systems, laser-mode locking based on a saturable absorber, and high noise-suppression capability, as reported by Set *et al.*[49] and Yamashita *et al.*[50]

4. Concluding Remarks

The hotplate technique has shown success for the synthesis of metal oxide nanostructures directly on metal foils or metal coated substrates. With this simple technique, a wide range of products have been fabricated. These materials include CuO nanowires, α-Fe_2O_3 nanoflakes, Co_3O_4 nanowalls, $WO_{3\text{-}x}$ nanowires, MoO_3 and V_2O_5 nanobelts, and hybrid systems such as ZnO/CuO and ZnO/CNTs. Most products have uniform morphologies, single crystalline structures and pure chemical components. By using oxygen plasma in a closed chamber with controlled ambient, the morphology of Co_3O_4 can be controlled as nanowires or nanowalls. In addition, some nanostructures like NiO nanowalls, which cannot be grown under normal ambient conditions, can be fabricated with the assistance of an oxygen plasma. Based on the nanomaterials synthesized with the hotplate technique, a few applications such as field emitters, Li-ion battery electrodes, gas sensors and ultrafast optical devices have been demonstrated. In particular, the field emission properties of these oxide nanostructures have been systematically investigated and methods including plasma etching, laser irradiation and laser pruning have been utilized to improve their field emission performance.

All these examples have shown that the hotplate technique is versatile for the fabrication of metal oxide nanostructures. The method provides a relatively simple and cost-effective route for the synthesis of oxide nanostructures. This chamber-free method makes it possible to grow nanostructures on a large scale, which is essential for future industrial applications. On a hotplate, the complicated and extensive parameter exploration, which is often needed for a closed-chamber method, is simplified. This would significantly shorten the investigation process for the fabrication of those materials *en route* to novel morphologies. In addition, in view of the relatively low synthesis temperature for this method, we can readily combine it with current device technologies based on silicon and other low-melting-point polymers.

In this review, only a few high-melting-point metals have been investigated using the hotplate method to obtain their nanostructure counterparts. To improve the versatility of this method, it is necessary to test more materials in the future. The growth of low-melting-point metal oxide by heating pure metal plates using the hotplate method, e.g. ZnO, remains a challenge. Although ZnO has been obtained from brass and Zn foils, the morphological control is still not satisfactory. More work is needed to determine the suitable parameters for the direct oxidization of pure low-melting-point metals such as Zn, Sn, Al, Mn, Pb and so on, because many of these metal oxide nanostructures have shown superior electronic and optical properties. It will be interesting to further elucidate the growth kinetics of the nanostructures, especially under ambient conditions. Some *in-situ* methods such as growth under the monitoring of Raman and XRD could give more information on the details of the growth process. Furthermore, it is worth noting that besides the ease of fabrication, environmental compatibility is also a very important issue for future research. Thus, it is necessary to analyze the chemical components of exhaust products during growth, and to find suitable ways to eliminate their effects on our environment.

In future work, the range of characterization and application studies should be broadened. In addition to conventional structural and chemical component characterizations, other properties of our as-grown nanostructures such as mechanical modulus and electrical transport need to be investigated. In fact, three point studies have shown that $WO_{3\text{-}x}$ nanowires have a typical Young's modulus at GPa order[20] and a high breaking strength.[51] Electrical mechanical resonance is being developed to further study the mechanical properties of Co_3O_4 nanowires and V_2O_5 nanobelts. The conductivity of our nanostructures remains unknown, although preliminary measurements have shown most of them to have high resistances of up to GΩ. Four probe measurements may be useful to reduce or eliminate the effect of contact resistance. Other measurements such as field effect transistor, electromechanical coupling and electro-optical coupling studies will further promote the use of the hotplate technique.

References

1. Moriarty P, Nanostructured materials, *Rep Prog Phys* **64**:297–381, 2001.
2. Hosono H, Mishima Y, Takezoe H and MacKenzie KJD, *Nanomaterials: From Research to Applications*, Elsevier, 2006.
3. Harriott LR, Limits of lithography, *Proc IEEE* **89**:366–374, 2001.
4. Lu W and Lieber CM, Nanoelectronics from the bottom-up, *Nat Mater* **6**:841–850, 2007.
5. Rao CNR, Deepak FL, Gundiah G and Govindaraj A, Inorganic nanowires, *Prog Solid State Chem* **31**:5–147, 2003.
6. Pfefferkorn G, *Umschau Wiss u Tech* **21**:654, 1954.
7. Arnold SM and Koonce SE, Filamentary growths on metals at elevated temperatures, *J Appl Phys* **27**:964, 1956.

8. Yu T, Zhao X, Shen ZX, Wu YH and Su WH, Investigation of individual CuO nanorods by polarized micro-Raman scattering, *J Crystal Growth* **268**:590–595, 2004.
9. Zhu YW, Yu T, Cheong FC, Xu XJ, Lim CT, Tan VBC, Thong JTL and Sow CH, Large-scale synthesis and field emission properties of vertically oriented CuO nanowire films, *Nanotechnol* **16**:88–92, 2005.
10. Tan EPS, Zhu Y, Yu T, Dai L, Sow CH, Tan VBC and Lim CT, Crystallinity and surface effects on Young's modulus of CuO nanowires, *Appl Phys Lett* **90**:163112, 2007.
11. Lim KY, Sow CH, Lin J, Cheong FC, Shen ZX, Thong JTL, Chin KC and Wee ATS, Laser pruning of carbon nanotubes as a route to static and movable structures, *Adv Mater* **15**:300–303, 2003.
12. Yu T, Sow CH, Gantimahapatruni A, Cheong FC, Zhu Y, Chin KC, Xu X, Lim CT, Shen Z, Thong JTL and Wee ATS, Patterning and fusion of CuO nanorods with a focused laser beam, *Nanotechnol* **16**:1238–1244, 2005.
13. Chuang CH, Lin MT, Zhu YW, Sow CH *et al.*, unpublished (2008).
14. Yu T, Zhu Y, Xu X, Yeong KS, Shen Z, Chen P, Lim CT, Thong JTL and Sow CH, Substrate-friendly synthesis of metal oxide nanostructures using a hotplate, *Small* **2**:80–84, 2006.
15. Yu T, Zhu Y, Xu X, Shen Z, Chen P, Lim CT, Thong JTL and Sow CH, Controlled growth and field-emission properties of cobalt oxide nanowalls, *Adv Mater* **17**:1595–1599, 2005.
16. Quek WT and Sow CH, Hybrid nanosystem, NUS Thesis (2005).
17. Teo CH, Zhu Y, Gao X, Wee ATS and Sow CH, Field emission from hybrid CuO and $CuCO_3$ nanosystem*s*, *Solid State Commun* **145**:241–245, 2008.
18. Zong B, Wu Y, Han G, Yang B, Luo P, Wang L, Qiu J and Li K, Synthesis of iron oxide nanostructures by annealing electrodeposited Fe-based films, *Chem Mater* **17**:1515–1520, 2005.
19. *CRC Handbook of Chemistry and Physics*, 67th ed., CRC Press, Boca Raton, 1979.
20. Cheong FC, Varghese B, Zhu YW, Tan EPS, Dai L, Tan VBC, Lim CT and Sow CH, $WO_{3\text{-}x}$ nanorods synthesized on a thermal hot plate, *J Phy Chem C* **111**:17193–17199, 2007.
21. Frey GL, Rothschild A, Sloan J, Rosentsveig R, Popvitz-Biro RP and Tenne RJ, Investigation of the nonstoichimetric tungsten oxide nanoparticles, *J Solid State Chem* **162**:300–314, 2001.
22. Varghese B, Teo CH, Zhu Y, Reddy MV, Chowdari BVR, Wee ATS, Tan VBC, Lim CT and Sow CH, Co_3O_4 nanostructures with different morphologies and their field-emission properties, *Adv Funct Mater* **17**:1932–1939, 2007.
23. Varghese B, Reddy MV, Zhu Y, Chang SL, Teo CH, Rao GVS, Chowdari BVR, Wee ATS, Lim CT and Sow CH, Fabrication of NiO nanowall electrodes for high performance lithium ion battery, *Chem Mater* **20**:3360–3367, 2008.
24. Zhu Y, Sow CH, Yu T, Zhao Q, Li P, Shen Z, Yu D and Thong JTL, Co-synthesis of ZnO–CuO nanostructures by directly heating brass in air, *Adv Funct Mater* **16**:2415–2422, 2006.
25. Zhu Y, Elim H, Foo YL, Yu T, Liu Y, Ji W, Lee JY, Shen Z, Wee ATS, Thong JTL and Sow CH, Multiwalled carbon nanotubes beaded with ZnO nanoparticles for ultrafast nonlinear optical switching, *Adv Mater* **18**:587–592, 2006.
26. Wang YH, Lin J, Huan CHA and Chen GS, Synthesis of large area aligned carbon nanotube arrays from C_2H_2–H_2 mixture by rf plasma-enhanced chemical vapor deposition, *Appl Phys Lett* **79**:680–682, 2001.
27. Fowler RH and Nordheim LW, Electron emission in intense electric fields, *Proc R Soc Lond A* **119**:173–181, 1928.

28. Good RH and Mueller EW, Field emission, in *Handbook der Physik*, Vol. 21, Ed. S. Flügge, Springer-Verlag, Berlin, 1956, pp. 176–231.
29. Xu NS and Huq SE, Novel cold cathode materials and application, *Mater Sci Eng Rep* **48**:47–189, 2005.
30. Hsieh CT, Chen JM, Lin HH and Shih HC, Field emission from various CuO nanostructures, *Appl Phys Lett* **83**:3383–3385, 2003.
31. Zhu YW, Yu T, Sow CH, Liu YJ, Wee ATS, Xu XJ, Lim CT and Thong JTL, Efficient field emission from α-Fe_2O_3 nanoflakes on an atomic force microscope tip, *Appl Phys Lett* **87**:023103, 2005.
32. Bonard JM, Maier F, Stöckli T, Châtelain A, de Heer WA, Salvetat JP and Forró L, Field emission properties of multiwalled carbon nanotubes, *Ultramicroscopy* **73**:7–15, 1998.
33. Collins PG and Zettl A, Unique characteristics of cold cathode carbon-nanotube-matrix field emitters, *Phys Rev B* **55**:9391–9399, 1997.
34. Zhou J, Gong L, Deng SZ, Chen J, She JC, Xu NS, Yang R and Wang ZL, Growth and field-emission property of tungsten oxide nanotip arrays, *Appl Phys Lett* **87**:223108, 2005.
35. Lovall D, Buss M, Graugnard E, Andres RP and Reifenberger R, Electron emission and structural characterization of a rope of single-walled carbon nanotubes, *Phys Rev B* **61**:5683–5691 (2000).
36. Zhu YW, Thong JTC and Sow CH, Enhanced field emission from CuO nanowire arrays by in situ laser irradiation, *J Appl Phys* **102**:114302, 2007.
37. Zhu YW, Moo AM, Yu T, Xu XJ, Lim CT, Ong CK, Shen ZX, Wee ATS, Thong JTL and Sow CH, Enhanced field emission from O_2 and CF_4 plasma-treated CuO nanowires, *Chem Phys Lett* **419**:458–463, 2006.
38. Zhu YW, Teo CH, Xu XJ, Yu T, Gao X, Lim CT, Ong CK, Wee ATS, Thong JTL and Sow CH, Effects of O_2 reactive iron etching on the field emission properties of aligned CuO nanowire films, *Solid State Phenom* **121**–**123**:793–796, 2007.
39. Poizot P, Laruelle S, Grugeon S, Dupont L and Taracon JM, Nano-sized transition-metal oxides as negative-electrode materials for lithium-ion batteries, *Nature* **407**:496–498, 2000.
40. Arico AS, Bruce PG, Scrosati B, Tarascon JM and Schalkwijk WV, Nanostructured materials for advanced energy conversion and storage devices, *Nat Mater* **4**:366–377, 2005.
41. Reddy MV, Yu T, Sow CH, Shen ZX, Lim CT, Rao CVS and Chowdari BVR, α-Fe_2O_3 nanoflakes as an anode material for Li-ion batteries, *Adv Funct Mater* **17**:2792–2799, 2007.
42. Llobet E, Molas G, Molinas P, Calderer J, Vilanova X, Brezmes J, Sueiras JE and Correig X, Fabrication of highly selective tungsten oxide ammonia sensors, *J Electrochem Soc* **147**:776–779, 2000.
43. Ponzoni A, Comini E, Sberveglieri G, Zhou J, Deng SZ, Xu NS, Ding Y and Wang ZL, Ultrasensitive and highly selective gas sensors using three-dimensional tungsten oxide nanowire networks, *Appl Phys Lett* **88**:203101, 2006.
44. Xie Y, Cheong FC, Varghese B, Zhu YW, Ramanathan M and Sow CH, Photo and gas sensing properties of discrete crystalline tungsten oxide nanowires, submitted (2008).
45. Fan Z and Lu JG, Zinc oxide nanostructures: Synthesis and properties, *J Nanosci Nanotechnol* **5**:1561–1573, 2005.
46. Johnson J, Choi HJ, Knutsen KP, Schaller RD, Yang P and Saykally RJ, Single gallium nitride nanowire lasers, *Nat Mater* **1**:106–110, 2002.

47. Elim HI, Ji W, Ma GH, Lim KY, Sow CH and Huan CHA, Ultrafast absorptive and refractive nonlinearities in multiwalled carbon nanotube films, *Appl Phys Lett* **85**:1799–1801, 2004.
48. He J, Qu YL, Li HP, Mi J and Ji W, Three-photon absorption in ZnO and ZnS crystals, *Opt Exp* **13**:9235–9247, 2005.
49. Set SY, Yaguchi H, Tanaka Y and Jablonski M, Laser mode locking using a saturable absorber incorporating carbon nanotubes, *J Lightwave Technol* **22**:51–56, 2004.
50. Yamashita S, Inoue Y, Maruyama S, Murakami Y, Yaguchi H, Jablonski M and Set SY, Saturable absorbers incorporating carbon nanotubes directly synthesized onto substrates and fibers and their application to mode-locked fiber lasers, *Opt Lett* **29**:1581–1583, 2004.
51. Zhang YS, Zhu YW, Tan EPS, Dai L, Tan VBC, Sow CH and Lim CT, Bending strength of individual tungsten oxide nanowires, submitted (2008).

Part 4

MOLECULAR ENGINEERING

π–d INTERACTION BASED MOLECULAR CONDUCTING MAGNETS: HOW TO INCREASE THE EFFECTS OF THE π–d INTERACTION

AKIRA MIYAZAKI*,[a] and TOSHIAKI ENOKI
Department of Chemistry, Tokyo Institute of Technology
Ookayama, Meguro-ku, Tokyo 152-8551, Japan
**miyazaki.a.aa@m.titech.ac.jp*

The crystal structures and electronic and magnetic properties of conducting molecular magnets developed by our group are reviewed from the viewpoints of our two current strategies for increasing the efficiency of the π–d interaction. $(EDTDM)_2FeBr_4$ is composed of quasi-one-dimensional donor sheets sandwiched between magnetic anion sheets. The ground state of the donor layer changes from the insulator state to the metallic state by the application of pressure. When it is near to the insulator–metal phase boundary pressure, the magnetic order of the anion spins considerably affects the transport properties of the donor layer. The crystal structure of $(EDO\text{–}TTFBr_2)_2FeX_4$ (X = Cl, Br) is characterized by strong intermolecular halogen–halogen contacts between the organic donor and FeX_4 anion molecules. The presence of the magnetic order of the Fe^{3+} spins and relatively high magnetic order transition temperature proves the role of the halogen–halogen contacts as exchange interaction paths.

Keywords: Molecular conductors; molecular magnets; π–d interaction.

1. Introduction

The physical properties of molecular metals and superconductors based on TTF (tetrathiafulvalene) derivatives are one of the principal areas of interest in the fields of solid-state physics and chemistry.[1–3] The hybridization of molecular metals and transition metal complexes having localized magnetic moments of unpaired d-electrons yields molecular conducting magnets, where an exchange interaction between the organic donor π-electron and anion d-electron systems, termed the π–d exchange interaction, plays an important role in their physical properties. If the ground state of the π-electron layer is metallic, these materials can be regarded as the molecular version of the RKKY (Ruderman–Kittel–Kasuya–Yosida)[4–6] system such as rare-earth magnetic metals having an s–f interaction. Even if the organic π-electron systems have insulating ground states, the spins of the localized

---

[a] Present address: Department of Environmental Applied Chemistry, University of Toyoma, 3190 Gofuku, Toyama-shi, Toyama 930-8555 Japan

π-electrons can be coupled with the magnetic moments of d-electrons through the π–d exchange interaction to produce novel magnetic systems.

From these viewpoints, we have developed a number of molecular magnets based on TTF derivatives and investigated their electronic and magnetic properties in detail,[7–14] some of which have been summarized in our preceding review articles.[15–18] For example, $(DMET)_2FeBr_4$ (DMET = dimethyl(ethylenedithio)-diselena-dithiafulvalene)[19] undergoes an antiferromagnetic transition at $T_N = 4\,K$, and a clear one-to-one correspondence between the magnetization curve and magnetoresistance directly proves the existence of the π–d interaction between the donor and anion layers. Radical ion salts $(DIEDO)_2M(mnt)_2$ (DIEDO = diiodoethylenedioxotetrathiafulvalene, mnt = maleonitriledithiolate, M = Ni, Pt),[20,21] show the coexistence of metallic conductivity of the donor layer and one-dimensional (1D) ferromagnetic chain of the transition metal complex layer. A molecular weak ferromagnet (BDH-TTP)$[Cr(isoq)_2(NCS)_4]$ (BDH-TTP = 2,5-bis(1′,3′-dithiolan-2′-ylidene)-1,3,4,6-tetrathiapentalene, isoq = isoquinoline),[23,24] is characterized by alternating chains of organic donors and transition metal complex anions, and the single-ion anisotropy of the anions and strong π–d interaction along the alternate chain lead to the spin-canted ferrimagnetic order of spins. Such π–d interaction based conducting molecular magnets have also led many research groups to make developments in the field of molecule-based magnets.[24–28] One of the typical examples is λ-$(BETS)_2FeCl_4$ (BETS = bis(ethylenedithio)tetraselenafulvalene),[29,30] in which a magnetic insulating state is destroyed by a magnetic field and lead to field-induced superconductivity.

In this review, we discuss our two current strategies for increasing the effectiveness of the π–d interaction with respect to the physical properties of the molecular systems. The first strategy is the use of quasi-1D electronic systems as the π-electron layers. It is known that such systems lead to a metal–insulator transition due to the electronic instability, and their ground state often becomes a spin density wave (SDW) state[31] due to the electron correlation. This SDW state has a fractional magnetic moment and can be easily converted into the metallic state by the application of low external pressure. At the boundary of the metallic and SDW states, even a small perturbation by external stimuli, e.g. a magnetic field strongly influences the physical properties of the π-electron system, which can be observed in forms such as anomalies in their electrical conductivity and/or magnetoresistance.

The other strategy is to increase the magnitude of the π–d interaction itself by the introduction of intermolecular halogen–halogen contacts. So far, the π–d interaction has generally been realized by intermolecular van der Waals contacts; the magnitude of the interaction is estimated to be of the order of maximum 1 K.[32] On the other hand, the halogen–halogen contacts have a covalency and are evidently stronger than van der Waals contacts; so, they are occasionally referred to as "halogen bonds"[33,34] in analogy to hydrogen bonds. As a result, we expect that these contacts can function as exchange paths between the conduction π-electrons on the donors and localized d-electrons on the anions, although the introduction of these

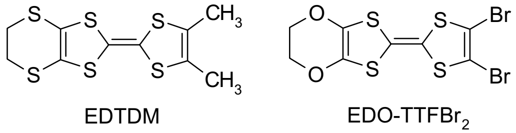

Fig. 1. Molecular structure of organic donor molecules.

contacts to molecular conductors has been investigated mainly from the viewpoint of controlling their crystal structures.[35–39]

In this review, we focus on the transport properties and magnetism of two molecular conducting magnets, each of which corresponds to the two above-mentioned strategies. In Sec. 2, $(EDTDM)_2FeBr_4$ (Fig. 1) is introduced as an example of our first strategy, in which the transport properties of the π-electron system at the metal–insulator boundary are strongly influenced by an external magnetic field to generate a large negative magnetoresistance effect.[40] As an example of our second strategy, the physical properties of $(EDO\text{-}TTFBr_2)_2FeCl_4$ and $(EDO\text{-}TTFBr_2)_2FeBr_4$ (Fig. 1) are discussed in Sec. 3, where the intermolecular halogen–halogen contacts play an important role in their magnetic and magnetotransport properties.[41]

2. Pressure-Induced Negative Magnetoresistance in $(EDTDM)_2FeBr_4$

The crystal structure of the radical ion salt $(EDTDM)_2FeBr_4$ is shown in Fig. 2, and it is characterized by an alternating stack of donor and anion layers along the c-axis. The donor layer consists of slightly dimerized donor columns directed along the $a \pm b$ direction. The intrachain transfer integrals are approximately 10 times

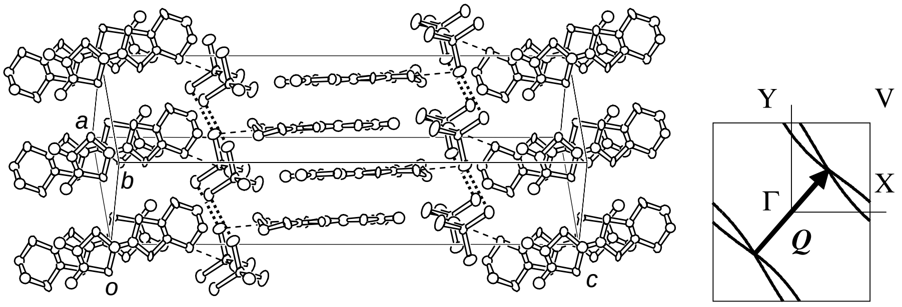

(a) (b)

Fig. 2. (a) Crystal structure of $(EDTDM)_2FeBr_4$. The dotted and dashed lines denote the intermolecular anion–anion and donor–anion contacts, respectively. (b) Fermi surfaces obtained for a donor layer around $z = 1/2$ using the tight-binding approximation without on-site Coulomb repulsion. The solid arrow represents the nesting vector $\boldsymbol{Q} \sim (\boldsymbol{a}^* \pm \boldsymbol{b}^*)/2$.

larger than the interchain transfer integrals; therefore, the donor layer is characterized as a quasi-1D system. As a result, the Fermi surfaces obtained using the tight-binding approximation have wavy shapes, as shown in Fig. 2(b); the surfaces have a possible nesting vector $\boldsymbol{Q} \sim (\boldsymbol{a}^* \pm \boldsymbol{b}^*)/2$ indicated by the arrow, showing the instability of the electron system. In the anion layer, the tetrahedral $FeBr_4$ anions form a distorted 2D square lattice by means of weak Br–Br contacts. Short intermolecular S–Br contacts are present between the donor and anion layers, and they are responsible for the realization of the π–d interaction.

Here, we first discuss the electronic structure of the π-electron layer of $(EDTDM)_2FeBr_4$ using a reference compound $(EDTDM)_2GaBr_4$ that has the same crystal structure but no unpaired d-electrons in the anion layer. According to its electrical conductivity, static magnetic susceptibility and ESR measurements, this salt is in the metallic state from room temperature down to $T_{\mathrm{MI}} \sim 11$ K, below which it undergoes a metal–insulator transition. The low temperature insulator phase is characterized as a SDW state, since the ESR signals of the donor cation radical broaden below T_{MI}, indicating the presence of magnetic order in the donor layer. From the temperature dependence of the susceptibility, the magnetic moment in the donor chain is estimated as 0.29 μ_B per donor molecule. On the other side, for the d-electron layer of $(EDTDM)_2FeBr_4$, the ground state is characterized as an antiferromagnet with a transition temperature of $T_{\mathrm{N}} \sim 3$ K.

By the application of pressure, this salt behaves as a metal down to 1.8 K above $p_{\mathrm{C}} \sim 9.2$ kbar, and the interaction between the π- and d-electron layers becomes prominent near this pressure boundary between the SDW and metallic states. Under this pressure, the temperature dependence of resistivity shows a distinct anomaly around 4 K, which corresponds to an antiferromagnetic long-range order transition of the localized d-electron system. The magnetoresistance in the $FeBr_4$ complex measured at $T = 1.8$ K has large negative values (Fig. 3(a)), and the similarity between

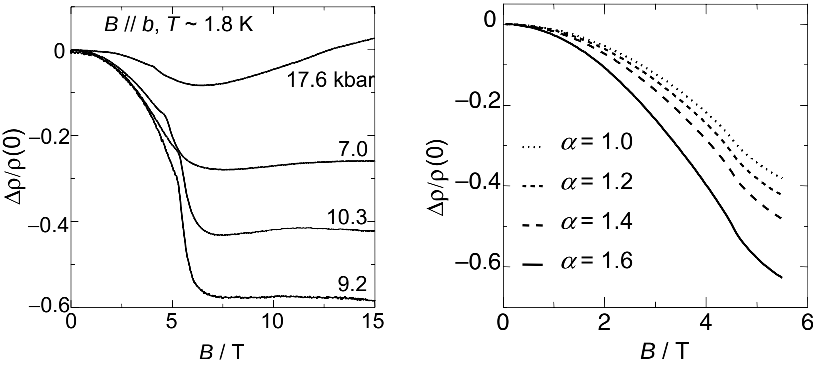

(a) (b)

Fig. 3. (a) Field dependence of the intralayer magnetoresistance of $(EDTDM)_2FeBr_4$ at $T \sim 1.8$ K under pressures of 5.4, 7.0, 10.3 and 17.6 kbar. (b) Calculated field dependence of the magnetoresistance under various pressures, expressed with an empirical parameter α (see text).

the field dependence of the magnetoresistance and the magnetization curve suggests that the behavior of the d-electron spins is responsible for this large negative magnetoresistance effect. It should be noted that this negative magnetoresistance effect is most significant around p_C. This suggests the important role of the quasi-1D electronic instability in the appearance of this negative magnetoresistance effect.

These experimental results are effectively reproduced by the tight-binding electronic structure calculation including the on-site Coulomb repulsion interaction U and the π–d exchange interaction $J_{\pi d}$. Due to the quasi-1D nature, the π-electron system is most sensitive to a perturbation by the wave vector $\boldsymbol{Q} \sim (\boldsymbol{a}^* \pm \boldsymbol{b}^*)/2$, which corresponds to that of the antiferromagnetic spin alignment in the anion layer. The d-electron spins $\boldsymbol{S}_d(\boldsymbol{Q})$ induce the internal field to the π-electron layers to trigger the spin polarization $\delta \boldsymbol{s}_\pi(\boldsymbol{Q})$ of the π-electron layer, which then influence the SDW energy gap to realize the magnetoresistance effect. Using this model, the magnetoresistance is calculated as a function of the applied field and pressure, as shown in Fig. 3(b), where the pressure effect is introduced to the interchain transfer integrals using an empirical factor α as $t_\perp(p) = \alpha\ t_\perp(0)$. The good agreement between the experimental (Fig. 3(a)) and calculation (Fig. 3(b)) results strongly supports the supposition that the quasi-1D electronic instability is responsible for the large anomalous negative magnetoresistance of this material by amplifying the effect of the d-electron spins on the electron transport of the π-electrons of the donor system through the π–d interaction.

3. Effect of Halogen–Halogen Interactions in (EDO-TTFBr$_2$)$_2$FeX$_4$ (X = Cl, Br)

The two radical ion salts (EDO-TTFBr$_2$)$_2$FeCl$_4$ and (EDO-TTFBr$_2$)$_2$FeBr$_4$ have the same crystal structure, as shown in Fig. 4(a). The organic donor molecules

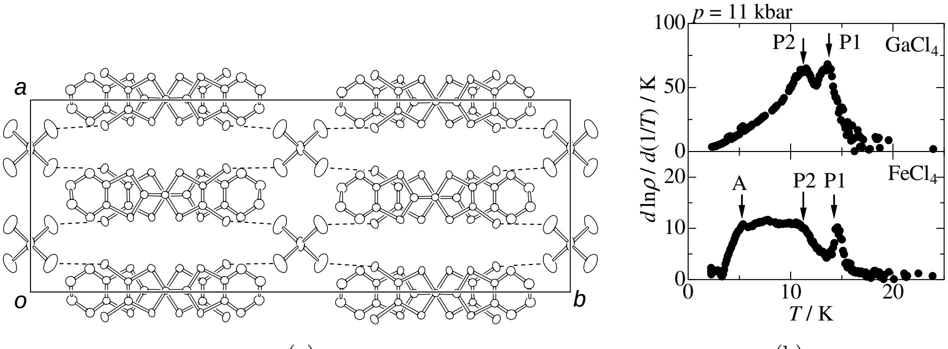

(a) (b)

Fig. 4. (a) Crystal structure of (EDO-TTFBr$_2$)$_2$FeCl$_4$. The dashed lines denote close intermolecular donor–anion contacts. (b) Temperature dependence of $d \ln \rho / d(T^{-1})$, i.e., slope of the Arrhenius plot, of (EDO-TTFBr$_2$)$_2$GaCl$_4$ and (EDO-TTFBr$_2$)$_2$FeCl$_4$ at 11 kbar. The anomalies P1, P2 and A (see text) are indicated by arrows.

form uniform quasi-1D columns along the *c*-axis (perpendicular to the drawing plane), and the anions are sandwiched between them. Inside the anion layers, the halogen–halogen distances are longer than the van der Waals distances; therefore, the intermolecular halogen–halogen contacts are negligibly small. The most remarkable intermolecular contacts are short Br–Br or Br–Cl contacts observed between the bromide substituent of the donors and the anion ligands, which are significantly shorter than the corresponding van der Waals distances.

These salts exhibit metallic behavior around room temperature regardless of the counter anions. In the low-temperature region, the metallic behavior of this salt gradually changes to semiconductive. From the ESR spectra and static magnetic susceptibilities, the ground state of the π-electron layer is characterized as the SDW states. The metal–insulator transition is most remarkably observed in the form of peaks in the plot of the activation energy $E_{\mathrm{A}} = d\ln \rho/d(T^{-1})$ (ρ = resistivity) as a function of temperature, which become more prominent under pressure (Fig. 4(b)). For the $\mathrm{GaCl_4}$ salt without any magnetic anions, two anomalies P1 and P2 that show successive transitions are observed (upper panel). When the counter anions are replaced with magnetic $\mathrm{FeCl_4}$, another peak A appears around 5 K (lower panel), indicating the interaction between the π- and *d*-electron systems.

The magnetic susceptibilities of the $\mathrm{FeCl_4}$ and $\mathrm{FeBr_4}$ salts obey the Curie–Weiss law, and negative Weiss temperatures ($\mathrm{FeCl_4}$: -9.0 K, $\mathrm{FeBr_4}$: -23 K) indicate the presence of the antiferromagnetic exchange interaction between the *d*-electron spins. The susceptibility of the $\mathrm{FeCl_4}$ salt shows a broad peak around 7 K due to the magnetic short-range ordering (Fig. 5(a)); then, it undergoes an antiferromagnetic phase transition at $T_{\mathrm{N}} = 4.2$ K. It should be noted that no significant Cl–Cl contacts are observed between the magnetic ions in the $\mathrm{FeCl_4}$ salt; therefore, the magnetic ordering in this salt must be realized with anion–donor–anion contacts.

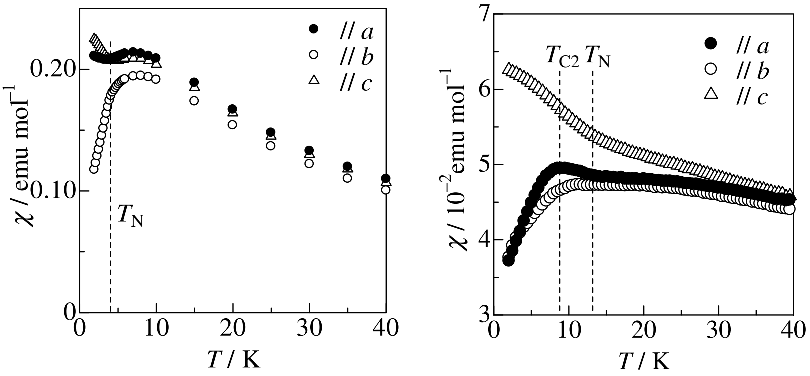

(a) (b)

Fig. 5. Temperature dependence of the static magnetic susceptibility of (a) $\mathrm{FeCl_4}$ and (b) $\mathrm{FeBr_4}$ salts measured at an external field of B = 1 T after the core diamagnetic contributions are subtracted.

On the other hand, the magnetic properties of the $\mathrm{FeBr_4}$ salt show a complicated behavior (Fig. 5(b)). An antiferromagnetic transition occurs at $T_\mathrm{N} = 13.5\,\mathrm{K}$, and at $T_\mathrm{C2} = 8.5\,\mathrm{K}$, the susceptibility along the *a*-axis is the maximum and begins to decrease as the temperature decreases. These magnetic order temperatures are higher than those of the usual π–d interaction based molecular conducting magnets, indicating the effectiveness of the halogen–halogen contacts as exchange interaction paths. In the lowest temperature region, the susceptibilities along the *a*- and *b*-axes decrease and approach finite positive values, suggesting the presence of a helical-ordered spin state. This possibility is also supported by a model calculation in which the exchange interaction between the anions through the donor layer is taken into account. In other words, the complex magnetic behavior observed in this salt is also a consequence of the π–d interaction originating from the intermolecular halogen–halogen contacts.

The magnetoresistance of the $\mathrm{FeCl_4}$ salt shows more complicated behaviors, as shown in Fig. 6. In a low-field region, two stepwise increases are observed at $B_{\mathrm{SF}-\pi} \sim 1\,\mathrm{T}$ and $B_{\mathrm{SF}-d} \sim 2\,\mathrm{T}$, as indicated by arrows, which are attributed to the spin-flop transitions of the π-electron spins and *d*-electron spins, respectively. In the field above, the saturation field $B_{\mathrm{Sat}-d} \sim 12\,\mathrm{T}$ of the $\mathrm{FeCl_4}$ anions, the magnetoresistance begins to decrease as the field increases. It should also be noted that a small hysteretic behavior of the magnetoresistance curve is observed in the field range of 0 to 10 T (in the figure, only the data at 9 kbar are shown for simplicity). This complex behavior in the magnetoresistance can be qualitatively explained as the frustration of the triangles composed of one $\mathrm{EDO\text{-}TTFBr_2}$ molecule and two neighboring $\mathrm{FeCl_4}$ anions that affects the SDW state of the donor layer. This frustration diminishes successively after the spin flop of the donor and anion layers at $B_{\mathrm{SF}-\pi}$ and $B_{\mathrm{SF}-d}$, respectively, which stabilizes the SDW state to increase the resistivity. When the field reaches the saturation field of the *d*-electron spins ($B_{\mathrm{Sat}-d}$), all the

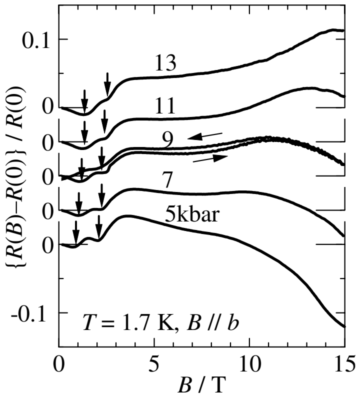

Fig. 6. Magnetoresistance of $\mathrm{(EDO\text{-}TTFBr_2)_2FeCl_4}$ under various pressures. The stepwise anomalies are indicated by arrows, and the hysteresis is shown for $p = 9\,\mathrm{kbar}$.

anion spins align along the magnetic field direction and the stabilization of the SDW state through the π–d interaction is lost; therefore, the magnetoresistance decreases above this field.

4. Summary

We have developed molecular conducting magnets based on TTF-type donors and magnetic counter anions by adopting two strategies to increase the effectiveness of the π–d interaction with respect to the physical properties. The ground state of the quasi-1D π-electron system in $(\mathrm{EDTDM})_2\mathrm{FeBr}_4$ changes from the SDW state to the metallic state by applying pressure, and near the pressure-induced insulator–metal transition point, the spin alignment of the magnetic anion layer affects the transport properties of the organic donor layer. The crystal structures of $(\mathrm{EDO\text{-}TTFBr}_2)_2\mathrm{Fe}X_4$ (X = Br, Cl) are characterized by the presence of close intermolecular halogen–halogen contacts between the donor and anion layers, which function as exchange interaction paths to produce the magnetic ordered state of the anion spins and complicated magnetotransport properties in the donor π-electron system. It is expected that the molecular conducting magnets developed by these strategies will offer a new viewpoint in the development of molecular electronics and/or spintronics driven by magnetic fields.

Acknowledgment

This work was supported by the Grant-in-Aid (Nos. 15073211 and 19550133) from the Ministry of Education, Culture, Sports, Science and Technology of Japan.

References

1. Kagoshima S, Kanoda K and Mori T (eds.), *Organic Conductors*, special topics section in *J Phys Soc Jpn* **75**: 2006.
2. Batail P (ed.), *Molecular Conductors*, special issue in *Chem Rev* **104**: 2004.
3. Ishiguro T, Yamaji K and Saito G, *Organic Superconductors*, Springer-Verlag, Heidelberg, Germany, 1998.
4. Ruderman MA and Kittel C, Indirect exchange coupling of nuclear magnetic moments by conduction electrons, *Phys Rev* **96**:99–102, 1954.
5. Kasuya T, A theory of metallic ferro- and antiferromagnetic metals, *Prog Theor Phys* **16**:45–57, 1956.
6. Yosida K, Magnetic properties of Cu–Mn alloys, *Phys Rev* **106**:893–898, 1957.
7. Miyazaki A, Okabe K, Enomoto K, Nishijo J, Enoki T, Setifi F, Golhen S, Ouahab L, Toita T and Yamada J, π–d interaction-based molecular magnets, *Polyhedron* **22**:2227–2234, 2003.
8. Enoki T, Yamazaki H, Okabe K, Nishijo J, Enomoto K, Enomoto M and Miyazaki A, Magnetism in new classes of TTF-based charge transfer complexes, *Mol Cryst Liq Cryst* **379**:131–140, 2002.
9. Miyazaki A, Enomoto M, Enomoto K, Nishijo J, Enoki T, Ogura E, Kuwatani Y and Iyoda M, π–d interaction-based molecular magnets in TTF-type salts, *Mol Cryst Liq Cryst* **376**:535–542, 2002.

10. Enomoto M, Miyazaki A and Enoki T, Magnetic properties of mixed triangle-based ladder magnets $(\mathrm{C_1TET\text{-}TTF})(\mathrm{FeBr_4})_{1-x}(\mathrm{FeCl_4})_x$(C1TET-TTF: 4,5-ethylenedithio-4′,5′-bis(methylthio)tetrathiafulvalene), *Bull Chem Soc Jpn* **74**:459–470, 2001.
11. Miyazaki A, Umeyama T, Enoki T, Ogura E, Kuwatani Y, Iyoda M, Nishikawa H, Ikemoto I and Kikuchi K, Novel molecular magnets based on organic complexes, *Mol Cryst Liq Cryst* **334**:379–388, 1999.
12. Enoki T, Umeyama T, Enomoto M, Yamaura J, Yamaguchi K, Miyazaki A, Ogura E, Kuwatani Y, Iyoda M and Kikuchi K, Novel TTF-based molecular magnets, *Synth Metals* **103**:2275–2278, 1999.
13. Miyazaki A, Enomoto M, Enoki T and Saito G, Molecular antiferromangets based on TTF-type radical ion salts, *Mol Cryst Liq Cryst* **305**:425–434, 1997.
14. Yamaura J, Suzuki K, Kaizu Y, Enoki T, Murata K and Saito G, Magnetic properties of organic conductor $(\mathrm{BEDT\text{-}TTF})_3\mathrm{CuBr_4}$, *J Phys Soc Jpn* **65**:2645–2654, 1996.
15. Enoki T and Miyazaki A, Magnetic TTF-based charge-transfer complexes, *Chem Rev* **104**:5449–5477, 2004.
16. Ouahab L and Enoki T, Multiproperty molecular materials: TTF-based conducting and magnetic molecular materials, *Eur J Inorg Chem* **2004**:933–941, 2004.
17. Miyazaki A, Enomoto K, Okabe K, Yamazaki H, Nishijo J, Enoki T, Ogura E, Ugawa K, Kuwatani Y and Iyoda M, Conducting molecular magnets based on TTF-derivatives, *J Solid State Chem* **168**:547–562, 2002.
18. Enoki T, Yamaura J and Miyazaki A, Molecular magnets based on organic charge transfer complexes, *Bull Chem Soc Jpn* **70**:2005–2023, 1997.
19. Enomoto K, Yamaura J, Miyazaki A and Enoki T, Electronic and magnetic properties of organic conductors $(\mathrm{DMET})_2\mathrm{MBr_4}$ (M = Fe, Ga), *Bull Chem Soc Jpn* **76**:945–953, 2003.
20. Nishijo J, Ogura E, Yamaura J, Miyazaki A, Enoki T, Takano T, Kuwatani Y and Iyoda M, Ferromagnetic interaction and metallic conductivity of radical ion salts $(\mathrm{DIEDO})_2\mathrm{M(mnt)_2}$ (M = Ni, Pt), *Synth Metals* **133–134**:539–541, 2003.
21. Nishijo J, Miyazaki A, Enoki T, Ogura E, Takano T, Kuwatani Y, Iyoda M and Yamaura J, Molecular metals with ferromagnetic interaction between localized magnetic moments, *Solid State Commun* **116**:661–664, 2000.
22. Kudo S, Miyazaki A, Enoki T, Golhen S, Ouahab L, Toita T and Yamada J, Pressure effect on bulk weak ferromagnets: $(\mathrm{BDH\text{-}TTP})[\mathrm{M(isoq)_2(NCS)_4}]$ (M = $\mathrm{Cr^{III}}$, $\mathrm{Fe^{III}}$; isoq = Isoquinoline), *Inorg Chem* **45**:3718–3725, 2006.
23. Setifi F, Ouahab L, Golhen S, Miyazaki A, Okabe K, Enoki T, Toita T and Yamada J, Bulk weak ferromagnet in ferrimagnetic chains of organic–inorganic hybrid materials based on BDH-TTP and paramagnetic thiocyanato complex anions: $(\mathrm{BDH\text{-}TTP})[\mathrm{M(isoq)_2(NCS)_4}]$, M = $\mathrm{Cr^{III}}$, $\mathrm{Fe^{III}}$, *Inorg Chem* **41**:3786–3790, 2002.
24. Coronado E and Day P, Magnetic molecular conductors, *Chem Rev* **104**:5419–5448, 2004.
25. Wang M, Xiao X, Fujiwara H, Sugimoto T, Noguchi S, Ishida T, Mori T and Aruga-Katori H, Antiferromagnetic or canted antiferromagnetic orderings of Fe(III) *d* Spins of $\mathrm{FeX_4^-}$ Ions in $\mathrm{BEDT\text{-}TTFVO(S)\cdot FeX_4}$ (X = Cl, Br) [BEDT-TTFVO(S) = Bis(ethylenedithio)tetrathiafulvalenoquinone(-thioquinone)-1,3-dithiolemethide], *Inorg Chem* **46**:3049–3056, 2007.
26. Naito T and Inabe T, Structural, electrical, and magnetic properties of $\alpha\text{-}(\mathrm{ET})_7[\mathrm{MnCl_4}]_2\cdot(1,1,2\text{-}\mathrm{C_2H_3Cl_3})_2$ (ET = Bis(ethylenedithio)tetrathiafulvalene), *Bull Chem Soc Jpn* **77**:1987–1995, 2004.
27. Hanasaki N, Matsuda M, Tajima T, Ohmichi E, Osada T, Naito T and Inabe T, Giant negative magnetoresistance reflecting molecular symmetry in dicyano(phthalocyaninato) iron compounds, *J Phys Soc Jpn* **75**:033703, 2006.

28. Coronado E, Galán-Mascarós JR, Gómez-García CJ and Laukhin V, Coexistence of ferromagnetism and metallic conductivity in a molecule-based layered compound, *Nature* **408**:447, 2000.
29. Kobayashi H, Cui HB and Kobayashi A, Organic metals and superconductors based on BETS (BETS = Bis(ethylenedithio)tetraselenafulvalene), *Chem Rev* **104**:5265–5288, 2004.
30. Kobayashi H, Kobayashi A and Cassoux P, BETS as a source of molecular magnetic superconductors (BETS = bis(ethylenedithio)tetraselenafulvalene), *Chem Soc Rev* **29**:325–333, 2000.
31. Grüner G, *Density Waves in Solids*, Frontiers in Physics, Addison-Wesley, Massachusetts, 1994.
32. Mori T and Katsuhara M, Estimation of π–d-interactions in organic conductors including magnetic anions, *J Phys Soc Jpn* **71**:826–844, 2002.
33. Legon C, Prereactive complexes of dihalogens XY with Lewis bases B in the gas phase: A systematic case for the halogen analogue BXY of the hydrogen bond$\cdots$BHX, *Angew Chem Int Ed Engl* **38**:2687–2714, 1999.
34. Ouvrard C, Le Questel JY, Berthelot M and Laurence C, Halogen-bond geometry: A crystallographic database investigation of dihalogen complexes, *Acta Cryst B* **59**:512–526, 2003.
35. Domercq B, Devic T, Fourmigué M, Auban-Senzier P and Canadell E, Hal$\cdots$Hal interactions in a series of three isostructural salts of halogenated tetrathiafulvalenes? Contribution of the halogen atoms to the HOMO–HOMO overlap interactions, *J Mater Chem* **11**:1570–1575, 2001.
36. Imakubo T, Shirahata T, Hervé K and Ouahab L, Supramolecular organic conductors based on diiodo-TTFs and spherical halide ion X– (X = Cl, Br), *J Mater Chem* **16**:162–173, 2006.
37. Suizu R and Imakubo T, Synthesis and properties of hetero-halogenated TTFs, *Org Biomol Chem* **1**:3629–3631, 2003.
38. Imakubo T, Tajima N, Tamura M, Kato R, Nishio Y and Kajita K, A supramolecular superconductor -$(\mathrm{DIETS})_2[\mathrm{Au(CN)}_4]$, *J Mater Chem* **12**:159–161, 2002.
39. Imakubo T, Maruyama T, Sawa H and Kobayashi K, Novel molecular conductors, $(\mathrm{DIETS})_4\mathrm{M(CN)}_4$(M = Ni, Pd, Pt): Highly reticulated donor anion contacts by –I NC- interaction, *Chem Commun* 1667–1668, 1995.
40. Okabe K, Yamaura JI, Miyazaki A and Enoki T, Electronic and magnetic properties of π–d interaction system $(\mathrm{EDTDM})_2\mathrm{FeBr}_4$, *J Phys Soc Jpn* **74**:1508–1520, 2005.
41. Miyazaki A, Yamazaki H, Aimatsu M, Enoki T, Watanabe R, Ogura E, Kuwatani Y and Iyoda M, Crystal structure and physical properties of conducting molecular antiferromagnets with a halogen-substituted donor: $(\mathrm{EDO\text{-}TTFBr}_2)_2\mathrm{FeX}_4$ (X = Cl, Br), *Inorg Chem* **46**:3353–3366, 2007.

RECENT DEVELOPMENTS ON PORPHYRIN ASSEMBLIES

RICHARD CHARVET*, JONATHAN P. HILL†, YONGSHU XIE†,
YUTAKA WAKAYAMA‡ and KATSUHIKO ARIGA†,§,a
**International Center for Young Scientists (ICYS)*
†*Supermolecules Group*
‡*Advanced Device Materials Group*
§*WPI Center for Materials Nanoarchitectonics (MANA)*
National Institute for Materials Science (NIMS), Japan

The porphyrin macrocycle is one of the most frequently investigated functional molecular entities and can be incorporated into advanced functional nanomaterials upon formation of organized nanostructures. Thus, study of the science and technology of porphyrin assemblies has attracted many organic, biological and supramolecular chemists. A wide variety of nanostructures can be obtained by supramolecular self-assembly because the porphyrin moiety is amenable to chemical modifications through thoughtful synthetic design and moderate preparative effort. Some recent developments in porphyrin assembly, obtained through various supramolecular approaches, are briefly summarized. Topics described in this review are classified into four categories: (i) non-specific assemblies; (ii) specific assemblies; (iii) assemblies in organized films; (iv) molecular-level arrangement. We present examples in the order of structural precision of assemblies.

Keywords: Porphyrins; self-assembly; supermolecules; thin films; molecular arrangement.

1. Introduction

Porphyrins and related molecules have essential roles in many biological systems. For example, they are involved in the most important reactions within photosynthetic systems that are composed of sophisticated supramolecular assemblies of proteins and dyes.[1] The antenna complexes of photosynthetic bacteria consist of a core light-harvesting antenna (LH1) and a peripheral light-harvesting antenna (LH2) that contribute to the collection of light energy. The excitation energy migrates within the wheel-like arrays of chlorophylls in the LH1 and LH2 complexes and is finally funneled into the chlorophyll dimer (special pair) at the photosynthetic reaction center.

---

[a] Correspondence to Dr. Katsuhiko Ariga, Mailing Address: WPI Center for Materials Nanoarchitectonics (MANA) and Supermolecules Group, National Institute for Materials Science (NIMS), 1-1 Namiki, Tsukuba 305-0044, Japan. Tel.: +81-29-860-4597, Fax: +81-29-860-4832, E-mail: ARIGA.Katsuhiko@nims.go.jp

Such elegant processes associated with assemblies of porphyrin molecules have attracted many organic, biological and supramolecular chemists. One of the first widely used approaches to mimic the structure and activity of naturally-occurring assemblies is the synthesis of covalent conjugates. For example, Osuka and coworkers synthesized several kinds of porphyrin oligomers of varying discrete lengths up to a 128-mer, and their specific photoelectronic properties were investigated.[2,3] Imahori, Fukuzumi and coworkers have extensively investigated these systems in which the porphyrin moiety is physically coupled with other functional components such as fullerene or ferrocene in order to develop artificial energy conversion devices.[4–6] With respect to their photoelectronic functions, the chemistry and physics of porphyrin oligomers and conjugates have been extensively researched as shown in some recent examples reported by Anderson, Albunsson and coworkers,[7] Tsuji, Tamao, and coworkers[8] and Cramariuc *et al.*[9] In addition to these small conjugates, porphyrin polymers appended with dendritic moieties have also been used as species for light harvesting.[10]

Porphyrin derivatives are often used as modules for the construction of supramolecular conjugate structures with specific functions, especially molecular recognition. Guo *et al.* synthesized and studied the molecular recognition behavior of an attractive porphyrin dimeric host system with novel inter-chromophore bridging by oligopeptide chains.[11] Tashiro, Aida and coworkers utilized a sandwiched porphyrin array for the preferential trapping of hetero-guest pairs thanks to an inter-guest electronic communication through the π-conjugated host molecule.[12] Rowan and coworkers prepared a double cavity porphyrin that showed negative allosteric effects for the same guest molecules.[13] Tiede *et al.* synthesized a precisely designed macrocyclic host and demonstrated shape-persistent molecular recognition using a predesigned guest.[14] Inomata and Konishi reported the preparation of a novel container-type hexaporphyrin cage complex in which a 1.4 nm gold cluster could be confined.[15] Jiang, Aida and coworkers reported the synthesis of a series of dendritic macromolecules functionalized with multiple zinc porphyrin units and highlighted a clear cooperative effect on the chiroptical sensing of an asymmetric ligating molecule.[16] Canary synthesized a chiral tripodal ligand having two monosubstituted tetraphenylporphyrin moieties that showed chelation of Cu(II), resulting in strong exciton-coupled circular dichroism.[17] Guilard, Fukuzumi and coworkers reported the formation of a π-complex of a freebase bisporphyrin with acridinium perchlorate and the related photodynamics.[18] Hosseini *et al.* constructed bisporphyrin structures using a calixarene scaffold, the so-called jaws porphyrin hosts, for the supramolecular binding of fullerene guests.[19] Fullerene affinities were optimized by varying the nature of the covalent linkage of the porphyrins to the calixarenes. Nguyen, Mirkin and coworkers reported the synthesis of cofacial porphyrin complexes that utilize flexible porphyrin-based hemilabile ligands and metal complex precursors to form macrocyclic products that can be chemically stimulated to change shape.[20] Apart from these approaches based on the covalent linking of porphyrin modules, the formation of structures containing multiple porphyrin molecules using self-assembly processes is also an attractive strategy. A wide variety of structures can be obtained through supramolecular self-assembly thanks to the molecular design flexibility of porphyrins, which can be easily modified with relatively little synthetic efforts. In this review, we survey some recent developments on porphyrin assembly. As shown in Fig. 1, the porphyrin-based supramolecular assemblies are classified into four categories: (i) non-specific assemblies; (ii) specific assemblies; (iii) assemblies in organized films; (iv) molecular arrangement. We will present examples in the order of structural precision of assemblies. Other excellent reviews of related aspects of this research field have also been published recently.[21–23]

2. Porphyrin Assemblies by Non-Specific Interactions

For the formation of large porphyrin assemblies, rather ambiguous (less specific) interactions such as hydrophobic interactions and electrostatic interactions are often used as the driving forces of assembly. Some of the porphyrin aggregates obtained have been interesting research subjects for physical chemistry. Okada and Segawa investigated a series of protonated porphyrin J-aggregates of various water-insoluble tetraphenylporphyrin derivatives prepared at the liquid–liquid or gas–liquid interface.[24] Their results indicate that the nature of the exciton coupling of the lower exciton transition dipole moment can be varied systematically by changing the porphyrin substituents. Scolaro *et al.* described a simple method for the deposition of aggregates of porphyrin tetrakis(4-pyridyl)porphyrin having sizes ranging from hundreds of nanometers up to tens of microns from a chlorinated solvent solution onto a silica surface.[25] The possibility of tuning the photophysical properties of the meso-aggregates by changing the metal ions or the substituents on the porphyrin introduces possibilities for a variety of applications, for example, in the field of electrooptical devices.

Liquid crystals, crystals and macroscopic patterns composed of porphyrins have also been investigated. Camerel, Ziessel and coworkers synthesized wedge-shaped, charged amphiphilic molecules bearing an ammonium group at their extremity that are able to organize negatively-charged luminophores such as tetrakis(4-sulfonatophenyl)porphyrin through an ionic self-assembly process ultimately leading to discotic liquid crystalline materials.[26] Guo, Chen and coworkers reported crystal structures of various synthetic 5-fluoroalkylporphyrin molecules designed for self-assembly.[27] The self-organization of the fluoroalkylporphyrins in the solid state was characterized by X-ray analysis, and atomic force microscopy (AFM) indicated the formation of regular two-dimensional arrays on the substrate. Liquid crystalline behaviors were also confirmed by a combination of differential scanning calorimetry (DSC) and polarizing optical microscopy (POM) techniques. Elemans and coworkers constructed highly periodic patterns at macroscopic length scales, over square millimeter areas, by combining the self-assembly of disk-like porphyrin dyes with physical dewetting phenomena.[28] The patterns consisted of equidistant 5 nm wide lines spaced 0.5–1 mm apart, forming single porphyrin stacks containing millions of

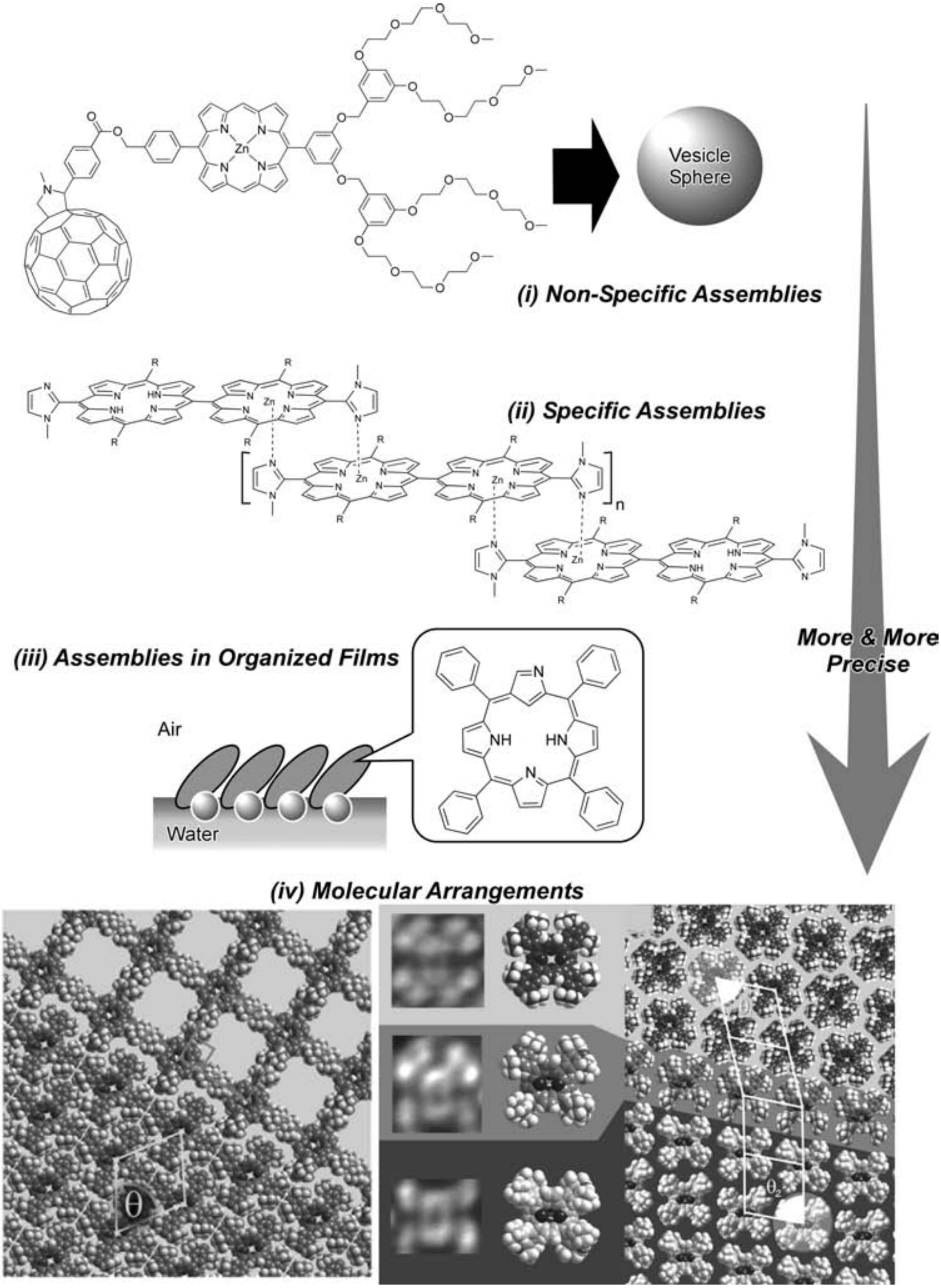

Fig. 1. Illustration of typical examples of topics described in this review: (i) non-specific assembly; (ii) specific assembly; (iii) assembly in organized films; (iv) molecular arrangement.

molecules. They were formed spontaneously upon drop-casting of a solution of the molecules onto a mica surface.

The formation of unique structures such as channels, tubes, sheets, fibers and particles by the self-assembly of porphyrin derivatives has become an attractive topic in supramolecular chemistry. For example, Harada and Kojima prepared self-assembled structures using distorted porphyrins that can form unique curved surfaces rather than the normal planar structures.[29] The curve-shaped saddle-distorted dication dodecaphenylporphyrin building blocks self-organized into nanochannel structures as shown in Fig. 2. This type of cationic porphyrin channel is expected to be formed through concomitant π–π interactions and hydrogen bonding, the double protonation generates hydrogen bonding receptor sites. Therefore, functional molecules such as quinones can be included by non-covalent interactions into the channels. The same research group reported the preparation of tubular and ring structures from a saddle-distorted molybdenum(V)-dodecaphenylporphyrin complex by recrystallization from toluene with vapor diffusion of methanol.[30] Straight tubes of *ca.* 20 nm diameter were detected. Electron diffraction and EDX spectra

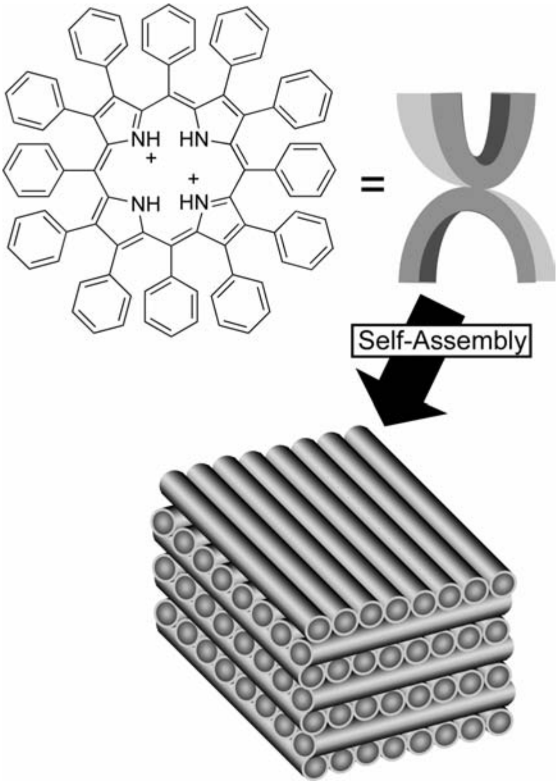

Fig. 2. Nanochannel structures from the saddle-distorted dodecaphenylporphyrin. Reprinted with permission from Ref. 29, © 2006, Royal Society of Chemistry.

confirmed that the tubes observed were composed of molybdenum and oxygen. Dark field imaging and electron diffraction indicated the existence of Mo clusters as polycrystals. Ring structures with a diameter of almost 200 nm were also observed.

Shelnutt and coworkers reported the synthesis of discrete free-standing porphyrin nanosheets using a reprecipitation method,[31] in which an ethanolic solution of Sn(IV) 5-(4-pyridyl)-10,15,20-triphenylporphyrin dichloride was simply injected into deionized water at room temperature under vigorous stirring. The same research group demonstrated that phase-transfer reactions could be used to generate porphyrin nanofiber bundles by the phase-transfer ionic self-assembly of water-soluble porphyrins with water-insoluble porphyrins.[32] Gong *et al.* reported the first synthesis and characterization of porphyrin nanoparticles.[33] Stable 20–200 nm diameter porphyrin nanoparticles were prepared from a wide variety of meso-arylporphyrins using mixing solvent techniques. Detailed investigation of this method was recently reported[34] where the authors suggested that the proposed principles, concepts and methodologies are applicable to a wide variety of organic dyes.

Vesicles and spherical objects with an empty inner core have also attracted much attention since they can be used in biological applications, for example, in drug delivery systems. Charvet *et al.* reported the self-assembly of a non-lipid type π-electronic amphiphile consisting of a zinc porphyrin–fullerene dyad (see Fig. 3(a)) into uniformly-sized microvesicles in aqueous media.[35] This compound was soluble in THF, giving a homogeneous pink solution. When this solution was added drop-wise to water, a reddish brown solution resulted. Scanning electron microscopy (SEM) and transmission electron microscopy (TEM) revealed the presence of uniformly-sized spherical particles composed of a core–shell architecture with a shell thickness of 25–30 nm (see illustrations in Figs. 3(b) and 3(c)). UV–Vis spectroscopy of an aqueous solution of the vesicles suggested that the multilamellar vesicular membrane was composed of an interdigitated structure, in which the fullerene moieties are sandwiched by the zinc porphyrin units. While ordinary lipid vesicles are easily disrupted upon addition of surfactants, vesicles composed of this zinc porphyrin–fullerene dyad amphiphile were resistant to membrane lysis reagents and displayed a remarkable thermal stability.

The co-assembly of porphyrin-type molecules with other entities to generate composite materials is of great interest in material science. Sessler and coworkers found that single walled carbon nanotubes (SWNTs) bind strongly to sapphyrin, the quintessential pentapyrrolic "expanded porphyrin" macrocycle, through donor–acceptor stacking interactions.[36] In the complexes formed, a rapid decay of the sapphyrin excited states was observed, which does not occur in sapphyrin solutions in the absence of SWNTs. Yoon and coworkers synthesized novel photoactive trititanate ($H_2Ti_3O_7$)-type TiO_2 nanofibers by intercalating electron acceptor molecules such as a trans-dihydroxo[5,10,15,20-tetrakis(*p*-tolyl)porphyrinato]tin(IV) into trititanate layers in a one-step hydrothermal reaction.[37] In the porphyrin–trititanate composite material, the optoelectronic properties (the photoinduced electron

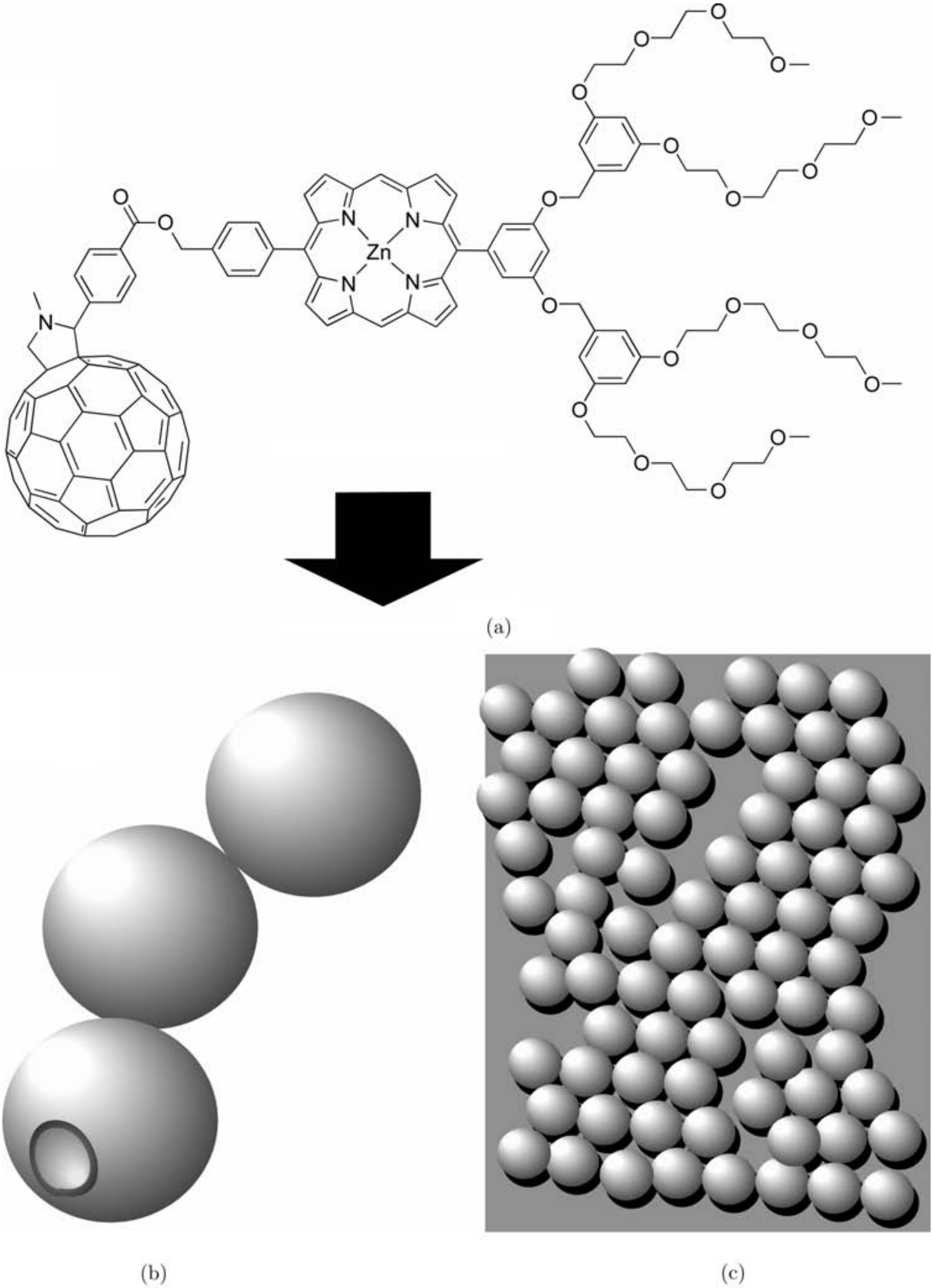

(a)

(b)

(c)

Fig. 3. (a) π-electronic amphiphile consisting of a zinc porphyrin–fullerene dyad. (b) and (c) Uniformly-sized micro-vesicles from this amphiphile in aqueous media. Reprinted with permission from Ref. 35, © 2004, Royal Society of Chemistry.

transfer and its dynamics) were examined by using femtosecond-transient diffuse reflectance absorption and photoluminescence spectral techniques; the result indicated that the porphyrin-trititanate hybrid composites have high photocatalytic activity.

3. Porphyrin Assemblies through Specific Interactions

Porphyrin derivatives containing a central metal cation show coordination activity with specific ligands. As coordination complexes have fixed geometries, the use of coordination interactions is beneficial for construction of porphyrin assemblies of desired geometries and morphologies. Coordination-based porphyrin assemblies have been recently summarized in the excellent reviews by Kobuke[38] and Alessio and coworkers.[39] In addition, the preparation of specific assemblies from porphyrin derivatives has also been attempted through the introduction of functional groups with molecular recognition capabilities at the peripheral positions of the porphyrin ring. In the following section some recent examples of porphyrin assemblies, formed through specific molecular interactions, are summarized.

Among the various approaches towards particular porphyrin assemblies, coordination to the porphyrin metal core is the most frequently applied method. Additional ligands can be introduced, which subsequently bind to the porphyrin core. For example, Anderson and coworkers reported that a series of conjugated zinc porphyrin oligomers form stable ladder complexes with linear bidentate ligands such as 1,4-diazabicyclo[2.2.2]octane (DABCO) or 4,4′-bipyridyl.[40–42] Formation–dissociation equilibria of the ladder complexes showed an interesting cooperativity effect with a large Hill constant, resulting in “all-or-nothing” type formative and dissociative behavior. Ladder type porphyrin assemblies were recently discussed by Hunter, Tomas and coworkers using thermodynamic considerations.[43,44] Linear oligomeric supramolecular assemblies with defined lengths have been generated using the Vernier principle. Two molecules containing a different number of mutually complementary binding sites, separated by the same distance, interact with each other to form an assembly. The assembly grows in the same way as simple supramolecular polymers, but at a molecular stop signal, i.e. when the binding sites come into register, the assembly terminates, giving an oligomer of defined length. This strategy has been realized using tin and zinc porphyrin oligomers as molecular building blocks (Fig. 4). In the presence of isonicotinic acid, a zinc porphyrin trimer and a tin porphyrin dimer form a 3:4 triple stranded Vernier assembly of the length of six porphyrins. If the porphyrin oligomer coordination could slip out of register, larger assemblies would be formed. However, such species are not observed because the dissociation into two smaller assemblies is favored (Fig. 4(b)).

Rowan and coworkers self-assembled disk-shaped porphyrin molecules into linear arrays through metal coordination.[45] A hexakis(porphyrinato)benzene, composed of six porphyrins connected to a central benzene core, can be regarded as a disk-shaped molecule in which three pairs of porphyrins form a propeller-like unit.

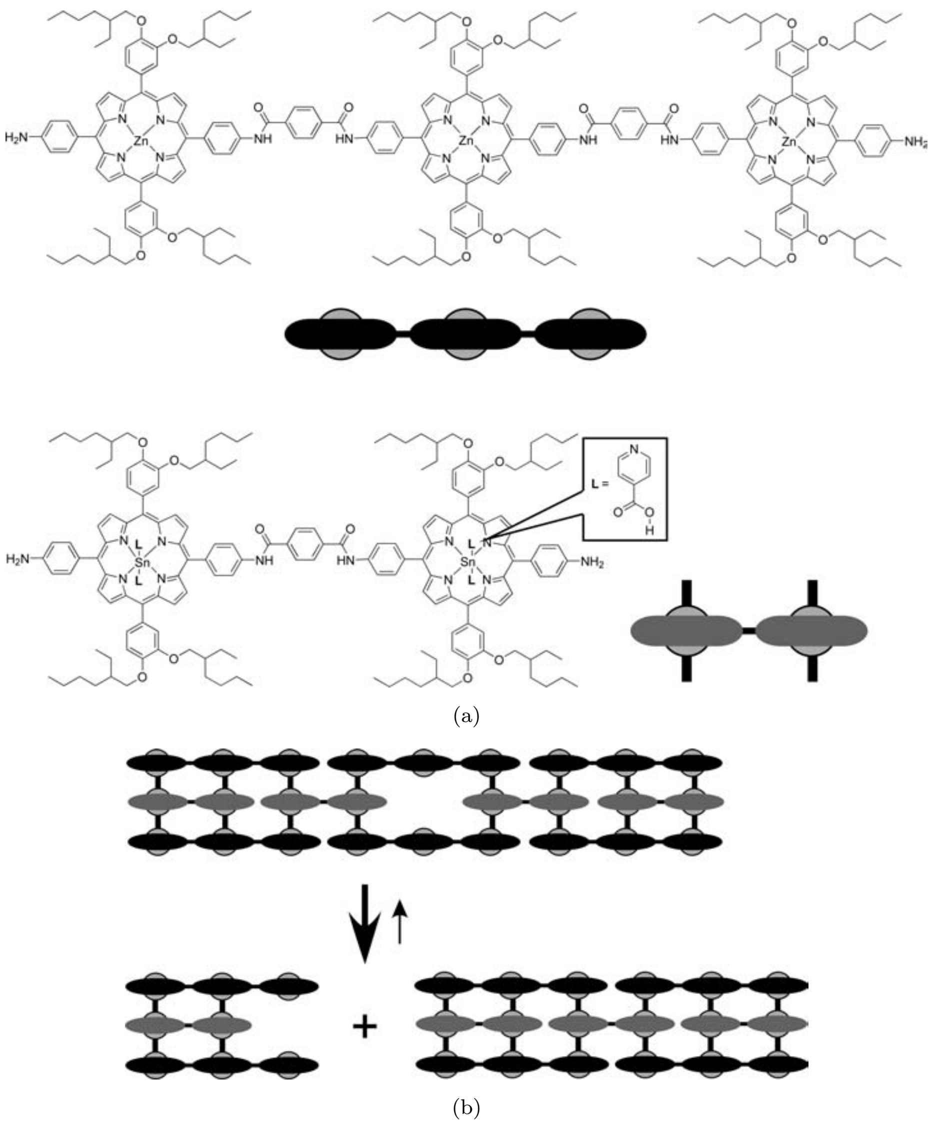

Fig. 4. (a) Zinc porphyrin trimer and tin porphyrin dimer. (b) Assemblies of defined length based on the Vernier principle. Reprinted with permission from Ref. 44, © 2006, American Chemical Society.

When a zinc ion is inserted in the porphyrin macrocycle, appropriate bidentate ligands such as DABCO can coordinate the zinc ions, connecting neighboring molecules to generate columnar supermolecules. Wasielewski and coworkers reported the synthesis and photophysical characterization of a multi-chromophore array constructed from four zinc 5-phenyl-10,15,20-tri(n-pentyl)-porphyrins attached to the 1,7,N,N'-positions of perylene-3,4:9,10-bis(dicarboximide).[46] The structure of this assembly was determined using solution-phase X-ray scattering techniques. Both efficient light harvesting and facile charge separation and transport using multiple pathways were characterized. D'Souza, Ito and coworkers have been attempting to obtain a biomimetic bacterial photosynthetic reaction center complex using well-defined self-assembly supramolecular approaches.[47] A "special pair" donor consisted of a cofacial porphyrin dimer, was formed via potassium ion induced dimerization of meso-(benzo-[15]crown-5)porphyrinatozinc. The dimer was subsequently self-assembled with functionalized fullerenes via axial coordination and crown ether–alkyl ammonium cation complexation to form the donor–acceptor pairs. Hupp and coworkers recently reported on the formation of well-defined prism-shaped assemblies featuring three, six or nine porphyrins and comprising, triplicate sets of porphyrin monomers, dimers or trimers respectively.[48] These supramolecular porphyrin prisms were similarly prepared via coordinative self-assembly with the triethynylpyridylbenzene ligand.

Covalent connection between a metalloporphyrin and a ligand unit is sometimes useful for formation of discrete assemblies with unique properties due to the restriction of conformational freedom in the self-organized state. Tsuda, Aida and coworkers reported a novel thermochromic system, via the self-assembly of a π-extended zinc porphyrin complex functionalized with a metal-ligating 3-pyridyl group.[49] The studied system exhibited multi-color thermochromism upon heating as the thermally-induced axial coordination dynamics of the studied porphyrin were reflected in the absorption spectrum change. Kobuke and coworkers adopted a trick for the construction of porphyrin conjugate systems from relatively simple units, principally by using coordination between metal ions incorporated at the porphyrin macrocycle and imidazole attached at the porphyrin meso-position.[50,51] The length of the supramolecular complex shown in Fig. 5(a) can be simply controlled by changing the ratio between the porphyrin-dimer containing two zinc centers and the porphyrin-dimer containing a single zinc center. These compounds showed large third-order optical nonlinearities, making them potential candidates for photonic applications such as ultra fast optical switching and modulation. In contrast, the use of a structural unit with a spatial orientation of 120° resulted in the formation of a closed ring under appropriate conditions (Fig. 5(b)).[52–54] The resulting macrocycle is of major importance for a better understanding of the mechanisms involved in the natural photosynthetic systems. The same research group recently reported the construction of a supramolecular photosynthetic triad composed of a slipped cofacial porphyrin dimer, a ferrocene unit and a fullerene moiety organized by coordination assembly.[55] Long-lived charge separated species after efficient photoinduced electron transfer and charge migration reactions were characterized.

Kamada *et al.* reported self-sorting assembly of meso-cinchomeronimide appended Zn(II) porphyrin derivatives.[56] While the meso-cinchomeronimide appended Zn(II) porphyrin molecules formed a lone cyclic trimer, the bisporphyrin analog displayed a high-fidelity self-sorting assembly process, and discrete cyclic trimer, tetramer and pentamer with large association constants were obtained

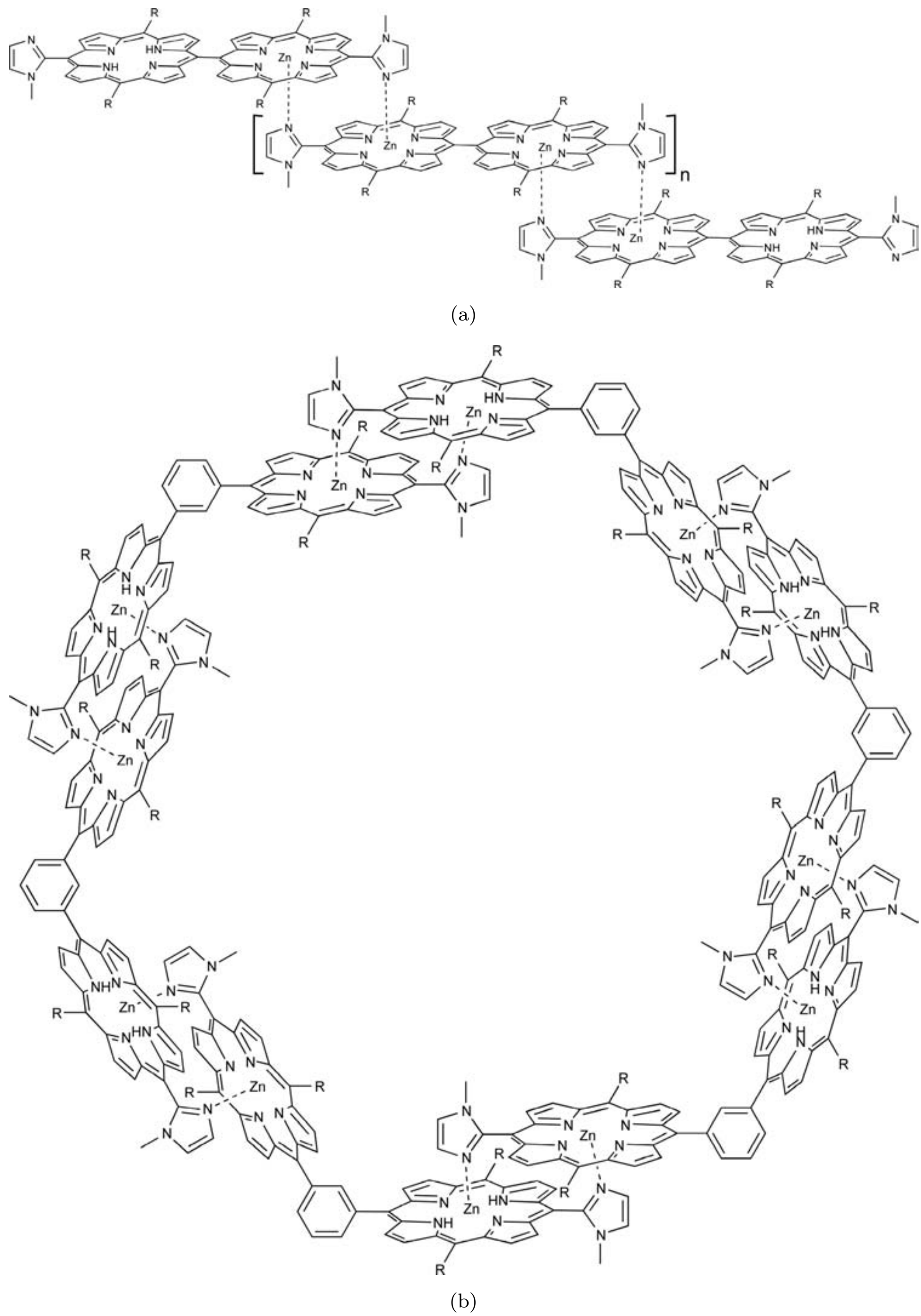

(a)

(b)

Fig. 5. Assemblies from porphyrin-imidazole conjugate: (a) linear assembly; (b) closed ring assembly. Reprinted with permission from Refs. 50 and 52, © 2002 and © 2003, American Chemical Society.

through almost perfect discrimination of the enantiomeric and conformational differences of the meso-cinchomeronimide substituents. Matano *et al.* reported the synthesis, structures and properties of meso-phosphorylporphyrins, which were found to undergo self-organization through coordination, leading to cofacial porphyrin dimers or oligomers.[57] Kuroda and coworkers reported porphyrin assemblies containing 17 porphyrin molecules.[58] The central porphyrin has pyrazine arms to coordinate the zinc porphyrin dimers prepared through the dimerization of carboxy groups. The excitation of the central porphyrin core was directly enhanced by absorption by the antenna pigments, even given such a large scale assembly; the antenna effect for this system resulted in a 77 times enhancement of the central free base porphyrin fluorescence emission. Prodi *et al.* used this "side-to-face" assembling strategy with Ru-pyridyl and Zn-pyridyl molecules for the preparation of pentameric and hexameric arrays.[59] Efficient energy transfer from the metalloporphyrins to the free base pyridylporphyrin was observed, at the triplet level in the pentameric array and at the singlet level in the hexameric array. Structure-predictable nanocrystal growth of well-defined multi-porphyrin arrays at liquid–liquid interfaces was reported by Qian and coworkers.[60] Using metal ions with discrete coordination geometries, nanocrystals with specific shapes such as regular cubic and wire-like structures of $Hg^{2+}/Ag^{+}/PtCl_4^{2-}$-mediated and $Cd^{2+}/PtCl_6^{2-}$-mediated multi-porphyrin arrays were grown at the water–chloroform interface and the growth was monitored by transmission electron microscopy (TEM).

Coordination to metal species at the periphery of the porphyrin macrocycle is another approach towards porphyrin self-assembly. Schmittel and coworkers prepared a bis(zinc porphyrin) tweezer using the heteroleptic bisphenanthroline coordination concept.[61] Upon addition of nitrogenous spacers of different length, namely 4,4′-bipyridine or DABCO to an orthogonally binding phenanthroline-appended porphyrin derivative, structures identified as bridged mono-tweezers, doubly bridged double tweezers and triply bridged double tweezers were assembled. Shinkai and coworkers applied the concept of pyridyl-Pd linkages to porphyrin-based supramolecular assemblies.[62] A porphyrin molecule bearing eight pyridyl groups could self-assemble into molecular capsules and polymeric structures through the formation of *cis*-Pd(II) complexes. They also developed a novel molecular design for chiral porphyrin-based molecular capsules and polymeric assemblies; the helicity is conveniently induced by the presence of an optically active ligand. Goldberg and coworkers proposed the formation of 5,10,15,20-tetra(carboxyphenyl)porphyrin-based single-framework coordination polymers with open architectures. These 3-D macrostructures were obtained by the interaction of free-base 5,10,15,20-tetra(carboxyphenyl)porphyrin with the $Pr_2(oxalate)_3$, $Nd_2(oxalate)_3$ and $Dy_2(oxalate)_3$ hydrated salts.[63]

Other specific interactions have been used for porphyrin assembly. In a milestone work using hydrogen bonding coordination, Sessler and coworkers demonstrated the efficient energy transfer from a cytosine tethered zinc–porphyrin to a guanine linked free-base porphyrin congener (in both the singlet and triplet excited states).[64] In addition, they reported a higher order trimeric complex assembly, wherein two zinc–porphyrins are able to funnel energy into a central free-base porphyrin, which serves as an energy trap. Aoyama and coworkers reported the construction of supramolecular network solids stabilized by hydrogen bonding between porphyrin-bis-resorcinol units.[65,66] This porous porphyrinic structure can selectively accommodate solvent molecules based on hydrogen bonding and size matching. Takeuchi, Shinkai and coworkers designed porphyrin-based organogelators, using porphyrin derivatives having hydrogen-bond-donating (carboxylic acid)/hydrogen-bond-accepting (pyridine) substituents or electron-donating (dialkylamino)/electron-withdrawing (pyridine) substituents at their peripheral positions.[67] Nishide and coworkers reported the selective formation of a cyclic tetramer from a readily synthesized metalloporphyrin with two self-complementary quadruple hydrogen-bonding units.[68] A stable cyclic tetramer based on a tetraphenylporphyrin derivative could be formed over a wide concentration range because of the substituent quadruple hydrogen-bonding unit, 2-ureido-4[1H]-pyrimidinone. The same research group also synthesized a 5,15 meso-substituted methyluracyl porphyrin derivative bearing 6-methyluracyl units at the meso positions.[69] The atropisomers were mixed with alkylated melamine as a complementary hydrogen-bonding unit and the hydrogen-bonded assemblies analyzed by diffusion-ordered spectroscopy in solution. It was found that the $\alpha\alpha$ isomer formed a face-to-face dimer, whereas the $\alpha\beta$ isomer adopted a zigzag conformation. Sada and coworkers reported the construction of a double-stranded helix generated by the twisting of a polymeric supramolecular ladder as shown in Fig. 6.[70] The stable supramolecular ladder relies on the stacking of the bridging porphyrins at the inner ladder region and on the complementary hydrogen bonds formed between two nitrogen atoms of the 2,6-bis(2-oxazolyl)pyridine porphyrin substituents and two protons of the secondary dialkylammonium cations of the polymeric backbone.

Gulino *et al.* reported some supramolecular assemblies using the interaction between the tetracationic meso-tetrakis(N-methyl-4-pyridyl)porphyrin (H_2TMPyP) and its metallo-derivatives with the octa-anionic form of 5,11,17,23-tetrasulfonato-25,26,27,28-tetrakis(hydroxycarbonylmethoxy)calix[4]arene. A series of complex species was generated via electrostatic inclusion complexation since the stoichiometry and porphyrin sequence can be easily tuned.[71] Ng and coworkers reported the formation of a stable 1:1 host–guest assembly between a silicon(IV) phthalocyanine axially conjugated with two permethylated β-cyclodextrin units and a tetrasulfonated porphyrin.[72] The assembly exhibited light-harvesting properties and works as an efficient photosensitizing system for photodynamic therapy. Takeuchi, Shinkai and coworkers recently proposed the use of porphyrin conjugates to trigger the alignment of conjugated polymers within their self-assembled microstructures through the formation of poly-pseudorotaxane structures.[73] Flamigni *et al.* also reported a porphyrin assembly prepared using the catenane approach,[74] the photoinduced processes were investigated in a [2]catenane assembly containing a zinc(II) porphyrin, a gold(III) porphyrin, two free phenanthroline binding sites and in the corresponding copper(I) phenanthroline complex.

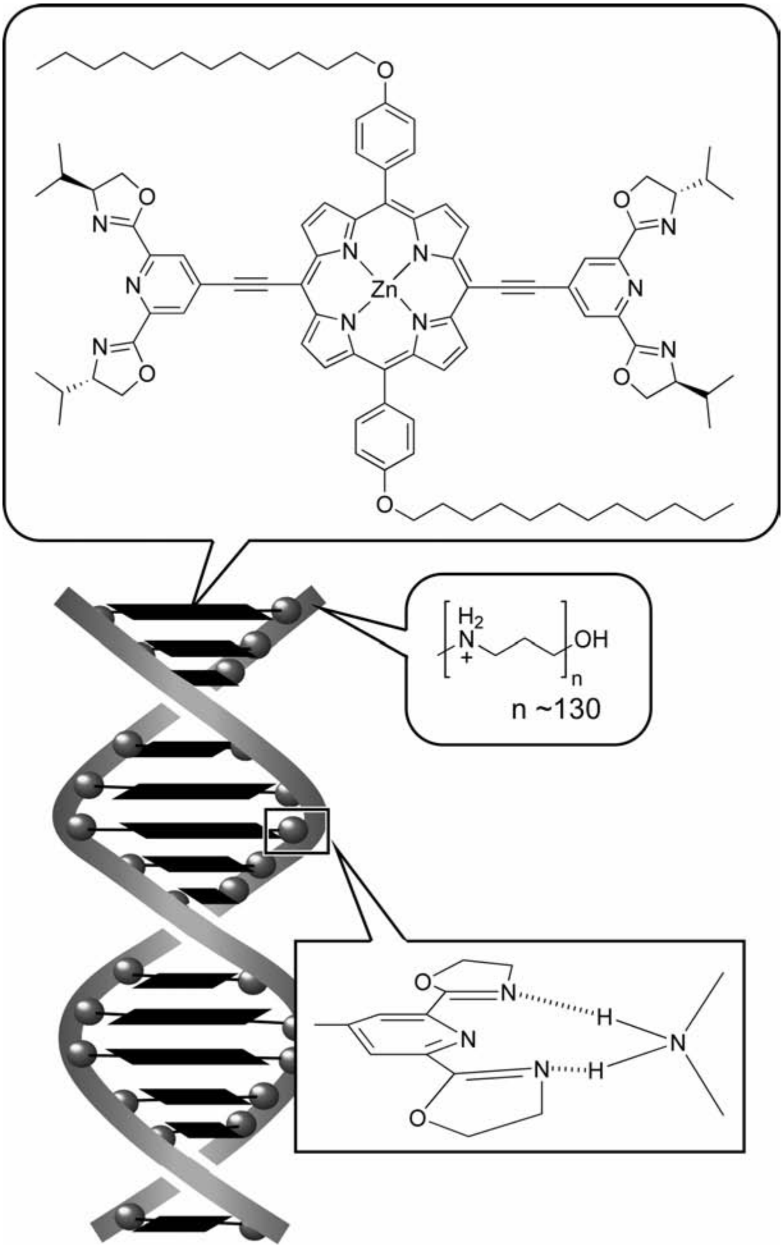

Fig. 6. Supramolecular ladder formed by porphyrins with bis(2,6-bis(2-oxazolyl)pyridine) ligands and secondary dialkylammonium cationic polymers. Reprinted with permission from Ref. 70, © 2007, American Chemical Society.

4. Porphyrin Assemblies in Organized Films

Embedding porphyrin molecules into organized thin films is one of the most powerful methods for immobilization of porphyrin moieties into well-oriented structures. Self-assembled monolayers (SAM), Langmuir–Blodgett (LB) films and layer-by-layer (LbL) assemblies are often used as thin film media. These thin film techniques are also advantageous since porphyrin functionalities within the solid-state device can be studied readily simply by using electrodes.

Mirkin, Hoffman and coworkers reported the preparation of two novel porphyrazine derivatives designed to position themselves quite differently when attached to a surface[75]: one forms a standard SAM where molecules lie roughly horizontally on the surface, while the other porphyrazine derivative positions itself perpendicularly to the surface. Although both molecules had similar reduction potentials in solution, the corresponding values within SAM structures differed. Gulino *et al.* showed that 5-(4-hydroxyphenyl)-10,15-tris(4-dodecyloxyphenyl)-20-porphyrin had a good affinity for O_2 and it was used in the fabrication of a monolayer-based optical gas sensor.[76] An advantage of the monolayer system with respect to porous multilayer films and matrices lies in the fact that the latter can behave as sponges, which are difficult to restore. Interestingly, exposure of the porphyrin monolayer-based O_2 sensor presented here for only a few seconds to a N_2 atmosphere was sufficient to fully reset the system. Jiao *et al.* reported the stepwise formation and characterization of covalently linked multi-porphyrin-imide architectures on Si(100).[77] A triallyl-porphyrin bearing an amino group serves as the base unit on Si(100), the alternating application of a dianhydride (3,3′,4,4′-biphenyltetracarboxylic dianhydride) and a porphyrin–diamine for reaction enables the rapid and simple buildup of oligomers composed of 2–5 porphyrins. The increased charge densities within the porphyrin multilayers may prove important for the fabrication of molecular-based information-storage devices.

The flexible nature of the Langmuir monolayer on water is a definite advantage when dealing with dynamic functions. Ariga *et al.* demonstrated the selective detection and binding of aqueous iodide ion through dynamic aggregate formation of *N*-confused tetraphenylporphyrin (NC-TPP).[78] As shown in Fig. 7, iodide anions in the subphase specifically induce red shifts in the UV–Vis spectra upon J-aggregate formation of the NC-TPP molecules embedded in the lipid matrix. In contrast, the NC-TPP monolayer adopts an H-aggregate type organization in the presence of the other halogen anions. It was also noted that free-base NC-TPP at pH 11 forms a J-aggregate structure. Transfer of these monolayers onto a solid surface provides surfaces for the selective detection of halogen anions. Loosely bound fluoride, chloride and bromide ions were detached from NC-TPP, leading to stable free-base J-aggregates. In contrast, iodide ions are not lost during the transfer process and the assembly mode of the NC-TPP molecules remained unchanged. The size of bound iodide may be responsible for stabilizing the J-aggregate structure, which explains its incorporation during the transfer process. Porphyrin sensors are also being

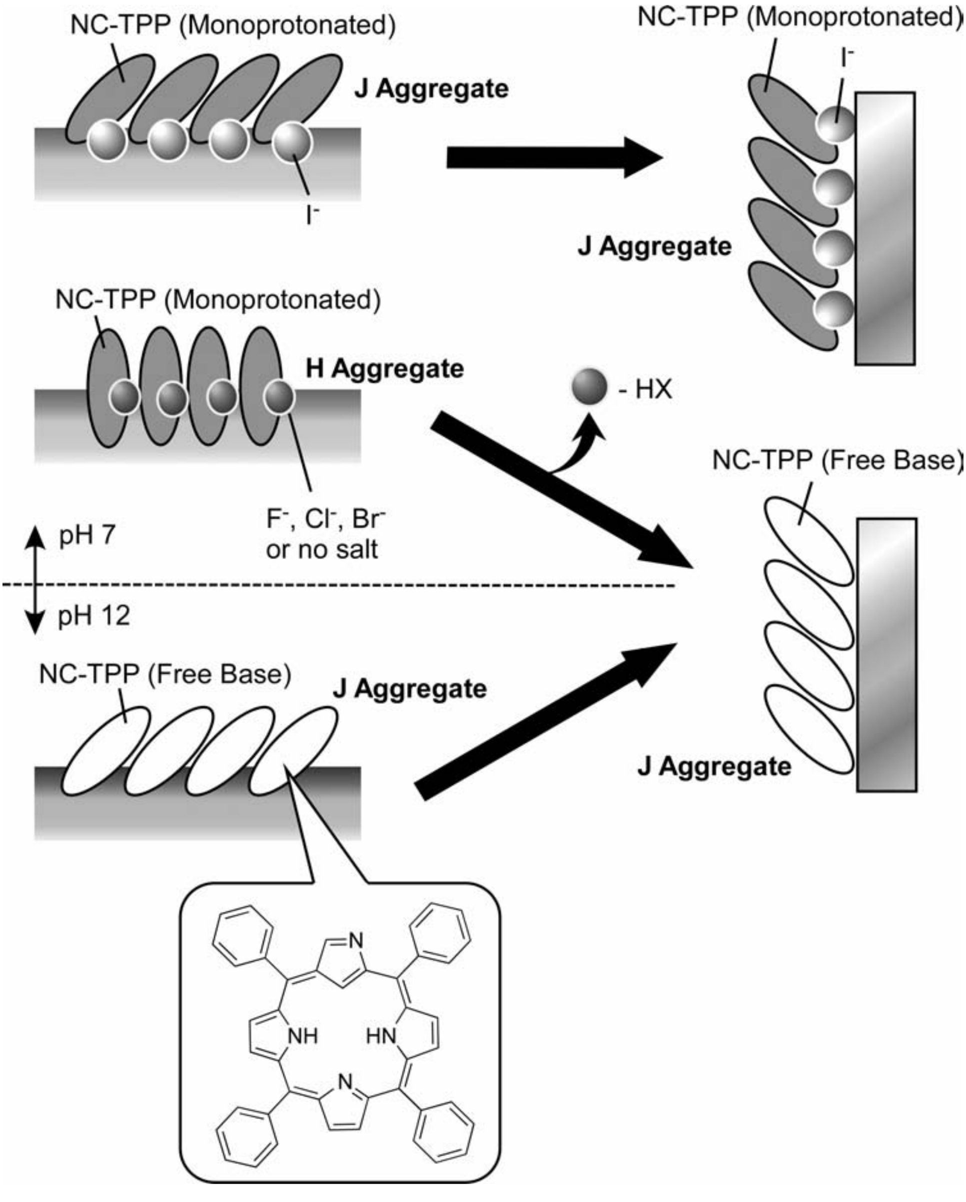

Fig. 7. Selective detection and binding of aqueous iodide ion through dynamic aggregate formation of N-confused tetraphenylporphyrin (NC-TPP). Reprinted with permission from Ref. 78, © 1996, Royal Society of Chemistry.

incorporated into single use colorimetric sensor arrays for the detection of volatile organic compounds. Dunbar *et al.* recently reported changes in the absorption spectra of the LB solid-state films of the Zn(II), Sn(IV), Mg(II) and free-base derivatives of 5,10,15,20-tetrakis[3,4-bis(2-ethylhexyloxy)phenyl]-21*H*,-23*H*-porphine induced by their exposure to various organic compounds, therefore creating an optical gas sensor.[79] In another unique example, Liu and coworkers reported chirality amplification of porphyrin assemblies on water.[80] The two achiral porphyrin derivatives, 5,10,15,20-tetrakis(4-methoxyphenyl)-21*H*,23*H*-porphine or 5,10,15,20-tetrakis (4-hydroxyphenyl)-21*H*,23*H*-porphine were spread separately onto water and were then transferred onto solid substrates by using the Langmuir–Schäfer (LS) method. Although both of the porphyrin derivatives are achiral species, the transferred LS multi-layer films showed macroscopic supramolecular chirality, which was suggested to result from the spontaneous symmetry breaking that occurs at the air–water interface. Small amounts of chiral assemblies formed in the as-deposited LS film can increase in size following the "sergeants and soldiers" principle during the annealing process.

LB films of porphyrin molecules provide excellent media for investigation of their photoelectronic properties. Valli *et al.* reported photoresponsive LB films from the co-assembly of cationic amphiphilic cyclodextrins and anionic porphyrins.[81] Densely-packed hybrid monolayers of amphiphilic cyclodextrins incorporating hydrophilic porphyrins were formed at the air–water interface through electrostatic interaction and could be transferred onto quartz substrates by LS deposition. The resulting multilayers exhibited a good response to light excitation as proven by fluorescence emission, triplet–triplet absorption and singlet oxygen photogeneration. Marczak *et al.* studied the photoelectrochemical properties of LB films from a cationic zinc porphyrin-imidazole-functionalized fullerene dyad.[82] Highly-ordered film stacking favors vectorial electron transfer within the dyad, gives rise to the highest internal photon-to-current efficiency values of 2.5% determined for a photoanode that was composed of around 20 monolayer films. Noworyta, D'Souza and coworkers investigated the effect of "two-point" interactions of Zn(II) and Co(II) metalloporphyrins bearing 15-crown-5 ether peripheral substituents following their assembly in Langmuir and LB films.[83] The central metal ion of the metalloporphyrin was axially coordinated to a nitrogen-containing ligand in the non-submerged region of the Langmuir film on one hand, and a suitably selected cation contained in the subphase solution was supramolecularly complexed by the crown ether moiety in the submerged part of the film on the other. Tkachenko and coworkers also studied exciplex–exciplex energy transfer and annihilation in LB films of porphyrin–fullerene dyads.[84] The same research group also used the time-resolved Maxwell displacement charge method to study the photoinduced electron transfer processes occurring in bilayer structures consisting of an electron donor–acceptor (porphyrin–fullerene) dyad and a conductive polymer (polyhexylthiophene) monolayer, both layers have been prepared by using the LB method.[85]

Haga and coworkers fabricated alternating multilayer films composed of titania nanosheets and Zn porphyrins using the LB method.[86] The setup for their photoelectrochemical device is shown in Fig. 8. Ag paste was deposited on the top of the graduated multilayered film, monochromatized light was irradiated only on the layered electrode side, and a lead wire was connected to the bottom ITO (indium tin

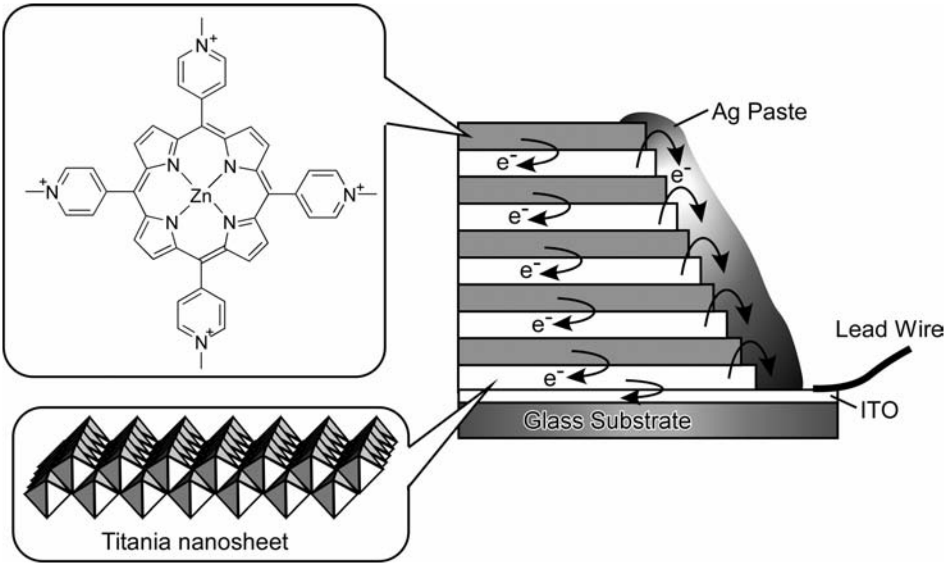

Fig. 8. Photoelectrochemical devices composed of LB films of titania nanosheets and Zn porphyrins. Reprinted with permission from Ref. 86, © 2007, Royal Society of Chemistry.

oxide) electrode. Significant improvement of the photocurrent was observed, even though each titania layer contained a significant number of crystallite boundaries of submicrometer size. A layer of closely packed titania nanosheets can be fabricated by using the LB transfer method while minimizing the overlap between two nanosheets on the solid substrate. The close packing of the titania nanosheets plays an important role in the lateral current extraction.

Alternate layer-by-layer (LbL) assembly is now known as a versatile method for fabrication of layered structures[87] of various functional molecules including dye molecules.[88] Yu and coworkers reported the preparation of porphyrin multilayers via controlled layer-by-layer covalent immobilization.[89] Solid supports such as glass slides and ITO electrodes, carefully cleaned and dried, were dipped into a CH_2Cl_2 solution of $SiCl_2$-functionalized tetraphenylporphyrin to form an initial monolayer. Subsequently, the monolayer was immersed in deionized water to transform the surface Si–Cl groups to Si–OH groups. The resulting monolayer containing Si–OH groups could be used for further immobilization by repetitive deposition. The amount of deposited redox-active porphyrins, which is proportional to the oxidation charge, increased quite linearly with the number of layers, as confirmed by cyclic voltammetry (CV) measurements. Jiang and Liu developed a dye-DNA LbL film system which exhibited a reversible change in chirality.[90] The cationic tetrakis(*N*-methylpyridinium-4-yl)porphyrin dye was incorporated into an assembled DNA/PAH (poly(allylamine hydrochloride)) film, and displayed induced circular dichroism. Mu and coworkers reported the fabrication of multilayer films of CdS particles and meso-tetrakis(4-trimethylaminophenyl)porphyrin cobalt iodide via the

LbL assembly technique.[91] The linear structure formation can be interpreted by the mechanism of dipole–dipole attraction.

5. Porphyrin Assemblies with Precise Molecular Arrangement

As a more advanced example of organization from porphyrin molecules, two-dimensional assemblies with molecular-level precision have also been recently targeted, as highlighted in a recent review by Yoshimoto.[92] Technical progress in molecular level observation using scanning tunneling microscopy (STM) enables us to characterize porphyrin-based assembled structures with molecular level precision. In the remainder of this review, recent examples of porphyrin assemblies having precise molecular arrangements are briefly summarized.

Itaya *et al.* proposed a unique strategy for control of the electrochemical redox reaction of ferrocene. A 1:1 supramolecularly assembled film of C_{60}–ferrocene dyad and a metallooctaethylporphyrin on a Au (111) electrode was constructed and extensively studied by STM.[93] Molecules of the C_{60}–ferrocene dyad directly attached to the Au (111) electrode gave a poorly defined electrochemical response. Conversely, when co-assembled with a porphyrin, a clear electrochemical redox reaction of the ferrocene group of the C_{60}–ferrocene dyad molecule was observed at 0.78 V versus the reversible hydrogen electrode. The well-defined electrochemical response of the ferrocenyl group was clearly due to the control of orientation of the C_{60}–ferrocene dyad molecules. The same research group recently reported molecular images of supramolecular nanobelt arrays consisting of a cobalt(II) "picket-fence" porphyrin, cobalt(II) 5,10,15,20-tetrakis(R,R,R,R-2-pivalamidophenyl)porphyrin, on Au surfaces.[94] Otsuki *et al.* recently reported that some porphyrins can assemble into various patterns on the basis of STM observation. Monolayer arrays of a series of meso-tetra-substituted porphyrins containing octadecyloxy and carboxyl (or pyridyl) groups were prepared on a HOPG surface at the liquid–solid interface.[95] Specifically, slightly undulating rows are obtained from 5-(4-pyridyl)-10,15,20-tris(4-octadecyloxyphenyl)porphyrin. The same research group also reported surface patterns composed of double-decker species.[96] Three double-decker complexes of cerium(IV), with a common 5,10,15,20-tetrakis(4-docosyloxyphenyl)porphyrin moiety as one of the two tetrapyrrole rings, were synthesized. These complexes assemble into ordered arrays at the interface of 1-phenyloctane and the highly oriented pyrolytic graphite surface because of the affinity of the long alkyl chains toward the surface, as revealed by means of molecular-resolution STM. Feringa and coworkers observed a self-organized monolayer of meso-tetradodecylporphyrin coordinated to Au(111) surface.[97] High-resolution STM images revealed that physisorption on Au(111) induced a distortion of the porphyrin macrocycle out of planarity, probably due to the coordination of the lone pairs of the imine (-CdN-) nitrogen atoms of the porphyrin macrocycle to Au (111). Auwärter and coworkers reported controlled metalation of self-assembled porphyrin nanoarrays in two-dimensions.[98] Spillmann and coworkers presented a detailed investigation of the adsorption and dynamics of

C_{60} and C_{70} fullerenes hosted in a self-assembled, two-dimensional, nanoporous porphyrin network on a solid Ag surface.[99] Wakayama and coworkers reported adsorption-induced chiral conformations of a porphyrin molecule on a Cu surface, resulting in the formation of twin superstructures.[100]

Obtaining regular patterns based on molecular–molecular interactions of porphyrins is an attractive research goal. Yokoyama and coworkers reported the preparation of two-dimensional artificial molecular patterns of porphyrin derivatives via hydrogen bonding, at a Au (111) surface (Fig. 9).[101] Two kinds of tetraphenylporphyrin that contain two cyano groups in different relative positions (*cis*-isomer and *trans*-isomer) were used. Cyano groups introduced at the porphyrin phenyl substituents can dimerize through hydrogen bond formation. Tetrameric cyclic domains

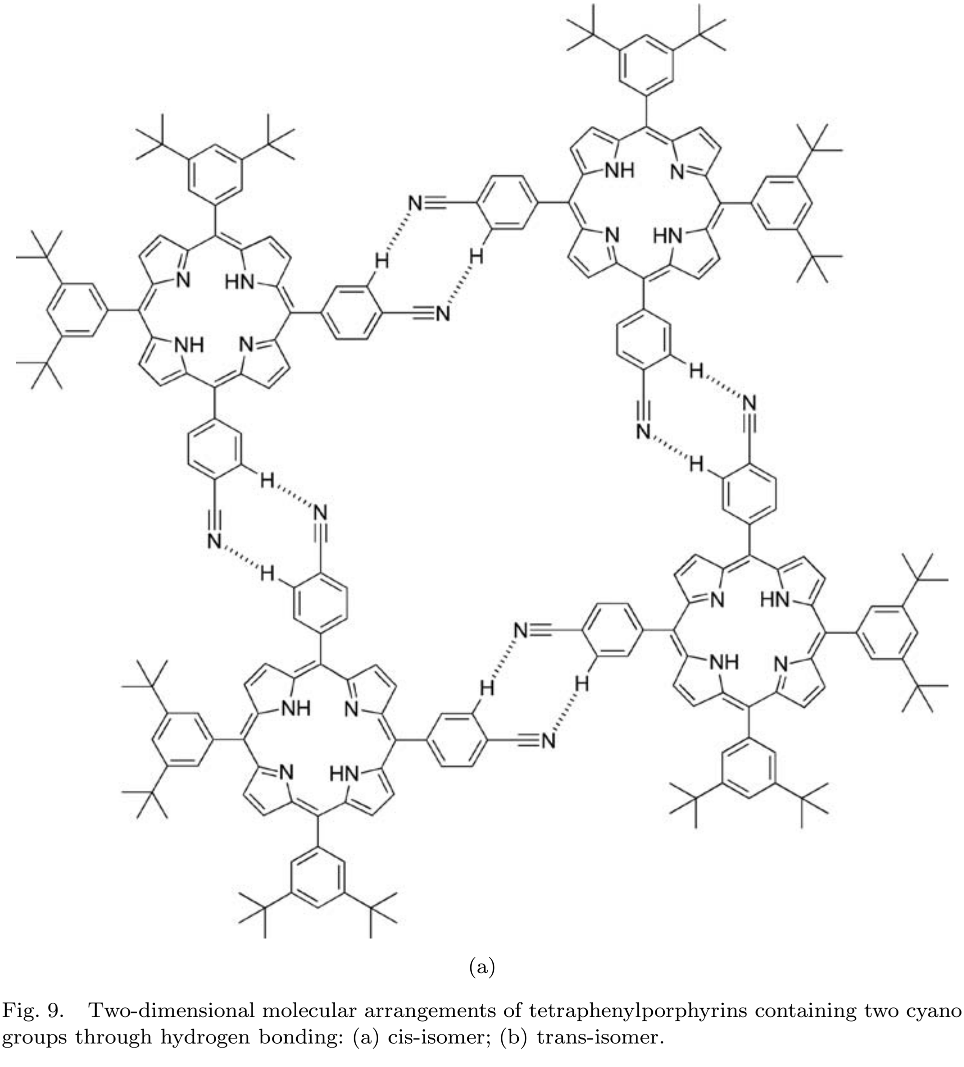

(a)

Fig. 9. Two-dimensional molecular arrangements of tetraphenylporphyrins containing two cyano groups through hydrogen bonding: (a) cis-isomer; (b) trans-isomer.

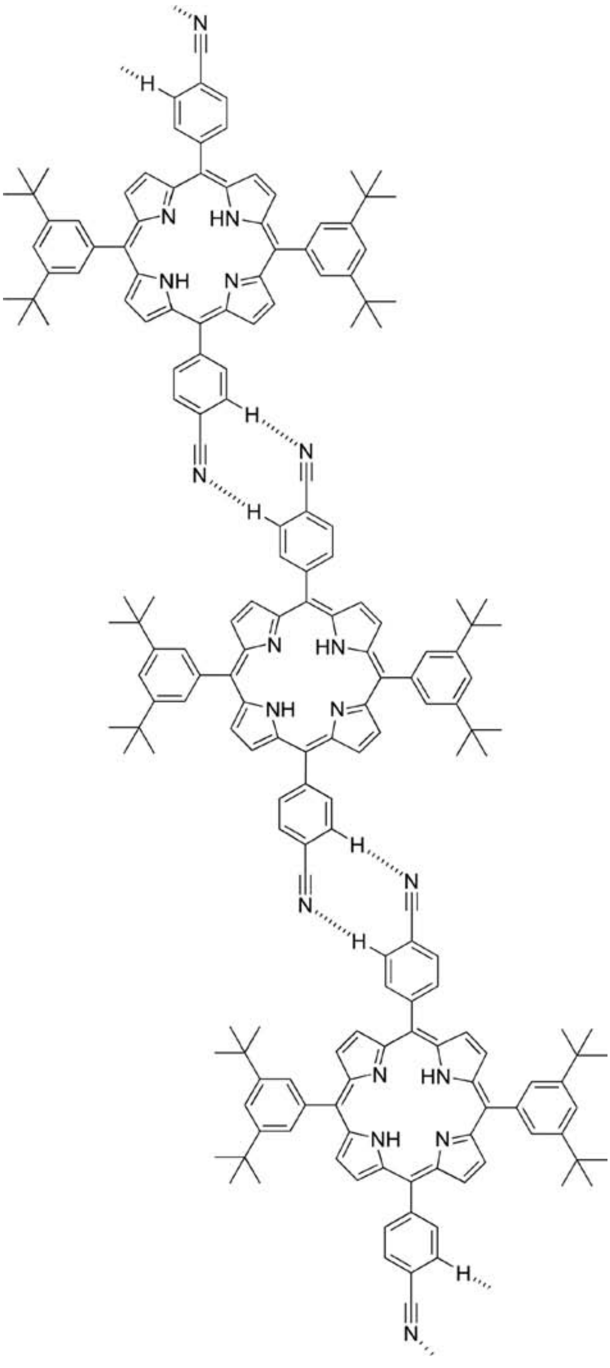

(b)

Fig. 9. (*Continued*)

were formed preferentially (Fig. 9(a)) in the case of the *cis*-isomer, while linear molecular wires were found in STM observations of the *trans*-isomer (Fig. 9(b)). This example demonstrates that only a small difference in molecular structures can be reflected in the patterns of the porphyrin array that can be said to be programmed by the structures of the subunit molecules. The same research group recently reported the multilayer thin film growth of carboxyphenyl-substituted porphyrins on Au (111).[102]

In a more advanced strategy, the dynamic control of porphyrin arrays in a two-dimensional plane has been recently reported by Hill *et al.*[103–106] The porphyrin derivative used in that research was tetrakis(3,5-di-tert-butyl-4-hydroxyphenyl) porphyrin (see Fig. 10(I)), with an essentially planar tetrapyrrole core subtending an angle of 60° with the phenyl substituents. Submonolayer coverage of this porphyrin

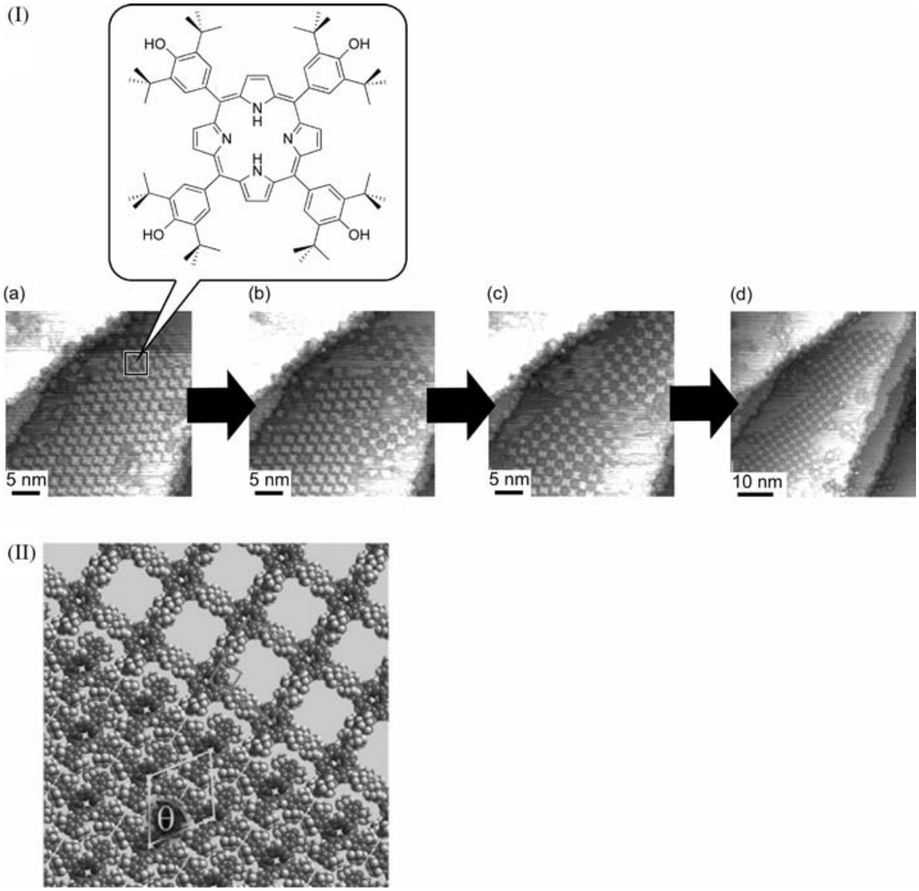

Fig. 10. Real time observation of hexagonal to grid phase transition of tetrakis(3,5-di-tert-butyl-4-hydroxyphenyl)porphyrin on a Cu(111) surface: (I) chemical formulae and STM images; (II) molecular model of the transition. Reprinted with permission from Ref. 103, © 2006, Royal Society of Chemistry.

derivative on a Cu(111) surface consisted of surface-mobile hexagonally-packed domain islands interspersed in a two-dimensional gas phase. The disc-like shape of the planar conformations of this molecule favored a hexagonal arrangement to optimize intermolecular van der Waals contacts. This hexagonally-packed structure underwent a transition at ambient temperature to the square packed grid motif (Fig. 10(I), from (a) to (d), and see also a model in Fig. 10(II)). Square packing is associated with a molecular conformation in which a large dihedral angle between the porphyrin macrocyclic plane and the phenyl substituents is present, while hexagonal packing is observed where the dihedral angle is low. Interestingly, the oxidized form of the porphyrin adsorbed at Cu(111) surfaces with submonolayer coverage showed only one type of surface-immobile hexagonal supramolecular structure at room temperature and transition to the square phase was not observed.

Very recently Hill *et al.* have further demonstrated the importance of conformation in individual molecules at domain boundaries in two-dimensional molecular patterns.[104] Spontaneous formation of a mixed conformer of tetrakis (3,5-di-tert-butyl-4-hydroxyphenyl)porphyrin adsorbed on a Cu(111) surface has been observed to compensate for differences between the lattices of two kinds of two-dimensional crystal structures. When tetrakis(3,5-di-tert-butyl-4-hydroxyphenyl) porphyrin is deposited on a Cu(111) surface with submonolayer coverage under ultrahigh vacuum, domains are formed in hexagonally-packed arrangement where the porphyrin molecules adopt a conformation in which the phenyl substituent groups and tetrapyrrole macrocycle approach coplanarity (Fig. 11a(I)). In the other domain, the conformer composed of eight bright spots, corresponding to the tert-butyl groups, surrounding two parallel oblong protrusions, which are due to the β-positions of opposing pyrrole rings, are detected. Only these β-positions can be observed since rotation of the phenyl substituents to a low dihedral angle (in response to surface adsorption) causes distortion of the tetrapyrrole core to a saddle shape (Fig. 11a(II)). The boundary region is characterized by a highly ordered structure, which is due solely to the existence of the mixed molecular conformation. A model of the packing of the domain is shown in Fig. 11(b) together with space-filling representations of the three differing molecular conformations present. Such an understanding of lattice mismatches in molecularly-patterned surfaces is important, since it can seriously affect the performance of devices prepared in this way.

6. Future Perspectives

Porphyrin derivatives have been widely studied and their use as sensors has also been demonstrated. Not limited to the examples described above, uses of porphyrin derivatives in attractive fields such as biomedical applications[107,108] and nonlinear optics[109,110] becomes more important. Because the chemistry of porphyrins and porphyrin derivatives is well mature, incorporating such functional modules into useful materials and devices is of great importance for instigation of future research

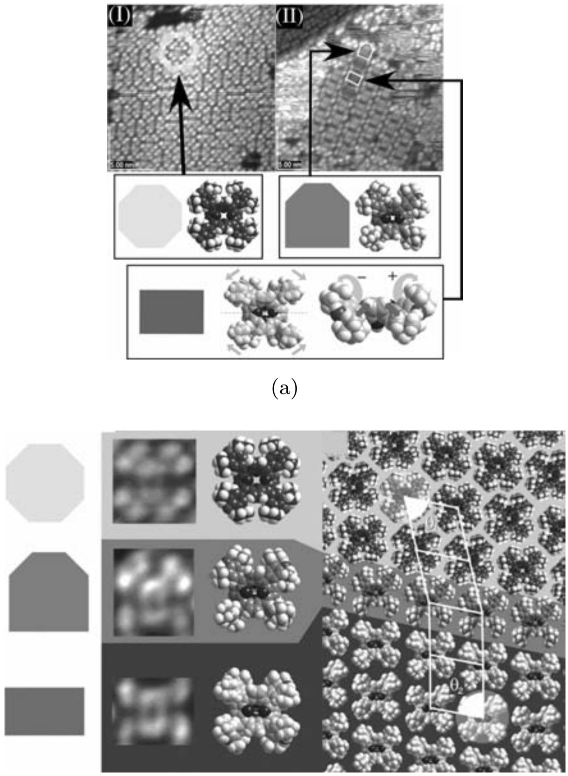

(a)

(b)

Fig. 11. Spontaneous formation of a mixed conformer of tetrakis(3,5-di-tert-butyl-4-hydroxyphenyl)porphyrin adsorbed on a Cu(111) surface between two kinds of two-dimensional crystal domains: (a) STM images and molecular models of the corresponding conformers; (b) schematic illustration of the domain boundary. Reprinted with permission from Ref. 104, © 2006, Royal Society of Chemistry.

directions in porphyrin science and technology. Assembling porphyrin derivatives in desirable arrangements and morphologies on appropriate surfaces will become of critical importance. For example, Hill *et al.* recently developed porphyrin molecules as multi-color indicators for the detection of various ions.[111] Molecularly patterned arrays of these molecules on device surfaces would generate ultra-small universal sensors of ionic species. Although the methods explained here are excellent techniques for the fabrication of various assemblies, they are not always suitable for construction of design of intentionally irregular arrangements of functional molecules. Such complicated and surprisingly highly functional molecular arrangements are commonly seen in biological systems, and can be regarded as some of the ultimate prototypes of molecular devices. Therefore, an astute combination of supramolecular approaches based on self-assembly processes together with highly sophisticated nanolithography techniques will be crucial to attain this final goal.

Acknowledgment

The research described in this review was partially supported by Grant-in Aid for Scientific Research on Priority Areas "Chemistry of Coordination Space" and a Grant-in-Aid for Science Research in a Priority Area "Super-Hierarchical Structures" from Ministry of Education, Science, Sports and Culture of Japan, and a Grants-in-Aid for Scientific Research (B) from Japan Society for the Promotion of Science.

References

1. McDermott G, Prince SM, Freer AA, Hawthornthwaite-Lawless AM, Papiz MZ, Cogdell RJ and Issacs NW, Crystal structure of an integral membrane light-harvesting complex from photosynthetic bacteria, *Nature* **374**:517–521, 2002.
2. Aratani N, Osuka A, Kim YH, Jeong D and Kim D, Extremely long, discrete *meso–meso*-coupled porphyrin arrays, *Angew Chem Int Ed* **39**:1458–1462, 2000.
3. Tsuda A and Osuka A, Fully conjugated porphyrin tapes with electronic absorption bands that reach into infrared, *Science* **293**:79–82, 2001.
4. Imahori H, Giant multiporphyrin arrays as artificial light-harvesting antennas, *J Phys Chem B* **108**:6130–6143, 2004.
5. Tkachenko NV, Vehmanen V, Nikkanen JP, Yamada H, Imahori H, Fukuzumi S and Lemmetyinen H, Porphyrin–fullerene dyad with a long linker: Formation of charge transfer conformer in Langmuir–Blodgett film, *Chem Phys Lett* **366**:245–252, 2002.
6. Imahori H, Guldi DM, Tamaki K, Yoshida Y, Luo C, Sakata Y and Fukuzumi S, Charge separation in a novel artificial photosynthetic reaction center lives 380 ms, *J Am Chem Soc* **123**:6617–6628, 2001.
7. Winters MU, Kalrnbratt J, Eng M, Wilson CJ, Anderson HL and Albinsson B, Photophysics of a butadiyne-linked porphyrin dimer: Influence of conformational flexibility in the ground and first singlet excited state, *J Phys Chem C* **111**:7192–7199, 2007.
8. Sasaki M, Shibano Y, Tsuji H, Araki Y, Tamao K and Ito O, Oligosilane chain-length dependence of electron transfer of zinc porphyrin–oligosilane–fullerene molecules, *J Phys Chem A* **111**:2973–2979, 2007.
9. Cramariuc O, Hukka TI, Rantala TT and Lemmetyinen H, TD-DFT description of photoabsorption and electron transfer in a covalently bonded porphyrin–fullerene dyad, *J Phys Chem A* **110**:12470–12476, 2006.
10. Jiang DL and Aida T, Photoisomerization in dendrimers by harvesting of low-energy photons, *Nature* **388**:454–456, 1997.
11. Guo YM, Oike H and Aida T, Chiroptical transcription of helical information through supramolecular harmonization with dynamic helices, *J Am Chem Soc* **126**:716–717, 2004.
12. Sato H, Tashiro K, Shinmori H, Osuka A, Murata Y, Komatsu K and Aida T, Positive heterotropic cooperativity for selective guest binding via electronic communications through a fused zinc porphyrin array, *J Am Chem Soc* **127**:13086–13087, 2005.
13. Thordarson P, Bijsterveld EJA, Elemans JJAW, Kasák P, Nolte RJM and Rowan AE, Highly negative homotropic allosteric binding of viologens in a double-cavity porphyrin, *J Am Chem Soc* **125**:1186–1187, 2003.
14. Tiede DM, Zhang R, Chen LX, Yu L, and Lindsey JS, Structural characterization of modular supramolecular architectures in solution, *J Am Chem Soc* **126**:14054–14062, 2004.

15. Inomata T and Konishi K, Gold nanocluster confined within a cage: Template-directed formation of a hexaporphyrin cage, its confinement capability, *Chem Commun* 1282–1283, 2003.
16. Li WS, Jiang DL, Suna Y and Aida T, Cooperativity in chiroptical sensing with dendritic zinc porphyrins, *J Am Chem Soc* **127**:7700–7702, 2005.
17. Holmes AE, Das D and Canary JW, Chelation-enhanced circular dichroism of tripodal bisporphyrin ligands, *J Am Chem Soc* **129**:1506–1507, 2007.
18. Tanaka M, Ohkubo K, Gros CP, Guilard R and Fukuzumi S, Persistent electron-transfer state of a π-complex of acridinium ion inserted between porphyrin rings of cofacial bisporphyrins, *J Am Chem Soc* **128**:14625–14633, 2006.
19. Hosseini A, Taylor S, Accorsi G, Armaroli N, Reed CA and Boyd PDW, Calix[4]arene-linked bisporphyrin hosts for fullerenes: Binding strength, solvation effects, and porphyrin-fullerene charge transfer bands, *J Am Chem Soc* **128**:15903–15913, 2006.
20. Oliveri CG, Gianneschi NC, SonBinh T, Nguyen ST, Mirkin CA, Stern CL, Wawrzak Z and Pink M, Supramolecular allosteric cofacial porphyrin complexes, *J Am Chem Soc* **128**:16286–16296, 2006.
21. Elemans JAAW, van Hameren R, Nolte RJM and Rowan AE, Molecular materials by self-assembly of porphyrins, phthalocyanines and perylenes, *Adv Mater* **18**:1251–1266, 2006.
22. Guldi DM, Nanometer scale carbon structures for charge-transfer systems and photovoltaic applications, *Phys Chem Chem Phys* **9**:1400–1420, 2007.
23. Imahori H, Creation of fullerene-based artificial photosynthetic systems, *Bull Chem Soc Jpn* **80**:621–636, 2007.
24. Okada S and Segawa H, Substituent-control exciton in J-aggregates of protonated water-insoluble porphyrins, *J Am Chem Soc* **125**:2792–2796, 2003.
25. Scolaro LM, Romeo A, Castriciano MA, de Luca C, Patanè S and Micali N, Porphyrin deposition induced by UV irradiation, *J Am Chem Soc* **125**:2040–2041, 2003.
26. Camerel F, Ulrich G, Barberá J and Ziessel R, Ionic self-assembly of ammonium-based amphiphiles and negatively charged bodipy and porphyrin luminophores, *Chem Eur J* **13**:2189–2200, 2007.
27. Jin LM, Yin JJ, Chen L, Zhou JM, Xiao JC, Guo CC and Chen QY, Self-assembly and liquid-crystalline properties of 5-fluoroalkylporphyrins, *Chem Eur J* **12**:7935–7941, 2006.
28. van Hameren R, Schön P, van Buul AM, Hoogboom J, Lazarenko SV, Gerritsen JW, Engelkamp H, Christianen PCM, Heus HA, Maan JC, Rasing T, Speller S, Rowan AE, Elemans JAAW and Nolte RJM, Macroscopic hierarchical surface patterning of porphyrin trimers via self-assembly and dewetting, *Science* **314**:1433–1436, 2006.
29. Harada R and Kojima T, A porphyrin nanochannel: Formation of cationic channels by a protonated saddle-distorted porphyrin and its inclusion behavior, *Chem Commun* 716–718, 2005.
30. Kojima T, Harada R, Nakanishi T, Kaneko K and Fukuzumi S, Porphyrin nanotubes based on self-assembly of Mo(V)-dodecaphenylporphyrin complexes and inclusion of Mo-Oxo clusters: Synthesis and characterization by X-ray crystallography and transmission electron microscopy, *Chem Mater* **19**:51–58, 2007.
31. Wang Z, Li Z, Medforth CJ and Shelnutt JA, Self-assembly and self-metallization of porphyrin nanosheets, *J Am Chem Soc* **129**:2440–2441, 2007.
32. Wang Z, Ho KJ, Medforth CJ and Shelnutt JA, Porphyrin nanofiber bundles from phase-transfer ionic self-assembly and their photocatalytic self-metallization, *Adv Mater* **18**:2557–2560, 2006.

33. Gong X, Milic T, Xu C, Batteas JD and Drain CM, Preparation and characterization of porphyrin nanoparticles, *J Am Chem Soc* **124**:14290–14291, 2002.
34. Drain CM, Smeureanu G, Patel S, Gong X, Garnod J and Arijeloyea J, Porphyrin nanoparticles as supramolecular systems, *New J Chem* **30**:1834–1843, 2006.
35. Charvet R, Jiang DL and Aida T, Self-assembly of a π-electronic amphiphile consisting of a zinc porphyrin–fullerene dyad: Formation of micro-vesicles with a high stability, *Chem Commun* 2664–2665, 2004.
36. Boul PJ, Cho DG, Rahman GMA, Marquez M, Ou Z, Kadish KM, Guldi DM and Sessler JL, Sapphyrin-nanotube assemblies, *J Am Chem Soc* **129**:5683–5687, 2007.
37. Jang JH, Jeon KS, Oh S, Kim HJ, Asahi T, Masuhara H and Yoon M, Synthesis of Sn–porphyrin-intercalated trititanate nanofibers: Optoelectronic properties and photocatalytic activities, *Chem Mater* **19**:1984–1991, 2007.
38. Kobuke Y, Artificial light-harvesting systems by use of metal coordination, *Eur J Inorg Chem* 2333–2351, 2006.
39. Iengo E, Zangrando E and Alessio E, Synthetic strategies and structural aspects of metal-mediated multiporphyrin assemblies, *Acc Chem Res* **39**:841–851, 2006.
40. Taylor PN and Anderson HL, Cooperative self-assembly of double-strand conjugated porphyrin ladders, *J Am Chem Soc* **121**:11538–11545, 1999.
41. Anderson HL, Building molecular wires from the colours of life: Conjugated porphyrin oligomers, *Chem Commun* 2323–2330, 1999.
42. Screen TEO, Thorne JRG, Denning RG, Bucknall DG and Anderson HL, Two methods for amplifying the optical nonlinearity of a conjugated porphyrin polymer: Transmetallation and self-assembly, *J Mater Chem* **13**:2796–2808, 2003.
43. Camara-Campos A, Hunter CA and Tomas S, Cooperativity in the self-assembly of porphyrin ladders, *Proc Natl Acad Sci USA* **103**:3034–3038, 2006.
44. Hunter CA and Tomas S, Accurate length control of supramolecular oligomerization: Vernier assemblies, *J Am Chem Soc* **128**:8975–8979, 2006.
45. Elemans JAAW, Lensen MC, Gerritsen JW, van Kempen H, Speller S, Nolte RJM and Rowan AE, Scanning probe studies of porphyrin assemblies and their supramolecular manipulation at a solid–liquid interface, *Adv Mater* **15**:2070–2073, 2003.
46. Kelley RF, Shin WS, Rybtchinski B, Sinks LE and Wasielewski MR, Photoinitiated charge transport in supramolecular assemblies of a 1,7, *N*,*N*'-tetrakis (zincporphyrin)-perylene-3,4:9,10-bis(dicarboximide), *J Am Chem Soc* **129**:3173–3181, 2007.
47. D'Souza F, Chitta R, Gadde S, Rogers LM, Karr PA, Zandler ME, Sandanayaka ASD, Araki Y and Ito O, Photosynthetic reaction center mimicry of a "special pair" dimer linked to electron acceptors by a supramolecular approach: Self-assembled cofacial zinc porphyrin dimer complexed with fullerene(s), *Chem Eur J* **13**:916–922, 2007.
48. Lee SJ, Mulfort KL, O'Donnell JL, Zuo X, Goshe AJ, Wesson PJ, Nguyen ST, Hupp JT and Tiede DM, Supramolecular porphyrinic prisms: Coordinative assembly and solution phase X-ray structural characterization, *Chem Commun* 4581–4583, 2006.
49. Tsuda A, Sakamoto S, Yamaguchi K and Aida T, A novel supramolecular multicolor thermometer by self-assembly of a π-extended zinc porphyrin complex, *J Am Chem Soc* **125**:15722–15723, 2003.
50. Ogawa K, Zhang T, Yoshihara K and Kobuke Y, Large third-order optical nonlinearity of self-assembled porphyrin oligomers, *J Am Chem Soc* **124**:22–23, 2002.
51. Ogawa K, Ohashi A, Kobuke Y, Kamada K and Ohta K, Strong two-photon absorption of self-assembled butadiyne-linked bisporphyrin, *J Am Chem Soc* **125**:13356–13357, 2003.

52. Takahashi R and Kobuke Y, Hexameric macroring of gable-porphyrins as a light-harvesting antenna mimic, *J Am Chem Soc* **125**:2372–2373, 2003.
53. Ikeda C, Satake A and Kobuke Y, Proofs of macrocyclization of gable porphyrins as mimics of photosynthetic light-harvesting complexes, *Org Lett* **26**:4935–4938, 2003.
54. Kuromachi Y, Satake A and Kobuke Y, Light-harvesting macroring accommodating a tetrapodal ligand based on complementary and cooperative coordinations, *J Am Chem Soc* **126**:8668–8669, 2004.
55. Nakagawa H, Ogawa K, Satake A and Kobuke Y, A supramolecular photosynthetic triad of slipped cofacial porphyrin dimer, ferrocene and fullerene, *Chem Commun* 1560–1562, 2006.
56. Kamada T, Aratani N, Ikeda T, Shibata N, Higuchi Y, Wakamiya A, Yamaguchi S, Kim KS, Yoon ZS, Kim D and Osuka A, High fidelity self-sorting assembling of meso-cinchomeronimide appended meso-mesolinked Zn(II) diporphyrins, *J Am Chem Soc* **128**:7670–7678, 2006.
57. Matano Y, Matsumoto K, Terasaka Y, Hotta H, Araki Y, Ito O, Shiro M, Sasamori T, Tokitoh N and Hiroshi IH, Synthesis, structures, and properties of meso-phosphorylporphyrins: Self-organization through P–oxo–zinc coordination, *Chem Eur J* **13**:891–901, 2007.
58. Sugou K, Sasaki K, Kitajima K, Iwaki T and Kuroda Y, Light-harvesting heptadecameric porphyrin assemblies, *J Am Chem Soc* **124**:1182–1183, 2002.
59. Prodi A, Chiorboli C, Scandola F, Iengo E, Alessio E, Dobrawa R and Würthner F, Wavelength-dependent electron and energy transfer pathways in a side-to-face ruthenium porphyrin/perylene bisimide assembly, *J Am Chem Soc* **127**:1454–1462, 2005.
60. Liu B, Qian DJ, Huang HX, Wakayama T, Hara S, Huang W, Nakamura C and Miyake J, Controllable growth of well-defined regular multiporphyrin array nanocrystals at the water–chloroform interface, *Langmuir* **21**:5079–5084, 2005.
61. Kishore RSK, Paululat T and Schmittel M, From supramolecular porphyrin tweezers to dynamic $A_nB_mC_lD_k$ multiporphyrin arrangements through orthogonal coordination, *Chem Eur J* **12**:8136–8149, 2006.
62. Ayabe M, Yamashita K, Sada K, Shinkai S, Ikeda A, Sakamoto S and Yamaguchi K, Construction of monomeric and polymeric porphyrin compartments by a Pd(II)-pyridine interaction and their chiral twisting by a BINAP ligand, *J Org Chem* **68**:1059–1066, 2003.
63. George S, Lipstman S and Goldberg I, Porphyrin supramolecular solids assembled with the aid of lanthanide ions, *Cryst Growth Des* **12**:2651–2654, 2006.
64. Sessler JL, Wang B and Harriman A, Photoinduced energy transfer in associated but noncovalently linked photosynthetic model systems, *J Am Chem Soc* **117**:704–714, 1995.
65. Kobayashi K, Koyanagi M, Endo K, Masuda H and Aoyama Y, Self-assembly of porphyrin arrays by hydrogen bonding in the solid state: An orthogonal porphyrin–bisresorcinol system, *Chem Eur J* **4**:417–424, 1998.
66. Matsuura K, Ariga K, Endo K, Aoyama Y and Okahata Y, Dynamic analyses on induced-fit gaseous guest binding to organic crystals with a quartz-crystal microbalance, *Chem Eur J* **6**:1750–1756, 2000.
67. Tanaka S, Shirakawa M, Kaneko K, Takeuchi M and Shinkai S, Porphyrin-based organogels: Control of the aggregation mode by a pyridine–carboxylic acid interaction, *Langmuir* **21**:2163–2172, 2005.
68. Ohkawa H, Takayama A, Nakajima S and Nishide H, Cyclic tetramer of a metalloporphyrin based on a quadruple hydrogen bond, *Org Lett* **8**:2225–2228, 2006.

69. Arai S, Niwa D, Nishide H and Takeoka S, Atropisomers of meso-conjugated uracyl porphyrin derivatives and their assembling structures, *Org Lett* **9**:17–20, 2007.
70. Sugimoto T, Suzuki T, Shinkai S and Sada K, A double-stranded helix by complexation of two polymer chains with a helical supramolecular assembly, *J Am Chem Soc* **129**:270–271, 2007.
71. Gulino FG, Lauceri R, Frish L, Evan-Salem T, Cohen Y, De Zorzi R, Geremia S, Di Costanzo L, Randaccio L, Sciotto D and Purrello R, Noncovalent synthesis in aqueous solution and spectroscopic characterization of multi-porphyrin complexes, *Chem Eur J* **12**:2722–2729, 2006.
72. Leng X, Choi CF, Lo PC and Ng DKP, Assembling a mixed phthalocyanine–porphyrin array in aqueous media through host–guest interactions, *Org Lett* **9**:231–234, 2007.
73. Wakabayashi R, Kubo Y, Kaneko K, Takeuchi M and Shinkai S, Olefin methathesis of aligned assemblies of conjugated polymers constructed through supramolecular building, *J Am Chem Soc* **128**:8744–8745, 2006.
74. Flamigni L, Talarico AM, Chambron JC, Heitz V, Linke M, Fujita N and Sauvage JP, Photoinduced electron transfer in multiporphyrinic interlocked structures: The effect of copper(I) coordination in the central site, *Chem Eur J* **10**:2689–2699, 2004.
75. Vesper BJ, Salaita K, Zong H, Mirkin CA, Barrett AGM and Hoffman BM, Surface-bound porphyrazines: Controlling reduction potentials of self-assembled monolayers through molecular proximity/orientation to a metal surface, *J Am Chem Soc* **126**:16653–16658, 2004.
76. Gulino A, Giuffrida S, Mineo P, Purrazzo M, Scamporrino E, Ventimiglia G, van der Boom ME and Fragalà I, Photoluminescence of a covalent assembled porphyrin-based monolayer: Optical behavior in the presence of O_2, *J Phys Chem B* **110**:16781–16786, 2006.
77. Jiao J, Anariba F, Tiznado H, Izabela Schmidt I, Lindsey JS, Zaera F and Bocian DF, Stepwise formation and characterization of covalently linked multiporphyrin-imide architectures on Si(100), *J Am Chem Soc* **128**:6965–6974, 2006.
78. Ariga K, Kunitake T and Furuta H, Specific binding of iodide ion to *N*-confused tetraphenylporphyrin (NC-TPP) at the air–water interface, *J Chem Soc Perkin Trans* **2**:667–672, 1996.
79. Dunbar ADF, Richardson TH, McNaughton AJ, Hutchison J and Hunter CA, Investigation of free base, Mg, Sn and Zn substituted porphyrin LB films as gas sensors for organic analytes, *J Phys Chem B* **110**:16646–16651, 2006.
80. Chen P, Ma X, Duan P and Liu M, Chirality amplification of porphyrin assemblies exclusively constructed from achiral porphyrin derivatives, *Chem Phys Chem* **7**:2419–2423, 2006.
81. Valli L, Giancane G, Mazzaglia A, Scolaro LM, Conocid S and Sortino S, Photoresponsive multilayer films by assembling cationic amphiphilic cyclodextrins and anionic porphyrins at the air/water interface, *J Mater Chem* **17**:1660–1663, 2007.
82. Marczak R, Sgobba V, Kutner W, Gadde S, D'Souza F and Guldi DM, Langmuir-Blodgett films of a cationic zinc porphyrin–imidazole-functionalized fullerene dyad: Formation and photoelectrochemical studies, *Langmuir* **23**:1917–1923, 2007.
83. Noworyta K, Marczak R, Tylenda R, Sobczak JW, Chitta R, Kutner W and D'Souza F, "Two-point" assembling of Zn(II) and Co(II) metalloporphyrins derivatized with a crown ether substituent in Langmuir and Langmuir–Blodgett films, *Langmuir* **23**:2555–2568, 2007.

84. Lehtivuori H, Lemmetyinen H and Tkachenko NV, Exciplex–exciplex energy transfer and annihilation in solid films of porphyrin–fullerene dyads, *J Am Chem Soc* **128**:16036–16037, 2006.
85. Vuorinen T, Kaunisto K, Chukharev V, Tkachenko NV, Efimov A and Lemmetyinen H, Kinetics of photoinduced electron transfer in polythiophene–porphyrin–fullerene molecular films, *J Phys Chem B* **110**:19515–19520, 2006.
86. Akatsuka K, Ebina Y, Muramatsu M, Sato T, Hester H, Kumaresan D, Schmehl RH, Sasaki T and Haga M, Photoelectrochemical properties of alternating multilayer films composed of titania nanosheets and Zn porphyrin, *Langmuir* **23**:6730–6736, 2007.
87. Ariga K, Hill JP and Ji Q, Layer-by-layer assembly as a versatile bottom-up nanofabrication technique for exploratory research and realistic application, *Phys Chem Chem Phys* **19**:2319–2340, 2007.
88. Ariga K, Lvov Y and Kunitake T, Assembling alternate dye-polyion molecular films by electrostatic layer-by-layer adsorption, *J Am Chem Soc* **119**:2224–2231, 1997.
89. Lee DC, Morales GM, Lee Y and Yu L, Cofacial porphyrin multilayers *via* layer-by-layer assembly, *Chem Commun* 100–102, 2006.
90. Jiang S and Liu M, A chiral switch based on dye-intercalated layer-by-layer assembled DNA film, *Chem Mater* **16**:3985–3987, 2004.
91. Zhang B, Mu J and Li X, Linear assemblies of aged CdS particles and cationic porphyrin in multilayer films, *Appl Surf Sci* **252**:4990–4994, 2006.
92. Yoshimoto S, Molecular assemblies of functional molecules on gold electrode surfaces studied by electrochemical scanning tunneling microscopy: Relationship between function and adlayer structures, *Bull Chem Soc Jpn* **79**:1167–1190, 2006.
93. Yoshimoto S, Saito A, Tsutsumi E, D'Souza F, Ito O and Itaya K, Electrochemical redox control of ferrocene using a supramolecular assembly of ferrocene-linked C_{60} derivative and metallooctaethylporphyrin array on a Au(111) electrode, *Langmuir* **20**:11046–11052, 2004.
94. Yoshimoto S, Sato K, Sugawara S, Chen Y, Ito O, Sawaguchi T, Niwa O and Itaya K, Formation of supramolecular nanobelt arrays consisting of cobalt(II) "picket-fence" porphyrin on Au surfaces, *Langmuir* **23**:809–816, 2007.
95. Otsuki J, Nagamine E, Kondo T, Iwasaki K, Asakawa M and Miyake K, Surface patterning with two-dimensional porphyrin supramolecular arrays, *J Am Chem Soc* **127**:10400–10405, 2005.
96. Otsuki J, Kawaguchi S, Yamakawa T, Asakawa M and Miyake K, Arrays of double-decker porphyrins on highly oriented pyrolytic graphite, *Langmuir* **22**:5708–5715, 2006.
97. Katsonis N, Vicario J, Kudernac T, Visser J, Pollard MM and Feringa BL, Self-organized monolayer of meso-tetradodecylporphyrin coordinated to Au(111), *J Am Chem Soc* **128**:15537–15541, 2006.
98. Auwärter W, Alexander W-BA, Susan BS, Riemann A, Schiffrin A, Ruben M and Barth JV, Controlled metalation of self-assembled porphyrin nanoarrays in two dimensions, *Chem Phys Chem* **8**:250–254, 2007.
99. Kiebele A, Bonifazi D, Cheng F, Stöhr M, Diederich F, Jung T and Spillmann H, Adsorption and dynamics of long-range interacting fullerenes in a flexible, two-dimensional, nanoporous porphyrin network, *Chem Phys Chem* **7**:1462–1470, 2006.
100. Sekiguchi T, Wakayama Y, Yokoyama S, Kamikado T and Mashiko S, Adsorption-induced conformational changes of porphyrin derivatives and formation of twin superstructures on a copper surface, *Thin Solid Films* **464–465**:393–397, 2004.

101. Yokoyama T, Yokoyama S, Kamikado T, Okuno Y and Mashiko S, Selective assembly on a surface of supramolecular aggregates with controlled size and shape, *Nature* **413**:619–621, 2001.
102. Nishiyama F, Yokoyama T, Kamikado T, Yokoyama T and Mashiko S, Layer-by-layer growth of porphyrin supramolecular thin films, *Appl Phys Lett* **88**:253113, 2006.
103. Hill JP, Wakayama Y, Schmitt W, Tsuruoka T, Nakanishi T, Zandler ML, McCarty AL, D'Souza F, Milgrom LR and Ariga K, Regulating the stability of 2D crystal structures using an oxidation state-dependent molecular conformation, *Chem Commun* 2320–2322, 2006.
104. Hill JP, Wakayama Y and Ariga K, How molecules accommodate a 2D crystal lattice mismatch: An unusual 'mixed' conformation of tetraphenylporphyrin, *Phys Chem Chem Phys* **8**:5034–5037, 2006.
105. Wakayama Y, Hill JP and Ariga K, Real-time STM observation of molecular dynamics on a metal surface, *Surf Sci* **601**:3984–3987, 2007.
106. Hill JP, Wakayama Y, Akada M and Ariga K, Self-assembly structures of a phenol-substituted porphyrin in the solid state: Hydrogen bonding, kagomé lattice, and defect tolerance, *J Phys Chem C* **111**:16174–16180, 2007.
107. Sessler JL and Miller RA, Texaphyrins — New drugs with diverse clinical applications in radiation and photodynamic therapy, *Biochem Pharmacol* **59**:733–739, 2000.
108. Ackroyd R, Kelty C, Brown N and Reed M, The history of photodetection and photodynamic therapy, *Photochem Photobiol* **74**:656–669, 2001.
109. Rath H, Sankar J, PrabhuRaja V, Chandrashekar TK, Nag A and Goswami D, Core-modified expanded porphyrins with large third-order nonlinear optical response, *J Am Chem Soc* **127**:11608–11609, 2005.
110. Kumar R, Misra R, Chandrashekar TK, Nag A, Goswami D, Suresh E and Suresh CH, One-pot synthesis of core-modified rubyrin, octaphyrin and dodecaphyrin: Characterization and nonlinear optical properties, *Eur J Org Chem* 4552–4562, 2007.
111. Hill JP, Schumacher AL, D'Souza F, Labuta J, Redshaw C, Elsegood MRJ, Aoyagi M, Nakanishi T and Ariga K, Chromogenic indicator for anion reporting based on an *N*-substituted oxoporphyrinogen, *Inorg Chem* **45**:8288–8296, 2006.

Part 5

BIONANOTECHNOLOGY AND NANOMEDICINE

This page intentionally left blank

NANOSTRUCTURES FROM DESIGNER PEPTIDES

BOON TEE ONG, PARAYIL KUMARAN AJIKUMAR
and SURESH VALIYAVEETTIL*
Department of Chemistry
National University of Singapore
Singapore 117543
*chmsv@nus.edu.sg

The present article reviews the self-assembly of oligopeptides to form nanostructures, both in solution and in solid state. The solution structures of the peptides were examined using circular dichroism and dynamic light scattering. The solid state assembly was examined by adsorbing the peptides onto a mica surface and analyzing it using atomic force microscopy. The role of pH and salt concentration on the peptide self-assembly was also examined. Nanostructures within a size range of 3–10 nm were obtained under different conditions.

Keywords: Peptides; self-assembly; nanostructures.

1. Introduction

During the past two decades, molecular self-assembly has attracted considerable attention due to its use in the design and fabrication of nanostructures leading to the development of advanced materials.[1,2] Within the past few years, a few research groups have investigated the self-assembly of small oligopeptides into sheets, films and other structures.[3] Designer peptides, not only offer the possibility of incorporating biofunctionality into the material but also bring the exciting possibility of understanding the structure — property — function triad relationship. There are many potential applications for oligopeptides as model systems for understanding the diseases such as Alzheimer's disease, use as a scaffold in tissue engineering, controlled drug delivery and molecular engineering. It has been known that changes in the secondary structures such as α-helices and β-sheets have significant influence in determining the overall function of the peptide.[4–6]

In the present work, we designed and synthesized a few peptides which are expected to form interesting materials. It is known that peptides with alternating hydrophobic–hydrophilic residues self-assemble into β-sheet structures. Also, ionic-strength of the medium[7,8] and pH may shield the electrostatic repulsive forces and allow attractive hydrophobic and van der Waals forces to dominate.[9] Table 1 gives a summary of the amino acid sequence, observed and theoretical masses and the

Table 1. Amino acid sequence, theoretical and observed masses and isoelectric points (pI) for all the peptides synthesized.

Amino acid sequence	Theoretical mass (Da)	Observed mass (Da)	Isoelectric points (pI)
ADAELDPRGDFPDLEADA (P1)	1916.945	1916.53 ± 0.69	3.57
IELKPRGDFPDLEA (P2)	1599.805	1599.72 ± 0.05	4.32
LPLLKGDLRI (P3)	1137.455	1137.25 ± 0.69	8.75
RADARADARADARADA (P4)	1671.695	1671.52 ± 0.74	6.10

calculated isoelectric points (pI). Among the four, two peptides (**P1** and **P2**) are incorporated with cell adhesion motif "RGD" in the middle. This tripeptide motif is a well studied and an important group in the integrin family of the cell adhesion receptors. In addition, we have also incorporated proline residue in the sequence to reduce the flexibility and introduce a kink. To determine whether only the above design will give stable secondary structures, another peptide (**P3**) was designed and synthesized, which consist of mostly hydrophobic amino acid residues with a mimic of the cell adhesion motif "KGD" situated in the middle of the peptide. The fourth peptide (**P4**) consists of sequence with alternating acidic and basic residues. Herein, we investigated the role of primary sequence, ionic strength and pH towards the self-assembly characteristics of the peptides.

2. Materials and Methods

2.1. *Peptide synthesis*

Fmoc–Ala–PEG–PS and all the N^{α}–Fmoc–L–amino acids were purchased from Novabiochem (San Diego, CA). The peptides were synthesized using the Pioneer Peptide Synthesizer from the Applied Biosystems. The peptides P1, P2 and P4 were assembled on Fmoc–Ala–PEG–PS (0.240 mmol/g) resin whereas P3 were assembled on Fmoc–Ile–PEG–PS (0.22 mmol/g). Both peptides were synthesized on a 0.1 mmol scale using the extended cycle protocol. The completed peptides were deprotected and cleaved by treating with the cleavage cocktail (88% trifluoroacetic acid (TFA), 5.0% phenol, 5.0% water, 2.0% triisopropylsilane (TIPS)) for 3 hours at room temperature. The mixture was filtered and filtrate was concentrated to reduce the volume. The peptides were precipitated by adding ice-cold ether. The precipitated peptide was centrifuged using an ultracentrifuge, followed by repeated washings with ice-cold ether to remove all impurities. Finally, the peptides were lyophilized from 10% acetic acid solution and obtained as white powder. These crude peptides were further purified on a BioCAD Workstation high performance liquid chromatography (HPLC) using the Phenominex C18 reverse-phase column (250 × 10 mm, 10 μm). The solvent system used for the purification include: Solvent A, 0.1%TFA and Solvent B, 0.1% TFA in 80% acetonitrile, a linear gradient (2 mL/min) 25–50% B over 50 min was used. The purity of the peptides was confirmed by electrospray ionization-mass spectrometry (ESI-MS). Circular dichroism

(CD) spectra were recorded in the wavelength range of 190–280 nm with an accumulation of 3 scans. Secondary structure fractions were deduced from the spectra using software provided with the instrument. An aliquot of 150–200 μl of the peptide solutions was used to perform dynamic light scattering (DLS) experiments by using PDDLS/batch light scattering instrument (Precision Detectors, Franklin, MA). Intensity data from each sample were collected in duplicate and analyzed using the PRECISION DECONVOLVE program. For atomic force microscope (AFM) investigation, freshly cleaved mica was immersed in the peptide solutions for about 15–30 min to optimize the adsorption of peptides and then rinsed thoroughly with deionized water. The mica surface with the adsorbed peptides was then dried in air and imaged in air using AFM (Multimode, Digital Instruments, Santa Barbara, CA) operating on tapping mode. Soft silicon cantilevers were chosen (FESP model, Digital Instruments, Santa Barbara, CA) with spring constant of 1–5 N/m and tip radius of curvature of 5–10 nm. AFM scans were taken at 256 × 256 pixels resolution and produced topographic images of the samples, in which the brightness of features increased as a function of height. Typical scanning parameters were as follows: tapping frequency 207 kHz, RMS amplitude before engage 1–1.2 V, integral and proportional gains 0.2–0.6 and 0.3–1 respectively, set point 0.8–1 V, scanning speed 1–2 Hz.

2.2. *Self-assembly investigation using dynamic light scattering*

The dynamic light-scattering technique is a rapid screening method for studying aggregation and showed structures with very discrete sizes. It is used to estimate the average aggregate size of the peptides as a function of pH and salt solutions. The DLS results were recorded for each peptide at pH 3 and 5 (± 0.3). It is seen that an increase in pH from 3 to 5 resulted in an increase in the hydrodynamic radius ($<R_H>$) i.e. from 3 to 10 nm (Fig. 1).

In salt solutions, the peptides formed smaller structures as compared to the pH induced self-assembly (Fig. 2). In the presence of NaCl, the four peptides showed a broader distribution compared with the presence of $CaCl_2$ solution. This may be due to the increased solubility of peptides in water with increase in concentration of salts. The size of the aggregates decreased in the presence of salt. We are not able to obtain the exact particle size for P3 at pH ~ 3 and in 10 mM $CaCl_2$ solution, which could be due to low aggregated size.

Table 2 gives the summary of DLS data collected for all peptide under various experimental conditions.

3. Characterization of Self-Assembly using Circular Dichroism

The CD spectra revealed the secondary structures of the peptides in water at different pHs and salt solutions (Figs. 3 and 4). In the case of **P1** at pH ~ 3, a negative minimum at 195 nm and 199 nm and a small shoulder at, 223 nm corresponds to a random coil with a bend or β-turn conformation (Fig. 3(a)). Analysis of the data

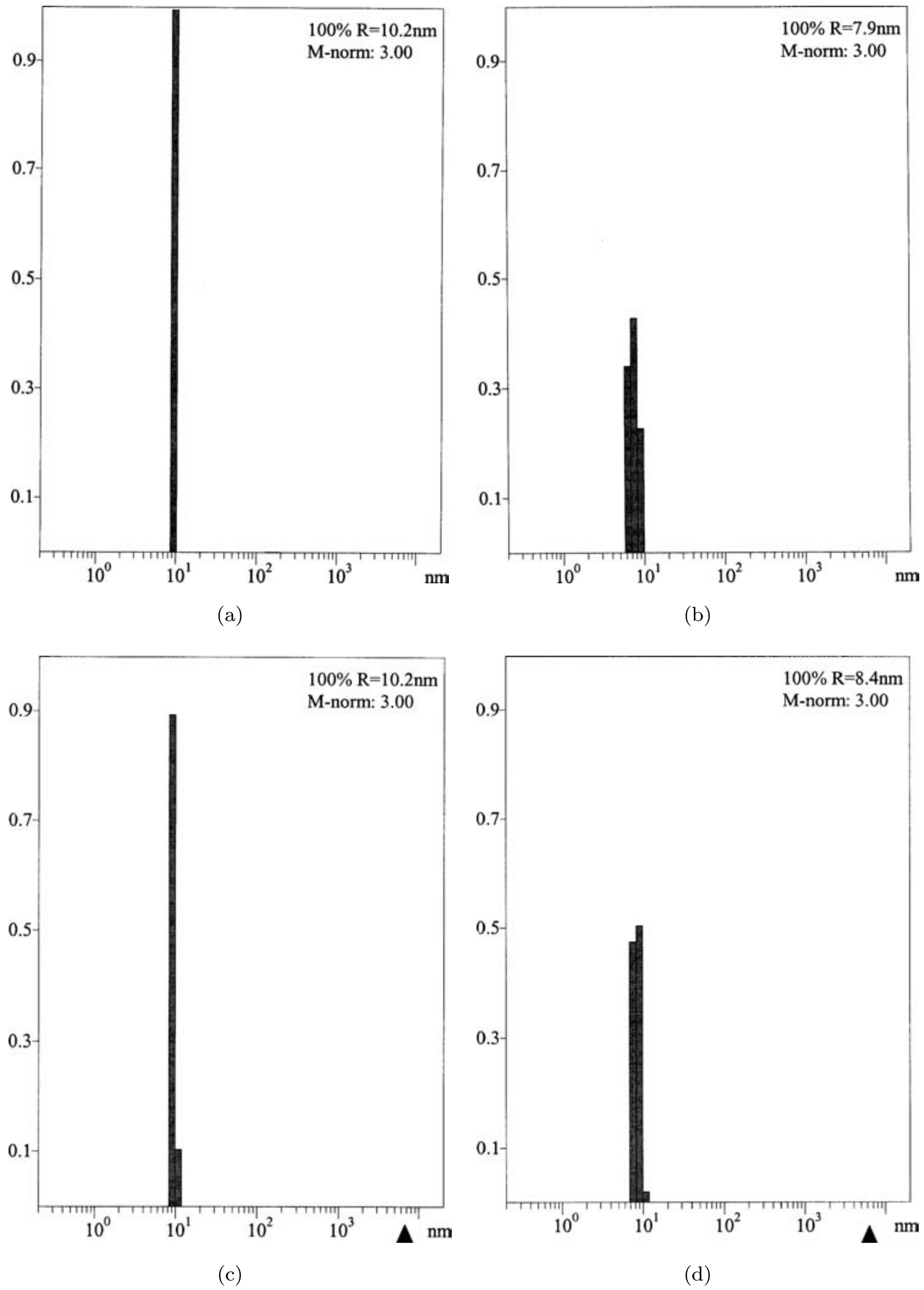

(a) (b) (c) (d)

Fig. 1. Particle size distribution of P1 to P5 in water at pH = 5 obtained by dynamic light scattering: (a) P1; (b) P2; (c) P3 and (d) P4. *X*-axis indicates the size of the particles and *Y*-axis represents the fraction distribution.

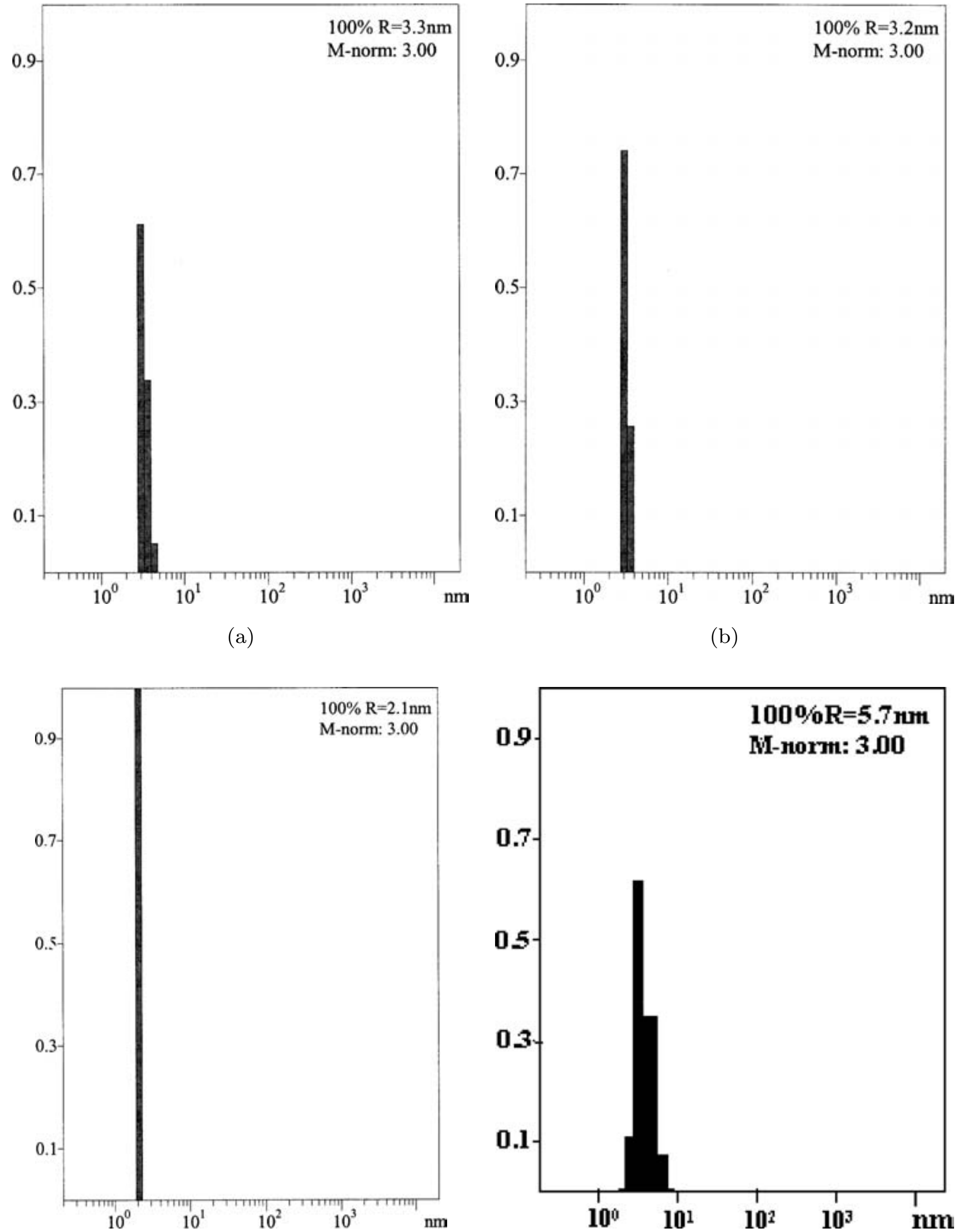

(a) (b)

(c) (d)

Fig. 2. Particle size distribution of P1–P4 in NaCl obtained by dynamic light scattering at pH 5: (a) P1; (b) P2; (c) P3 and (d) P4. X-axis indicates the size of the particles and Y-axis represents the fraction distribution.

Table 2. DLS data of the peptides at two pH values and salt solutions.

Peptides pH/salt	P1 (nm)	P2 (nm)	P3 (nm)	P4 (nm)
At pH ~ 3	3.0	3.6	—	6.3
At pH ~ 5	10.2	7.9	10.2	8.4
In 10 mM $CaCl_2$	3.1	2.2	—	5.7
In 10 mM NaCl	3.3	3.2	2.1	12.9

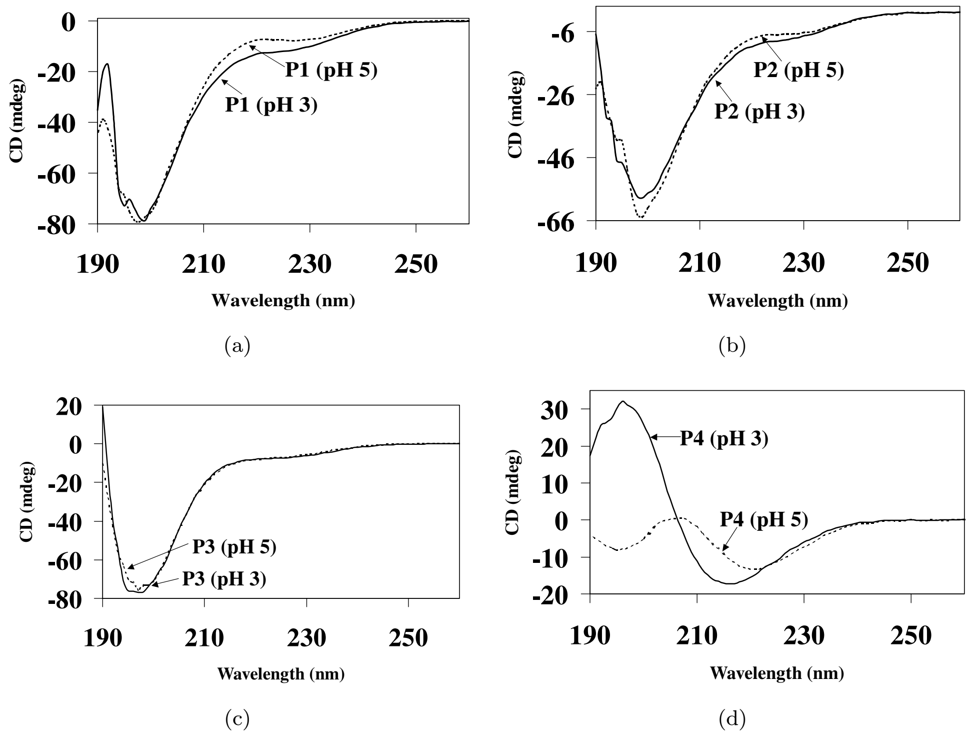

(a) (b)

(c) (d)

Fig. 3. CD spectra of the peptides at 1 mg/ml in water: (a) P1; (b) P2; (c) P3 and (d) P4 at pH ~ 3 and 5, respectively.

further by using the CD Spectra Deconvolution Software (CDNN)[10] confirmed the major contribution from the random coil structure (~ 40%). The CD spectrum of the **P1** in presence of 10 mM NaCl showed a sharp negative minimum at 204 nm and positive maxima at 191 nm, 197 nm and 201 nm, which indicate the presence of random coil conformation (Fig. 4(a)). The appearance of small shoulder at 225 nm corresponds to a bend or β-turn conformation. Analysis of the CD data revealed ~ 34% random coil and ~ 30% β-sheet structure, whereas in the presence of $CaCl_2$ (10 mM), the spectrum contained a positive maximum at 191 nm and a negative minimum at 200 nm, which belongs to random coil conformation. Here also the

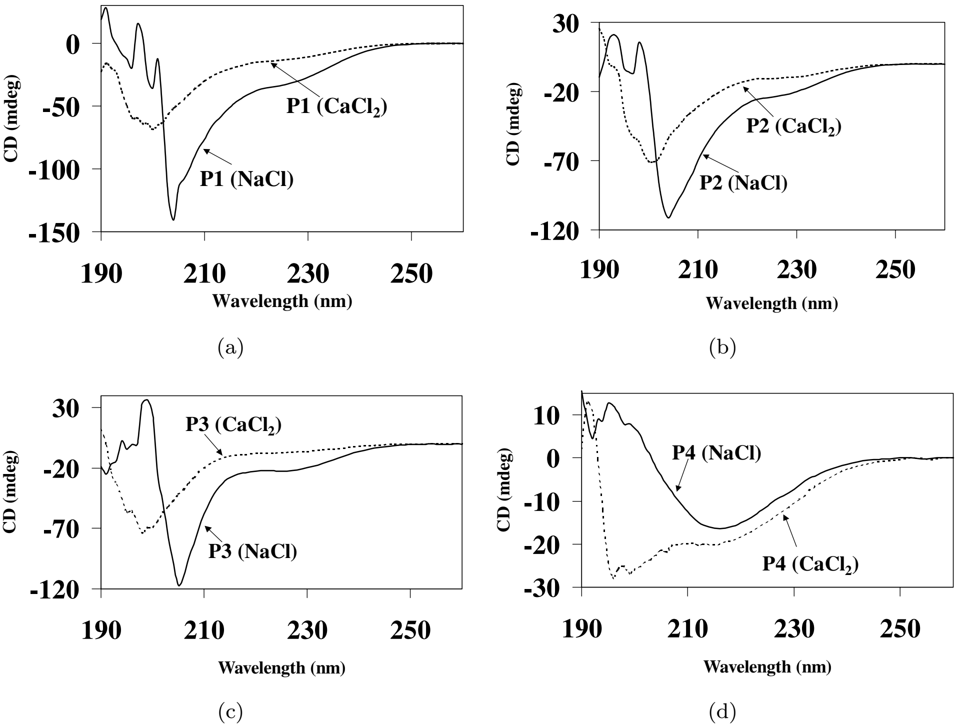

(a) (b)

(c) (d)

Fig. 4. CD spectra of the peptides at 1 mg/ml in 10 mM of NaCl and $CaCl_2$ solution at pH ∼ 3: (a) P1; (b) P2; (c) P3 and (d) P4.

appearance of shoulder at 224 nm indicates the bend/turn conformation. CD spectra analysis showed 36% random coil and 38% β-sheet structures.

In the case of **P2** at pH ∼ 3, a strong negative minimum at 198 nm and small shoulder at 227 nm represents the major contribution of random coil or bend/turn conformation (Fig. 3(b)) and calculations indicated ∼20.1% β-turn and 33.7% random coil. With an increase in pH to 5, and additional negative maximum at 191 nm was observed. The shoulder at 227 nm at pH ∼ 3 shifted slightly to 230 nm. Here also the analysis data revealed equal contribution from the random coil or β-sheet conformations. In the presence of salt solution (10 mM NaCl), there is a slight change in the spectrum with positive maximums at 193 nm and 198 nm and a negative minimum at 204 nm with a shoulder at 227 nm (Fig. 4(b)). The data showed equal amounts of β-sheet and random coil conformation (33%). In $CaCl_2$ solution, the negative minimum has a blue shift of 3 nm (201 nm) and the positive maximum was not observed. The CDNN data quantified a β-sheet content of ∼ 38% and a random coil content of ∼ 35%. We also observed from the CD spectra that the intensities of the negative bands are higher in salt solutions than in water at different pH. This shows that the peptides are able to self-assemble better in salt solutions than in water, giving more ordered structures. Figure 3(c) shows the CD spectra of the peptide **P3** at pH ∼ 3 and 5, a negative minimum at 197 nm corresponding to a random coil conformation. The data analysis indicated a major contribution from the random coil structure (∼ 39%), 30% of β-sheet and 23% β-turn. Increasing the pH to 5 did not change the conformation significantly but resulted in a slight decrease in the intensity of the negative band. Figure 4(c) shows the CD spectra of peptide **P3** studied at 25°C at 1 mg/ml in 10 mM NaCl and $CaCl_2$ solution. In the presence of 10 mM NaCl, a sharp negative minimum at 205 nm and a positive maximum at 199 nm were observed, which confirmed the presence of a random coil

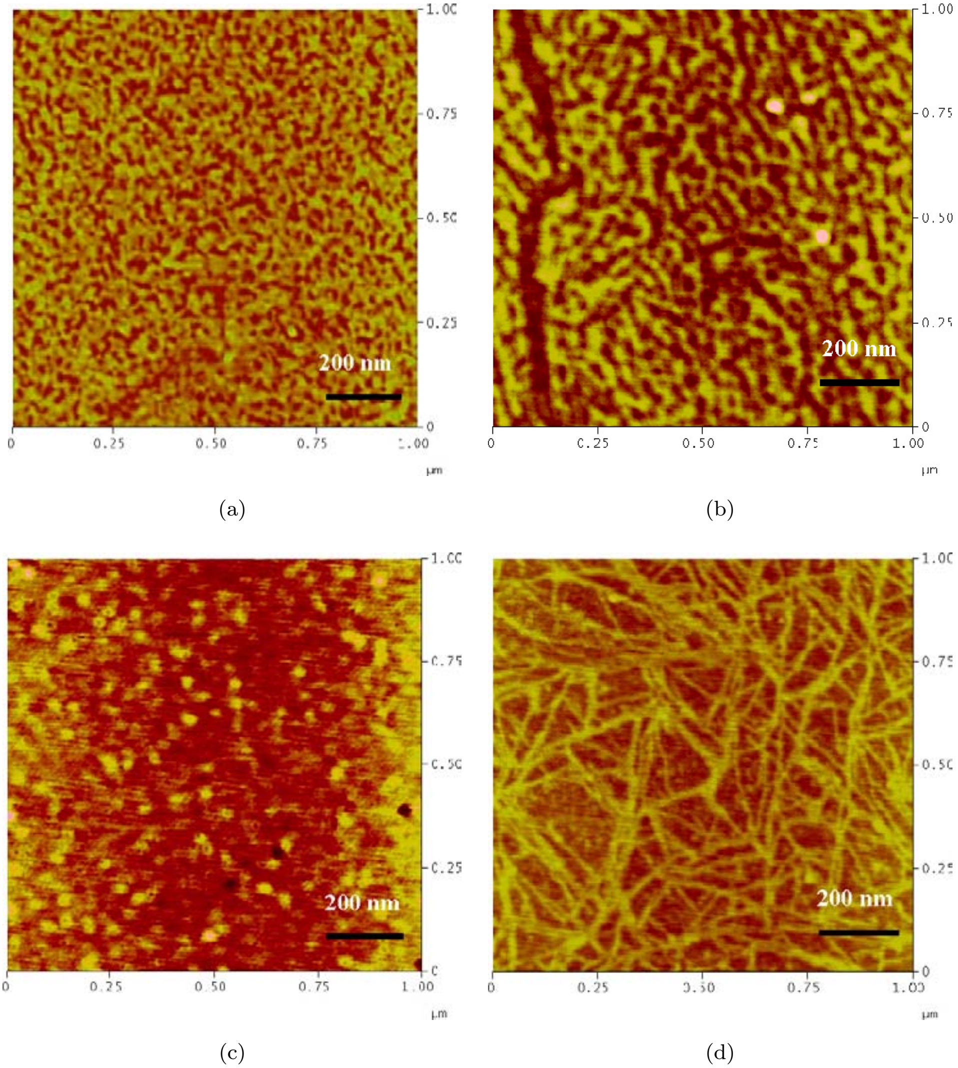

(a)

(b)

(c)

(d)

Fig. 5. Images of AFM scans of peptides at 1 mg/ml in water at pH ∼ 5: (a) P1; (b) P2; (c) P4 and (d) P5. The image is 1 μm × 1 μm in size.

conformation. A small shoulder was observed at 225 nm indicating the presence of a bend or β-turn conformation. Analysis of the CD data indicates a random coil conformation of $\sim$ 32% and a β-sheet conformation of $\sim$ 30%. Similar results were obtained in 10 mM $CaCl_2$ solution with a random coil content of $\sim$ 34 % and $\sim$ 39% β-sheet conformation. CD spectra of the peptide **P4** at 25°C in water at 1 mg/ml at pH $\sim$ 3 and 5 are given in Fig. 3(d). In salt solution, **P4** showed a minimum around 216 nm and a maximum around 196 nm which indicates the formation of a β-sheet conformation, β-sheet $\sim$ 46%, β-turn (18%) and random coil content of 35%, respectively (Fig. 4(d)). Increasing the pH to 5, a red shift was observed with two negative minima at 195 and 220 nm and a maximum at 207 nm, indicating the presence of β-sheet and random coil conformations.

3.1. *Self-assembly using atomic force microscopy*

Self-assembly of the peptides on mica surface was performed in air to study the morphology of the peptides under different conditions. The preliminary results showed that spherical structures at pH $\sim$ 3 with a diameter of about 25–30 nm. Upon increasing the pH to 5, no islands were observed but worm-like structures were formed (Fig. 5). For **P2,** large spherical islands were observed at pH $\sim$ 3 and the size distribution for **P2** is greater than **P1**. As the pH is increased to 5, thick worm-like structures were observed. **P3** gave similar observation, but **P4** forms a fiber-like morphology on mica surface. The effects of the self-assembly in salt solutions were also studied. In most cases, the morphology did not change significantly in salt solution. A detailed analysis of such morphologies are underway to correlate the self-assembly features in solution and in solid state.

4. Discussions

As mentioned above, several peptides with alternating hydrophobic–hydrophilic residues are known to self-assemble into β-sheet structure, but the presence of prolines (results in conformation inflexibility) in **P1** to **P3**, a stable β-sheet structure was not observed. The amino acid sequence for all the peptides are shown in Table 1. Both **P1** and **P2** gave an overall negative charge while **P3** and **P4** showed a net charge of zero. The DLS studies gave an aggregation size of 10 nm and CD spectra indicated a mixture of conformations. **P1** gave different types of morphologies for both pH because **P1** has an isoelectric point of 3.57. This means that at this point, the peptide has a net charge of zero. A slight increase in the intensity at 223 nm in the CD spectrum for **P1** and the larger particle size distribution shows a more aggregated structure. **P2** showed random coil with a bend or β-turn conformation with a spherical morphology. From the AFM images, **P3** and **P4** gave the fiber-type morphology independent of pH. In addition, the CD results for **P3** and **P4** were also consistent with the above observation. Even though the CD spectrum of **P4** did not give the same pattern at both pH, but it gave the fiber-like structure mainly because there is a much higher β-sheet content as compared to random coil conformation. Overall, there is no great difference in morphology for **P1** and **P2** in $CaCl_2$ solution. From the CD spectra, **P1**, **P2** and **P3** formed more ordered structure in monovalent ion than divalent ion. Fiber-like morphology was formed by **P4** due to the stable β-sheet structure. For P1, P2 and P4, all of them consist of alternating hydrophobic and hydrophilic amino acid residues and only **P4** forms fiber-like structure in both salt solutions. This could be due to the presence of the proline in **P1** and **P2**, which limits the flexibility of the conformation. Even though **P3** has the same conformation as **P1** and **P2**, it has no proline residue in the middle. Currently, we are pursuing research activities correlating the observed structure with the function of the peptides in biomineralization and related areas and the results will be published at a later date.

5. Conclusions

In conclusion, we have demonstrated the self-assembly of a few designer peptides under different conditions. All peptides aggregate in solution and they showed significant dependence on pH and salt concentration. In addition, the CD spectra indicated a mixture of secondary structures in solution. Self-assembly of all peptides with alternating hydrophilic and hydrophobic residues showed fiber-like morphology at high pH. The aggregation behavior and morphology of the aggregated structures changes significantly based on the primary sequence of the peptides, pH of the medium and salt concentration. Experiments to correlate the structure and functions of the peptides are currently underway in our lab.

Acknowledgments

The authors thank the Agency for Science and Technology (A*STAR) for financial support and Associate Professor Xu Guo Qin for allowing the use of the AFM instrument.

References

1. Whitesides GM, Mathias JP and Seto CT, Molecular self-assembly and nanochemistry: A chemical strategy for the synthesis of nanostructures, *Science* **254**:1312–1319, 1991.
2. Lehn JM, Supramolecular chemistry, *Science* **260**:1762–1763, 1993.
3. Gorman J, One-upping nature's materials, *Science News* **158**:364–367, 2000.
4. Pauling L, *The Nature of Chemical Bond,* 3rd ed., Cornell University Press, New York, 1960.
5. Schulz GE and Schirmer RH, *Principles of Protein Structure*, Springer-Verlag, New York, 1979.
6. Creighton TE, *Proteins: Structures and Molecular Principles*, 2nd ed., WF Freeman & Co, New York, 1993.
7. Zhang S, Holmes T, Lockshin C and Rich A, Spontaneous assembly of a self-complementary oligopeptide to form a stable macroscopic membrane, *Proc Natl Acad Sci USA* **90**:3334–3338, 1993.
8. Zhang S, Holmes T, Lockshin C and Rich A, Unusually stable β-sheet formation in an ionic self-complementary oligopeptide, *Biopolymers* **34**:663–672, 1994.

9. Caplan MR, Schwartzfarb EM, Zhang S, Kamm RD and Lauffenburger DA, Control of self-assembling oligopeptide matrix formation through systematic variation of amino acid sequence, *Biomaterials* **23**:219–227, 2002.
10. Zhang S and Rich A, Direct conversion of an oligopeptide from a β-sheet to an α-helix: A model for amyloid formation, *Proc Natl Acad Sci USA* **94**:23–28, 1997.

NANOTECHNOLOGY AND HUMAN DISEASES

GABRIEL YEW HOE LEE
Singapore–MIT Alliance
4 Engineering Drive 3, Singapore 117576

CHWEE TECK LIM*
Division of Bioengineering, National University of Singapore
7 Engineering Drive 1, Singapore 117576
Department of Mechanical Engineering, National University of Singapore
9 Engineering Drive 1, Singapore 117576
Singapore–MIT Alliance, 4 Engineering Drive 3, Singapore 117576
NUS Nanoscience & Nanotechnology Initiative
2 Engineering Drive 3, Singapore 117576
ctlim@nus.edu.sg

Tissues, cells and biomolecules can experience changes in their structural and mechanical properties during the occurrence of certain diseases. Recent advances in the fields of nanotechnology, biomechanics and cell and molecular biology have led to the development of state-of-the-art and novel biophysical and nanotechnological tools to probe the mechanical properties of individual living cells and biomolecules. Here we will review the basic principles and application of some of these nanotechnological tools used to relate changes in the elastic and viscoelastic properties of cells to alterations in the cellular and molecular structures induced by diseases such as malaria and cancer. Knowing the ways and the extent to which mechanical properties of living cells are altered with the onset of disease progression will be crucial for us to gain vital insights into the pathogenesis and pathophysiology of malaria and cancer, and potentially offers the opportunity to develop new and better methods of detection, diagnosis and treatment.

Keywords: Nanotechnology; nanobiomechanics; human diseases; malaria; cancer.

1. Introduction

As a physical structure, the human body is perpetually subjected to stresses and strains throughout life. In particular at the cellular and molecular levels, any deviations in the structural and mechanical properties of the living cells and biomolecules will not only affect their physiological functions, but may also lead to diseases such as malaria and cancer.[1,2]

---

[*] Corresponding author.

The composition and organization of the structural features of a cell is likely to undergo alterations in an occurrence of a disease, which can be simply defined as any abnormal conditions arising from within our body that have a tendency to impair bodily functions.[1] Subsequently, the structural and mechanical properties of the cell, such as its deformability and surface adhesiveness, will change accordingly as these properties are reflective of any changes occurring in the molecular composition and organization of the cell. Since these changes often occur at the nanoscale, nanotechnology can aid in the study of human diseases. By borrowing tools from nanotechnology, we hope to better understand changes occurring in diseased cells at the nanoscale. As the disease progresses, nanotechnology tools can also provide a quantitative way of studying these physical changes occurring in individual cells.[3] More importantly, these tools may provide an alternative means of assessing certain human disease states.

With the recent advances in nanotechnology, biomechanics and cell and molecular biology, it is now possible to characterize these mechanical influences acting on biological structures such as individual cells and biomolecules. Nanobiomechanics — the fusion of nanotechnology, mechanics, and cell and molecular biology, has recently been identified as an emerging technology that is making significant contributions to the understanding of human diseases.[1,4] Since mechanics is known to play a role in the occurrence of a disease, nanobiomechanics can help to establish connections between mechanics of living cells and the pathophysiology of diseases. As a result, some novel and state-of-the-art nanotechnological and biophysical tools have been developed and adapted for the purpose of studying and characterizing biological structures at both the cellular and molecular levels. These tools include the optical tweezers, the micropipette aspiration assay, magnetic tweezers, atomic force microscope, molecular force microscope, flow cytometer, magnetic twisting cytometer, cytoindenter, microplate manipulator, microfluidic system and the optical stretcher, of which some have been reviewed elsewhere.[2,5–7]

This article will highlight some nanotechnology-based tools being adapted to probe human diseases, such as malaria and cancer since they are examples of diseases which exhibit changes in mechanical properties at the cellular and molecular levels, so that new and better methods of detection and diagnosis may be developed.

2. Nanotechnology and the Study of Malaria

Malaria infects about 350–500 million people and gives rise to about 1.3–3 million deaths each year.[1] It is the deadliest parasitic human disease on earth and is caused by a mosquito-borne parasite. In the human body, highly deformable healthy red blood cells (RBCs) deliver oxygen to different parts of the body by squeezing their way through narrow capillaries. With malaria, infected RBCs lose their ability to deform and stretch. Upon invading a RBC, the malarial parasite will introduce extensive modifications to the molecular structure of the RBC, making it to be stiff and sticky (cytoadherent). Thus, malaria-infected RBCs are unable to squeeze through tiny blood vessels to deliver oxygen to tissues and organs in the body. This can often result in fatal consequences such as blood clogging, severe anemia, coma or even death.[8]

The stiffness and stickiness of these infected RBCs can be precisely studied using nanotechnology. In this section, we describe some nanotechnological and biophysical tools used to probe malaria-infected RBCs.

2.1. *Optical tweezers*

The optical tweezers is essentially a tool which uses a laser to trap, control and manipulate tiny transparent particles in a medium. It was invented by Ashkin *et al.*[9,10] in 1986, but this tool made its debut in the biological sciences when Block *et al.* used it to manipulate a bacterium so as to study bacterial flagella in 1989.[11] Since then, optical trapping has evolved into an indispensable research tool used by both biologists and physicists alike; and it is increasingly being used as an experimental tool for both single cell and single molecule biomechanics experiments.[2]

The basic components of the optical tweezers would consist of an inverted microscope and a laser beam that is directed up the microscope through a high numerical aperture objective. Optical tweezers work on the principle that forces are exerted onto matter due to the scattering, emission and absorption of light. The fact that optical tweezers are able to trap objects is precisely due to the radiation pressure which arises from the change in momentum as light refracts off an object.[12] The optical trapping of a dielectric particle is depicted in Fig. 1. Optical tweezers are able to manipulate objects using a focused laser beam that generates a spring-like force. Depending on the power of the laser used, the optical tweezers can exert forces in the order of 10's to 100's pN. To perform a cell stretching experiment, two transparent microbeads are first attached diametrically across the cell. For a single optical trap system, one microbead is trapped and manipulated with a laser

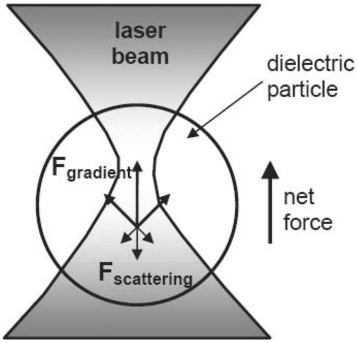

Fig. 1. Schematic diagram depicting the optical trapping of a dielectric particle by a laser beam. When a laser beam is directed onto a particle whose refractive index is different from that of the medium, a resultant trapping force is induced which will cause the particle to move towards the focal point of the laser beam as a consequence of gradient and scattering forces. Reprinted with permission from Ref. 2, © 2006, Elsevier.

trap while the other microbead is attached to a substrate. The cell is subsequently stretched by moving the sample stage where the substrate is mounted on.

Figure 2 shows a schematic diagram of the stretching of a single RBC using the optical tweezers.[13–15] Suresh *et al.* used the optical tweezers to quantitatively measure the change in the shear modulus of the membrane of the malaria-infected RBC infected at the various stages of the infection.[16] In their study, the different stage infected cells were stretched using the optical tweezers. Figure 3 shows that the late-stage infected cell was observed to have hardly stretched as compared with the cell at the earlier stages of infection, thus showing the loss of deformability as the

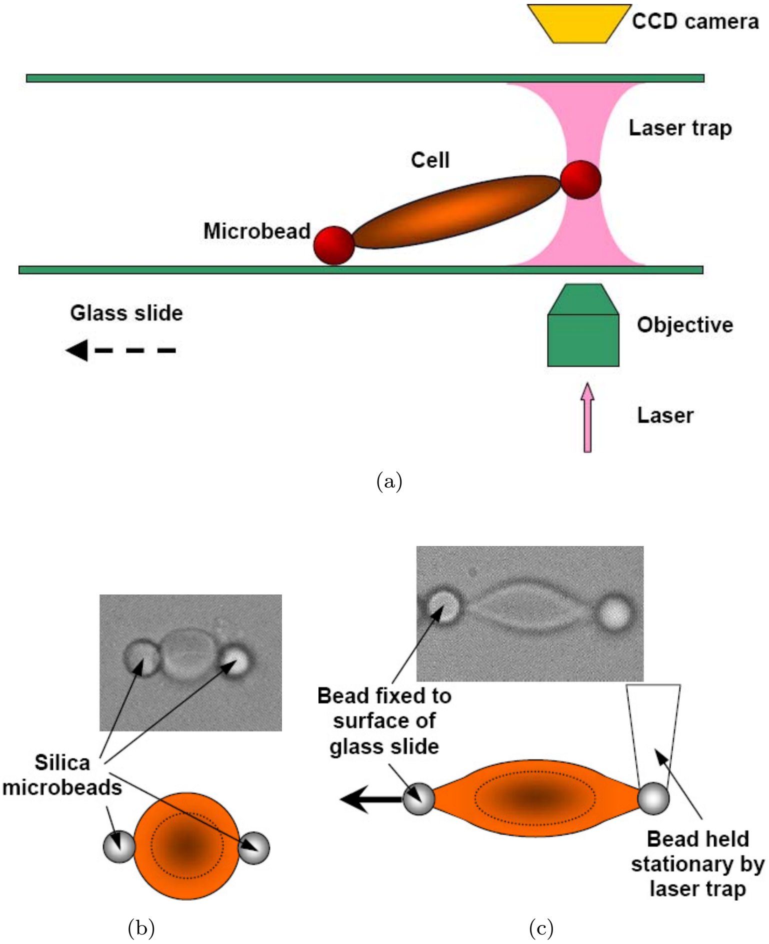

(a)

(b)

(c)

Fig. 2. (a) Schematic diagram of the optical tweezers setup for the stretching of a single cell. (b) To carry out the stretching experiment, two silica microbeads were non-specifically attached diametrically across the RBC with the left bead adhered to the glass slide. The laser beam was subsequently used to trap the right bead. By pulling the glass slide towards the left, the RBC was then stretched. (c) An optical image showing the stretched RBC. Reprinted with permission from Ref. 1, © 2007, Elsevier.

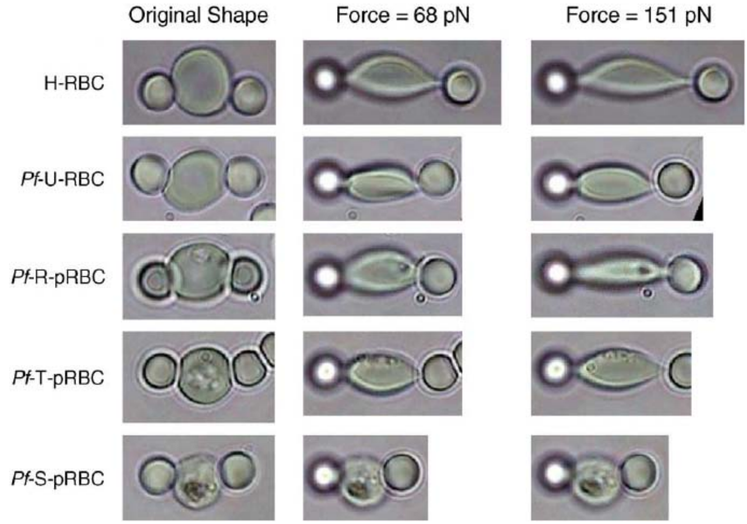

Fig. 3. Optical images showing healthy RBC (H-RBC), healthy control RBC (*Pf*-U-RBC), early-stage infected RBC (*Pf*-R-pRBC), mid-stage infected RBC (*Pf*-T-pRBC) and late-stage infected RBC (*Pf*-S-pRBC) at room temperature (left column) before stretching, when stretched at a force of about 68 pN (middle column) and when stretched at a force of about 151 pN (right column). Reprinted with permission from Ref. 16, © 2005, Elsevier.

disease progresses. They also showed that the shear modulus of the cell membrane at the late stage exhibited a ten-fold increase when compared with that for the uninfected cell.[16]

The optical tweezers can also be used to compliment the work carried out on the genetic manipulation of the malarial parasite to investigate how knocking out individual proteins might affect the membrane elasticity of the infected cell. During infection, the malarial parasite export proteins to the RBC membrane causing it to be stiff and sticky. By removing individual proteins from the parasite and subsequently using the optical tweezers to probe the shear elastic modulus of an RBC infected with these mutant parasites, the role played by a specific parasite exported protein in contributing to the stiffening of malaria-infected RBCs could be better understood. This kind of measurement and manipulation can potentially lead to new therapies for this disease. Using the optical tweezers, Mills *et al.* found that RBCs infected with a mutant malarial parasite, in which the gene for a parasite protein called RESA (ring-infected erythrocyte surface antigen) was knocked out, to be less stiff.[17]

2.2. *Atomic force microscope*

The atomic force microscope (AFM), well known for its high-resolution topographical imaging capabilities and its ability to be used as a force sensor with piconewton resolution, is emerging as a powerful mechanical probe in single cell and single molecule biomechanics experiments.[1,2] The ability to carry out real-time measurements on samples in fluids is one key advantage of the AFM, since it allows probing of biological samples to take place in their natural physiological conditions. The AFM was invented by Binnig *et al.*[18] in 1986, and remains one of the foremost tools in nanotechnology used for imaging and probing matter at the nanoscale.

A schematic diagram of the AFM is depicted in Fig. 4. The working principle of the AFM is based on the ability of a very sensitive cantilever in sensing forces at the piconewton scale. When measuring the attractive or repulsive forces between the cantilever tip and the surface of the sample, the vertical deflection of the cantilever is monitored and captured by the laser beam to give the local height and variations in topography of the sample. Thus, by scanning the surface of the sample, images with nanoscale resolution can be obtained. In addition, forces of interaction between the sample and the cantilever tip can also be measured with piconewton range accuracy making the AFM a suitable tool for studying molecular interactions.

One key feature of the pathophysiology of malaria is the increased cytoadherence or stickiness exhibited by infected RBCs. In light of this, Li *et al.* carried out an AFM study of both normal and malaria-infected RBCs to investigate the cell morphology at different stages of the parasite development.[19] Their studies revealed the presence of nanoscale knob-like structures and protrusions on the surface of the infected RBCs (see Fig. 5). The AFM images not only allow the density of these knobs,

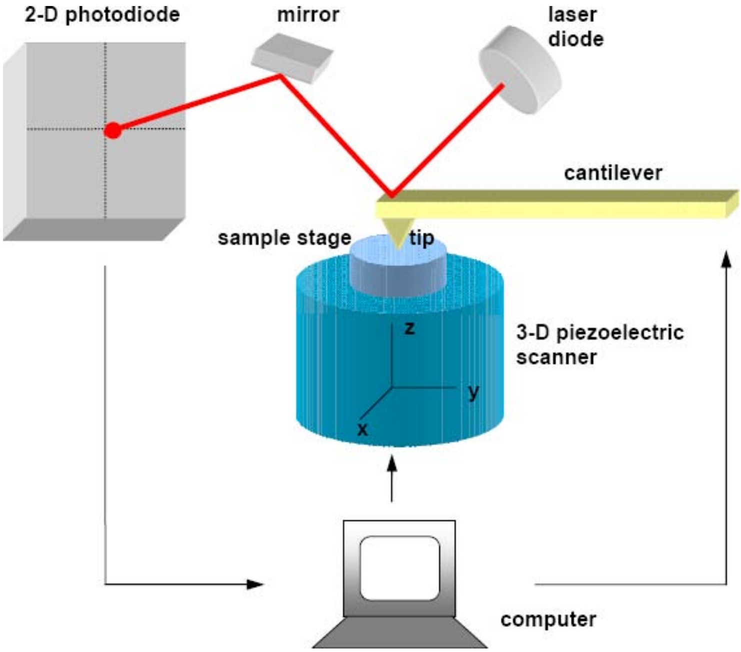

Fig. 4. Schematic diagram of the AFM. Reprinted with permission from Ref. 2, © 2006, Elsevier.

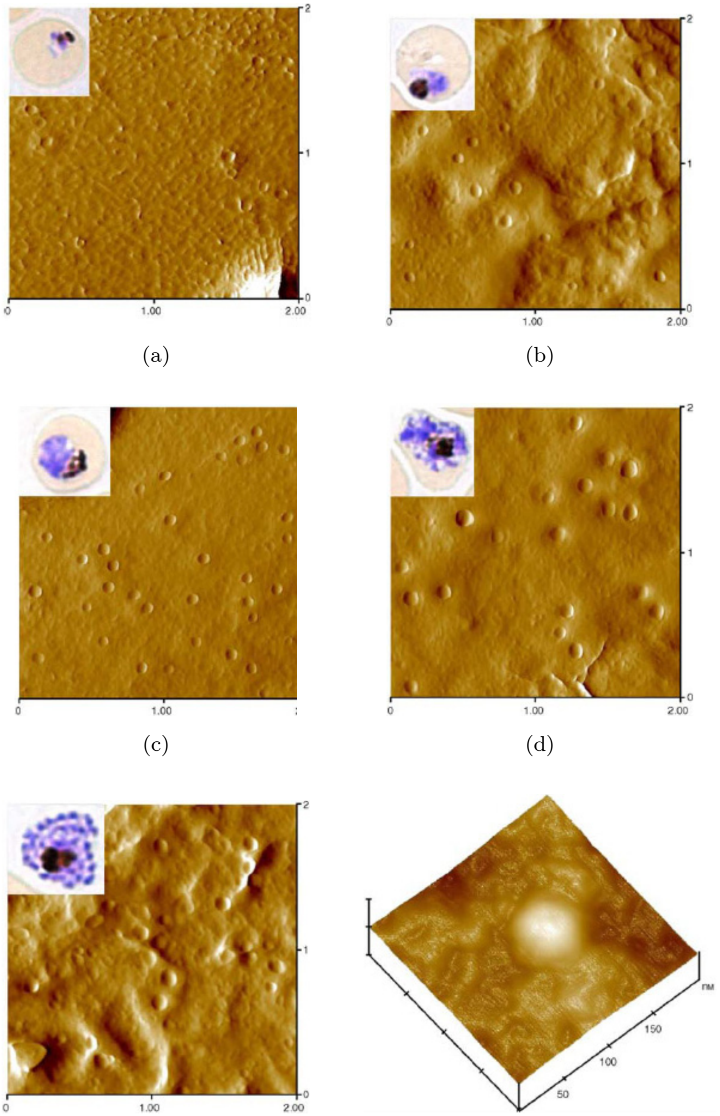

(a) (b)

(c) (d)

(e) (f)

Fig. 5. AFM images of knob-like structures and their distributions at different stages (a–e) of the malarial parasite's development with (a) and (e) being the early and late stages of infection, respectively. (f) Three-dimensional image of a single knob-like structure. Reprinted with permission from Ref. 19, © 2006, Elsevier.

but also their three-dimensional structure and size to be determined. Therefore, the AFM is able to offer an effective way of visualizing the surface morphology of malaria-infected RBCs due to its ability to image and probe samples at the nanometer and piconewton scale.

3. Nanotechnology and the Study of Cancer

Every year, about 7 million people die of cancer and more than 11 million people are diagnosed to be suffering from the disease.[1] Cancer is one of the leading causes of death worldwide and the World Health Organization has estimated that there will be 15 million new cases of cancer each year by 2020.[20] Cancer develops when cells in the human body acquired the ability to divide uncontrollably. This arises due to mutations occurring in genes that are responsible for cell growth and repair. These aberrant cells then infiltrate and destroy surrounding normal body tissue. The ability to treat and cure cancer is highly dependent on the ability to detect the slight presence of these highly invasive metastatic cancerous cells at the earliest opportunity and to eradicate them to prevent them from spreading to other parts of the body.

Since one pathophysiological outcome of cancer is that metastatic cells are more deformable (softer) than their normal counterparts[21–23] and mechanical factors are known to play a role in metastasis (migration of cancer cells),[24] it would seem appropriate to use nanobiomechanics to study cancer. In this section, we will look at how nanotechnology can be adapted to study cancer, so as to better understand how cancer cells become softer, move more easily and consequently spread to other parts of the body. This may prove useful in the fight against cancer.

3.1. *Optical stretcher*

The optical stretcher is a recent nanobiomechanical tool used in the study of cancer cells. It was first developed by Guck *et al.*[25] in 2000 to probe the deformation of single individual cells and is capable of providing a detailed and quantitative biorheological characterization of single suspended cells.[23,25,26] Figure 6 shows a schematic diagram of the optical stretcher.

In the optical stretcher, two counter-propagating, low power, divergent laser beams act as an optical trap for cells which are at the center between the two laser beams. Subsequently, a higher laser power is applied which will stretch or deform the trapped cells axially (see Fig. 7).[25] The optical stretcher makes use of the underlining fact that the total force acting on a dielectric object is zero, with surface forces being additive when the dielectric object is placed between two divergent laser beams.[26] This results in a force "pulling" on either side of the cell, thus stretching it. One advantage of this technique is that the entire cell surface is stretched by a global distribution of the laser induced force which reveals an overall mechanical property of the cell.[23] This is in direct contrast to other nanotechnology-based and biophysical tools such as the micropipette aspiration assay,[27,28] optical tweezers[13,14] and AFM[29–32] which involve the application of forces at very localized areas of the cell surface. However, as the optical stretcher only allows for measurements of cells in suspension, adherent cells are not normally probed in their physiological state.

The optical stretcher was used to study the creep behavior of individual suspended fibroblasts. It was found that cancerous mouse fibroblast cells deform 50%

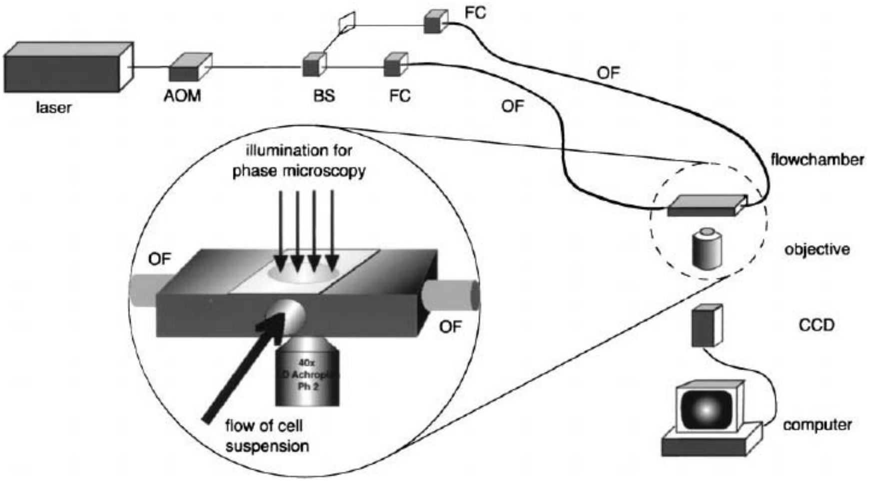

Fig. 6. Schematic diagram of the optical stretcher. The acousto-optic modulator (AOM) serves to control the intensity of the laser beam, which is split evenly into two by a beam splitter (BS) and subsequently coupled into two optical fibers (OF) by means of fiber couplers (FC). The optical fibers (OF) were aligned opposing each other and within a flow chamber (see inset) to trap and stretch cells. Data is recorded using a computer and a CCD camera. Reprinted with permission from Ref. 26, © 2001, Biophysical Society.

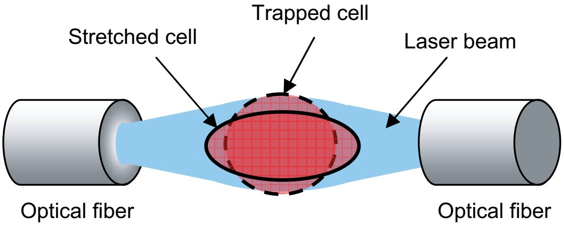

Fig. 7. Schematic diagram showing the axial stretching of a cell using an optical stretcher. The cell is trapped by optical forces arising from two divergent laser beams and subsequently stretched along the laser beam axis when a higher laser power is used. Reprinted with permission from Ref. 1, © 2007, Elsevier.

more than their healthy counterparts.[23] In another separate work carried out using the optical stretcher to probe the elasticity of human breast cancer cells, it was discovered that breast cancer cells were able to stretch to about five times more than their healthy counterparts, while metastatic (invasive) breast cancer cells stretch to about twice as much as non-metastatic (non-invasive) cancer cells.[33] This increased deformability (softness) of cancer cells may raise the probability of cell migration to another site in the body, which is a critical step in cancer metastasis. Such connections between mechanical properties and biological function could provide further insights into the progression of cancer. The optical stretcher is thus an example of a tool which might be useful in the diagnosis of cancer because current diagnostic methods are still not able to detect the disease at the individual cellular level.[34] Moreover, the optical stretcher can be easily incorporated into a microfluidic device to produce a high throughput flow-cytometric system capable of sorting and trapping cells without intruding into their underlying biological functions so that further analysis and therapeutic measurements could be made.

3.2. *Nanoindentation*

In addition to its unique imaging capabilities, the AFM can also be used to determine the stiffness of cells. This is often achieved by indenting the cell with the tip of an AFM probe, which can act as a nanoscale indenter. As the cantilever indents the cell, the deflection of the cantilever is recorded and the data is collected. Since the cantilever deflection is linearly proportional to the loading force for small deflections, a linear elastic model of the cell based on Hertzian mechanics is normally used together with the collected deflection data to obtain the stiffness of the investigated cell.[35] Nanoindenters and those employing AFM tips have been used in indenting materials such as thin films[36] and biological structures such as individual living cells,[37] respectively with the aim of determining their mechanical properties.

The rigidity of cancer cells was first probed by indentation when Goldmann *et al.* used an AFM tip to indent wild and vinculin-deficient mouse F9 embryonic carcinoma cells, and compared the values of Young's modulus obtained for these two types of cancerous cells.[38,39] Following that, Lekka *et al.* performed an indentation study on normal and cancer cells of the same type. In the case of normal human bladder epithelial and their cancerous counterparts, they reported that cancer cells are softer than normal cells, and this difference in the degree of softness can be up to one order of magnitude.[40,41] More recently, Park *et al.* measured the local rigidity differences between normal mouse fibroblasts (BALB 3T3) and cancer cells (SV-T2 and H-*ras* transformed mouse fibroblasts). An obvious decrease in the Young's moduli of the cancer cells was subsequently reported.[42] Thus, changes in elasticity which occur during the malignant transformation of cells can be detected by a nanoscale indenter in the form of AFM probe tips. This change in elasticity may have important consequences on how cancerous cells are able to migrate to other sites in the body leading to the formation of secondary tumors during metastasis.

4. Future Perspectives and Conclusions

Although nanoscale measurement of the mechanical properties of biological cells is still in its infancy, borrowing tools from nanotechnology to make these measurements has provided an important alternative in the study of certain human diseases like malaria and cancer. Using nanotechnology to probe changes in the mechanical properties of a cell can help reveal its state of health, and may lead to a clearer and better understanding of the pathophysiology of the disease. The mechanical properties of diseased cells can also be utilized as a potential biological marker in the detection and diagnosis of human diseases. In addition, the efficacy of drugs used in the treatment of malaria and cancer can be determined by using some of the nanotechnological tools highlighted in this article to monitor the change in the mechanical properties of drug-treated diseased cells. It is hoped that nanotechnology can help in the development of new assays and better diagnostic devices that are highly sensitive in the early detection of diseases, especially when clinical symptoms are hardly evident.

Acknowledgments

The support received from the Singapore–MIT Alliance is gratefully acknowledged.

References

1. Lee GYH and Lim CT, Biomechanics approaches to studying human diseases, *Trends Biotechnol* **25**:111–118, 2007.
2. Lim CT, Zhou EH, Li A, Vedula SRK and Fu HX, Experimental techniques for single cell and single molecule biomechanics, *Mat Sci & Eng C — Biomim* **26**:1278–1288, 2006.
3. Lim CT, Zhou EH and Quek ST, Mechanical models for living cells — A review, *J Biomech* **39**:195–216, 2006.
4. Fitzgerald M, Ten emerging technologies: Nanobiomechanics, *Technol Rev* **109**:67, 2006.
5. Cooke BM and Lim CT, Mechanical and adhesive properties of healthy and diseased red blood cells, in Baskurt O, Meiselman HJ, Hardeman MR, Rampling M (eds.), Handbook of Hemorheology and Hemodynamics, IOS Press, 2007.
6. Lim CT, Single cell mechanics study of the human disease malaria, *J Biomech Sci Eng* **1**:82–92, 2006.
7. Van Vliet KJ, Bao G and Suresh S, The biomechanics toolbox: Experimental approaches for living cells and biomolecules, *Acta Mater* **51**:5881–5905, 2003.
8. Cooke BM, Mohandas N and Coppell RL, The malaria-infected red blood cell: Structural and functional changes, *Advances in Parasit* **50**:1–86, 2001.
9. Ashkin A, Bjorkholm JE and Chu S, Caught in a trap, *Nature* **323**:585–585, 1986.
10. Ashkin A, Dziedzic JM, Bjorkholm JE and Chu S, Observation of a single-beam gradient force optical trap for dielectric particles, *Opt Lett* **11**:288–290, 1986.
11. Block SM, Blair DF and Berg HC, Compliance of bacterial flagella measured with optical tweezers, *Nature* **338**:514–518, 1989.
12. Gordon JP, Radiation forces and momenta in dielectric media, *Phys Rev A* **8**:14–21, 1973.
13. Lim CT, Dao M, Suresh S, Sow CH and Chew KT, Large deformation of living cells using laser traps, *Acta Mater* **52**:4065–4066, 2004.
14. Lim CT, Dao M, Suresh S, Sow CH and Chew KT, Large deformation of living cells using laser traps, *Acta Mater* **52**:1837–1845, 2004.
15. Mills JP, Qie L, Dao M, Lim CT and Suresh S, Nonlinear elastic and viscoelastic deformation of the human red blood cell with optical tweezers, *Mech Chem Biosyst* **1**:169–180, 2004.
16. Suresh S, Spatz J, Mills JP, Micoulet A, Dao M, Lim CT, Beil M and Seufferlein T, Connections between single-cell biomechanics and human disease states: Gastrointestinal cancer and malaria, *Acta Biomater* **1**:15–30, 2005.
17. Mills JP, Diez-Silva M, Quinn DJ, Dao M, Lang MJ, Tan KSW, Lim CT, Milon G, David PH, Mercereau-Puijalon O, Bonnefoy S and Suresh S, Effect of plasmodial

RESA protein on deformability of human red blood cells harboring Plasmodium falciparum, *Nat Acad Sci USA* **104**:9213–9217, 2007.

18. Binnig G, Quate CF and Gerber C, Atomic force microscope, *Phys Rev Lett* **56**:930–933, 1986.
19. Li A, Mansoor AH, Tan KSW and Lim CT, Observations on the internal and surface morphology of malaria infected blood cells using optical and atomic force microscope, *J Microbiological Methods* **66**:434–439, 2006.
20. Stewart BW and Kleihues P (eds.), *World Cancer Report, International Agency for Research on Cancer*, World Health Organisation, 2003.
21. Gast FU, Dittrich PS, Schwille P, Weigel M, Mertig M, Opitz J, Queitsch U, Diez S, Lincoln B, Wottawah F, Schinkinger S, Guck J, Kas J, Smolinski J, Salchert K, Werner C, Duschl C, Jager MS, Uhlig K, Geggier P and Howitz S, The microscopy cell (MicCell), a versatile modular flowthrough system for cell biology, biomaterial research, and nanotechnology, *Microfluid Nanofluid* **2**:21–36, 2006.
22. Guck J, Schinkinger S, Lincoln B, Wottawah F, Ebert S, Romeyke M, Lenz D, Erickson HM, Ananthakrishnan R, Mitchell D, Kas J, Ulvick S and Bilby C, Optical deformability as an inherent cell marker for testing malignant transformation and metastatic competence, *Biophys J* **88**:3689–3698, 2005.
23. Wottawah F, Schinkinger S, Lincoln B, Ebert S, Muller K, Sauer F, Travis K and Guck J, Characterizing single suspended cells by optorheology, *Acta Biomater* **1**:263–271, 2005.
24. Chambers AF, Groom AC and MacDonald IC, Dissemination and growth of cancer cells in metastatic sites, *Nat Rev Cancer* **2**:563–572, 2002.
25. Guck J, Ananthakrishnan R, Moon TJ, Cunningham CC and Kas J, Optical deformability of soft biological dielectrics, *Phys Rev Lett* **84**:5451–5454, 2000.
26. Guck J, Ananthakrishnan R, Mahmood H, Moon TJ, Cunningham CC and Kas J, The optical stretcher: A novel laser tool to micromanipulate cells, *Biophys J* **81**:767–784, 2001.
27. Discher DE, Mohandas N and Evans EA, Molecular maps of red cell deformation: Hidden elasticity and in situ connectivity, *Science* **266**:1032–1035, 1994.
28. Hochmuth RM, Micropipette aspiration of living cells, *J Biomech* **33**:15–22, 2000.
29. Mahaffy RE, Shih CK, MacKintosh FC and Kas J, Scanning probe-based frequency-dependent microrheology of polymer gels and biological cells, *Phys Rev Lett* **85**:880–883, 2000.
30. Mahaffy RE, Park S, Gerde E, Kas J and Shih CK, Quantitative analysis of the viscoelastic properties of thin regions of fibroblasts using atomic force microscopy, *Biophys J* **86**:1777–1793, 2004.
31. Rotsch C, Jacobson K and Radmacher M, Dimensional and mechanical dynamics of active and stable edges in motile fibroblasts investigated by using atomic force microscopy, *Nat Acad Sci USA* **96**:921–926, 1999.
32. Rotsch C and Radmacher M, Drug-induced changes of cytoskeletal structure and mechanics in fibroblasts: An atomic force microscopy study, *Biophys J* **78**:520–535, 2000.
33. Lincoln B, Erickson HM, Schinkinger S, Wottawah F, Mitchell D, Ulvick S, Bilby C and Guck J, Deformability-based flow cytometry, *Cytom Part A* **59A**:203–209, 2004.
34. Simon MS, Ibrahim D, Newman L and Stano M, Efficacy and economics of hormonal therapies for advanced breast cancer, *Drugs Aging* **19**:453–463, 2002.
35. Radmacher M, Measuring the elastic properties of living cells by the atomic force microscope, *Method Cell Biol* **68**:67–90, 2002.
36. Jung YG, Lawn BR, Martyniuk M, Huang H and Hu XZ, Evaluation of elastic modulus and hardness of thin films by nanoindentation, *J Mater Res* **19**:3076–3080, 2004.

37. Rabinovich Y, Esayanur M, Daosukho S, Byer K, El-Shall H and Khan S, Atomic force microscopy measurement of the elastic properties of the kidney epithelial cells, *J Colloid Interf Sci* **285**:125–135, 2005.
38. Goldmann WH and Ezzell RM, Viscoelasticity in wild-type and vinculin-deficient (5.51) mouse F9 embryonic carcinoma cells examined by atomic force microscopy and rheology, *Exp Cell Res* **226**:234–237, 1996.
39. Goldmann WH, Galneder R, Ludwig M, Xu WM, Adamson ED, Wang N and Ezzell RM, Differences in elasticity of vinculin-deficient F9 cells measured by magnetometry and atomic force microscopy, *Exp Cell Res* **239**:235–242, 1998.
40. Lekka M, Laidler P, Gil D, Lekki J, Stachura Z and Hrynkiewicz AZ, Elasticity of normal and cancerous human bladder cells studied by scanning force microscopy, *Eur Biophys J Biophys Lett* **28**:312–316, 1999.
41. Lekka M, Lekki J, Marszalek M, Golonka P, Stachura Z, Cleff B and Hrynkiewicz AZ, Local elastic properties of cells studied by SFM, *Appl Surf Sci* **141**:345–349, 1999.
42. Park S, Koch D, Cardenas R, Kas J and Shih CK, Cell motility and local viscoelasticity of fibroblasts, *Biophys J* **89**:4330–4342, 2005.

NANOMEDICINE: NANOPARTICLES OF BIODEGRADABLE POLYMERS FOR CANCER DIAGNOSIS AND TREATMENT

S. S. FENG

Department of Chemical & Biomolecular Engineering
National University of Singapore, Block E5, 02-11
4 Engineering Drive 4, Singapore 117576

Division of Bioengineering, National University of Singapore
7 Engineering Drive 1, Singapore 117576

NUS Nanoscience & Nanotechnology Initiative
2 Engineering Drive 3, Singapore 117576

Nanomedicine is to apply and further develop nanotechnology to solve problems in medicine, i.e. to diagnose, treat and prevent diseases at the cellular and molecular level. This article demonstrates through a full spectrum of proof-of-concept research, from nanoparticle preparation and characterization, *in vitro* drug release and cytotoxicity, to *in vivo* pharmacokinetics and xenograft model, how nanoparticles of biodegradable polymers could provide an ideal solution for the problems encountered in the current regimen of chemotherapy. A system of vitamin E TPGS coated poly(lactic-co-glycolic acid) (PLGA) nanoparticles is used as an example for paclitaxel formulation as a model drug. *In vitro* HT-29 cancer cell viability experiment demonstrated that the paclitaxel formulated in the nanoparticles could be 5.64 times more effective than Taxol® after 24 hr of treatment. *In vivo* pharmacokinetics showed that the drug formulated in the nanoparticles could achieve 3.9 times higher therapeutic effects judged by area-under-the curve (AUC). One shot can realize sustainable chemotherapy of 168 hr compared with 22 hr for Taxol® at a single 10 mg/kg dose. Xenograft tumor model further confirmed the advantages of the nanoparticle formulation versus Taxol®.

Keywords: Biomaterials; cancer nanotechnology; chemotherapeutic engineering; molecular imaging; nanobiotechnology.

1. Introduction

Nanomedicine is to apply and further develop nanotechnology to solve problems in medicine, i.e. to diagnose, treat and prevent diseases at the cellular and molecular level, which would make many fatal diseases such as cancer, cardiovascular disease and AIDS curable at its earliest stage. Let us use cancer as an example. Cancer is a leading cause of death and has become the number 1 killer in many countries including Singapore. Cancer is responsible for approximately 25.9% in 2003, 27.1% in 2004 and 26.4% in 2005 of all Singapore fatalities. Moreover, it is estimated that global cancer rates could increase by 50% to 15 million patients and Asia cancer rates could increase by 60% to 7.1 million patients by 2020. In spite of such serious situation, no substantial progress could be observed before the end of the last century in fighting cancer. The cancer death rate in US was 1.939‰ of the total population in 1950 and still remains at 1.940‰ in 2001. Beyond these staggeringly dismal numbers, however, recent statistics has found that the cancer-survival rate is actually increasing for the first time in the past five decades, which led to a slight decrease of cancer death rate to 1.901‰ in 2003 and 158.8‰ in 2004 in US. This may largely benefited from the significant achievements in cellular and molecular biology, from which, new cancer-diagnostic and therapeutic techniques have been developed. This article will focus on cancer chemotherapy to show how Nanomedicine can solve the problems encountered in the current regimen of chemotherapy.[1–6]

Chemotherapy is often related to cancer treatment. Nevertheless, a more general definition of chemotherapy could mean "curing disease by drugs" or as given by Dr Paul Ehrlich, the father of modern chemotherapy, "curing by chemicals".[7] With recent achievements in cellular and molecular biology, nowadays drugs can also include biologically active macromolecules such as proteins and peptides. Chemotherapy is thus involved in the entire internal medicine. Chemotherapy is a complicated procedure in which many factors are involved in determining its success or failure. It carries a high risk due to drug toxicity, and the more effective drugs tend to be more toxic. Problems still exist even for successful chemotherapy. The patients have to tolerate severe side effects and sacrifice their quality of life. Chemotherapy should become more important and more effective if its problems in pharmacokinetics and pharmacodynamics could be solved, which include toxicity of the drugs; problems in drug adsorption, distribution, metabolism and excretion (ADME); drug resistance at various physiological levels from organs such as the 1st pass by liver and kidney, to cells and molecules such as the various physiological drug barriers including the gastrointestinal (GI) barrier and the blood-brain barrier (BBB). The problems could be solved by adopting two kinds of approaches: medical solution and engineering solution. The former is to use other drug or drugs to overcome the complications caused by the prescribed one. A typical example is the co-administration of cyclosporine A, a P-gp/P450 inhibitor, to make paclitaxel orally bioavailable, i.e. deliverable into the blood system through the oral route. However, cyclosporine A suppresses the body immune system and thus may cause severe side effects. Moreover, cyclosporine A has its own problem in formulation. The engineering solution is to modify the molecular structure of the drug or to formulate the drug in various carriers such as micelles, liposomes and biodegradable nanoparticles, i.e. "engineering the drugs", to deliver the drug across the GI barrier. Feng and Chien recognized the challenge by applying engineering, especially chemical engineering principles to solve the problems in chemotherapy and defined the strategy as chemotherapeutic engineering in 2003. Together with tissue engineering, which will revolutionize the concept of surgery from "cut and throw the diseased tissue or organ" to "repair and replace them by biologically engineered tissue or organ", chemotherapeutic engineering will contribute towards 21st century medicine.[1] US National Cancer Institute (NCI), National Institute of Health (NIH) and Department of Health & Human Services jointly published a white paper on cancer nanotechnology in 2004, which predicted that cancer nanotechnology will radically change the way we diagnose, treat and prevent cancer (http://www.nci.org). Nanoparticles of biodegradable polymers could be one of the most prospective areas of chemotherapeutic engineering or cancer nanotechnology, or nanomedicine, and will eventually provide ideal solutions for cancer and other fatal diseases such as cardiovascular restenosis and AIDS.[2–6]

This article demonstrates through a full spectrum of proof-of-concept research how nanoparticle technology could provide an ideal solution and with further development, promote a new concept of chemotherapy, which may include sustained, controlled and targeted chemotherapy; personalized chemotherapy; chemotherapy across various physiological drug barriers; and eventually, chemotherapy at home. Vitamin E TPGS coated poly(lactic-co-glycolic acid) (PLGA) nanoparticles are used as an example to formulate paclitaxel as model drug. Drug-loaded nanoparticles are characterized by various state-of-the-art techniques, including laser light scattering for size and size distribution, scanning electron microscopy (SEM) and atomic force microscopy (AFM) for surface morphology, X-ray photoelectron spectroscopy (XPS) and Fourier transformed infrared spectroscopy (FTIR) for surface chemistry, and Zeta-potential for surface charge. Drug encapsulation efficiency and *in vitro* drug release profile are measured by high performance liquid chromatography (HPLC). The cellular uptake of fluorescent nanoparticles is quantitatively investigated by confocal laser scanning microscopy with Caco-2 cancer cells employed as *in vitro* gastrointestinal drug barrier model for oral chemotherapy. *In vitro* HT-29 cancer cell viability experiment demonstrates that the paclitaxel formulated in nanoparticles could be 46 times more effective than Taxol® after 24 hr of treatment. *In vivo* pharmacokinetics showed that the drug formulated in the nanoparticles could achieve 3.9 times higher therapeutic effects judged by area-under-the curve (AUC) and 23.0 times longer half-life than Taxol®. One shot of vitamin E TPGS coated PLGA can realize sustainable chemotherapy of 168 hr compared with 22 hr for Taxol® at a single 10 mg/kg dose. Xenograft tumor model confirmed the advantages of the nanoparticle formulation versus Taxol®.

2. Nanoparticle Preparation and Characterization

2.1. *Nanoparticle preparation*

Paclitaxel-loaded nanoparticles of biodegradable polymers demonstrated in this research were prepared by the solvent extraction/evaporation method (single emulsion).[8–20] In brief, a dichloromethane (DCM) solution of paclitaxel and poly (DL-lactide-co-glycolide) (PLGA, 50:50) was slowly poured into an aqueous phase containing PVA or vitamin E TPGS, and emulsified using a microchip probe sonicator (XL2000, Misonix Incorporated, NY). The polymer solution can also contain

0.05% (w/v) coumarin-6 as fluorescent marker for the cellular uptake experiment. The resulting oil-in-water emulsion was then stirred at room temperature by a magnetic stirrer to evaporate DCM. The formed nanoparticles were collected by centrifugation (5810R, Eppendorf, 10,000 rpm, 15 min, 18°C) and washed with Millipore water 3 times to remove excessive emulsifier or fluorescent marker. The nanoparticle suspension was then freeze-dried (Christ, Alpha-2, Martin Christ, Germany) to obtain fine powder of nanoparticles, which was kept in a vacuum desiccator.

Other methods used in our Chemotherapeutic Engineering Laboratory at the National University of Singapore (NUS) for nanoparticle preparation include the dialysis method, spray dry and high pressure homogenization.[21–24]

2.2. *Nanoparticle characterization*

2.2.1. *Particle size and size distribution*

The size and size distribution of the formulated nanoparticles can be determined by laser light scattering with particle size analyzer. 90 Plus (Brookhaven Inst, Huntsville, NY) was used to measure the particle size and size distribution of the paclitaxel-loaded, TPGS emulsified PLGA nanoparticles, which is conducted at a fixed angle of 90° at 25°C. The mean size for the sample shown in Fig. 1 is 288 nm with standard deviation of 11.67 nm.

2.2.2. *Surface morphology*

The shape and surface morphology of the produced nanoparticles were investigated by the scanning electron microscopy (SEM, JEOL, JSM-5600 LV) and the atomic force microscopy (AFM, Multimode Scanning Probe Microscope, Digital

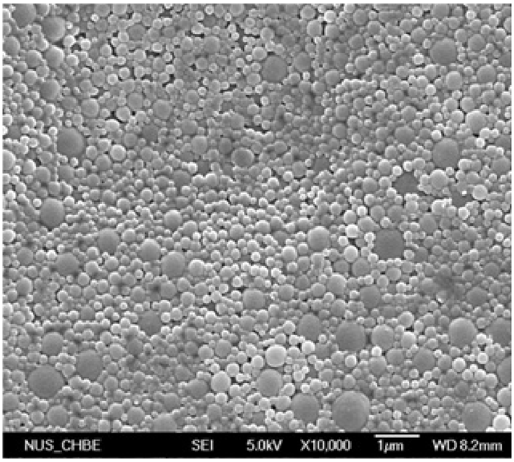

Fig. 1. FESEM images of paclitaxel-loaded PLGA nanoparticles (10% loading) prepared with vitamin E TPGS as emulsifiers. Reprinted with permission from Ref. 4, © 2007, Elsevier.

Instruments). SEM requires a coating of the sample with platinum, which was performed in an Auto Fine Coater (JEOL, JFC-1300). AFM was conducted with Nanoscope IIIa in the tapping mode. Before observation, the nanoparticles sample was fixed on a double-sided sticky tape that was stuck onto the standard sample stand.

Figure 1 shows a SEM image of the paclitaxel-loaded, TPGS-emulsified PLGA nanoparticles, which are prepared by the single emulsion method. It can be seen that all nanoparticles were in fine spherical shape with smooth surfaces and without any aggregation or adhesion.

2.2.3. *Surface charge*

Surface charge was measured by the Zeta potential analyzer. (Zeta Plus, Brookhaven Instruments Corporation, Huntsville, NY, USA). The Zeta-potential for the paclitaxel-loaded, TPGS-emulsified PLGA nanoparticle prepared in this article is $-21.45 \pm 3.57\,\mathrm{mV}$.

2.2.4. *Surface chemistry*

The X-ray photoelectron spectroscopy (XPS, AXIS His-165 Ultra, Kratos Analytical, Shimadzu) was utilized for analyzing the surface chemistry of the nanoparticles. The angle of X-ray used in XPS analysis was 90°. The analyzer was used in fixed transmission mode with pass energy of 80 eV for the survey spectrum covering a binding energy which ranges from 0 to 1200 eV. Peak curve fitting of the C1s (atomic orbital 1s of carbon) envelope was performed using the software provided by the instrument manufacturer.

Figure 2 shows a XPS spectrum of the paclitaxel-loaded, TPGS-emulsified PLGA nanoparticles, which are prepared by the single emulsion method. The surface property of the nanoparticles exhibits critical effects on their *in vitro* and *in vivo* behavior. There are various analytical techniques for surface analysis of the particles. The analytical resolution, detection limit and the depth resolution are different. Among them, SEM, FTIR and ESCA (XPS) are adopted extensively to evaluate the surface characteristics of powdered drugs in pharmaceutics. The current work utilized SEM, AFM, XPS and FTIR-PAS to characterize the surface property of the produced nanoparticles.

2.2.5. *Physical status of drug in nanoparticles*

The physical status of the paclitaxel inside the nanoparticles was characterized by the differential scanning calorimetry thermogram analysis (DSC, 2920 Modulated, Universal V2.6D TA instruments). 8 mg of sample was sealed in standard aluminum pans with lids. The samples were purged with pure dry nitrogen at a flow rate of 40 ml/min. A temperature ramp speed was set at 10°C/min and the heat flow was recorded from 0 to 250°C. Indium was used as the standard reference material to

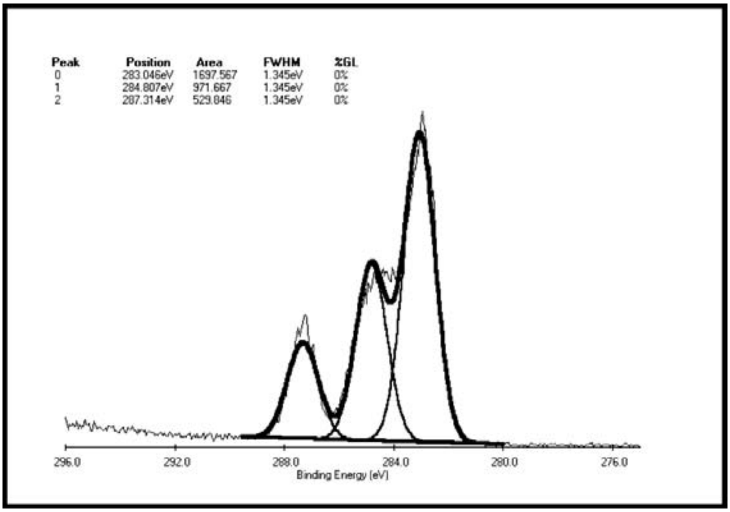

Peak	Position	Area	FWHM	%GL
0	283.046eV	1697.567	1.345eV	0%
1	284.807eV	971.667	1.345eV	0%
2	287.314eV	529.846	1.345eV	0%

Fig. 2. Surface analysis of paclitaxel-loaded, TPGS-emulsified PLGA nanoparticles by XPS. Reprinted with permission from Ref. 10, © 2002, Elsevier.

calibrate the temperature and energy scales of the DSC instrument. DSC analysis of pure paclitaxel was previously carried out to identify the melting point peak. As a control, the physical mixtures of paclitaxel and placebo nanoparticles of 1% and 10% paclitaxel proportion were analyzed to observe the change of the melting endotherm of crystallized paclitaxel in the mixture. Subsequently, the nanoparticles with 10% loading level of paclitaxel were analyzed as needed by the sensitivity of the apparatus.

Figure 3 shows the DSC thermogram analysis, which provided qualitative and quantitative information about the physical status of the drug in the nanoparticles and the control samples, which are the pure drug and the physical mixture of pure paclitaxel and placebo PLGA nanoparticles. The pure paclitaxel showed an endothermic peak of melting at 223.0°C (sample 1), which was broadened and shifted to a lower temperature at about 218.0°C (sample 2) for the 10% paclitaxel–placebo nanoparticles physical mixture. There was no peak observed at the temperature range of 150–250°C for the placebo nanoparticles and all drug loaded nanoparticles (samples 3, 4, 5). The DSC study did not detect any crystalline drug material in the nanoparticles samples. It can thus be concluded that the paclitaxel formulated in the four batches of nanoparticles was in an amorphous or disordered-crystalline phase of a molecular dispersion or a solid solution state in the polymer matrix after the fabrication. Moreover, the glass transition temperature of the polymer PLGA employed in all the four batches of nanoparticles was not influenced obviously by the procedure, which meant that the surfactant stabilizer did not influence the thermogram property of polymeric material significantly.

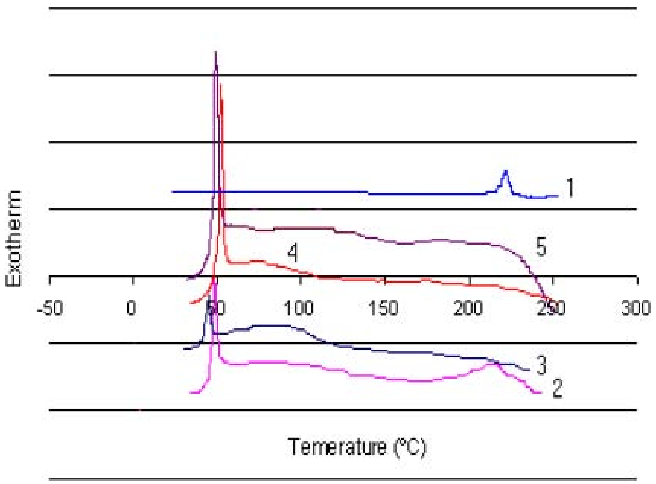

Fig. 3. DSC thermograms of (1) 100% paclitaxel; (2) Physical mixture of 10% paclitaxel and 90% PLGA; (3) Paclitaxel loaded nanoparticles with TPGS added in water; (4) Paclitaxel-loaded nanoparticles TPGS+PVA as emulsifier; (5) Paclitaxel-loaded nanoparticles with TPGS added in oil. Reprinted with permission from Ref. 5, © 2004, Bentham Science.

2.2.6. *Drug encapsulation efficiency*

The drug encapsulated in the nanoparticles was determined in triplicate by HPLC (Agilent LC1100). A reverse phase Inertsil® ODS - 3 column (150 × 4.6 mm inner diameter (i.d.), pore size 5 μm, GL Science Inc, Tokyo, Japan) was used. 3 mg of nanoparticles was dissolved in 1 ml of DCM and 5 ml of acetonitrile–water (50:50) was then added. A nitrogen stream was introduced to evaporate the DCM till a clear solution was obtained. The solution was put into a vial for HPLC to detect the paclitaxel concentration. The mobile phase consisted of a mixture of acetonitrile and water (50:50, v/v), and was delivered at a flow rate of 1.00 ml/min with a pump (HP 1100 High pressure Gradient Pump). A 100 μl aliquot of the sample was injected with an autoinjector (HP 1100 Autosampler). The column effluent was detected at 227 nm with a variable wavelength detector (HP 1100 VWD). The calibration curve for the quantification of paclitaxel was linear over the range of standard concentration of paclitaxel at 60–60,000 ng/ml with a correlation coefficient of $R^2 = 1.0$. The solvent for calibration is the mixture of acetonitrile and water (50:50, v/v). As inefficient extraction may exist, a correction of the calculated encapsulation efficiency is needed. The recovery efficiency factor of the extraction procedure on encapsulation efficiency was determined according to the following method. A certain weight of pure paclitaxel which was similar to the amount loaded in a certain amount of nanoparticles and 3.0–5.0 mg of placebo nanoparticles or polymer were dissolved in 1 ml of DCM. 5 ml of acetonitrile–water (50:50) was added. The same extraction procedure as described above was done. The resulted factor was

100%, which means that about 100% of the original amount of the paclitaxel could be detected. The encapsulation efficiency of paclitaxel was obtained as the mass ratio between entrapped amount of paclitaxel in nanoparticles and the drugs used in the preparation.[10]

The drug encapsulation efficiency (EE) for the paclitaxel-loaded, TPGS-emulsified PLGA nanoparticles prepared in this article is 97.6%. 100% EE could be achieved by using TPGS as emulsifier, which was shown in our report.[10]

2.2.7. *In vitro drug release*

The release of paclitaxel from the nanoparticles was measured in triplicate in phosphate-buffered saline, PBS (pH 7.4). 10 mg of paclitaxel-loaded nanoparticles were suspended in 10 ml of buffer solution in a screw capped tubes and placed in an orbital shaker water bath (GFL-1086, Lee Hung Technical Company, Bukit Batok Industrial Park A, Singapore), which was maintained at 37°C and shaken horizontally at 120 rpm. At particular time interval, the tubes were taken out of the water bath and centrifuged at 8000 rpm for 10 min. The precipitated nanoparticles were resuspended in 10 ml of fresh buffer before being put back in the shaker bath. The supernatant was taken for analysis of paclitaxel concentration, which was first extracted with 1 ml of DCM, followed by adding 3 ml of the mixture of acetonitrile and water (50:50, v/v), then evaporated until a clear solution was obtained under a stream of nitrogen. HPLC analysis was then conducted as previously described. Similar to the measurement of encapsulation efficiency, the extraction procedure needs to be analyzed for the extraction recovery efficiency due to inefficient extraction. Similarly, known mass at a certain range of pure paclitaxel was dealt with the same procedure as mentioned above. The determined factor was 77.5%, which meant that the obtained extraction solution only contained 77.5% of the original paclitaxel after all undergoing the related process. The data obtained for analysis of the *in vitro* release were corrected accordingly.

Figure 4 shows the *in vitro* drug release profiles of paclitaxel-loaded PLGA nanoparticles in PBS. The drug release from the nanoparticles showed a multiphase behavior in general, which included an initial burst (about 40% in the first day), a fast zero-order release (about 10% in the 2–5 days), and a slow zero-order release afterwards. The release sustained for more than one month. It should be pointed out that the *in vivo* drug release could be very different from that obtained in the *in vitro* experiments, since the environmental condition may have significant effects on drug release from the nanoparticles.[25] The *in vitro* experiments, however, can provide certain guidance for prediction of the possible effects of the pre-designed chemotherapy, especially the comparison of different formulations studied under the same condition. Recently, several groups have designed *in vitro* assays that can better predict *in vivo* release.[26] The *in vitro* and *in vivo* drug release kinetics is determined by the composition and process parameters of the drug-loaded nanoparticles, which are adjustable to achieve a desired pattern.[4]

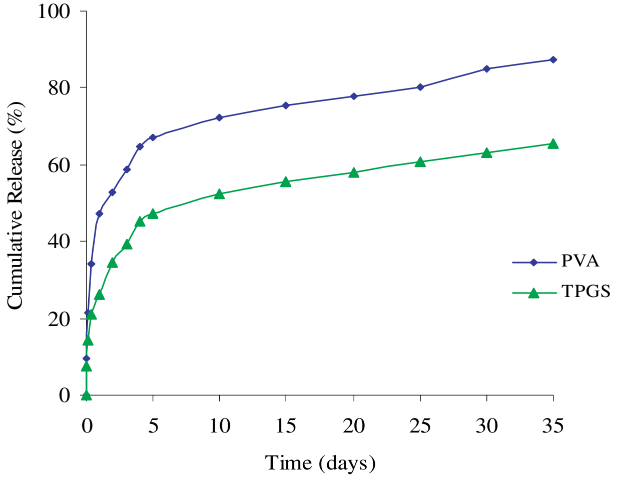

Fig. 4. The *in vitro* release curves for paclitaxel-loaded PLGA nanoparticles with PVA and vitamin E TPGS emulsifiers. Reprinted with permission from Ref. 4, © 2007, Elsevier.

3. *In vitro* Cellular Uptake of Nanoparticles

MCF-7 breast cancer cells were cultured in Dulbecco's Modified Eagle Medium (DMEM) supplemented with 10% fetal calf serum, 1% penicillin–streptomycin in atmosphere of 5% CO_2 on the Lab-Tek® chambered cover glass (Nalge Nunc International, Naperville, IL, USA), which was maintained at 37°C and 90% relative humidity for 24 hr. The cell monolayer was then incubated for 2 hr with a suspension of coumarin-6-loaded, TPGS-emulsified PLGA nanoparticles or the control TPGS-emulsified PLGA nanoparticles without coumarin-6-encapsulated at the same 250 μg/ml nanoparticle concentration in the medium. Coumarin-6 was used as a fluorescent marker for cellular internalization of the host nanoparticles because of their low leakage rate and high fluorescence activity. Following the removal of the nanoparticle suspension, the cell monolayers were rinsed thrice with cold PBS to remove the excess nanoparticles not taken up by the cells. After fixation with ethanol for 20 min, the cells were washed twice again with PBS. The cell nuclei were then stained with propidium iodide (PI, 20 μg/ml in PBS) for 40 min and rinsed with PBS to remove the free dye. The cells were viewed and imaged by using a confocal laser scanning microscope (CLSM, Zeiss LSM 410, Germany) equipped with the Fluoview FV300 imaging software. Fluorescein isothiocyanate (FITC) filter and PI filter were selected to get images for coumarin-6-loaded nanoparticles and PI-stained nucleus, respectively.

Figure 5 shows the CLSM images of a MCF-7 cell for the FITC (b), PI (c) and combined FITC+PI (a) channels (obtained by using appropriate filters), respectively, after 2 hr incubation with coumarin-6-loaded, TPGS-emulsified PLGA nanoparticle at 37°C. The nucleus was stained by PI (red). The uptake of coumarin-6-loaded nanoparticles (green) in the MCF-7 cell was visualized by overlaying the

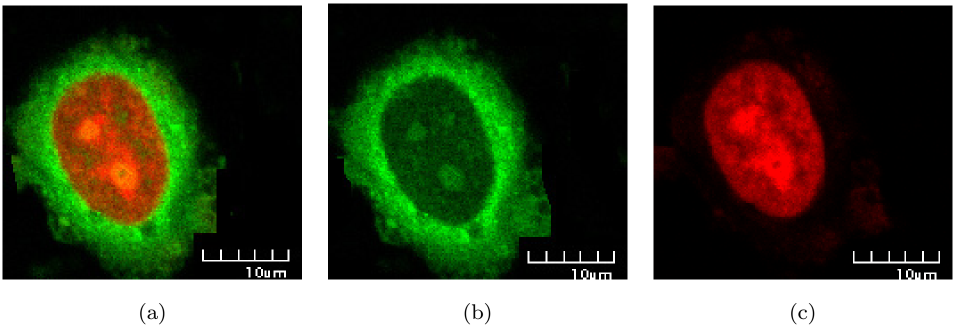

Fig. 5. MCF-7 cancer cells incubated with coumarin-6-loaded, TPGS-emulsified PLGA nanoparticles for 2 hr: (a) combined FITC+PI channels; (b) FITC channel and (c) PI channel. The nanoparticles concentration in the incubation medium was 250 μg/ml and the experiments were conducted at 37°C in both cases. Reprinted with permission from Ref. 4, © 2007, Elsevier.

images obtained through the FITC filter and the PI filter. We also obtained CLSM images of a MCF-7 cell treated with the placebo (control) TPGS-emulsified PLGA nanoparticles at the same nanoparticle concentration and in the same period. And we found that both the cell and the TPGS-emulsified PLGA nanoparticles have no auto-fluorescence (imaged not shown). It can be observed that the coumarin-6-loaded nanoparticles (green) were aggregated markedly around the nucleus. Some have penetrated into the nucleus.

It may be concerned that the fluorescent coumarin-6 markers formulated in the nanoparticles would have leakage that may affect the result of the cellular uptake measurement. To address this problem, we have conducted experiment to measure the *in vitro* release of coumarin-6 from the nanoparticles and our results showed that the leakage for the first 24 hr was less than 5% and thus negligible.[13]

4. *In vitro* Cytotoxicity

The therapeutic effects of nanoparticle formulation of the drug of interest can be investigated *in vitro* by using various cell lines in close comparison with those of the original drug. The advantages of *in vitro* cell viability experiment are that various experimental conditions such as drug concentration, nanoparticles size and surface coatings, pH and temperature can be easily realized and quantitative results can be obtained. *In vitro* cell viability investigation can give preliminary evaluation for screening of the nanoparticle formulations under development although *in vitro* and *in vivo* correlation has yet to be investigated.

In vitro cell viability of the therapeutic agent formulated in nanoparticles of biodegradable polymers can be investigated by using the MTT assay.[5,14] In order to determine the cytotoxic effect of the polymer used to prepare the nanoparticles, the employed cells were also incubated with placebo nanoparticles (with no drug encapsulated). The effect of different dosage forms of paclitaxel on the cell viability was assessed by the colorimetric MTT assay. This assay is based on

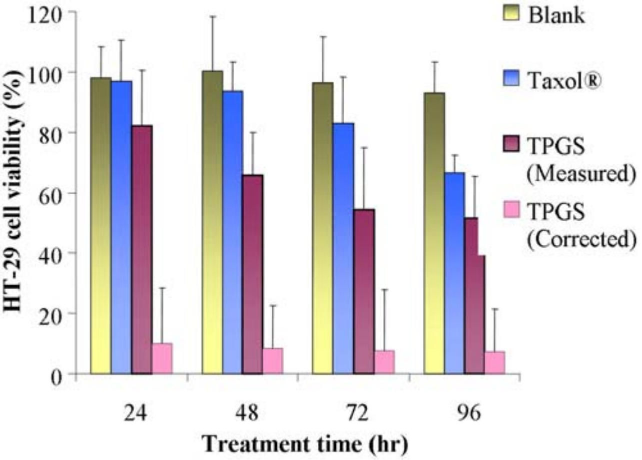

Fig. 6. Viability of HT-29 cells indicating effect of the treatment time when incubated with 0.25 μg/ml of paclitaxel in different formulations: Taxol® and vitamin E TPGS-coated PLGA nanoparticles, for 24, 48, 72 and 96 hr at 37°C. Cell viability was determined by the MTT assay and expressed as a percentage of the control wells (cells without treatment). Results shown in this figure represent the mean ± standard deviation obtained for two independent experiments performed with $n = 5$.

the cellular reductive capacity of living cells to metabolize the yellow tetrazolium salt, 3-(4, 5-dimethylthizaol-2-yl)-3, 5-diphenyl tetrazolium bromide (MTT), to a chromophore, formazan product, whose absorbance can be determined by spectrophotometric measurement by a microplate reader. Technical details are refereed to our earlier publications.[5,14]

Figure 6 shows the viability of HT-29 cells, a colon cancer cell line, incubated with placebo TPGS-coated PLGA nanoparticles, paclitaxel-loaded, TPGS-coated PLGA nanoparticles, and Taxol® at the same 0.25 μg/ml paclitaxel concentration for 24, 48, 72 and 96 hr at 37°C, respectively. It can be seen that the mortality of the HT-29 cells after 24 and 96 hr incubation are 1.88 and 7.13% for the placebo PLGA nanoparticle (which means that the materials used for nanoparticle preparation are biocompatible); 3.19 and 33.5% for paclitaxel formulated in its current clinical dosage form Taxol®, and 18.0 and 48.6% for paclitaxel formulated in the TPGS-emulsified PLGA nanoparticles, respectively at the same 0.25 μg/ml paclitaxel concentration in the medium at 37°C. This means the nanoparticle formulation can be 5.64 and 1.45 times more effective than Taxol® for 24 and 96 hr, respectively after the administration. The results should be even better if we take into account the sustainable drug release feature of the nanoparticle formulation. It can be seen from Fig. 5 that only 24.4 and 27.7% of the drug encapsulated in the nanoparticles were released into the medium and thus available to treat the cancer cells after 24 and 96 hr, respectively. Since 24.4 and 27.7% of the drug encapsulated in the nanoparticles can achieve 5.64 and 1.45 times of the mortality effects of 100% paclitaxel in the Taxol® formulation, the effectiveness of 100% drug in the nanoparticle formulation would have been 46.2 and 10.5 times higher than that of Taxol® if evaluated in 24 and 96 hr, respectively.

The analysis of IC50, which is defined as the drug concentration needed to kill 50% of the cancer cells at a given period, confirmed such results since both of mortality of the cells and IC50 of the drug represent the effectiveness of the raw drug and the drug formulated in the nanoparticles (data not shown).

5. *In Vivo* Pharmacokinetics

The animal experiment protocols of this research were approved by the Institutional Animal Care and Use Committees (IACUC, Protocol no: 802/05), Office of Life Science, NUS. The *in vivo* PK of paclitaxel formulated as Taxol® or in our TPGS-emulsified PLGA nanoparticles were measured in male Sprague–Dawley rats (180–200 gm and 4–5 week old) supplied by the Laboratory Animals Center of Singapore and maintained at the Animal Holding Unit of NUS. Throughout the experiment, the animals were housed, four or five per cage, in standard cages, which were maintained at 22±2°C and 50–60% relative humidity under a 12-hr light/12-hr dark cycle. The animals were kept in these facilities for at least 5 days before the experiments. During the experiments, the animals were randomly assigned to two groups of three rats each. Group 1 received an intravenous (*i.v.*) injection of paclitaxel-loaded TPGS-emulsified PLGA nanoparticles and Group 2 received an injection of Taxol®. The paclitaxel-loaded nanoparticles and Taxol® were dispersed or diluted with saline and administrated through the tail vein at the same paclitaxel dose of 10 mg/kg body weight. All animals were observed for their general condition, clinical signs and mortality.

For Group 1, blood samples were collected at 0 (pre-dose), 1, 2, 4, 8, 10 and 24 hr, and then every 24 hr until 168 hr post-treatment. For Group 2, blood samples were collected at 0 (pre-dose), 0.25, 0.5, 1, 2, 4, 8, 12 and 24 hr after administration of the drug. Plasma samples were harvested by centrifugation at 1500 × g for 10 min and stored at −20°C for HPLC or LC/MS/MS analysis. Liquid–liquid extraction was performed prior to analysis. The *in vivo* PK of Taxol® and the TPGS-emulsified PLGA nanoparticle formulation is expressed in plots of the plasma drug concentration vs. time. The two key parameters for representation of therapeutic effects are AUC ("area under the curve" of plasma drug concentration vs. time) and the sustainable therapeutic time, i.e. the time at which the plasma paclitaxel concentration dropped below the minimum effective level (43 ng/ml).[27]

Figure 7 shows the plasma concentration–time profiles of paclitaxel formulated in Taxol® (10 mg/kg) and the TPGS-emulsified PLGA nanoparticles (10 mg/kg as well as 40 mg/kg) after *i.v.* administration to SD rats. The concentrations between the maximum-tolerable level (8,540 ng/ml) and the minimum-effective level (43 ng/ml) show the therapeutic window of the drug. We found that the AUC was 35,470 ng-hr/ml and for Taxol® and 27,200 ng-hr/ml for the nanoparticle formulation. Although Taxol® had a larger AUC, its PK was not as favorable as that

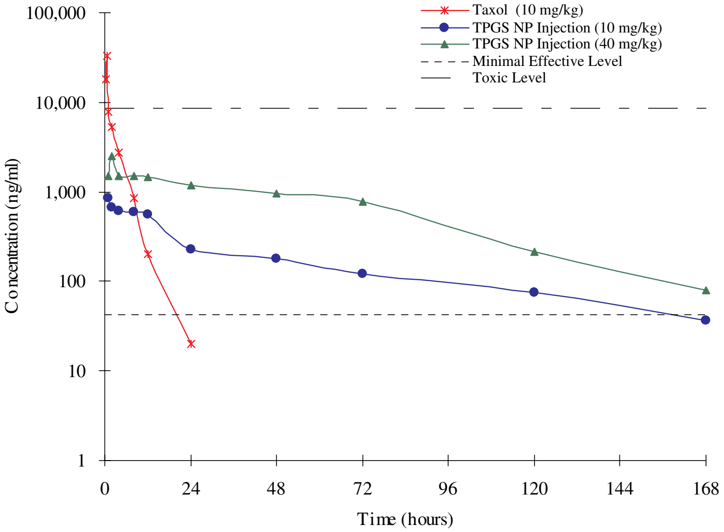

Fig. 7. The concentration–time curves of paclitaxel in rat after intravenous administration of 10 mg/ml and 40 mg/ml of vitamin E TPGS-emulsified nanoparticles. Reprinted with permission from Ref. 4, © 2007, Elsevier.

of the nanoparticles formulation. For Taxol®, of the 35,500 ng-hr/ml total AUC, 6,130 ng-hr/ml (17.3%) is located above the maximum tolerance level (8,540 ng/ml for paclitaxel), which would cause serious side effects. One of the advantages of the nanoparticle formulation is that it should cause much less side effects than Taxol®, which are evidenced by little AUC above the maximum tolerance drug level in the plasma.

The sustainable therapeutic time at which the plasma drug concentration dropped below the minimum effective level, was less than 22.2 hr for Taxol®, which means that one shot of the therapy lasted less than 22.2 hr. Instead, the sustainable therapeutic time for one shot of the TPGS-emulsified PLGA nanoparticle formulation at the same 10 mg/kg dose was almost 168 hr (i.e. 7 days), which is 7.6 times longer than that of Taxol®. The sustainability of a dosage form can also be evaluated from the half-life of the plasma drug concentration. The half-life for 10 mg/kg dose of Taxol® was 0.830 hr (50′), while it was 16.8 hr for the nanoparticle formulation, which is 20 times longer. This extension of the half-life of the nanoparticle formulation vs. Taxol® can achieve a much higher therapeutic efficacy.

Since the paclitaxel-loaded nanoparticles have the features of sustained and controlled drug release, we tested whether the nanoparticle formulation can provide higher dose tolerance than Taxol®. As shown in Fig. 8, an increase of the dosage of *i.v.* injection of the TPGS-emulsified PLGA nanoparticle formulation to 40 mg/kg yielded a total AUC of 111,540 ng-hr/ml with no portion of the curve located above the maximum tolerance level; this AUC is approximately three times that for 10 mg/kg dose of Taxol® and four times that for 10 mg/kg dose of the nanoparticle formulation. Furthermore, all rats receiving Taxol® at doses higher than 20 mg/kg showed apathy and died after ∼1 hr, whereas neither apathy nor death was observed for the animals receiving 40 mg/kg dose of the nanoparticle formulation. Thus, the nanoparticle formulation significantly increased the drug tolerance of the animals. These results suggest that sustainable chemotherapy of one shot for more than 7 days may be feasible for human patients by the nanoparticle formulation.

6. Xenograft Model

Tumor was induced by injection of 3×10^6 C6 cancer cells into the right flank of severely combined immuno-deficient (SCID) mice, that were aged 6–8 weeks and weighing above 200 g. Tumor nodules were allowed to grow to a noticeable volume (16 days after injection in this case) prior to initiation of the treatment, which was carried out by intratumoral injection of either the nanoparticles suspension or Taxol at the same 10 mg/ml dose. Tumor size was then measured day by day.

Figure 8 shows the changes in the size of C6 tumor nodules after intratumoral administration of saline, paclitaxel formulated in Taxol® and our paclitaxel-loaded TPGS-emulsified PLGA nanoparticles formulation on day 11, 16 and 21 at the same 10 mg/kg dose (mean ± SD, $n = 5, p = 0.05$). It can be seen from this figure that the tumors of the animal in Group 1 (control) had ∼10 and 29 times volume growth on day 21 and 31 without drug treatment. With three intratumoral injections of 10 mg/kg dose of paclitaxel formulated in Taxol® or in the nanoparticles drug treatment on day 11, 16 and 21, the tumors of the animal in Group 2

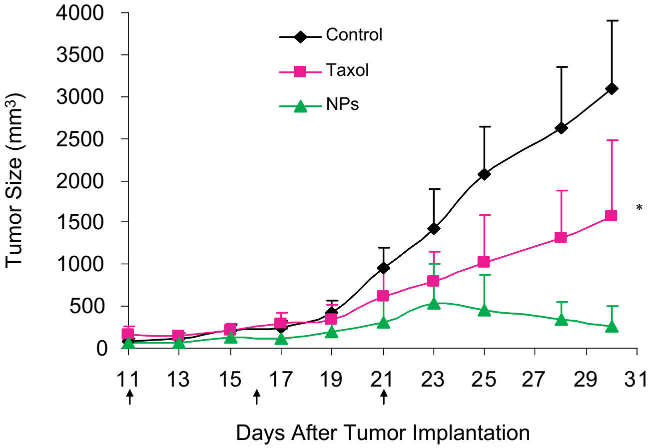

Fig. 8. Changes in the size of C6 tumor nodules after intratumoral injections on day 11, 16 and 21 with saline, Taxol and paclitaxel formulated in TPGS-emulsified PLGA nanoparticles at the same 10 mg/kg dose (mean ± SD, $n = 5, p = 0.05$). Reprinted with permission from Ref. 4, © 2007, Elsevier.

had ∼6 and 1.9 times volume growth and in comparison, those of the animal in Group 3 had only 1.5 and 1.25 times volume growth on day 21 and 31, respectively, which means that our nanoparticle formulation could be 4 times and 1.5 times more effective than Taxol® in suppressing tumor growth.

7. Conclusions

This article demonstrates a typical example of nanomedicine by using a full spectrum of proof-of-concept experiments, from nanoparticle formulation and characterization, *in vitro* drug release and cellular uptake, to *in vivo* pharmacokinetics and xenograft tumor model, to show how nanoparticles of biodegradable polymers could be developed to formulate anticancer drugs with no poisonous adjuvant (such as cremophor EL for Taxol®) as well as to realize a sustained and controlled chemotherapy. Our *in vitro* and *in vivo* experiments both showed that paclitaxel formulated in the TPGS-emulsified PLGA nanoparticles could result in a much higher therapeutic index (i.e. AUC) and a much longer sustainable therapeutic time (i.e. the half-life of the drug in the plasma) with much lesser side effects in comparison with Taxol®. Moreover, the nanoparticle formulation can significantly increase the tolerance of the animals to the drug. Scientifically, our *in vivo* experiments have provided quantitative physical evidence that nanoparticles of sufficiently small size and appropriate surface coating (e.g. the TPGS-emulsified PLGA nanoparticles of 100–300 nm in diameter) can avoid elimination by the RES. Xenograft model investigation further confirmed the advantages of our nanoparticle formulation of paclitaxel versus Taxol®. Paclitaxel was used in this study as a prototype drug. The nanoparticle technology developed in our research should be applicable for any other drug, either hydrophobic or hydrophilic. Moreover, nanoparticles can be conjugated to molecular probes for targeted delivery of diagnostic and therapeutic agents for cancer detection and treatment, which will make cancer curable at its earliest possible stage.[28,29] Also, nanoparticles of biodegradable polymers can be applied for safe and efficient delivery of biological macromolecules such as proteins and peptides.[30]

There have been two main concerns on nanotechnology for biomedical applications: feasibility and safety. Can the nanoparticles stay in the blood system to perform their function? Would they be recognized by our body defense system and thus be eliminated from the body? If the answer is positive, what could be the impact of the nanoparticles on health? Our research addressed the first concern. Scientifically, we showed that nanoparticles of small enough size and appropriate surface coating could escape from elimination by the reticuloendothelial system and thus realize sustained and controlled chemotherapy. With regard to safety, it is difficult to prove any product is absolutely safe. Nevertheless, when we say nanoparticles, more than 90% of them are non-degradable nanoparticles such as metal and inorganic nanoparticles, which are most likely incompatible. Our nanoparticles are degradable and the degradation rate can be controlled. The nanoparticles of biodegradable polymers are thus less harmful than other nanoparticles.

Acknowledgments

The author is grateful to his postdoctoral fellows and students Zhao Lingyun, Cui Weiyi, Zhang Zhiping, Gajadhar Bhakta, Khin Yin Win, Dong Yuancai, Ruan Gang and Sun Bingfeng at NUS for their hard work in the experiments. This research was supported by the A*STAR BMRC Singapore Cancer Syndicate Grant UU0028 (SS Feng, PI) and NUS FRC Grant R279-000-226-112 (SS Feng, PI).

References

1. Feng SS, New-concept chemotherapy by nanoparticles of biodegradable polymers — where are we now? *Nanomed* **1**:297–309, 2006.
2. Feng SS, Nanoparticles of biodegradable polymers for new concept chemotherapy, *Expert Rev Med Devices* **1**:115–125, 2004.
3. Feng SS and Chien S, Chemotherapeutic engineering: Application and further development of chemical engineering principles for chemotherapy of cancer and other diseases, *Chem Eng Sci* **58**:4087–4114, 2003.
4. Feng SS, Zhao LY, Zhang ZP, Bhakta G, Win KY, Dong YC and Chien S, Chemotherapeutic engineering: Vitamin E TPGS-emulsified nanoparticles of biodegradable polymers realized sustainable paclitaxel chemotherapy for 168 hours, *in vivo Chem Eng Sci* **62**:6641–6648, 2007.
5. Feng SS, Mu L, Win KY and Huang GF, Nanoparticles of biodegradable polymers for clinical administration of paclitaxel, *Curr Med Chem* **11**:413–424, 2004.
6. Pridgen EM, Lander R and Farokhzad OC, Biodegradable, polymeric nanoparticle delivery systems for cancer therapy, *Nanomed* **2**:669–680, 2007.
7. Ehrlich P, Chemotherapeutics: Scientific principles, methods and results, *Lancet* II: 445–451, 1913.
8. Feng SS, Huang GF and Mu L, Nanoparticles of biodegradable polymers: A system for clinical administration of an anticancer drug paclitaxel (Taxol®), *Ann Acad Med Singapore* **29**:633–639, 2000.
9. Feng SS and Huang GF, Effects of phospholipids as emulsifiers on controlled release of paclitaxel from nanoparticles of biodegradable polymers, *J Control Release* **71**:53–69, 2001.
10. Mu L and Feng SS, Vitamin E TPGS used as emulsifier in the solvent extraction/evaporation technique for fabrication of polymeric nanoparticles for controlled release of paclitaxel, *J Control Release* **80**:129–144, 2002.
11. Mu L and Feng SS, A novel controlled release formulation for anticancer drug paclitaxel (Taxol®): PLGA nanoparticles containing vitamin E TPGS, *J Control Release* **86**:33–48, 2003.
12. Mu L and Feng SS, PLGA/TPGS nanoparticles for controlled release of paclitaxel: Effects of the emulsifier and the drug loading ratio, *Pharm Res* **20**:1864–1872, 2003.
13. Khin YW and Feng SS, Effects of particle size and surface coating on cellular uptake of polymeric nanoparticles for oral delivery of anticancer drugs, *Biomater* **26**:2713–2722, 2005.
14. Khin YW and Feng SS, *In vitro* and *in vivo* studies on Vitamin E TPGS-emulsified poly(D,L-lactic-co-glycolic acid) nanoparticles for clinical administration of paclitaxel, *Biomater* **27**:2285–2291, 2006.
15. Dong YC and Feng SS, Paclitaxel-loaded methoxy poly(ethylene glycol)-poly(lactide) (MPEG-PLA) nanoparticles by nanoprecipitation method, *Biomater* **25**:2843–2849, 2004.

16. Dong YC and Feng SS, Nanoparticles of montmorillonite (MMT)/poly (D,L-lactide-co-glycolide) (PLGA) for oral delivery of anticancer drugs, *Biomater* **26**:6068–6076, 2005.
17. Dong YC and Feng SS, Nanoparticles of poly(D,L-lactide)/methoxy poly(ethylene glycol)-poly(D,L-lactide) blends for controlled release of paclitaxel, *J Biomed Mater Res* Part A **78A**:12–19, 2006.
18. Dong YC and Feng SS, *In vitro* and *in vivo* evaluation of methoxy polyethylene glycol-polylactide (MPEG-PLA) nanoparticles for small molecule drug chemotherapy, *Biomater* **28**:4154–4160, 2007.
19. Zhang ZP and Feng SS, The drug encapsulation efficiency, *in vitro* drug release, cellular uptake and cytotoxicity of paclitaxel-loaded poly(lactide)-tocopheryl polyethylene glycol succinate nanoparticles, *Biomater* **27**:4025–4033, 2006.
20. Zhang ZP and Feng SS, Nanoparticles of poly(lactide)/Vitamin E TPGS copolymer for cancer chemotherapy: Synthesis, formulation, characterization and *in vitro* drug release, *Biomater* **27**:262–270, 2006.
21. Zhang ZP and Feng SS, Self-assembled nanoparticles of poly(lactide)/Vitamin E TPGS copolymers for oral chemotherapy, *Int J Pharma* **324**:191–198, 2006.
22. Zhang ZP and Feng SS, *In vitro* investigation on poly(lactide)-tween 80 copolymer nanoparticles fabricated by dialysis method for chemotherapy, *Biomacromolecules* **7**:1139–1146, 2006.
23. Mu L and Feng SS, Fabrication, characterization and *in vitro* release of paclitaxel loaded poly(lactic-co-glycolic acid) (PLGA) nanoparticles prepared by the spray dry technique with phospholipids/cholesterol as additives, *J Control Release* **76**:239–254, 2001.
24. Dong YC and Feng SS, Poly(D,L-lactide-co-glycolide) (PLGA) nanoparticles prepared by high pressure homogenization for paclitaxel chemotherapy, *Int J Pharm* **342**:208–214, 2007.
25. Kim SY, Le YM, Baik DJ and Kang JS, Toxic characteristics of methoxy poly(ethylene glycol)/poly(epsilon-caprolactone) nanoparticles — *in vitro* and *in vivo* studies in the normal mice, *Biomater* **24**:55–63, 2003.
26. Kaul G and Amiji M, Tumor-targeted gene delivery using poly(ethylene glycol)-modified gelatin nanoparticles: *In vitro* and *in vivo* studies, *Pharm Res* **22**:951–961, 2005.
27. Liebmann J, Cook JA, Lipschultz C, Teague D, Fisher J and Mitchell JB, Cytotoxic studies of paclitaxel (Taxol) in human tumor cell lines, *Br J Cancer* **68**:1104–1109, 2003.
28. Sun BF, Ranganathan B and Feng SS, Multi-functional poly(D,L-lactide-co-glycolide)/montmorillonite (PLGA/MMT) nanoparticles decorated by Trastuzumab for targeted chemotherapy of breast cancer, *Biomater* **29**:475–486, 2008.
29. Zhang ZP, Lee SH and Feng SS, Folate-decorated poly(lactide-co-glycolide)-Vitamin E TPGS nanoparticles for targeted drug delivery, *Biomater* **28**:1889–1899, 2007.
30. Lee SH, Zhang ZP and Feng SS, Nanoparticles of poly(lactide)-tocopheryl polyethylene glycol(PLA-TPGS) copolymers for protein drug delivery, *Biomater* **28**:2041–2050, 2007.